

Environmentally Benign Synthesis of Sn(II)-based Metal-Organic Framework and its Derivative SnO₂ Nanoparticles for the Decontamination of Water

A Dissertation

*Submitted in the partial fulfillment for the degree of
Doctor of Philosophy*



Arnab Ghosh

(Roll No. 156152002)

Thesis Supervisor: Prof. Gopal Das

Thesis Co-Supervisor: Prof. Sasidhar Gumma

Centre for the Environment

Indian Institute of Technology Guwahati

India-781039

Environmentally Benign Synthesis of Sn(II)-based Metal-Organic Framework and its Derivative SnO₂ Nanoparticles for the Decontamination of Water

A Dissertation

*Submitted in the partial fulfillment for the degree of
Doctor of Philosophy*



Arnab Ghosh

(Roll No. 156152002)

Thesis Supervisor: Prof. Gopal Das

Thesis Co-Supervisor: Prof. Sasidhar Gumma

Centre for the Environment

Indian Institute of Technology Guwahati

India-781039

***Dedicated to my Parents and to the
memory of my late Grandmother***



INDIAN INSTITUTE OF TECHNOLOGY GUWAHATI

Centre for the Environment

STATEMENT

I do hereby declare that the matter embodied in this thesis is the result of investigations carried out by me in the Centre for the Environment, Indian Institute of Technology Guwahati, India, under the guidance of Prof. Gopal Das, Department of Chemistry & Centre for the Environment, and Prof. Sasidhar Gumma (co-supervisor), Department of Chemical Engineering, Indian Institute of Technology Tirupati, India.

In keeping with the general practice of reporting scientific observations, due acknowledgements have been made wherever this work is based on the findings of other investigators.

4th September, 2020

IIT Guwahati

Arnab Ghosh

(Arnab Ghosh)



INDIAN INSTITUTE OF TECHNOLOGY GUWAHATI

Centre for the Environment

CERTIFICATE

This is to certify that Mr. Arnab Ghosh has been working under my supervision since July, 2015 as a regular registered Ph.D. student. His thesis entitled “**Environmentally benign synthesis of Sn(II)-based metal-organic-framework and its derivative SnO₂ nanoparticles for the decontamination of water**” is authentic record of the results obtained from the research work carried out under my supervision in the Centre for the Environment, Indian Institute of Technology Guwahati, Assam, India. I am forwarding his thesis to submit for the award of degree of Doctor of Philosophy, from this institute. I hereby certify that he has fulfilled all the requirements, according to the rules of this institute regarding the investigations embodied in his thesis and this work has not been submitted elsewhere for a degree.

Prof. Sasidhar Gumma

(Thesis Co-Supervisor)

Professor

Department of Chemical Engineering

IIT Tirupati

Andhra Pradesh - 517506, India

Prof. Gopal Das

(Thesis Supervisor)

Professor

Department of Chemistry

IIT Guwahati

Assam - 781039, India

Acknowledgment

Foremost, I express my heartfelt gratitude to the supreme power ‘God-The Almighty’ and my late father Shri Asit Baran Ghosh for showering blessings on me and always guiding me in the right path of life.

Next, I would like to express my warmest thanks to my supervisor Prof. Gopal Das for his unwavering support during my Ph.D. study and research, for his patience, encouragement, constant guidance, and sharing immense knowledge. His expert advice and friendly guidance were of immense help during my research tenure. I could not have imagined having a better advisor and mentor for my Ph.D. study.

Besides my advisor, I would like to extend my sincere thanks to my doctoral committee members Prof. Sasidhar Gumma (co-supervisor), Prof. B.P. Mandal, Dr. L.M. Kundu, Dr. Akshai A.S. for their motivation, enlightening comments, and hard questions. I would also like to express my sincere gratitude to Prof. Aiyagari Ramesh, Centre for the Environment HOC Prof. Mihir Purkait, staff members Mr. Partha P. Bakal, Dr. Deemponi Deka, Mr. Kaustubh Rakshit, Mr. Rajeev Gogoi, Mr. Mridul Das for their sustained help and support throughout my Ph.D. work.

I render my deepest thanks to my dear friends and batchmates Tanushree, Jayakrisnan, Sayanti, Polomi, Himali, Anupama, Ankur, Priya, as well as wonderful lab mates Biswajit, Utsav, Rupinder, Nilotpal, Deepa, Debojit, Asesh, Shikhamoni, Senjuti, Sagnik, Megha, for their cooperation and support. Besides, I sincerely thank my Environmental along with Chemical Lab mates Rajneesh, Arun, Smruti, Saran, Dibyajyoti da, Somnath da, Gopi bhaiya, Prithwi, Avik da, Pradip and Satyanaarayana bhaiya for their cooperative support. I wish to acknowledge my sincere appreciation for my beloved M.Tech batchmates Nitish, Pushpendra and my school friend Pradip, whose invaluable memories of friendship I continue to cherish.

Last but not least, I am greatly indebted to my parents, sister, and brother-in-law for their unconditional love, moral support, and sacrifices, without which I would not have envisioned the journey of my Ph.D.

Finally, I am truly grateful to Centre for The Environment, IIT Guwahati, and MHRD, Govt of India, for providing me with the opportunity and fellowship support to continue my Ph.D. work. Still, the list is incomplete without many names who have directly or indirectly helped me and contributed to my success.

Arnab

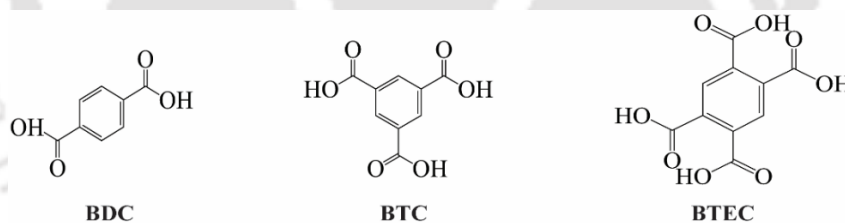
The contents of this synopsis report entitled “Environmentally benign synthesis of Sn(II)-based metal-organic-framework and its derivative SnO₂ nanoparticles for the decontamination of water” has been divided into six chapters based on the results of the experimental work performed during the research period.

Chapter 1: Introduction

This chapter outlines a brief introduction to “Metal-Organic-Framework (MOF)” as an interesting alternative to conventional adsorbents and its fascinating physico-chemical properties. In the past decade, researchers have shown a growing interest in the development of inorganic-organic hybrid porous materials known as metal-organic frameworks (MOFs). Generally, MOFs are composed of inorganic units of metal ions/ nodes and organic bridging units such as carboxylates or other organic anions (sulphonate, phosphonate, and heterocyclic compounds), which are connected via a coordination bond. In the past few years, MOFs have attracted wide attention due to their diverse chemical compositions, tunable pore size, a vast array of structures, high surface area, and coordinately unsaturated metal sites providing multiple functionalities regulating its adsorption capability. MOFs have shown potential applications in various fields, including catalysis, gas storage/adsorption, separation, drug delivery, chemical sensors, luminescence, adsorption of hazardous environmental pollutants. In comparison with the conventional porous materials such as zeolite and activated carbon, which require high temperature during synthesis, MOFs require less processing temperature. Besides, the pore size of the activated carbon and zeolites being limited to 0.3–1 nm, it potentially hinders the adsorption of large organic molecules and deters the desorption process. In contrast, due to the presence of abundant larger pores (micro to mesopores), adsorption of hazardous organic compounds is enhanced in MOFs providing, a promising removal efficiency for toxic environmental pollutants. All of the aforementioned advantages establish MOFs as a superior material for adsorption purposes.

However, the metal-ligand coordination bond is considered to be the weakest point in the MOFs, which determines its water stability. The interaction between the water and the MOFs results in competing for coordination to the metal ions/ nodes between the water molecules and the organic linkers. If the metal-organic linker coordination bond is not strong enough, it undergoes hydrolysis in the presence of water, thereby disrupting the MOF structure. Therefore, the strength of the metal-ligand bond in MOF illustrates its fundamental stability, which includes both thermodynamic and aqueous stability. According to Pearson’s hard/soft acid/ base (HSAB) concept, strong coordination bonds are formed between hard acid- hard base and soft acid- soft base. Carboxylates are regarded as hard bases and hence can coordinate

with the hard acid metal ions, namely Cr^{3+} , Al^{3+} , Fe^{3+} , and Zr^{4+} , to form water-stable MOFs. To date, very few MOFs like MIL-53(Fe, Cr, Al), UiO-66(Zr, Hf), and ZIFs-7,-8,-9 are reported being stable under aqueous environments. However, among the inorganic metal ions for MOF synthesis Sn(II) is the least explored. Sn(II), being a hard Lewis acid, can form a relatively stronger coordination bond with hard Lewis base, *i.e.*, carboxylate, resulting in the formation of a rigid interconnected framework structure. Sn(II)-dicarboxylate coordination polymers have been reported to be hydrothermally or solvothermally synthesized under alkaline conditions producing known homoleptic 1D and 2D architectures or 3D frameworks consisting of tin-oxide as secondary building units (SBUs). Recently, Lima et al., reported air and moisture stable Sn(II) coordination polymers with polytopic carboxylate based organic linkers. Moreover, tin being an environmentally benign material, has been used widely in food packaging. Tin salts possess low toxicity to the human body as they are poorly absorbed and rapidly excreted in the form of feces. Also, from the economic point of view, Sn(II) salts act as a low-cost precursor for material synthesis. To the best of our knowledge, a tin-based MOF has not been explored for water treatment applications, and there is a scarcity of studies with coordination polymers of Sn(II). The thesis reports a successful synthesis of Sn(II) based MOFs following hydrothermal/ solvothermal DMF free synthetic route using three different organic linkers viz. a) Benzene-1,4-dicarboxylic (BDC) acid b) Benzene-1,3,5-tricarboxylic acid (BTC) and c) 1,2,4,5-Benzenetetracarboxylic acid (BTEC).



The overall synthesis was carried out at moderate temperatures and in environmentally benign conditions. The different synthesis process parameters such as temperature, reaction time, solvent ratio, metal salt-organic linker ratio were optimized on the basis of final product yield and IR spectrum. Furthermore, the as-synthesized material was characterized using various characterization techniques and explored in water treatment applications.

Chapter 2: Experimental methods and characterization

In this chapter, a detailed, comprehensive report of the various reagents used in the synthesis of the MOFs, their synthetic process, specifications of analytical instruments employed in the characterization of the synthesized adsorbents, and detailed analysis of the results are represented thoroughly.

Chapter 3: Green synthesis of Sn(II)-BDC MOF and its application in the preferential adsorption of hazardous anionic dyes (*Microporous Mesoporous Mater.*, 2020, **297**, 110039)

In this chapter, Tin metal-organic framework [Sn(II)-BDC MOF] has been synthesized following the hydrothermal synthesis route in environmentally benign conditions. The material was applied for preferential and efficient removal of toxic anionic dyes *viz.* CR, EBT, and EY from aqueous solution. The thermal and aqueous stability of the material was confirmed using PXRD and FT-IR analysis. Adsorption kinetic study and the thermodynamic parameters were also investigated. A better fit with the second-order kinetic model indicated that the process is predominantly chemisorption. In a neutral solution, the surface of the MOF was found to be positively charged, while the dyes (CR, EBT, and EY) are negatively charged. Thus these anionic dyes get readily adsorbed on the surface of Sn(II)-BDC MOF through electrostatic interaction while adsorption of cationic dyes (MB, CV, BB, and RhB) was comparatively much lower owing to electrostatic repulsion. The Lewis base (NH₂) in CR interacts with the Lewis acid Sn sites present in Sn(II)-BDC MOF, thereby promoting favorable adsorption. Also, as reported in earlier works, π - π interaction between the benzene rings of the organic dyes and the MOF material is a significant factor for adsorption. The abundant amount of C=O and -OH functional groups present in Sn(II)-BDC MOF adsorbent plays a vital role in dye adsorption. Further, the Langmuir and Freundlich isotherm models were employed for validating the experimental data, where the Langmuir model provided a good fit. The maximum adsorption capacity (q_m) for three anionic dyes (CR, EBT, and EY) was 95.2 mg g⁻¹, 125 mg g⁻¹, and 208.3 mg g⁻¹, respectively. The actual evaluation of the adsorption performance was based on the partition coefficient (PC) values. At an initial concentration of 100 mg L⁻¹, the PC values for CR, EBT, and EY were 48.5, 65.63, and 62.18 mg g⁻¹ μ M⁻¹, respectively. Based on high PC values and maximum adsorption capacity, Sn(II)-BDC MOF turned out to be an excellent material for the removal of anionic dyes.

Further, retention of > 86 % of its adsorption efficiency after three adsorption-desorption cycles indicated the potential reusability of the synthesized material. The cheaper source of precursor material and the simple eco-friendly synthesis of the Sn(II)-BDC MOF without the use of any toxic solvents makes it an attractive option for dye adsorption. Also, the thermal and aqueous stability of the Sn(II)-BDC MOF for an extended period adds to its advantage as a robust adsorbent material. Therefore, the synthesized material can be a promising adsorbent for remediation of organic dye contaminated wastewater.

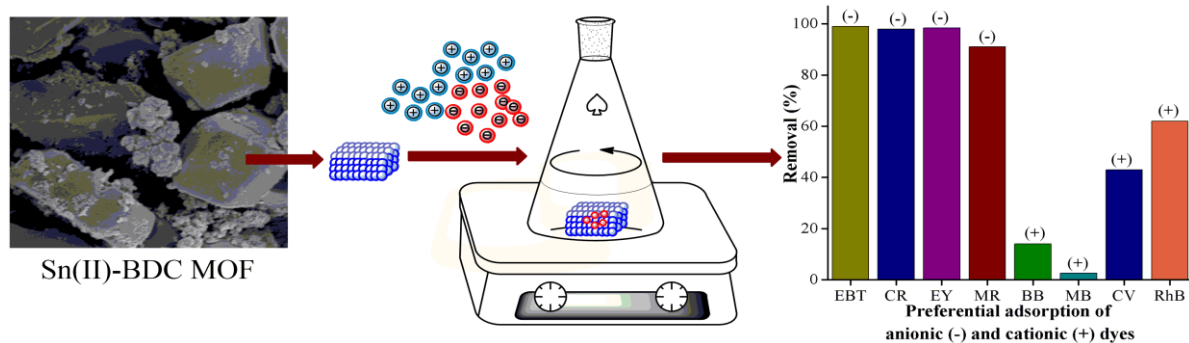


Fig. 1 Pictorial representation of the preferential adsorption dyes on Sn(II)-BDC MOF and key findings of the research work included in Chapter 3.

Chapter 4: Facile synthesis of a novel aqua-stable Sn(II)-TMA metal-organic framework (MOF): Promising adsorbent for fluoride over a broad pH range (*New. J. Chem.*, 2020, **44**, 1354-1361)

This chapter elucidates the synthesis of an Sn(II) based MOF using benzene-1,3,5-tricarboxylic acid (TMA) as an organic linker via a solvothermal route. PXRD and FT-IR studies confirmed the aqueous stability of the synthesized Sn(II)-TMA MOF. In a batch adsorption experiment, the equilibrium fluoride concentration was obtained at 1.6 mg L^{-1} with an initial concentration of 12 mg L^{-1} , i.e., ~84 % removal efficiency achieved over a pH range of 3 to 10. The adsorption of fluoride on the Sn(II)-TMA MOF was best described by the Langmuir isotherm model, and the thermodynamic analysis confirmed the adsorption process to be endothermic, spontaneous, and thermodynamically feasible. The maximum fluoride adsorption capacity was calculated to be 30.86 mg g^{-1} at 298 K. The experimental data were in good agreement with both the pseudo-first-order and pseudo-second-order kinetic model, suggesting that fluoride adsorption on the Sn(II)-TMA MOF is a combination of physisorption and chemisorption. It is reported that the metal sites in a MOF can electrostatically interact with the negatively charged fluoride ions because of unsaturated coordination on metal sites where it becomes partially positively charged. The coordinatively unsaturated Sn(II) centers in the Sn(II)-TMA MOF were coordinated by $-\text{OH}$. The adsorption of the fluoride ion occurred at the metal centers in the MOF, resulting in the formation of coordination bonds with the metal centers with the simultaneous displacement of $-\text{OH}$. To further investigate the adsorption mechanism, zeta potential and particle size analysis of the material were carried out after adsorption. It was observed that there is a decline in the zeta potential value from $+29.5 \text{ mV}$ to $+10.8 \text{ mV}$ and an increase in the particle size from 670 nm to 1611 nm after adsorption of fluoride. The aggregation and saturation of the adsorption sites with fluoride ions may lead to an increase in the particle size and polydispersity index (PDI) while decreasing the zeta potential. The result

suggests an exact state of electrostatic interaction, which drives the adsorption of negatively charged fluoride anions on the positively charged Sn(II)-TMA MOF surface. Notably, the fluoride removal efficiency was unaffected by interfering ions such as Cl^- , NO_3^- , SO_4^{2-} , and the high ionic strength of the aqueous medium. Furthermore, the practical utility of the Sn(II)-TMA MOF in the removal of fluoride from real water samples revealed its potential as a novel adsorbent for the treatment of fluoride contaminated water. This work would provide valuable insight into the eco-friendly synthesis of Sn(II)-TMA MOF and its applicability as a promising adsorbent for efficient fluoride removal from aqueous solution.

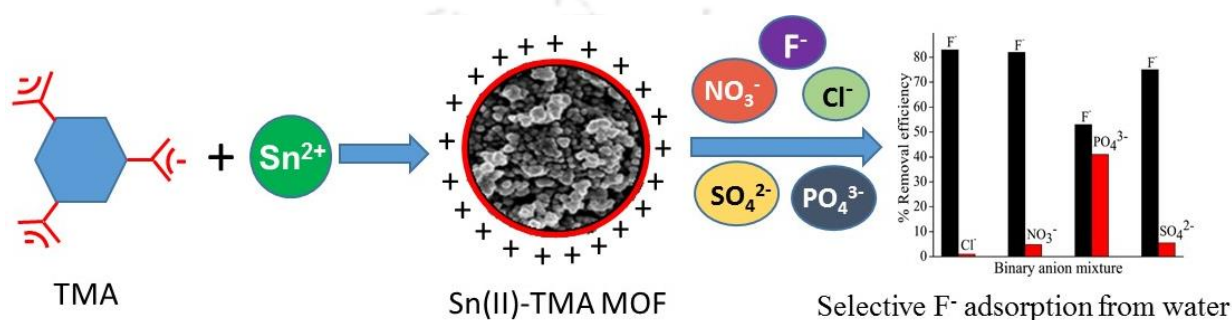


Fig. 2 Pictorial representation of selective fluoride adsorption on Sn(II)-TMA MOF and key findings of the research work included in chapter 4.

Chapter 5: Hydrolytically stable Sn(II)-BTEC hybrid material: A selective fluorogenic probe for selective detection of chromate ions in aqueous medium (*J. Photochem. Photobiol. A.*, 2020, **403**, 112863)

Highly efficient detection and sequestration of heavily toxic Chromate (CrO_4^{2-}) anion from the aqueous medium remains a challenging issue for the protection of public health and the ecosystem. Herein, we report a new thermally and hydrolytically stable Sn(II)-based hybrid organic-inorganic porous composite, **1**, and investigated its potential as a luminescent probe for instant and selective detection of chromate (CrO_4^{2-}) ions from the aqueous medium. The presence of chromate ions (CrO_4^{2-}) caused significant quenching (~95 %) of the luminescence intensity of **1**. The material displayed remarkable selectivity towards CrO_4^{2-} ions in the presence of interfering metal cations and anions. The selective quenching property can be attributed to the transfer of energy/electrons and the absorption of the excitation light. The luminescence emission intensity of **1** followed the Stern-Volmer equation at lower concentrations indicating that the quenching effect may be ascribed to the collision between anions and the framework. Further, the time-resolved photoluminescence (TRPL) analysis for **1** before and after the CrO_4^{2-} sorption proves the dynamic nature of the quenching process where the average fluorescence lifetime (τ) decreased from ~24 ns to ~11 ns after the addition

of CrO_4^{2-} . Besides, the stable luminescence intensity under acidic (pH 4), as well as alkaline (pH 9) conditions, confirms the excellent stability and applicability of **1** in a wide pH range. The detection limit of **1** for CrO_4^{2-} ions is calculated as low as $1.92 \mu\text{M}$, which is significant in terms of trace amount detection from the aqueous medium. Furthermore, the application of **1** as a chromate sensing probe in real water samples *viz.* tap water and lake water were examined. **1** displayed excellent chromate sensing capability and effectively reduced the Cr(VI) concentration within the US Environmental Protection Agency permissible limit of $100 \mu\text{g L}^{-1}$ for drinking water. Besides, the potential of **1** as an adsorbent for CO_2 was also explored in this work. **1** displayed a moderate CO_2 adsorption capacity of $\sim 1.6 \text{ mmol g}^{-1}$ at 293 K and 10 bar pressure. Despite having a comparatively lower surface area, the CO_2 adsorption capacity of **1** is found to be comparable with the reported phosphonate based Sn-MOF. This work highlights the utility of **1** as a novel material for efficient sorption and selective luminescent sensing of chromate ions in environmentally relevant conditions.

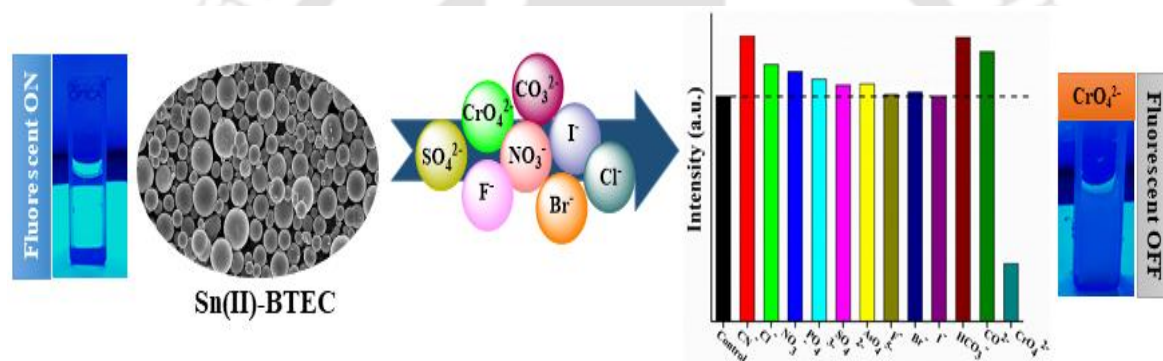


Fig. 3 Pictorial representation of selective quenching of emission intensity of Sn(II)-BTEC hybrid material in the presence of CrO_4^{2-} ions and crucial findings of the research work included in chapter 5.

Chapter 6: Environmentally benign synthesis of Sn(II)-MOF using waste PET bottles as an organic precursor and its derivative SnO₂ NPs: Efficient adsorption of cation and anion from aqueous medium (*J. Environ. Chem. Eng.* 2021, **9, 105288)**

In this chapter, a new Sn(II)-based metal-organic framework (MOF) has been solvothermally synthesized using post-consumer waste PET bottles as an organic linker source. The potential of the Sn(II)-MOF as an adsorbent material in the removal of arsenate (AsO_4^{3-}) and phosphate (PO_4^{3-}) from the aqueous medium was examined. The adsorption kinetics of the target anions followed the pseudo-second-order kinetic model, and the Langmuir isotherm best describes the adsorption profile. The DLS analysis proves that the adsorption of arsenate and phosphate on Sn(II)-MOF is predominantly driven by electrostatic interaction. The adsorbent displayed significant adsorption capacity of AsO_4^{3-} (90.90 mg g^{-1}) and PO_4^{3-} (126.58 mg g^{-1}). The

synthesized Sn(II)-MOF demonstrated promising anti-interference activity in the presence of co-existing anions, mainly, F^- , Cl^- , NO_3^- , and SO_4^{2-} . Besides, the synthesized adsorbent exhibited remarkable removal efficiency ($\sim 99\%$) of AsO_4^{3-} from actual water samples viz. tap water and lake water.

Further, the work elucidates the role of interfacial charge regulation where the positively charged Sn(II)-MOF is converted to negatively charged tin oxide nanoparticles (SnO_2 NPs) via a simple thermal decomposition route. The highly crystalline SnO_2 NPs (~ 25 nm) displayed excellent colloidal stability, as reflected from the zeta potential value of -36.8 mV. The synthesized SnO_2 NPs were explored in the adsorptive removal of manganese (Mn^{2+}), which is a significant groundwater contaminant. Batch adsorption study for Mn^{2+} removal was investigated in detail. The synthesized SnO_2 NPs displayed excellent Mn^{2+} adsorption capacity (q_m) of 52.63 $mg\ g^{-1}$, which is in good agreement with the experimental value (q_{exp}) of 56.96 $mg\ g^{-1}$. The zeta potential value of SnO_2 NPs decreased from -36.8 mV to -6.2 mV after Mn^{2+} adsorption due to the balancing of surface charge during electrostatic interaction. Moreover, the SnO_2 NPs displayed remarkable selectivity in Mn^{2+} adsorption despite the presence of other cations/anions. Overall, this work highlights a greener approach in the synthesis of the Sn(II)-MOF and its derivative SnO_2 NPs and their application in the remediation of AsO_4^{3-} , PO_4^{3-} , and Mn^{2+} with remarkable efficiency and significant anti-interference activity. Importantly, in this work, we have reported an economically viable approach for recycling waste PET bottles by converting it into value-added adsorbent material, which can be utilized in potential decontamination of water. Further, in the future, this work can be easily scaled up for bulk synthesis of adsorbent material and explored in other environmental allied fields.

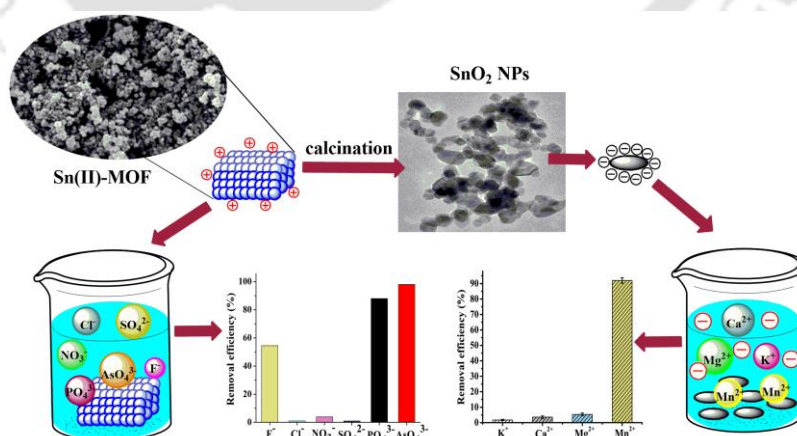


Fig. 4 Pictorial representation depicting the role of interfacial charge reversal in adsorptive removal of the cation (Mn^{2+}) and anion (AsO_4^{3-} , PO_4^{3-}) from aqueous medium and crucial findings of the research work included in chapter 6.

Conclusion

In summary, the thesis has some substantial and promising results in the domain of sustainable environmental chemistry and engineering where environmentally toxic organic compounds or cations/ anions are captured by a series of hydrothermally/ solvothermally synthesized water-stable Sn-based metal-organic-framework. Analytical methods, especially FT-IR, IC, DLS, and AAS, heavily corroborated the efficient sorption of the target analytes on the synthesized adsorbent material. In general, the findings will help understand the relatively underexplored space of Sn(II) as inorganic metal ion for stable composite material synthesis and its potential application in environmental remediation. Each of the synthesized Sn(II)-MOF unveiled interesting characteristic properties that were exploited in the remediation of toxic environmental pollutants from the aqueous medium.

The rhomboidal shaped benzene-1,4-dicarboxylate based Sn(II)-MOF illustrated excellent anionic dye removal capacity along with multi-cyclic reusability. The findings demonstrated that the low surface area of the adsorbent was not a limiting factor for dye removal from the aqueous medium. The findings clearly suggest that the electrostatic interaction and the presence of the abundant amount of C=O and –OH functional groups played a vital role in preferential adsorption of the anionic dye. On the other hand, the spherical Sn(II)- benzene-1,3,5-tricarboxylate MOF displayed significant fluoride removal efficiency and remarkable anti-interference activity in the presence of other co-existing anions. Besides, the 1,2,4,5-benzenetetracarboxylate based Sn(II)-MOF exhibited selective sensing of the CrO_4^{2-} ions from the aqueous medium and displayed good high-pressure CO_2 adsorption potential at atmospheric pressure. Furthermore, the Sn(II)-MOF synthesized using BDC recovered from waste PET bottles demonstrated remarkable removal efficiency of the environmentally hazardous anions *viz.* AsO_4^{3-} and PO_4^{3-} . Moreover, the SnO_2 NPs synthesized following the Sn(II)-MOF calcination route, displayed high colloidal stability. The present finding also elucidates the role of surface charge reversal in excellent Mn(II) ions removal efficiency from the aqueous medium. Importantly, the present work can prove to be an economically viable method of recycling the waste PET bottle into value-added adsorbent material for the decontamination of water.

CONTENTS

Chapter 1: Introduction

1.1. MOFs- An introduction	1
1.2 MOF superiority over conventional adsorbents	2
1.3 Water stability	4
1.4. Synthetic routes to MOFs	6
1.5. MOFs in water treatment	8
1.5.1. Removal of organic dyes	8
1.5.2. Removal of arsenate	9
1.5.3. Removal of fluoride	9
1.5.4. Removal of phosphate	10
1.5.5. Removal of heavy metals	10
1.6. Conclusion and outlook	12
1.7. Thesis objectives	14
References	15

Chapter 2: Experimental methods and Characterization

2.1. Materials and reagents	19
2.2. Characterization and analytical methods	19
2.3 Synthesis of different Sn-based MOFs	21
2.3.1. Synthesis of Sn(II)-BDC MOF	21
2.3.2. Synthesis of Sn(II)-TMA MOF	21
2.3.3. Synthesis of Sn(II)-BTEC chemosensor	21
2.3.4. Synthesis of Sn(II)-MOF	22
2.4. Experimental methods	23
2.4.1. Aqueous stability testing	23
2.4.2. Dye adsorption study	23
2.4.3. Fluoride removal study	24
2.4.4. UV-vis and Fluorescence spectroscopic studies	25
2.4.5. Arsenate and phosphate adsorption study	25
References	26

Chapter 3: Green synthesis of Sn(II)-BDC MOF and its application in the preferential adsorption of hazardous anionic dyes

3.1. Background and Focus of the Chapter	27
3.2. Results and Discussion	29
3.2.1. Characterization of Sn(II)-BDC MOF	29

3.3. Adsorption experiments	31
3.3.1. Preferential adsorption of different dyes	31
3.3.2. Effect of adsorbent dose	31
3.3.3. Effect of pH	31
3.3.4. Kinetic study	32
3.3.5. Thermodynamic study	33
3.3.6. Adsorption isotherm	35
3.3.7. Plausible mechanism of adsorption	39
2.4.4. Desorption and recyclability	41
2.4.5. Conclusion	42
References	42
Annexure 3	45

Chapter 4: Facile synthesis of a novel aqua-stable Sn(II)-TMA metal-organic framework (MOF): Promising adsorbent for fluoride over a broad pH range

4.1. Background and Focus of the Chapter	47
4.2. Results and Discussion	48
4.2.1. Characterization of Sn(II)-TMA MOF	48
4.2.2. Aqueous stability	50
4.2.3. Effect of adsorbent dose	50
4.2.4. Effect of pH on fluoride removal	50
4.2.5. Effect of contact time	51
4.2.6. Adsorption isotherm	53
4.2.7. Effect of temperature	54
4.2.8. Effect of co-existing anions	55
4.2.9. Effect of ionic strength	56
4.2.10. Proposed mechanism for adsorption	57
4.2.11. Fluoride adsorption from real water sample	58
4.3. Conclusion	58
References	59
Annexure 4	61

Chapter 5: Hydrolytically stable Sn(II)-BTEC hybrid material: A selective fluorogenic probe for selective detection of chromate ions in aqueous medium

5.1. Background and Focus of the Chapter	65
5.2. Results and Discussion	66
5.2.1. Characterization	66
5.2.2. Thermal and aqueous stability analysis	68

5.2.3. Luminescence properties	69
5.2.4. Hexavalent chromate sensing	70
5.2.5. Mechanism of quenching	72
5.2.6. Real water application	75
5.4. Conclusion	76
References	77
Annexure 5	79

Chapter 6: Environmentally benign synthesis of Sn(II)-MOF using waste PET bottles as an organic precursor and its derivative SnO₂ NPs: Efficient adsorption of cation and anion from aqueous medium

6.1. Background and Focus of the Chapter	87
6.2. Results and Discussion	89
6.2.1. Characterization of PET derived BDC	89
6.2.2. Characterization of Sn(II)-MOF	90
6.2.3. Characterization of SnO ₂ NPs	92
6.3. Part I- Adsorption of Arsenate and Phosphate	94
6.3.1. Effect of pH	94
6.3.2. Effect of contact time	94
6.3.3. Adsorption isotherm	98
6.3.4. Thermodynamic study	101
6.3.5. Effect of ionic strength and co-existing anions	102
6.3.5. Proposed adsorption mechanism	102
6.3.6. Real water application	104
6.4. Part II- Adsorption of manganese	104
6.4.1. Influence of pH	104
6.4.2. Effect of contact time	106
6.4.3. Adsorption isotherm	107
6.4.4. Thermodynamic study	108
6.4.5. Interfering cation effect and real water application	108
6.4.6. Proposed adsorption mechanism	109
6.4.7. Regeneration studies	110
6.5. Conclusion	111
References	112
Annexure 6	114

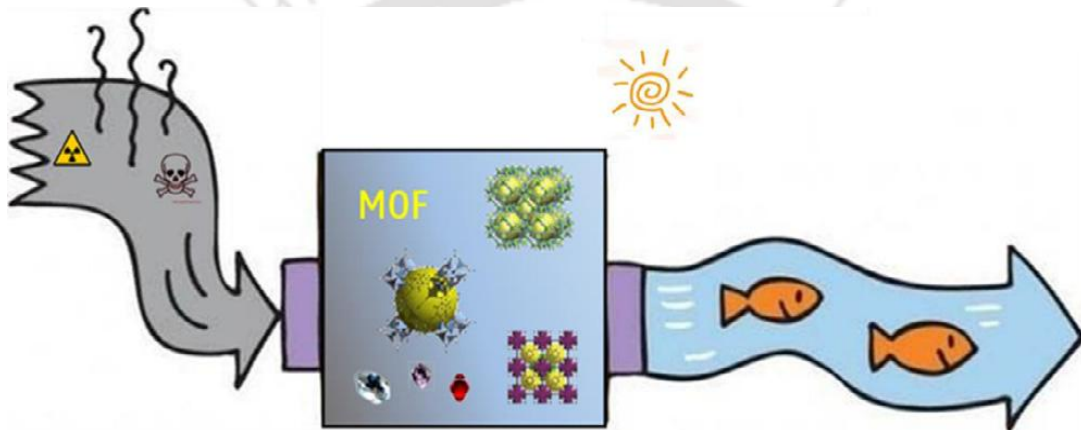
Conclusion and Future Perspective 124

List of Publications 126

Curriculum Vitae 127

Chapter 1

Introduction



1.1 MOFs: An introduction

Metal-organic frameworks (MOFs), as an advanced class of organic-inorganic hybrid materials, have gained wide attention among research communities for the past two decades because of its inherent porous structures and limitless tunability [1.1-1.7]. In 1999, Yaghi et al. reported MOF-5, the first framework to illustrate permanent porosity and structural stability when guest solvent molecules were removed from its pores [1.8]. MOFs are generally constructed from inorganic nodes connected by organic linkers via a coordination bond. A simplified schematic representation of a MOF is depicted in Fig. 1.1.

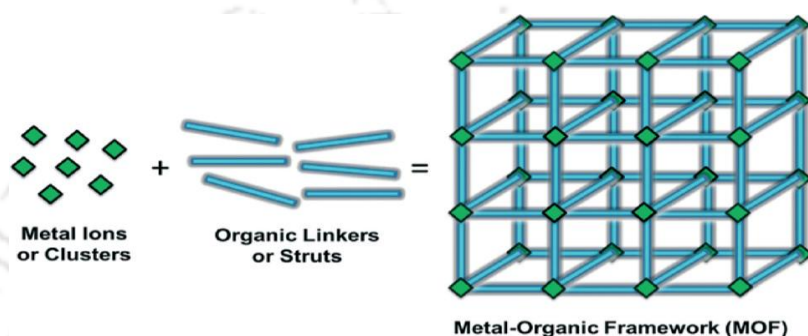


Fig. 1.1 Schematic representation of a MOF illustrating inorganic metal ion connected by the organic linker to form a 3D structure (adapted from Howarth et al., 2015)

The inorganic nodes are usually metal clusters/ ions [1.9, 1.10], while the organic ligands are generally carboxylates or other heterocyclic compounds [1.11]. The properties of MOFs can be systematically customized to achieve the desired functionality by tuning their structures [1.12]. For instance, modification of the inorganic nodes and organic linkers with specific functional groups, geometry, and length can impact the surface area, pore shape, and size of the synthesized MOF [1.13,1.14]. Cavka et al. reported an increase in surface area of MOF due to a change in the organic linker [1.15]. Besides, the inorganic moieties also influence some MOF attributes. For example, the chemical stability of MOF is primarily dictated by the inorganic node, as the metal-ligand bond, generally being unstable, is the weakest link of the MOF structure. Generally, the inorganic metal nodes are constructed from monovalent (Ag^+ , Cu^+), di-valent (Cu^{2+} , Zn^{2+} , Mn^{2+} , Mg^{2+} , Co^{2+} , Ni^{2+} , Cd^{2+} , Fe^{2+} , etc), tri-valent (Al^{3+} , Fe^{3+} , In^{3+} , Ga^{3+} , Sc^{3+} , V^{3+} , lanthanides $^{3+}$, etc), or tetravalent (Zr^{4+} , Hf^{4+} , Ce^{4+} , Ti^{4+} , etc) metal ions [1.16]. However, among all metal cations, Sn^{2+} for MOF synthesis has been least explored. As MOFs are constructed from a wide variety of metal nodes and organic linkers, the number of metal-organic combinations and hence the structural possibilities are nearly infinite. The highly tunable and modular characteristic of MOFs has catalyzed the exploration of these materials in potential applications including but not limited to catalysis [1.17-1.19], storage/release of gases [1.20-1.24], sensing [1.25,1.26], drug delivery [1.27,1.28], chemical separations [1.29-1.33],

ion-exchange [1.34], removal of pollutants from air/ water [1.35-1.36], conductivity [1.37], light-harvesting and energy conversion [1.38-1.40], and degradation of chemical warfare agents [1.41-1.42]. The diverse applications of MOF is represented in Fig. 1.2.

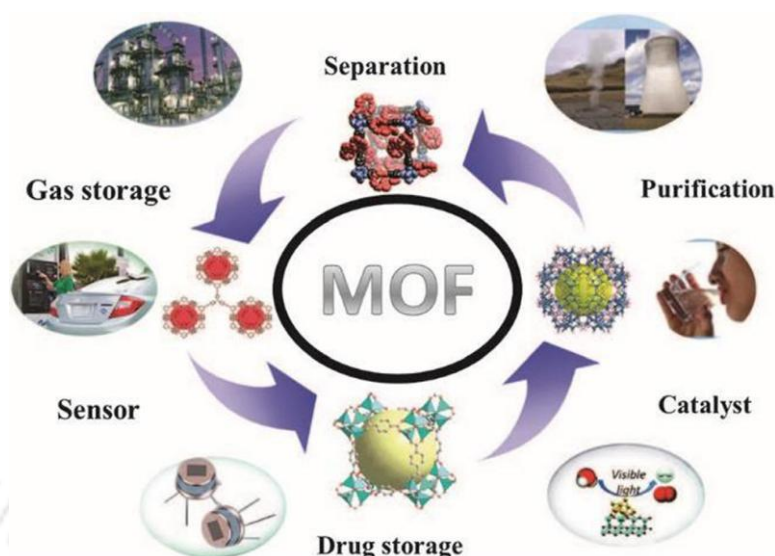


Fig. 1.2 Pictorial representation of diverse applications of MOFs (adapted from S. Chaemchuen et al. 2013).

1.2 MOF superiority over conventional adsorbents

Water purification from toxic metal ions as well as harmful organic pollutants continues to be a serious challenge concerning the protection of environment and human health. In this context, numerous traditional and modern techniques have been explored including, adsorption, coagulation, chemical co-precipitation, ultra-filtration, photocatalysis, oxidation/reduction, reverse osmosis, membrane-based techniques, and biological remediation [1.43-1.50]. However, the above-mentioned methods have their own limitations. For instance, chemical precipitation and biological treatments are ineffective regarding total removal of the metal ions, while photocatalysis gives rise to unnecessary by-products. Moreover, these methods require complicated instrumentation and space-consuming facilities, which may incur high start-up and maintenance costs [1.51]. In contrast, adsorption has become a more popular choice for wastewater treatment because of its high efficiency, simplicity, ease of operation, and cost-effectiveness [1.52-1.57]. Adsorption is a feasible alternative in the removal of toxic contaminants that are recalcitrant for biological methods. Moreover, adsorption restricts the generation of undesired by-products and exploits the utility of an extensive range of recoverable adsorbents. The adsorption mechanism is divided into two types: physical adsorption and chemical adsorption. Physical adsorption occurs due to weak inter-particle bonding (Vander Waals, hydrogen, and dipole-dipole interaction) between adsorbent and

adsorbate molecules, and the process is easily reversible [1.58]. Contrastingly, in chemical adsorption, strong inter-particle bond (ionic/ covalent bond) exists between the adsorbent and adsorbate molecules due to the sharing/exchange of electrons. The chemical adsorption is deemed not to be fully reversible and could require high energy for the regeneration process [1.59]. In quest to develop promising adsorbent, various porous materials are explored in the past decade. The conventional porous adsorbents include zeolites, activated carbon, and mesoporous silica (Fig. 1.3). Traditionally, porous materials have been classified into two types: organic and inorganic materials. Notably, the most common and widely reported organic porous material is activated carbon. Such materials are synthesized by the pyrolysis of carbon-rich materials, possess high surface area, and large adsorption capacity, though they lack a long-range of ordered structure [1.60]. Despite lacking an ordered structure, the porous carbon materials have been successfully utilized in the separation/storage of gases, solvent removal/recovery, and decontamination of water [1.61]. However, activated carbons find limited applicability in treating high concentration of dyeing wastewater and requires high regeneration cost [1.62,1.63]. On the other hand, inorganic porous material *viz.* zeolite possess a highly ordered structure and are synthesized using inorganic/ organic template having strong interaction with the inorganic framework of the material. As a consequence, the template removal can result in a collapse of the framework. Besides, the limited choice of elements (Al, Si, and chalcogens) during synthesis produces a lack of diversity in the inorganic framework of the material. Nevertheless, such inorganic frameworks find wide applications in catalysis and separations [1.64]. In addition, slow adsorption kinetics, low chemical and thermal stability, poor recyclability compounded with low adsorption capacity are some of the major drawbacks of conventional porous materials [1.65]. The limitations of both organic and inorganic porous materials can be overcome with the synthesis of porous organic-inorganic hybrid materials known as a metal-organic framework (MOF), which are both stable and ordered. MOFs are generally crystalline porous materials that possess some unique properties, particularly structural flexibility, an incredible degree of tunability, and remarkable internal surface area in conjunction with ultra-high porosity. The characteristic tunability of MOFs in the form of different analogs is illustrated in Fig. 1.4. Based on the discussed features MOFs are accounted to be the most comprehensively investigated material of the 21st century [1.66, 1.67]. MOFs have attracted attention from researchers worldwide because of its high specific surface area and large adsorption capacity compared to its counterparts [1.68-1.71]. The water decontamination using MOFs is primarily governed by four principal factors a) aqueous stability b) uptake capacity c) interactiveness, and d) regenerative capability of MOF. Most

importantly, among all, the aqua-stability of the MOFs is a challenging issue that restricts its application in water treatment. Besides, the adsorption potential of MOFs is directly influenced by the presence of functional groups/ active sites, which causes an interaction between MOFs and target pollutants to be removed. Lastly, the regenerative capability of the MOFs confirms its multi-cyclic recyclability.

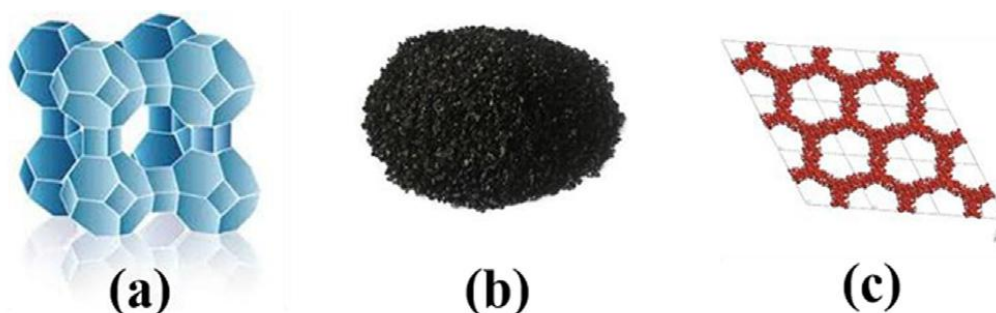


Fig. 1.3. Different conventional porous materials a) zeolite b) activated carbon and c) mesoporous silica used for adsorption purposes (adapted from Dhaka et al., 2019)

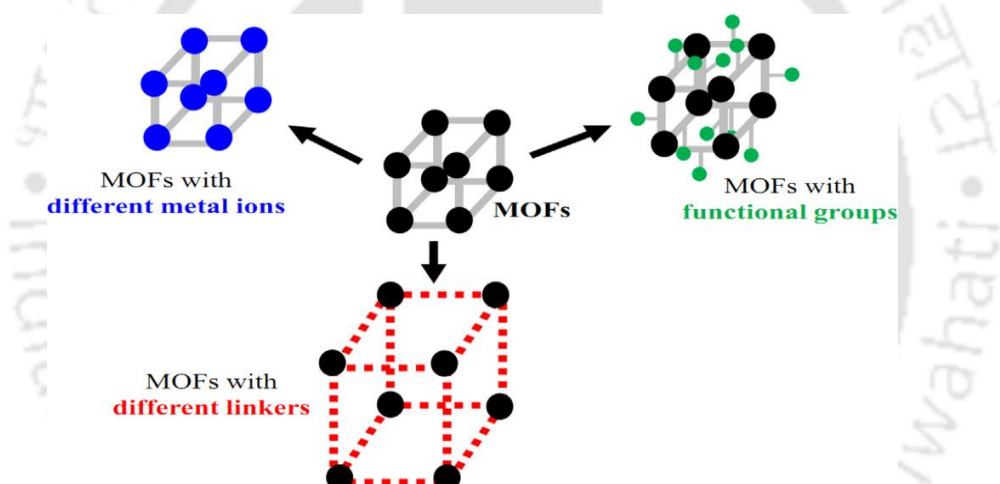


Fig. 1.4. Representation of different MOF analogs (adapted from Khan et al. 2017).

1.3 Water Stability

The stability of MOF in an aqueous medium is significantly important for application in the field of water treatment [1.72]. In this regard, several studies have been conducted to improve the aqua-stability and the issue has been addressed for some selected MOFs [1.73-1.74]. However, water instability remains a challenging issue for the majority of MOFs used for water treatment applications. The degradation of the MOF structure in an aqueous environment can be classified into two mechanisms. The first mechanism is attributed to the ligand displacement and the second is related to hydrolysis [1.75]. As highlighted in Fig.1.5, in the ligand displacement mechanism a water molecule is inserted into the metal-ligand bond resulting in the formation of cation-hydrate and the subsequent release of the linker [1.76].

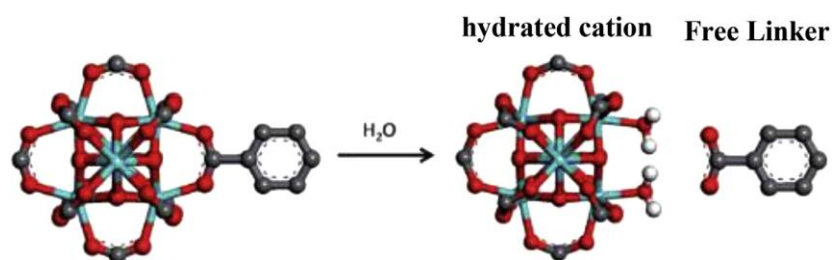


Fig. 1.5 Schematic illustrating the ligand displacement mechanism in the presence of water for a representative MOF material (Zr-MOFs) (adapted from DeCoste et al., 2013).

Contrastingly, the hydrolysis mechanism implies the disruption of the metal-ligand bond, causing the dissociation of water to form a hydroxylated cation and a free protonated ligand as illustrated below [1.72, 1.75]:



The first mechanism is more common in depicting the degradation of the MOF structure with the introduction of the water molecules [1.12].

The stability of MOFs is dictated by several factors, including the inorganic nodes, organic linkers, metal-ligand coordination bond and geometry, operation environment (temperature, pH), hydrophobic characteristics of the pore walls, structural defects, etc. [1.77, 1.78]. Among all the factors, the metal-ligand bond strength plays the most critical role in determining the stability of MOFs. Since it's difficult to measure the metal-ligand bond strength, the stability of the MOFs can be estimated from Pearson's HSAB (hard/soft acid/base) principle [1.79]. It is expected that robust coordination bonds are formed between hard Lewis acid and bases [1.80]/ soft Lewis acid and bases [1.15]. Carboxylate-based ligands are generally regarded as hard Lewis bases, which can form a strong coordination bond with hard Lewis acids (Zr^{4+} , Hf^{4+} , Cr^{3+} , Al^{3+} , Fe^{3+} , etc.). Therefore, the strength of the metal-ligand bond in MOF illustrates its fundamental stability, which includes both thermodynamic and aqueous stability [1.72, 1.77]. The overall stability of the MOFs can be enhanced by a dense and rigid structure formed by highly inter-linked metal-oxo clusters and bridged by rigid organic ligands. The water-stable MOFs are expected to preserve their X-ray diffraction (PXRD) pattern and Brunauer-Emmett-Teller (BET) surface area after water exposure.

In previous works, some representative MOFs displayed excellent stability in water include MIL (Material Institut Lavoisier) series, namely, MIL-53 [1.82], MIL-100 [1.83] and MIL-101 [1.80], and UiO (University of Oslo) series, examples are UiO-66, UiO-67, and UiO-68 [1.84]. Another class of stable MOFs is constructed by soft base azolate ligands (examples are imidazolates, pyrazolates, triazolates, and tetrazolates) and soft acid metal cations (including Ag^+ , Cu^{2+} , Zn^{2+} , Ni^{2+} , and Mn^{2+}). The most typical examples in this category are the zeolitic

imidazolate frameworks (ZIFs), which is assembled by Zn^{2+} metal ion coordinated to imidazolate linkers [1.85]. In recent years, synthesis of triazole and pyrazolate-based MOFs have been reported using Cu^{2+} , Ni^{2+} , Co^{2+} , and other transition metal ions, which demonstrated good aqueous stability even in strong basic environments [1.86-1.89]. The structures of some common representative MOFs are illustrated in Fig. 1.6 below.

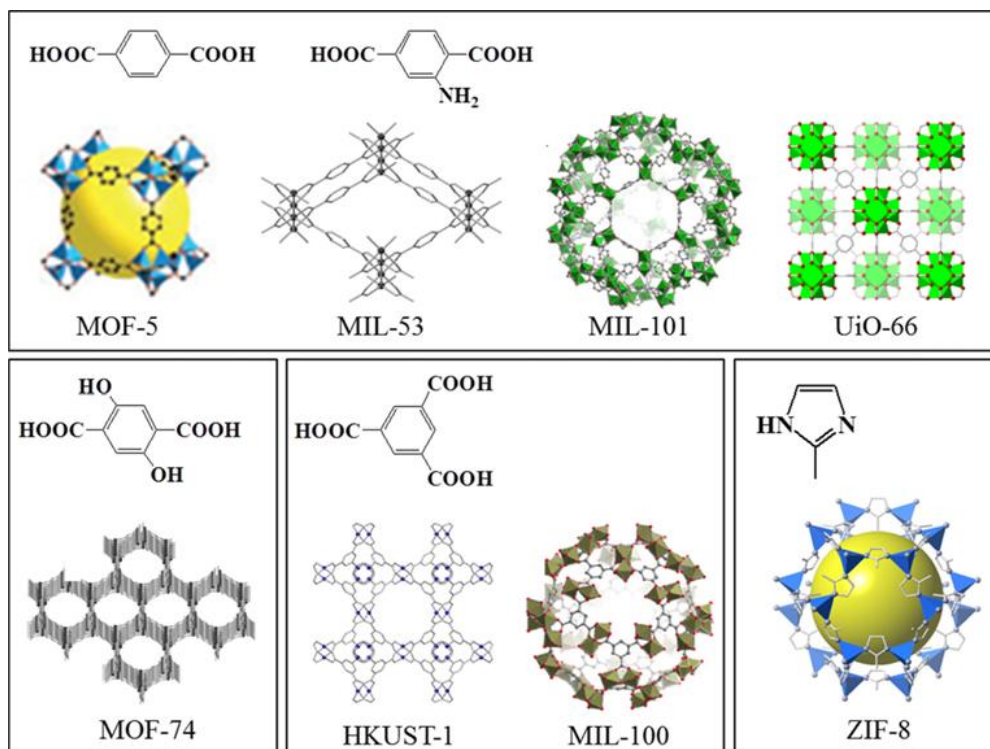


Fig. 1.6 Various structures of some representative MOFs (adapted from Lee et al., 2013).

1.4 Synthetic routes to MOFs

Several mechanical or chemical methods are followed to synthesize these highly structured porous materials. Among all synthetic routes, the solvothermal method is the most typical and popular method of MOF synthesis. The major advantage of this method includes the high solubility of the precursor materials and the formation of high-quality MOF crystals necessary for structural characterization. In a typical solvothermal reaction, the metal salts and organic ligands are combined and heated at relatively low temperatures ($< 300\text{ }^{\circ}\text{C}$) under autogenous pressure in a Teflon lined stainless steel autoclave or in a sealed vial [1.60]. Fig. 1.7 demonstrates a typical solvothermal process for MOF synthesis. The characteristics of the ligand viz. ligand length, bulkiness, bond angles, and chirality, etc. play an important role in deciding the nature of the framework. Besides, the MOF structure is also influenced by the tendency of the inorganic metal ions to attain specific geometries. The reactants are mixed in polar solvents such as water, alcohols, dialkyl formamides, dimethyl sulfoxide, or acetonitrile

and generally heated above the boiling point of the solvent. The crucial parameters of solvothermal synthesis include temperature, the concentrations of the precursors (metal salt and organic ligand), solution pH, and the extent of the solubility of the precursors in the given solvent. Even though the best conditions for MOF synthesis is dictated by the researcher's experience, experimentation and trial-and-error methods are often required. Earlier literature reports several published reviews on the synthesis and characterization of MOFs [1.90-1.95].

In addition to the popular solvothermal method, several other techniques of MOF synthesis are reported in the literature, including a) mass-transfer techniques, which involves growing of inorganic salt crystals by facilitating slow evaporation of a precursor solution, solution layering or slow diffusion of one reactant (for example amine) into the solution of a metal salt and organic linker [1.96], b) microwave-assisted synthesis, effectively reduces the time of MOF synthesis by raising the solution temperature with microwaves for an hour or more, however till date such method is not frequently applied to produce crystalline MOFs. Nevertheless, such method is pivotal in carrying out MOF synthesis at high speed [1.97] c) Electrochemical method, a fast and continuous process which involves the reaction between metal ions (obtained via anodic dissolution) and the organic linkers and electrolytes present in the reaction medium [1.98] d) mechanochemical method, a solvent-free synthetic route for large scale synthesis of MOFs where mechanical force is applied for grinding a mixture of a metal salt and organic linker in a ball mill [1.99], e) sonochemical method, employed for efficient and rapid synthesis of MOF by shortening the crystallization time with the application of ultrasound [1.100]. Apart from the discussed synthetic methods, other less conventional but reliable MOF synthetic techniques include iono-thermal, microfluidics, and dry-gel conversion [1.101].

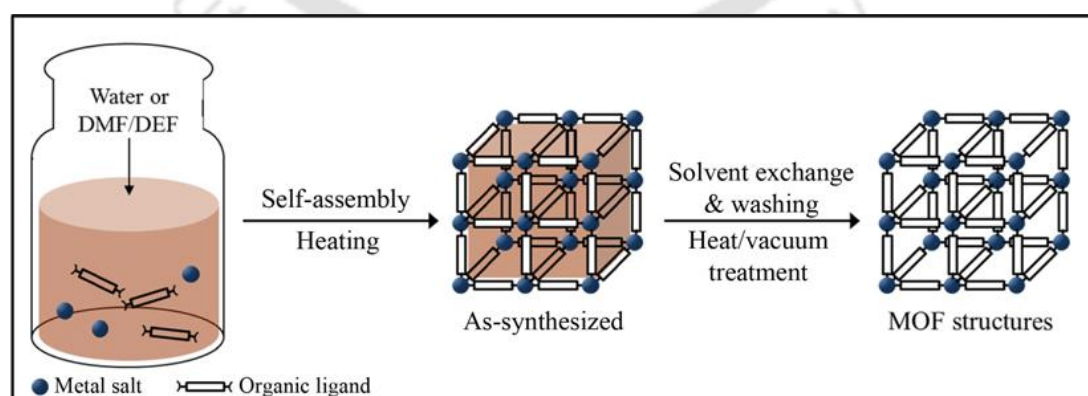


Fig. 1.7. Schematic representation of a conventional solvothermal process for MOF synthesis (adapted from Lee et al., 2013)

1.5 MOFs in water treatment

1.5.1. Removal of organic dyes

Dyes are regarded as a sub-class of organic contaminants that cause significant water pollution. Statistically, industries produce more than 100,000 various types of organic dyes at a generation rate of 70,000 metric tons/ year [1.102]. Haque et al. reported adsorptive removal of both cationic and anionic dyes *viz.* methylene blue (MB) and methyl orange (MO), respectively, using NH₂-MIL-101 (Al) MOF [1.103]. The findings indicated more selective adsorption of MB compared to MO on NH₂-MIL-101 (Al) MOF. Moreover, its adsorption performance was found to be superior to MIL-101(Al), illustrating the importance of the amino group (-NH₂) in improving the selectivity of MOF. However, the major limitation of this NH₂-MIL-101 (Al) MOF is its poor regenerative ability. Yi et al. assembled hexa[4-(carboxyphenyl)oxamethyl]-3-oxapentane acid (H₆L) ligand-based MOF using triscadmium ion to facilitate the removal of MB, MO, and Rhodamine B [1.104]. Besides, [Zn(bdc)(tib)] 3H₂O was examined for its adsorption performance towards the organic dyes Rhodamine B, MB, MO, and Congo Red (CR), respectively. It is observed that the assembled MOF is applicable for adsorption of only CR dye. Notably, [Zn(bdc)(tib)] 3H₂O retained its adsorption capacity up to five adsorption cycles after regeneration with ethanol washing [1.105-1.110]. Jia et al. employed MIL-100 (Fe) MOF as an adsorbent for effective removal of methylene blue (cationic dye) compared to methyl blue (anionic dye), thereby demonstrating the significant role of electrostatic interaction in dye removal from aqueous solution [1.111]. Tong et al. designed two different MOFs, namely MIL-100(Fe) and MIL-100(Cr), where the former demonstrated significant adsorption potential for both MO and MB, while the latter showed selective adsorption of MB from a MO-MB mixture [1.112]. This work highlighted the replacement of framework metal ion of MOF as an efficient way for tailoring its application in liquid phase separation of pollutants. However, the exact influencing mechanism of the metal ion needs to be investigated in detail through further experimentation and computational means. In a significant work, Duan et al. reported the synthesis of nano-sized metal-organic framework NMIL-100 (Fe) devoid of hydrofluoric acid (HF) and demonstrated its application in the efficient adsorption of both cationic and anionic dyes [1.113]. Unlike most other MOFs, NMIL-100 displayed a low surface area of 1.24 m² g⁻¹. However, the work highlighted the important role of electrostatic interaction and hydrogen bonding as a predominant mechanism of dye adsorption. Moreover, the work emphasized on the facile and environmentally benign synthesis of MOF under mild conditions for practical applications. Yılmaz et al. examined MIL-53 (Fe) for the adsorption of methyl red (MR) from the aqueous medium [1.114].

Interestingly, despite having a limited surface area ($23 \text{ m}^2 \text{ g}^{-1}$) MIL-53(Fe) showed high adsorption capacity for MR owing to its intrinsic characteristics such as structural flexibility and breathing effect. Leng et al. compared the uranine removal performance of MIL-101 (Cr) to that of activated carbon (AC) [1.115]. The study highlighted the importance of electrostatic interaction as well as the large pore size of MIL-101 for its superior adsorption performance.

1.5.2. Removal of arsenate

Arsenic is categorized as one of the highly toxic contaminants of water, when present beyond permissible limit, causing detrimental effects to human beings. Arsenic, in its pentavalent form As(V) (arsenate) is the most prevalent species in natural water systems [1.116]. Fe-BTC was the first MOF explored to remediate arsenic species and displayed an adsorption potential of 12.3 mg g^{-1} . The utility of several MOFs such as ZIF-8, MIL-96 is investigated for arsenic adsorption from aqueous medium [1.117,1.118]. ZIF-8 demonstrated great potential in sorption of arsenate, with a maximum uptake capacity of 90.92 mg g^{-1} , where favourable electrostatic interaction proved to be the driving force [1.118]. Similarly, the MIL family of MOFs such as MIL-53(Al), MIL-53(Al), MIL-100(Fe), MIL-100(Fe) are used for the removal of As(V). The MIL-96(Fe) demonstrated to be a promising adsorbent for As(V) because of its high aqueous stability. The As(V) adsorption capacity of MIL-96(Fe) proved to be 6 times and 36 times as much of iron oxide nanoparticles and commercially available powdered iron oxide, respectively [1.118]. Wang et al., for the first time, reported the utility of water-stable UiO-66(Zr) in the removal of As(V) at a high uptake capacity of 303 mg g^{-1} [1.119]. The superior As(V) adsorption performance is ascribed to the highly porous crystalline structure of UiO-66(Zr) with plenty of active sites and large contact area. However, in the aforesaid work, adsorption kinetics of As(V) is not studied. Li et al. employed MIL-53(Al) as a new adsorbent material for removal of As(V) from water [1.120]. The material showed promising adsorption capacity, but at a long equilibration time of 11h. In another work, Li et al. explored the uptake potential of ZIF-8 for trace As(V) removal from water [1.121]. The critical factors for satisfactory As(V) adsorption include sizeable accessible surface area, abundant active sites, and cooperative interaction facilitated by van der Waals' forces and hydrogen bonding at low surface coverage.

1.5.3. Removal of fluoride

Fluoride, a common groundwater contaminant, causes many serious health issues when present in excess amounts in drinking water. To achieve trace level of fluoride removal, Zhao et al. developed several MOFs including MIL-68, UiO-66(Zr, Hf), CAU-1,-6 (CAU stands for

Christian-Albrechts-University), MIL-53(Fe, Cr, Al) and ZIF-7,8,9, which are reported to be stable in water [1.122]. Among all, UiO-66(Zr) exhibited the best defluoridation performance and stability in the fluoride solution. The factors such as coordination number, pore topology, and inertness of metal centre proved to be significant for the stability of the tested MOFs in fluoride solution. Importantly, the findings suggested that an increase in the number of –OH groups can enhance the fluoride removal efficiency of MOFs. In a separate study, Zhang and co-workers evaluated the defluoridation potential of MIL-96(Al) MOF [1.123]. The fluoride removal efficiency of this MOF was found to be far superior to that of the conventional adsorbents like activated alumina and nano-alumina. Further, the spent MIL-96(Al) was easily regenerated using 0.01 M NaOH.

1.5.4. Removal of phosphate

Phosphate is one of the major pollutants of the wastewater streams and a primary nutrient that causes eutrophication. To remediate the phosphate pollution, Lin et al. proposed the use of UiO-66(Zr) MOF due to its exceptional water stability [1.124]. The interaction between the metal (Zr) sites and phosphate via the formation of Zr-O-P bonds accounted for efficient phosphate adsorption. Further, the work illustrated that UiO-66-NH₂ exhibited better phosphate removal performance than UiO-66, possibly because of amine functionality, which enhanced affinity for phosphate ions. Besides, the MOF exhibited high selectivity towards phosphate over other co-existing anions such as bromate, nitrite, and nitrate. Liu et al. studied the phosphate adsorption potential of La-MOFs [1.125]. The study revealed a ligand exchange reaction between La-MOFs and phosphate ions as a potential mechanism of phosphate adsorption. Moreover, the La-MOFs were easily regenerated using NaOH and reused for further phosphate separation.

1.5.5. Removal of heavy metals

Some heavy metals like Lead (Pb), cadmium (Cd), copper (Cu), manganese (Mn), and mercury (Hg) possess significant toxicity to the environment and human beings [1.126-1.129]. Saleem et al. introduced Zr-based MOF (UiO-66-NHC(S)NHMe) as a promising adsorbent with lead(II) uptake capacity from polluted water maximum up to 232 mg g⁻¹ [1.130]. A Cobalt(II)-MOF was reported earlier for lead(II) adsorption from contaminated water [1.131]. While the adsorption equilibrium reached in 100 min, the adsorption capacity of the material is unknown. Chakraborty and co-workers assembled a MOF (named as AMOF-1) based on zinc(II) and tetracarboxylate and examined its Pb(II) adsorption potential [1.132]. The lead(II) adsorption equilibrium was found to reach in 24 h with a maximum uptake capacity up to 71 mg g⁻¹. Cu-

MOF based on terephthalate has been examined for its Pb(II) removal performance [1.133]. The maximum uptake capacity was found to be 80 mg g^{-1} , and the adsorption process completed equilibrium in 120 min. Zou et al. employed a specific synthetic strategy for Copper(II) based HKUST-1 MOF (HKUST stands for Hong Kong University of Science and Technology) [1.134]. Functionalization of HKUST-1 facilitated the composition of HKUST-1-MW@H3PW12O40 framework, which demonstrated high efficiency in Pb(II) removal with a maximum adsorption capacity of 80 mg g^{-1} in a short equilibrium time of 10 min. Rivera and co-workers employed MOF-5 for lead(II) removal with a remarkable uptake capacity of 659 mg g^{-1} at $45 \text{ }^\circ\text{C}$ [1.135]. The study revealed that variations in pH and temperature might affect the lead(II) adsorption potential of MOF-5.

Though cadmium is one of the most toxic heavy metal, reports on cadmium removal by MOFs are relatively scarce. Ma et al. reported anchoring of $-\text{SO}_3\text{H}$ group into $\text{Cu}_3(\text{BTC})_2$ framework via post-synthetic modification and oxidation method. The synthesized sulfonic acid functionalized $\text{Cu}_3(\text{BTC})_2\text{-SO}_3\text{H}$ exhibited a maximum cadmium adsorption capacity of 88.7 mg g^{-1} , which outperformed most reported adsorbents [1.136]. Apart from the functional sites, the important role of the confined MOF cavity in Cd(II) adsorption was examined by Hong et al. [1.137]. In the reported work, they constructed a calcium-based MOF (named as FJI-H9) with 2,5-thiophenedicarboxylate as the organic linker. The adsorption study revealed a high Cd^{2+} uptake capacity of the reported MOF attributed to the synergistic interaction between the MOF cavity and strong hydrogen bonding. While the adsorption experiment was performed in acetonitrile solution, the study revealed some vital mechanistic insights of adsorption on MOF. Bakhtiari et al. reported Zinc based MOF (MOF-5) as an efficient adsorbent with Cu(II) uptake capacity of 290 mg g^{-1} [1.138]. The equilibrium reached fast in 30 min at an optimal pH of 5, and the adsorption capacity was found to increase with an increase in temperature. Likewise, several zirconium-based MOFs were explored to examine their Cu(II) adsorption performance. UiO-66(Zr)-2COOH demonstrated superior Cu(II) adsorption potential owing to the presence of two carboxyl groups, which enhanced the adsorption performance through the chelation process. The Cu(II) uptake capacity was found to improve with an increase in pH from 4 to 6 [1.139].

Using Pearson's HSAB principle, Xu et al. reported some exciting examples of mercury (II) removal using MOFs consisting of sulfur-containing linkers [1.140-1.142]. The thiol functionality resulted in the formation of Zr-DMBD MOF resembling the UiO-66 topology. Zr-DMBD MOF significantly lowered (99.9 % removal efficiency) the Hg(II) ions concentration (below 0.01 ppm) at room temperature after 12 h [1.143]. Chen et al., in their

contribution, reported novel sulfur functionalized MOF (FJI-H12) assembled with Co^{2+} , SCN^- , and 2,4,6-tri(1-imidazolyl)-1,3,5-triazine [1.144]. SCN^- comprising of chemically soft S atom and hard N atom, respectively, has been deemed as the ideal choice with a sulfur-containing group for Hg(II) removal, where the N atom can coordinate to the hard metal ion while providing access to the S atom to interact with the soft heavy metal ion. Further, the study highlighted the selective uptake of Hg(II) from an aqueous medium with a remarkable adsorption capacity of 439.8 mg g^{-1} . The plausible mechanisms of adsorption of various hazardous pollutants on MOF are highlighted in Fig. 1.8 below.

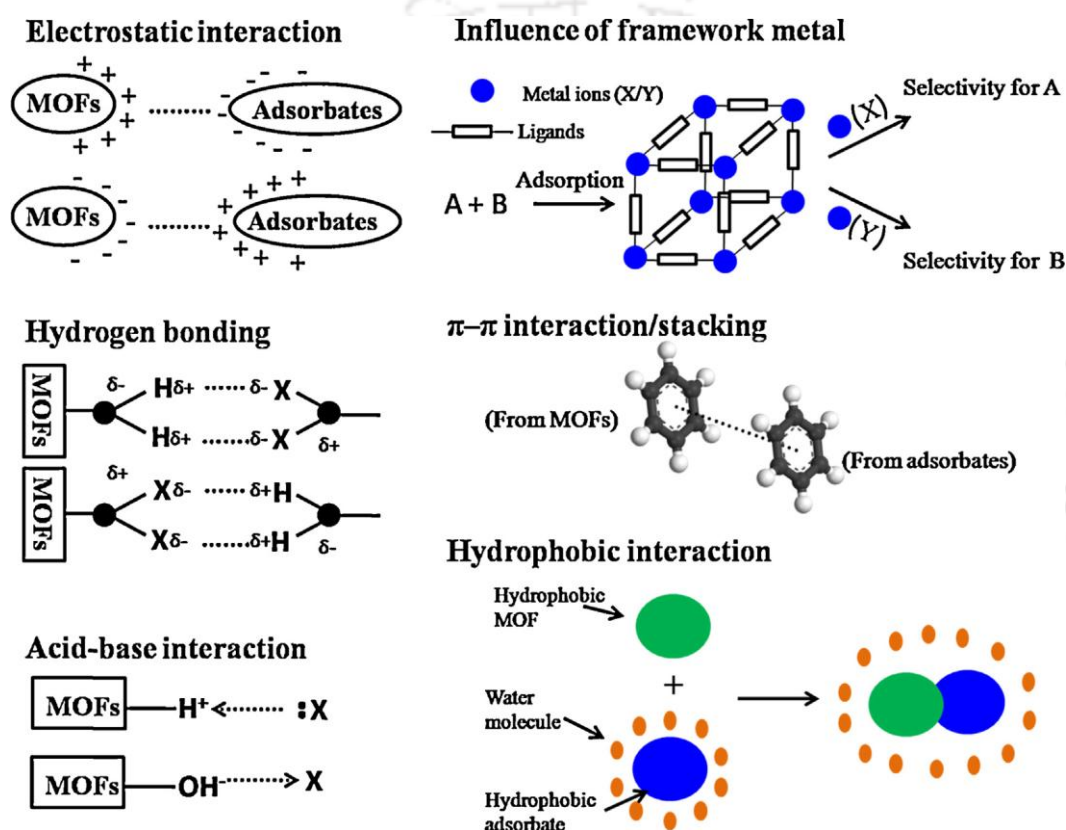


Fig. 1.8 Possible adsorption mechanisms of hazardous pollutants on MOFs (adapted from Hasan et al., 2015)

1.6 Conclusion and outlook

A comprehensive literature study highlighted MOF as a promising and advanced porous material that can be principally assembled from almost infinitely diverse functional components (metal ions and organic linkers). Moreover, their pore properties are highly tunable and modulated according to desired needs following the principles of reticular chemistry. In addition, high surface area and facile functionalization establishes MOF as a superior adsorbent compared to a conventional porous material such as activated carbon and zeolites. Despite the fascinating properties of MOFs, their practical applications are limited due to the issue of water stability and adverse environmental impacts generated by conventional

synthetic approaches. Besides, the pore diameter of most of the reported MOFs is in the microporous region. Therefore, the pore diameter should be improved to the mesoporous range for selective adsorption of contaminants.

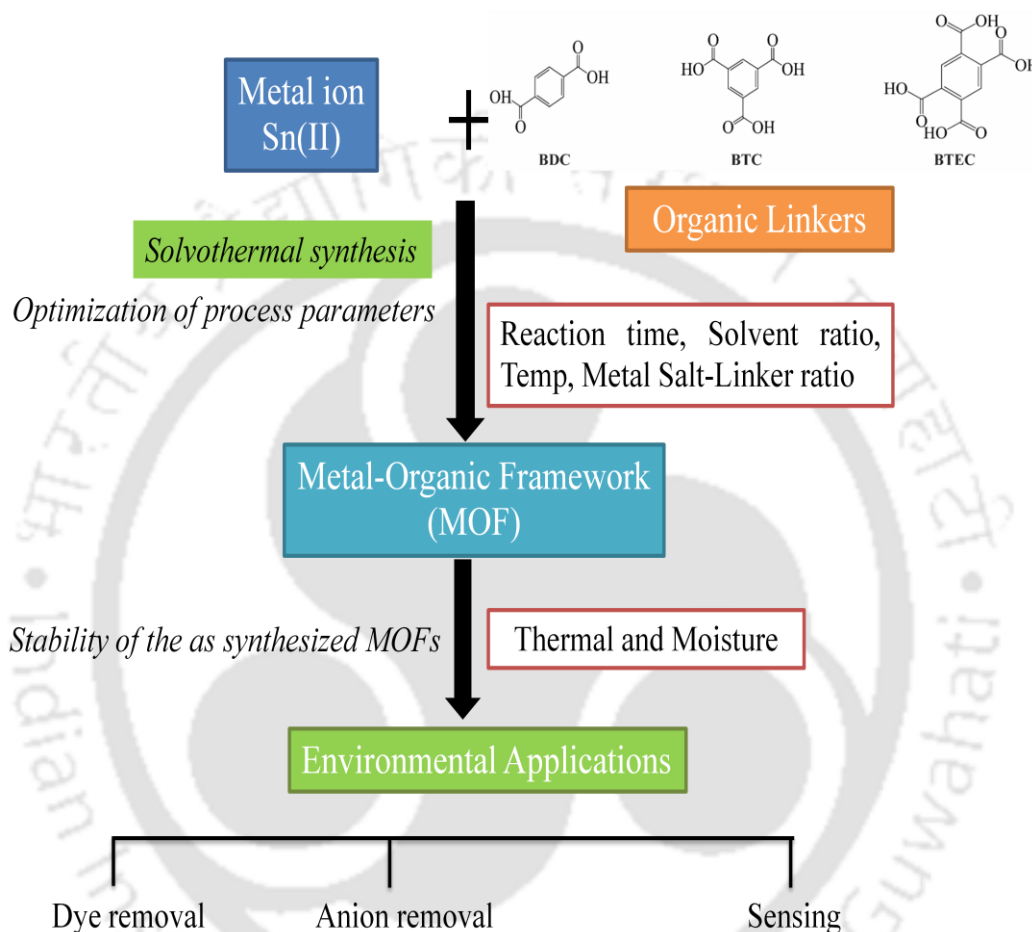
In context to water treatment applications, apart from adsorption capacity, the selectivity of MOFs is highly significant for practical applications and should be diligently considered. Moreover, it is necessary to combine a good adsorption performance with satisfactory cost-effective recyclability of the MOF material, and therefore sincere attempts are needed in this regard to develop reusable MOF based adsorbents. Besides, it is of paramount importance to synthesize water-stable MOFs for pollutant remediation from aqueous solution. Nevertheless, in the past decade, several successful pieces of research are performed in an endeavor to improve MOF stability. However, most reported MOFs (Cr-, Zr-MOFs) are synthesized from a toxic or expensive metal precursor. Therefore, attention needs to be given to the development of green and industrially acceptable MOF chemistry based on a sustainable choice of metal ions (low toxicity and readily available) in combination with a safer solvent/ or reaction medium. The diversity of central metal ion present in the framework of MOFs has led to a new strategy towards the adsorption of different toxic pollutants. The stability of central metal ion in MOF is very crucial in terms of the reusability of the adsorbents. Most of the MOF-based studies did not explicitly illustrate the potential reusability of the adsorbent, which may be due to the poor stability of the metal ions as a result of the leaching or redox phenomenon within MOF framework. The overall efficiency of an adsorbent mostly depends on its reusability, and therefore, sincere attempts are needed to develop reusable adsorbents. In this context, Sn(II) as an inorganic metal ion in MOF synthesis and its water treatment applications is relatively unexplored. Therefore, a detailed study is necessary to explore the potential of Sn-based metal-organic-framework in water treatment applications.

Despite the challenges and problems, with sustained efforts, the real field application of MOFs will soon become true.

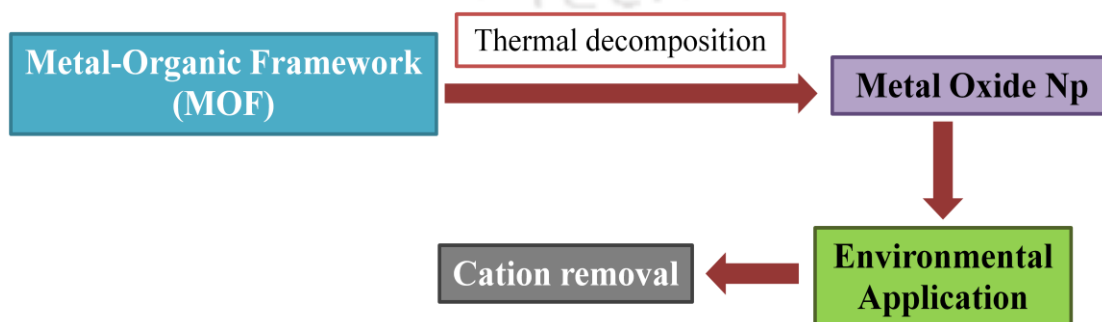
1.7 Thesis objectives

The objectives of the thesis work are broadly classified into two objectives, that are pictorially represented in the form of flow diagram below.

Objective 1:



Objective 2:



References

- [1.1] M. Eddaoudi, J. Kim, N. Rosi, D. Vodak, J. Wachter, M. O’Keeffe and O.M. Yaghi, *Science*, 2002, **295**, 469–472.
- [1.2] G. Férey, C.M. Draznieks, C. Serre, F. Millange, J. Dutour, S. Surblé and I. Margiolaki, *Science*, 2005, **309**, 2040–2042.
- [1.3] R. Banerjee, A. Phan, B. Wang, C. Knobler, H. Furukawa, M. O’Keeffe and O.M. Yaghi, *Science*, 2008, **319**, 939–943.
- [1.4] H. Furukawa, N. Ko, Y.B. Go, N. Aratani, S.B. Choi, E. Choi, A.O. Yazaydin, R.Q. Snurr, M. O’Keeffe, J. Kim and O.M. Yaghi, *Science*, 2010, **329**, 424–428.
- [1.5] W. Lu, Z. Wei, Z.Y. Gu, T.F. Liu, J. Park, J. Park, J. Tian, M. Zhang, Q. Zhang, T. Gentle Iii, M. Bosch and H.C. Zhou, *Chem. Soc. Rev.*, 2014, **43**, 5561–5593.
- [1.6] N. Stock and S. Biswas, *Chem. Rev.*, 2012, **112**, 933–969.
- [1.7] M. Li, D. Li, M. O’Keeffe and O.M. Yaghi, *Chem. Rev.*, 2014, **114**, 1343–1370.
- [1.8] H. Li, M. Eddaoudi, M. O’Keeffe and O.M. Yaghi, *Nature.*, 1999, **402**, 276–279.
- [1.9] M. Eddaoudi, D.B. Moler, H. Li, B. Chen, T.M. Reineke, M. O’Keeffe and O.M. Yaghi, *Acc. Chem. Res.*, 2001, **34**, 319–330.
- [1.10] D.J. Tranchemontagne, J.L. Mendoza-Cortes, M. O’Keeffe and O.M. Yaghi, *Chem. Soc. Rev.*, 2009, **38**, 1257–1283.
- [1.11] H. Furukawa, K.E. Cordova, M. O’Keeffe and O.M. Yaghi, *Science*, 2013, **341**, 1230444.
- [1.12] A. Ali, S.N. Mahdi, T. Bahareh and S. Mika, *Chemosphere*, 2016, **160**, 30–44
- [1.13] S.H. Jung, N.A. Khan and Z. Hasan, *CrysEngComm*, 14,7099-7109.
- [1.14] W. Lu, Z. Wei, Z.Y. Gu, T.F. Liu, J. Park, J. Park, J. Tian, M. Zhang, Q. Zhang, T. Gentle Iii, M. Bosch and H.C. Zhou, *Chem. Soc. Rev.*, 2014, **43**, 5561–5593.
- [1.15] J.H. Cavka, S. Jakobsen, U. Olsbye, N. Guillou, C. Lamberti, S. Bordiga, K.P. Lillerud, *J. Am. Chem. Soc.*, 2008, **130**, 13850–13851.
- [1.16] S. Yuan, J.-S. Qin, C. T. Lollar and H.-C. Zhou, *ACS Cent. Sci.*, 2018, **4**, 440–450
- [1.17] J. Lee, O.K. Farha, J. Roberts, K.A. Scheidt, S.T. Nguyen, J. T. Hupp, *Chem. Soc. Rev.*, 2009, **38**, 1450–1459.
- [1.18] J.M. Falkowski, S. Liu and W. Lin, *Isr. J. Chem.* 2012, **52**, 591–603.
- [1.19] J. Gascon, A. Corma, F. Kapteijn and F.X. Xamena, *ACS Catal.*, 2014, **4**, 361–378.
- [1.20] J.-R. Li; R. J. Kuppler and H.-C. Zhou, *Chem. Soc. Rev.*, 2009, **38**, 1477–1504.
- [1.21] J.A. Mason, M. Veenstra and J.R. Long, *Chem. Sci.*, 2014, **5**, 32–51.
- [1.22] Y. Peng, V. Krungleviciute, I. Eryazici, J.T. Hupp, O.K. Farha and T. Yildirim, *J. Am. Chem. Soc.*, 2013, **135**, 11887–11894.
- [1.23] T.M. McDonald, J.A. Mason, X. Kong, E.D. Bloch, D. Gygi, A. Dani, V. Crocella, F. Giordanino, S.O. Odoh, W.S. Drisdell, B. Vlasisavljevich, A.L. Dzubak, R. Poloni, S.K. Schnell, N. Planas, K. Lee, T. Pascal, L.F. Wan, D. Prendergast, J.B. Neaton, B. Smit, J.B. Kortright, L. Gagliardi, S. Bordiga, J.A. Reimer, J.R. Long, *Nature* 2015, 519, 303–308.
- [1.24] D.M. D’Alessandro, B. Smit and J.R. Long, *Angew. Chem., Int. Ed.*, 2010, **49**, 6058–6082
- [1.25] L.E. Kreno, K. Leong, O.K. Farha, M. Allendorf, R.P. Van Duyne and J.T. Hupp, *Chem. Rev.*, 2012, **112**, 1105–1125.
- [1.26] Z. Hu, B.J. Deibert and J. Li, *Chem. Soc. Rev.* 2014, **43**, 5815–5840.
- [1.27] P. Horcajada, C. Serre, M. Vallet-Regí, M. Sebban, F. Taulelle and G. Férey, *Angew. Chem., Int. Ed.*, 2006, **45**, 5974–5978.
- [1.28] R.C. Huxford, J.D. Rocca and W. Lin, *Curr. Opin. Chem. Biol.*, 2010, **14**, 262–268.
- [1.29] J.-R. Li, J. Sculley and H.-C. Zhou, *Chem. Rev.*, 2012, **112**, 869–932.
- [1.30] J.E. Bachman, Z.P. Smith, T. Li, T. Xu and J.R. Long, *Nat. Mater.*, 2016, **15**, 845–849.
- [1.31] Z.R. Herm, E.D. Bloch and J.R. Long, *Chem. Mater.*, 2014, **26**, 323–338.
- [1.32] P. Nugent, Y. Belmabkhout, S.D. Burd, A.J. Cairns, R. Luebke, K. Forrest, T. Pham, S. Ma, B. Space, L. Wojtas, M. Eddaoudi and M.J. Zaworotko, *Nature*, 2013, **495**, 80–84.
- [1.33] X. Cui, K. Chen, H. Xing, Q. Yang, R. Krishna, Z. Bao, H. Wu, W. Zhou, X. Dong, Y. Han, B. Li, Q. Ren and M.J. Zaworotko, B. Chen, *Science*, 2016, **353**, 141–144.
- [1.34] X. Zhao, X. Bu, T. Wu, S.-T. Zheng, L. Wang and P. Feng, *Nat. Commun.* 2013, **4**, 2344.

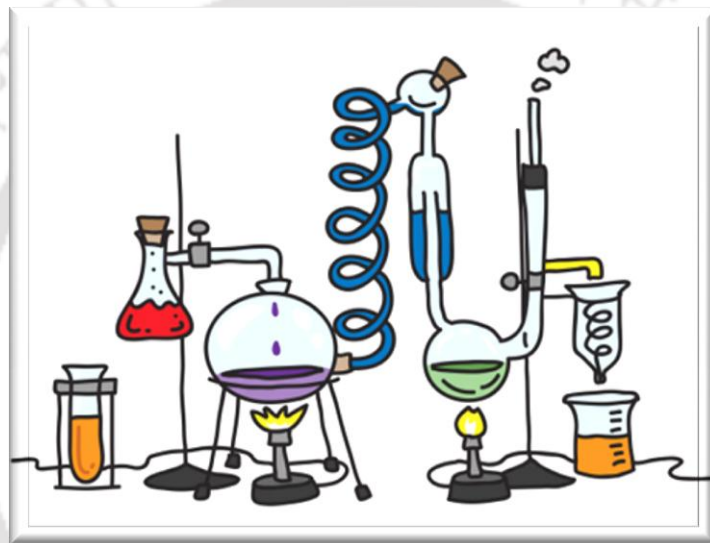
- [1.35] J.B. DeCoste and G.W. Peterson, *Chem. Rev.* 2014, **114**, 5695–727.
- [1.36] A.J. Howarth, Y. Liu, J.T. Hupp and O.K. Farha, *CrystEngComm.*, 2015, **17**, 7245–7253.
- [1.37] L. Sun, M.G. Campbell and M. Dincă, *Angew. Chem., Int. Ed.*, 2016, **55**, 3566–3579.
- [1.38] M.C. So, G.P. Wiederrecht, J.E. Mondloch, J.T. Hupp and O.K. Farha, *Chem. Commun.*, 2015, **51**, 3501–3510.
- [1.39] J.-L. Wang; C. Wang and W. Lin, *ACS Catal.* 2012, **2**, 2630–2640.
- [1.40] D.E. Williams and N.B. Shustova, *Chem. - Eur. J.*, 2015, **21**, 15474–15479
- [1.41] W. Bury, G.W. Wagner, M.G. Hall, J.B. DeCoste, G.W. Peterson, R.Q. Snurr, C.J. Cramer, J.T. Hupp and O.K. Farha, *Nat. Mater.* 2015, **14**, 512–516.
- [1.42] S.-Y. Moon, Y. Liu, J.T. Hupp and O.K. Farha, *Angew. Chem., Int. Ed.* 2015, **54**, 6795–6799.
- [1.43] Y. Sun, Z.Y. Wu, X. Wang, C. Ding, W. Cheng, S.H. Yu and X. Wang, *Environ. Sci. Technol.*, 2016, **50**, 4459-4467.
- [1.44] C. Ding, W. Cheng, Y. Sun and X. Wang, *Geochem. Cosmochim. Acta.*, 2015, **165**, 86-107.
- [1.45] I. Akin, G. Arslan, A. Tor, Y. Cengeloglu and M. Ersoz, *Desalination*, 2011, 281, 88-92.
- [1.46] M. Narayani and K.V. Shetty, *Crit. Rev. Environ. Sci. Technol.*, 2013, **43**, 955-1009.
- [1.47] A. Khan, N. Ali, M. Bilal, S. Malik, S. Badshah and H. Iqbal, *Appl. Sci.*, **9**, 5138.
- [1.48] N. Ali, F. Ali, Z.A. Sheikh, M. Bilal and I. Ahmad, *Water, Air, Soil Pollut.*, 2020, **231**, 59.
- [1.49] A. Aziz, N. Ali, A. Khan, M. Bilal, S. Malik, N. Ali and H. Khan, *Int. J. Biol. Macromol.*, 2020, **153**, 502-512.
- [1.50] H. Khan, K. Gul, B. Ara, A. Khan, N. Ali, N. Ali and M. Bilal, *J. Environ. Chem. Eng.*, 2020, **8**, 103927.
- [1.51] G. Montes-Hernandez, N. Concha-Lozano, F. Renard and E. Quirico, *J. Hazard. Mater.*, 2009, **166**, 788–795.
- [1.52] R. Sivashankar, A.B. Sathya, K. Vasantharaj, V. Sivasubramanian, *Nanotechnol. Monit. Manag.*, 2014, **1-2**, 36-49.
- [1.53] M.T. Yagub, T.K. Sen, S. Afroze and H.M. Ang, *Adv. Colloid Interface Sci.*, 2014, **209**, 172-184.
- [1.54] G.Z. Kyzas and K.A. Matis, *J. Mol. Liq.*, 2015, **203**, 159-168.
- [1.55] K.B. Tan, M. Vakili, B.A. Horri, P.E. Poh, A.Z. Abdullah and B. Salamatina, *Sep. Purif. Technol.*, 2015, **150**, 229-242.
- [1.56] B. Tanhaei, A. Ayati, F.F. Bamoharram, M. Lahtinen and M. Sillanpaa, *J. Chem. Technol. Biotechnol.* 2016, **91**, 1452-1460.
- [1.57] B. Tanhaei, A. Ayati, M. Lahtinen and M. Sillanpaa, *Chem. Eng. J.*, 2015, **259**, 1-10.
- [1.58] A.A Adeyemo, I.O. Adeoye and O.S. Bello, *Toxicol. Environ. Chem.*, 2012, **94**, 1846-1863.
- [1.59] S. Kwon, M. Fan, H.-F.M. Dacosta, A.-g. Russell, K.A. Berchtold and M.K. Dubey, chapter 10 - CO₂ sorption coal gasification and its applications, 2011, 293-339.
- [1.60] R.J. Kuppler, D. J. Timmons, Q.-R. Fang, J.-R. Li, T.A. Makal, M.D. Young, D. Yuan, D. Zhao, W. Zhuang and H.-C. Zhou, *Coord. Chem. Rev.* **253**, 2009, 3042–3066
- [1.61] S.M. Manocha, *Sadhana*, 2003, **28**, 335-348.
- [1.62] A. A. Attia, W. E. Rashwan and S. A. Khedr, *Dyes Pigm.*, 2006, **69**, 128
- [1.63] T. Shen, J. Luo, S. Zhang and X. Luo, *J. Environ. Chem. Eng.*, 2015, **3**, 1372–1383.
- [1.64] G. Ferey, *Chem. Soc. Rev.*, 2008, **37**, 191.
- [1.65] T. Rasheed, A.A. Hassan, M. Bilal, T. Hussain and K. Rizwan, *Chemosphere*, 2020, **259**, 127369.
- [1.66] G. Maurin, C. Serre, A. Cooper and G. Ferey, *Chem. Soc. Rev.*, 2017, **46**, 3104-3107.
- [1.67] J. Li, X. Wang, G. Zhao, C. Chen, Z. Chai and A. Alsaedi, *Chem. Soc. Rev.*, 2018, **47**, 2322-2356.
- [1.68] J. Cheng, J. Liang, L. Dong, J. Chai, N. Zhao, S. Ullah and G. Zheng, *RSC Adv.*, 2018, **8**, 40813-40822.
- [1.69] M. Lu, L. Li, S. Shen, D. Chen and W. Han, *New J. Chem.*, 2019, **43**, 1032-1037.
- [1.70] H. Qiu, M. Ye, Q. Zeng, W. Li, J. Fortner, L. Liu and L. Yang, *Chem. Eng. J.*, 2019, **360**, 621-630.
- [1.71] A.A. Pribylov, K.O. Murdmaa, O.V. Solovtsova and M.K. Knyazeva, *Russ. Chem. Bull.*, 2018, **67**, 1807-1813.
- [1.72] J. Canivet, A. Fateeva, Y. Guo, B. Coasne and D. Farrusseng, *Chem. Soc. Rev.*, 2014, **43**, 5594-5617.
- [1.73] T. Wu, L. Shen, M. Luebbers, C. Hu, Q. Chen, Z. Ni, R.I. Masel, *Chem. Commun.*, 2010, **46**, 6120-6122.
- [1.74] J.M. Taylor, R. Vaidhyanathan, S.S. Iremonger and G.K.H Shimizu, *Am. Chem. Soc.*, 2012, **134**, 14338-14340.
- [1.75] J.J. Low, A.I. Benin, P. Jakubczak, J.F. Abrahamian, S.A. Faheem and R.R. Willis, *J. Am. Chem. Soc.*, 2009, **131**, 15834-15842.

- [1.76] J.B. DeCoste, G.W. Peterson, H. Jasuja, T.G. Glover, Y.-G. Huang and K.S. Walton, *J. Mater. Chem. A*, 2013, **1**, 5642-5650.
- [1.77] N.C. Burtch, H. Jasuja and K.S. Walton, *Chem. Rev.* 2014, **114**, 10575–10612.
- [1.78] C. Wang, X. Liu, N.-K. Demir, J.P. Chen and K. Li, *Chem. Soc. Rev.* 2016, **45**, 5107–5134.
- [1.79] T. Devic and C. Serre, *Chem. Soc. Rev.*, 2014, **43**, 6097–6115.
- [1.80] G. Ferey, C.M.-Draznieks, C. Serre, F. Millange, J. Dutour, S. Surblé and I. Margiolaki, *Science*, 2005, **309**, 2040–2042.
- [1.81] J.H. Cavka, S. Jakobsen, U. Olsbye, N. Guillou, C. Lamberti, S. Bordiga and K.P. Lillerud, *J. Am. Chem. Soc.* 2008, **130**, 13850–13851.
- [1.82] C. Serre, C., F. Millange, C. Thouvenot, M. Nogues, G. Marsolier, D. Louer and G. Ferey, *J. Am. Chem. Soc.*, 2002, **124**, 13519-13526.
- [1.83] G. Ferey, C. Serre, C. M.-Draznieks, F. Millange, S. Surble, J. Dutour and I. Margiolaki, *Angew. Chem. Int. Ed.*, 2004, **43**, 6296-6301.
- [1.84] M. Feng , P. Zhang , H.-C. Zhou and K. Virender, *Chemosphere*, 2018, **209**, 783-800.
- [1.85] K.S. Park, Z. Ni, A.P. Cote, J.Y. Choi, R. Huang, F.J. Uribe-Romo, H.K. Chae, M. O’Keeffe and O.M. Yaghi, *Proc. Natl. Acad. Sci. U. S. A.*, 2006, **103**, 10186-10191.
- [1.86] M. Bosch, S. Yuan, W. Rutledge and H.C. Zhou, *Acc. Chem. Res.*, 2017, **50**, 857-865.
- [1.87] Z. Chang, D. Yang, J. Xu, T. Hu and X. Bu, *Adv. Mater.*, 2015, **27**, 5432-5441.
- [1.88] Z. Lin, J. Lü, M. Hong and R. Cao, *Chem. Soc. Rev.*, 2014, **43**, 5867-5895.
- [1.89] H.C. Zhou and S. Kitagawa, *Chem. Soc. Rev.*, 2014, **43**, 5415-5418.
- [1.90] S. Kitagawa, R. Kitaura and S. Noro, *Angew. Chem. Int. Ed. Engl.*, 2004, **43**, 2334.
- [1.91] G. Ferey, J. Cejka, H. van Bekkum, A. Corma and F. Schuth, *Stud. Surf. Sci. Catal.*, 2007, 168.
- [1.92] D. Zhao, D.Q. Yuan, H.C. Zhou, *Energy Environ. Sci.*, 2008, **1**, 222.
- [1.93] N.W. Ockwig, O. Delgado-Friedrichs, M. O’Keeffe and O.M. Yaghi, *Acc. Chem. Res.*, 2005, **38**, 176.
- [1.94] R. Robson, *Dalton Trans.*, 2008, 5113.
- [1.95] M. O’Keeffe, M. Eddaoudi, H.L. Li, T. Reineke and O.M. Yaghi, *J. Solid State Chem.*, 2000, **152**, 3.
- [1.96] J.L.C. Rowsell and O.M. Yaghi, *Microporous Mesoporous Mater.*, 2004, **73**, 3-14.
- [1.97] M. Safaei, M.M. Foroughi, N. Ebrahimpoor, S. Jahani, A. Omid and M. Khatami, *TrAC, Trends Anal. Chem.*, 2019, **118**, 401-425.
- [1.98] N. Campagnol, E.R. Souza, D.E. De Vos, K. Binnemans and J. Fransaer, *Chem. Commun.*, 2014, **50**, 12545–12547.
- [1.99] M. Pilloni, F. Padella, G. Ennas, S. Lai, M. Bellusci, E. Rombi, F. Sini, M. Pentimalli, C. Delitala, A. Scano, V. Cabras and I. Ferino, *Microporous Mesoporous Mater.*, 2015, **213**, 14–21.
- [1.100] M. Bigdeli and A. Morsali, *Ultrason. Sonochem.*, 2015, **27**, 416–422.
- [1.101] Y.R. Lee, J. Kim and W.S. Ahn, *Korean J. Chem. Eng.* 2013, **30**, 1667-1680.
- [1.102] H.C. Zhou, J.R. Long and O.M. Yaghi, *Chem. Rev.* 2012, **112**, 673–674.
- [1.103] E. Haque, V. Lo, A.I. Minett, A.T. Harris and T.L. Church, *J. Mater. Chem.*, 2014, **2**, 193-203.
- [1.104] F.Y. Yi, J.P. Li, D. Wu and Z.M. Sun, *Chem. A Eur. J.*, 2015, **21**, 11475-11482.
- [1.105] C. Zhang, L. Ai, and J. Jiang, *Ind. Eng. Chem. Res.*, 2015, **54**, 153-163.
- [1.106] C. Zhang, L. Ai and J. Jiang, *J. Mater. Chem.*, 2015, **3**, 3074-3081.
- [1.107] Q. Zhang, J. Yu, J. Cai, L. Zhang, Y. Cui and Y. Yang, *Chem. Commun.*, 2015, **51**, 14732-14734.
- [1.108] W.X. Zhang, P.Q. Liao, R.B. Lin, Y.S. Wei, M.H. Zeng and X.M. Chen, *Coord. Chem. Rev.*, 2015, **293**, 263-278.
- [1.109] X. Zhang, Y. Gao, H. Liu and Z. Liu, *CrystEngComm*, 2015, **17**, 6037-6043.
- [1.110] Y. Zhang, X. Zhao, H. Huang, Z. Li, D. Liu and C. Zhong, *RSC Adv.*, 2015, **5**, 72107-72112.
- [1.111] Y. Jia, Q. Jin, Y. Li, Y. Sun, J. Huo and X. Zhao, *Anal. Methods*, 2015, **7**, 1463-1470.
- [1.112] M. Tong, D. Liu, Q. Yang, S. Devautour-Vinot, G. Maurin and C. Zhong, *J. Mater. Chem. A*, 2013, **1**, 8534.
- [1.113] S. Duan, J. Li, X. Liu, Y. Wang, S. Zeng, D. Shao and T. Hayat, *ACS Sustainable Chem. Eng.* 2016, **4**, 3368–3378.
- [1.114] E. Yilmaz, E. Sert and F.S. Atalay, *J Taiwan Inst Chem E.*, 2016, **65** 323–330
- [1.115] F. Leng, W. Wang, X.J. Zhao, X.L. Hu and Y.F. Li, *Colloids Surf. A Physicochem. Eng. Asp.*, 2014, **441**, 164– 169
- [1.116] V.K. Sharma and M. Sohn, *Environ. Int.* 2009, **35**, 743–759.

- [1.117] B.J. Zhu, X.Y. Yu, Y. Jia, F.M. Peng, B. Sun and M.Y. Zhang, *J. Phys. Chem. C*, 2012, **116**, 8601-8607.
- [1.118] Y.N. Wu, M. Zhou, B. Zhang, B. Wu, J. Li and J. Qiao, *Nanoscale*, 2014, **6**, 1105-1112.
- [1.119] C. Wang, X. Liu, J.P. Chen and K. Li, *Sci. Rep.*, 2015, **5**, 16613.
- [1.120] J. Li, Y. Wu, Z. Li, M. Zhu and F. Li, *Water Sci. Technol.*, 2014, **70**, 1391-1397.
- [1.121] J. Li, Y. Wu, Z. Li, B. Zhang, M. Zhu, X. Hu, Y. Zhang and F. Li, *J. Phys. Chem. C*, 2014, **118**, 27382-27387.
- [1.122] X. Zhao, D. Liu, H. Huang, W. Zhang, Q. Yang and C. Zhong, *Microporous and Mesoporous Mater.*, 2014, **185**, 72-78.
- [1.123] N. Zhang, X. Yang, X. Yu, Y. Jia, J. Wang, L. Kong, Z. Jin, B. Sun, T. Luo, J. Liu, *Chem Eng J.*, 2014, **252**, 220-229.
- [1.124] K.A. Lin, S.-Y. Chen and A.P. Jochems, *Mater. Chem. Phys.*, 2015, **160**, 168-176.
- [1.125] H. Liu, W. Guo, Z. Liu, X. Li and R. Wang, *RSC Adv.*, 2016, **6**, 105282
- [1.126] C. Liu, Y. Huang, N. Naismith and J. Economy, *Environ. Sci. Technol.*, 2003, **37**, 4261-4268.
- [1.127] M.J. Manos, C.D. Malliakas and M.G. Kanatzidis, *Chem. Eur. J.*, 2007, **13**, 51-58.
- [1.128] B. Lee, Y. Kim, H. Lee and J. Yi, *Microporous Mesoporous Mater.*, 2001, **50**, 77-90.
- [1.129] F. Ke, L.-G. Qiu, Y.-P. Yuan, F.-M. Peng, X. Jiang, A.-J. Xie, Y.-H. Shen and J.-F. Zhu, *J. Hazard. Mater.*, 2011, **196**, 36-43.
- [1.130] H. Saleem, U. Rafique, R.P. Davies, *Microporous Mesoporous Mater.*, 2016, **221**, 238-244.
- [1.131] A. Abbasi, T. Moradpour and K.V. Hecke, *Inorg. Chim. Acta.*, 2015, **430**, 261-267.
- [1.132] A. Chakraborty, S. Bhattacharyya, A. Hazra, A.C. Ghosh and T.K. Maji, *Chem. Commun.*, 2016, **52**, 2831-2834.
- [1.133] E. Rahimi and N. Mohaghegh, *Mine Water Environ.*, 2016, **35**, 18-28.
- [1.134] F. Zou, R. Yu, R. Li and W. Li, *ChemPhysChem*, 2013, **14**, 2825-2832
- [1.135] J.M. Rivera, S. Rincon, C.B. Youssef and A. Zepeda, *J. Nanomater.* 2016.
- [1.136] Y. Wang, G.Q. Ye, H.H. Chen, X.Y. Hu, Z. Niu and S.Q. Ma, *J. Mater. Chem. A*, 2015, **3**, 15292-15298.
- [1.137] H. Xue, Q.H. Chen, F.L. Jiang, D.Q. Yuan, G.X. Lv, L.F. Liang, L.Y. Liu and M.C. Hong, *Chem. Sci.*, 2016, **7**, 5983-5988.
- [1.138] N. Bakhtiari and S. Azizian, *J. Mol. Liq.*, 2015, **206**, 114-118.
- [1.139] Y. Zhang, Z. Xie, Z. Wang, X. Feng, Y. Wang and A. Wu, *Dalton Trans.*, 2016, **45**, 12653-12660.
- [1.140] X.-P. Zhou, Z.T. Xu, M. Zeller, A.D. Hunter, S.S. Chui and C.-M. Che, *Inorg. Chem.*, 2008, **47**, 7459-7461.
- [1.141] X.-P. Zhou, Z.T. Xu, M. Zeller and A.D. Hunter, *Chem. Commun.*, 2009, 5439-5441.
- [1.142] J. He, K.-K. Yee, Z.T. Xu, M. Zeller, A.D. Hunter, S.S. Chui and C.-M. Che, *Chem. Mater.*, 2011, **23**, 2940-2947.
- [1.143] K.-K. Yee, N. Reimer, J. Liu, S.-Y. Cheng, S.-M. Yiu, J. Weber, N. Stock and Z.T. Xu, *J. Am. Chem. Soc.*, 2013, **135**, 7795-7798.
- [1.144] L.F. Liang, Q.H. Chen, F.L. Jiang, D.Q. Yuan, J.J. Qian, G.X. Lv, H. Xue, L.Y. Liu, H.-L. Jiang and M.C. Hong, *J. Mater. Chem. A*, 2016, **4**, 15370-15374.

Chapter 2

Experimental Methods and Characterization



In this chapter, a detailed report of the various reagents used in the synthesis of different Sn-based MOFs using polycarboxylate organic linkers, their synthetic procedures, specifications of instruments/equipment employed in the characterization of synthesized MOFs, water stability analysis, and finally, experimental methods used in their various water treatment applications are presented.

2.1 Materials and Reagents

All the reagents used in the experimental work were of an analytical grade and used without further purification. Stannous chloride dihydrate, terephthalic acid (BDC), trimesic acid (TMA), pyromellitic acid (BTEC), and sodium hydroxide were purchased from Sigma-Aldrich (USA). The different dyes viz. congo red, eosin yellow, methyl red, erichrome black T, methylene blue, crystal violet, rhodamine B, and bismark brown were procured from LOBA chemicals (India). The sodium salts of various anions (namely, fluoride, phosphate, nitrate, chloride, carbonate, bicarbonate, arsenate, sulfate, bromide, chromate, cyanide, permanganate, and perchlorate) and cations (namely, calcium, lead, cadmium, magnesium, manganese, nickel, copper, cobalt, and zinc) were purchased from Himedia (India). The organic solvents like ethanol, methanol, and acetone were procured from Merck (India). The Teflon lined stainless steel hydrothermal autoclave reactor used for material synthesis was purchased from AntsLab (India). The ion chromatography (IC) multi-element standard for anion analysis was purchased from Merck, India.

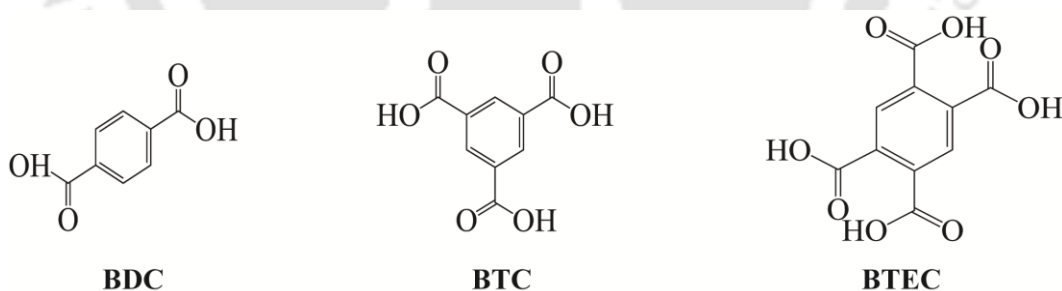


Fig. 2.1 Chemical structures of the organic ligands used for the synthesis of different MOFs.

2.2. Characterization and Analytical methods

The FT-IR spectra were recorded in the range 400 to 4000 cm^{-1} in the form of KBr pellets using PerkinElmer Spectrum 2 FT-IR spectrometer. The Raman spectrum was recorded using a Laser Micro Raman System (Make: Horiba Jobin Vyon, Model: LabRam HR) at 488 nm laser wavelength. Powder X-ray diffractometer (Rigaku, SmartLab) was used to record the PXRD pattern of dried powder sample at a diffraction angle (2θ) ranging from 20° to 70° with a step size of 0.02° . The surface area, total pore volume, and pore size distribution of the synthesized

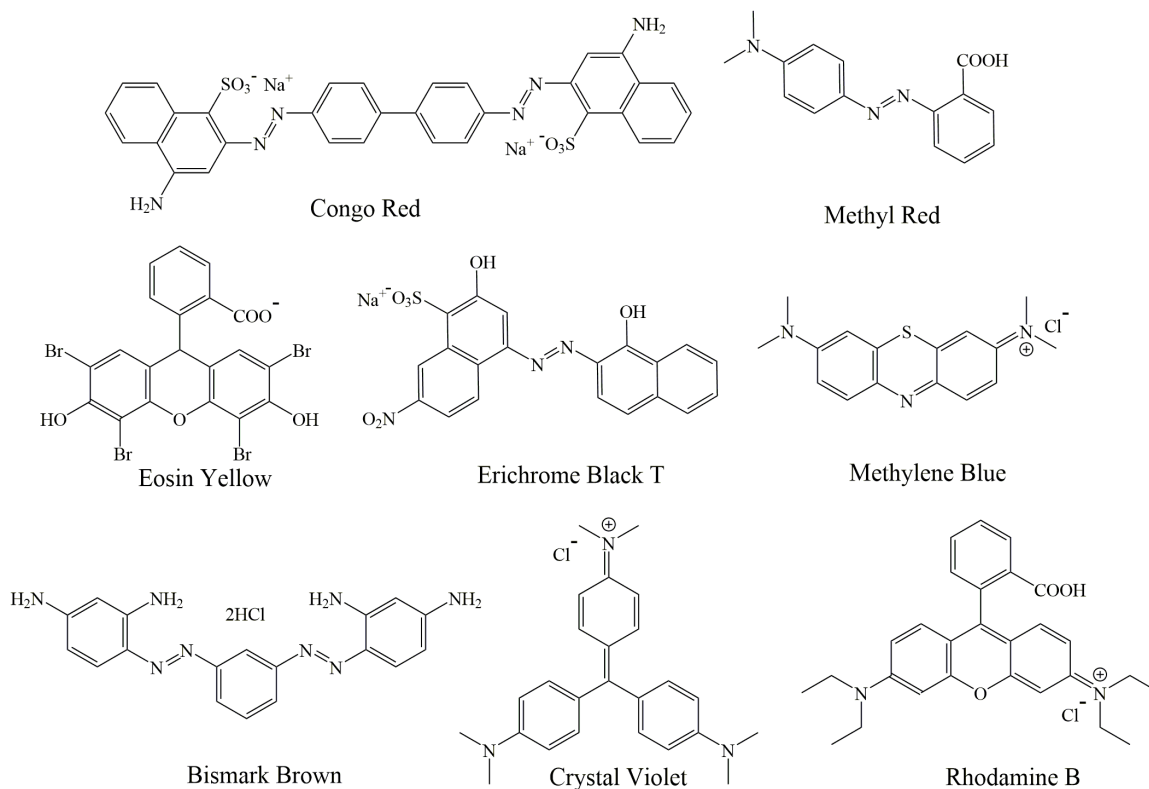


Fig. 2.2 Structures of different organic dyes examined in adsorption studies.

were analyzed using Surface area analyzer (Quantachrome, Autosorb-IQ MP). Before surface area analysis, the material was degassed at 150 °C for 6 h under vacuum. Field Emission Scanning Electron Microscope (Zeiss, Sigma 300) was employed to study the surface morphology of as-synthesized material, and the micrographs were captured at 20 kV, 130 eV. The thermal analysis of the sample was performed using Netzsch (STA449F3A00) TGA analyzer under an argon atmosphere. The zeta potential and particle size were measured using Anton Paar Litesizer 500. The absorbance spectra were recorded on a UV-vis spectrophotometer (Agilent Technologies, Cary 100), and the fluorescence studies were performed on a HoribaFluoromax-4 Spectrofluorometer with a slit width of 5 nm using 1 cm path length quartz cuvettes. The solid-state diffuse reflectance spectrum (DRS) of the synthesized material was recorded using Perkin Elmer (Lambda 750) UV-vis spectrophotometer. Time-resolved photoluminescence (TRPL) measurements were performed by using a LifeSpec II Edinburgh instrument. The cation concentration in aqueous solution was analyzed using Atomic Absorption Spectrometer (Varian, AA240, Netherlands). The anion concentration was determined with a Metrohm ion meter (Basic IC 792, Switzerland) equipped with Metrosep A Supp5 (4.0 x 250 mm) anion exchange column packed with polymethacrylate with quaternary ammonium groups as a stationary phase. The CO₂ adsorption experiment was performed in a high-pressure adsorption instrument (Quantachrome iSorbHP1-XKRLSPN100)

by the volumetric method. Before analysis, the samples were degassed 200 °C for 6h under a high vacuum. Ultrapure CO₂ (99.99%) was used during the high-pressure gas adsorption experiment.

2.3 Synthesis of different Sn-based MOFs

2.3.1. Synthesis of Sn(II)-BDC MOF

1.0 mmol SnCl₂·2H₂O was dissolved in 5.0 ml distilled water. 1.0 mmol BDC, along with a stoichiometric amount of NaOH (2.0 mmol) required to deprotonate the carboxylic groups of the linker, was dissolved in 10 ml water and sonicated for 10 minutes to form an apparent suspension. Subsequently, a 5.0 ml stannous salt solution was added slowly to the deprotonated linker solution. The dense milky white solution formed was transferred to a 25 ml Teflon lined stainless steel autoclave and tightly sealed. The autoclave was heated at 120 °C for 24 h in a hot air oven and then cooled to room temperature. The yellowish-white powder precipitate obtained was washed with distilled water (two times) and methanol (three times) by centrifugation at 7000 rpm for 3 minutes. The final product was dried in a hot air oven at 80 °C for 3 h and stored in a tightly sealed glass vial for further characterization. The product yield was calculated to be 55% based on the precursor salt.

2.3.2. Synthesis of Sn(II)-TMA MOF

1.2 mmol metal salt stannous chloride dihydrate (SnCl₂·2H₂O) was dissolved in 10 ml ethanol. Organic ligand solution was prepared by dissolving 0.6 mmol trimesic acid (TMA) in 10 ml ethanol under vortexing and sonicated for 10 minutes. The stannous salt solution was added dropwise to the ligand solution under constant stirring. The resultant solution was transferred to a 25 ml Teflon-lined stainless-steel autoclave and sealed. The autoclave was heated at 120 °C for 24 h in a hot air oven. After cooling down to room temperature, the yellowish-white powder precipitate was washed thoroughly with ethanol (two times) and acetone (three times) under centrifugation at 7000 rpm for 3 minutes. The final product was dried in a hot air oven at 80 °C for 3 h and kept in a tightly sealed glass vial for further characterization.

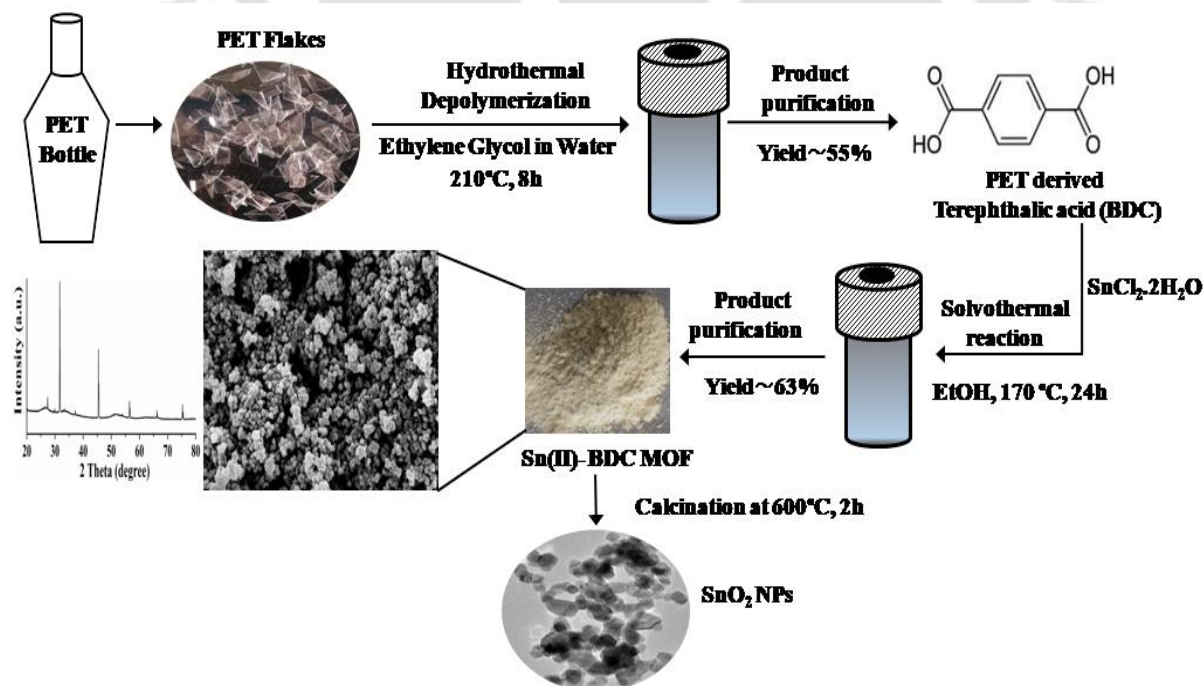
2.3.3. Synthesis of Sn(II)-BTEC chemosensor

A mixture of SnCl₂·2H₂O (0.6 mmol) and BTEC (0.6 mmol) was dissolved in 20 ml ethanol under sonication. The resulting solution was transferred to a 25 ml Teflon lined stainless steel autoclave, heated at 170 °C for 24 h under autogenous pressure, and after that naturally cooled to room temperature. The yellowish-white precipitate was washed with ethanol and soaked in acetone for 24 h to remove any unreacted organic ligand. The final product (yield ~ 65%, based on Sn) was dried at 80 °C for further characterization.

2.3.4. Synthesis of Sn(II)-MOF

The terephthalic acid (BDC) for Sn(II)-MOF synthesis was extracted following an earlier reported method [2.1]. Briefly, waste PET bottles were collected and washed thoroughly with tap water. After oven-dry, the PET bottles were shredded into small flakes, 0.5 g of which were suspended in 35 ml distilled water, and 5 ml ethylene glycol was added to it. The solution was transferred in a 50 ml Teflon lined stainless steel autoclave and heated at 210 °C for 8 h. After cooling down to room temperature, the product was centrifuged off, washed with ethanol (two times), and dried at 80 °C for 6 h. The yield of PET derived BDC was calculated at 55%. Further, the BDC extracted from waste PET bottles was utilized for the synthesis of Sn(II)-MOF.

The metal salt of $\text{SnCl}_2 \cdot 2\text{H}_2\text{O}$ (1 mmol) was dissolved in 10 ml ethanol under sonication. 2 mmol NaOH was added to 1 mmol PET derived BDC and sonicated in ethanol to form a homogeneous linker solution. The salt solution was added dropwise to the linker solution under slow stirring, and the final solution was transferred to a stainless steel autoclave and heated at 170 °C for 24 h. After the reaction, the autoclave was cooled down to room temperature; the product was separated via centrifugation and washed twice with ethanol and methanol, respectively. The yield of Sn(II)-MOF was calculated at 63% based on the metal salt. Next, the Sn(II)-MOF was used as a template for the synthesis of tin oxide nanoparticles (SnO_2 NPs) through the thermal decomposition route.



Scheme 2.1 Synthesis of Sn(II)-MOF and its derivative SnO_2 NPs via hydrothermal and solvothermal synthetic route.

An approximately 100 mg of as-synthesized Sn(II)-MOF was collected in a silica crucible and calcined in a muffle furnace at 600 °C for 3 h. The calcination process leads to the decomposition of the organic MOF template resulting in the formation of highly crystalline SnO₂ NPs. The synthesized SnO₂ NPs were washed with ethanol and dried overnight at 80 °C. All the materials synthesized above were found to be insoluble in tested organic solvents, namely, ethanol, methanol, acetone, and DMF. The process schematic for the synthesis of Sn(II)-MOF and its derivative SnO₂ nanoparticles (SnO₂ NPs) is illustrated in Scheme 2.1.

2.4. Experimental methods

2.4.1. Aqueous stability testing

20 mg of the synthesized material was suspended in 10 ml of water and left undisturbed at room temperature for 24 h. After the water exposure, the material was recovered through filtration and dried at 80 °C. To ensure that a portion of the material was not dissolved in the aqueous solution the final mass of the material was noted, and the percentage of the recovered material was calculated using the equation below [2.2].

$$\frac{mass_{\text{recovered}}}{mass_{\text{initial}}} \times 100 = \text{yield}\%$$

After confirming the mass balance, the identity of the recovered material was verified with the pristine material using powder XRD and FT-IR.

2.4.2. Dye adsorption study

The Sn(II)-BDC MOF was dried overnight at 80 °C prior to conducting the adsorption study. Stock solutions of 1000 mg L⁻¹ were prepared for different dyes. Varying concentrations of dyes EBT, CR, and EY were prepared by adequate dilution of the stock solutions. The adsorbent at 1.0 g L⁻¹ was added to 10 ml solutions of different dyes in a 50 ml falcon tube, and the mixture was incubated at 25 °C in an orbital shaker at 280 rpm for a defined time interval. An aliquot of the sample was collected after the incubation period and centrifuged at 7000 rpm for 5 min for further analysis. The pH study was conducted in a range of pH 4 - pH 9 with the initial dye concentration of 100 mg L⁻¹, keeping the shaking time constant at 2 h. For the kinetic studies, the supernatant was collected at different time intervals for the determination of unadsorbed dyes. The isotherm study was performed at different initial concentrations of the dyes (25-200 mg L⁻¹) and a fixed concentration of the MOF material (1.0 g L⁻¹) at 25 °C. The concentration of residual dye in the supernatant was analyzed using a UV spectrophotometer at λ_{max} of 535, 517, 497 nm for EBT, EY, and CR, respectively. The removal efficiency of the dyes by Sn(II)-BDC MOF was calculated using the following equation [2.3].

$$\text{Removal}(\%) = \frac{(C_0 - C_e)100}{C_0} \%$$

where C_0 (mg L^{-1}) and C_e (mg L^{-1}) are the initial and equilibrium concentrations of dye in solution.

The dye adsorption capacity of Sn(II)-BDC MOF was calculated from the equation illustrated as below [2.4]

$$q_e = \frac{(C_0 - C_e)V}{W}$$

where q_e is the equilibrium adsorption capacity (mg g^{-1}), C_0 and C_e are the initial and equilibrium concentrations of the dyes in mg L^{-1} . V in L is the volume of the solution, and W (g) is the mass of the adsorbent.

2.4.3. Fluoride removal study

The effect of adsorbent dose on fluoride removal efficiency was determined by varying different doses of Sn(II)-TMA adsorbent in 12 mg L^{-1} fluoride solution (10 ml) in a 50 ml centrifuge tube. The adsorbent-adsorbate mixture was shaken in an orbital shaker at 250 rpm for 4 h at 298 K. The supernatant was collected after centrifugation at 8000 rpm for 3 min and further syringed filtered with $0.22 \mu\text{m}$ cut-off nylon membrane. The filtrate was analyzed for fluoride concentration with Metrohm ion meter. The eluent was prepared using a mixture of $1 \text{ mM L}^{-1} \text{ NaHCO}_3$ and $3.2 \text{ mM L}^{-1} \text{ Na}_2\text{CO}_3$ in deionized water, and the flow rate was maintained at 0.7 ml min^{-1} at 10 MPa column pressure.

The fluoride adsorption kinetics was investigated at 298 K with 12 mg L^{-1} initial fluoride concentration. After a specified time interval (15-300 min) an appropriate volume of sample was collected and filtered with $0.22 \mu\text{m}$ filter paper for fluoride determination.

An adsorption isotherm study was conducted with the different initial concentrations of fluoride ($5\text{-}150 \text{ mg L}^{-1}$) at 298 K. The effect of coexisting anions (50 mg L^{-1} each) and ionic strength of solution on the fluoride removal efficiency was also investigated.

The fluoride adsorption capacity (mg g^{-1}) was calculated using the equation below.

$$q_e = \frac{(C_0 - C_e)V}{m}$$

where C_0 and C_e are the initial and equilibrium fluoride concentration (mg L^{-1}), respectively, V is the volume (L) of the fluoride solution and m the mass (g) of the Sn(II)-TMA MOF.

2.4.4. UV-vis and Fluorescence spectroscopic studies

Stock solutions (50mM) of various anions (I^- , Br^- , CN^- , F^- , Cl^- , NO_3^- , SO_4^{2-} , HPO_4^{2-} , CrO_4^{2-} , MnO_4^- , and ClO_4^-) and cations (Ca^{2+} , Pb^{2+} , Cd^{2+} , Mg^{2+} , Ni^{2+} , Cu^{2+} , Co^{2+} , Mn^{2+} , and Zn^{2+}) were prepared in de-ionized water. All the UV-vis and fluorescence experiments were carried out in de-ionized water (pH~7.2), given the practical applicability of Sn(II)-BTEC chemosensor in sensing small molecules from the aqueous environment. A stock solution of 1 mg ml⁻¹ of Sn(II)-BTEC was prepared in de-ionized water, sonicated to form a fine dispersion, and used after appropriate dilution for further spectroscopic studies. For the fluorescence titration experiments, a 0.1 mg ml⁻¹ of Sn(II)-BTEC in a quartz optical cell (path length~1 cm) was titrated with an increasing concentration of CrO_4^{2-} ions (0-500 μM).

The limit of detection (LOD) for CrO_4^{2-} ions was calculated using the following equation [5.5, 5.6]

$$LOD = 3\sigma/m$$

where σ is the standard deviation of the five blank measurements for Sn(II)-BTEC, and m is the slope of the linear curve plotted for the luminescence intensity (I) of Sn(II)-BTEC at the lower concentration region of the chromate ion addition.

2.4.5. Arsenate and phosphate adsorption study

The batch adsorption experiment using synthesized Sn(II)-MOF was performed by appropriately diluting the stock solution of the anions with an optimized adsorbent dose of 1 g L⁻¹ in a 50 ml falcon tube and shaken thoroughly at 250 rpm in an orbital shaker at room temperature. After the reaction, the adsorbent was separated via filtration, and the equilibrium concentration of arsenate and phosphate was determined by Atomic absorption spectrophotometer and Ion Chromatography, respectively. The removal efficiency of Sn(II)-MOF was calculated from the equation as expressed below.

$$\text{Removal(\%)} = \frac{(C_0 - C_e)100}{C_0} \%$$

where C_0 (mg L⁻¹) and C_e (mg L⁻¹) are the initial and equilibrium concentration of the anions in solution.

The adsorption experiments were conducted with an initial concentration of 1 mg L⁻¹ (arsenate) and 20 mg L⁻¹ (phosphate). The influence of solution pH and the effect of co-existing anions on the removal efficiency of the anions was examined in detail. The kinetic analysis was performed by withdrawing an appropriate quantity of the sample at regular time intervals, and

the filtered sample was analyzed by AAS and ion chromatography for the residual concentration of arsenic [As(V)] and phosphate respectively. The adsorption isotherm experiment was conducted in the concentration range of 0.5-100 mg L⁻¹ for arsenate and 10-200 mg L⁻¹ for phosphate, respectively. The adsorption capacity (mg g⁻¹) was calculated using the equation below.

$$q_e = \frac{(C_o - C_e)V}{m}$$

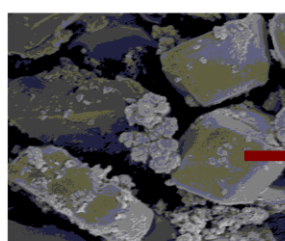
where C_o and C_e are the initial and equilibrium concentration (mg L⁻¹) of the anions (arsenate and phosphate), respectively, V is the volume (L) of the anion solution, and m the mass (g) of the Sn(II)- MOF adsorbent.

References

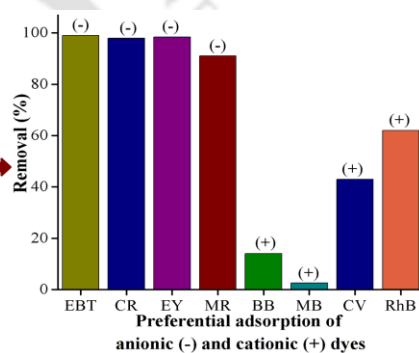
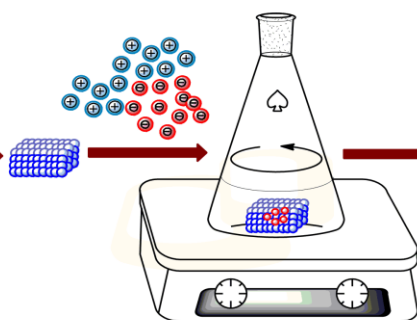
- [2.1] X. Dyosiba, J. Ren, N.M. Musyoka, H.W. Langmi, M. Mathe and M.S. Onyango, *Sustainable Mater. Technol.*, 2016, **10**, 10-13.
- [2.2] A.J. Howarth, A.W. Peters, N.A. Vermeulen, T.C. Wang, J.T. Hupp and O.K. Farha, *Chem. Mater.*, 2017, **29**, 26-39.
- [2.3] T. Wang, P. Zhao, N. Lu, H. Chen, C. Zhang, and X. Hou, *Chem. Eng. J.*, **295**, 403-413.
- [2.4] B. Saha, S. Das, J. Saikia and G. Das G. *J. Phys. Chem. C.*, 2011, **115**, 8024.
- [2.5] R. Lv, J. Wang, Y. Zhang, H. Li, L. Yang, S. Liao, W. Gu and X. Liu, *J. Mater. Chem. A.*, 2016, **4**, 15494–15500.
- [2.6] B. Joarder, A.V. Desai, P. Samanta, S. Mukherjee and S.K. Ghosh, *Chem. Eur. J.*, 2015, **21**, 965-969.

Chapter 3

Green synthesis of Sn(II)-BDC MOF and its application in the preferential adsorption of hazardous anionic dyes



Sn(II)-BDC MOF



Indian Institute of Technology Guwahati

3.1 Background and Focus of the Chapter

Synthetic dyes from various industrial sources such as paper, printing, textile cause pollution of the water bodies. Organic dyes, due to their complex structure, are resistant to biodegradation [3.1, 3.2]. Owing to their carcinogenic, toxic, and mutagenic nature, organic dyes possess a severe threat to living beings and the environment [3.3]. In addition to its health effects, the presence of dyes in wastewater streams is highly visible, which reduces the penetration of sunlight and lowers oxygen solubility, thereby affecting the aquatic ecosystem[3.4]. Thus it is of prime concern to remove such toxic dyes from our environment.

Physico-chemical treatment processes such as flocculation, coagulation, oxidation, membrane separation, chemical precipitation, and adsorption are primarily employed for dye removal from the aqueous environment [3.5-3.9]. However, among these methods, adsorption has been widely adopted owing to its simplicity, low cost, ease of operation, process efficiency, and environment-friendly nature [3.10]. Various adsorbents such as activated carbon, carbon nanotubes, resin, and activated diatomite have been explored for the adsorptive removal of dyes from aqueous solution [3.11,3.12]. However, these adsorbents were accompanied by certain limitations such as low adsorption capacity, poor selectivity, complex preparation techniques, and difficulty in regeneration [3.13]. Hence it is a prerequisite for an adsorbent to possess promising adsorption capacity along with potential recyclability. Metal-organic framework (MOF), which are a class of porous crystalline inorganic-organic hybrid material based on inorganic metal ion center coordinated to bridging organic ligand via coordination bond, has received extensive attention due to their potential applications in catalysis [3.14], gas adsorption/separation [3.15], drug delivery [3.16] and sensing [3.17]. In the past few years, MOFs have been explored for the removal of dyes from aqueous solutions due to their diverse chemical compositions, tunable pore size, a vast array of structures, high surface area, and coordinately unsaturated metal sites providing multiple functionalities regulating its adsorption capability.

Moreover, the breathing effect, presence of open metal sites, and framework of metal ions in MOFs are reported as potential mechanisms of dye removal [3.18-3.20]. In comparison with the conventional porous materials such as zeolite and activated carbon, which require high temperature during synthesis, MOFs require less processing temperature. The pore size of the activated carbon and zeolites being limited to 0.3 to 1 nm, it potentially hinders the adsorption of large dye molecules and deters the desorption process [3.21].

In contrast, due to the presence of abundant larger pores (micro to mesopores), adsorption of hazardous organic dyes is enhanced in MOFs providing, a promising removal efficiency for these harmful dyes. All of the aforementioned advantages establish MOFs as a superior material for adsorption purposes [3.22]. However, the drawback of MOFs has been its stability in aqueous solution due to the hydrophilic nature of the metal nodes where the metal-linker coordination bond gets hydrolyzed, thereby disrupting the framework structure [3.23]. To date, very few MOFs are reported to be stable under aqueous environment for a more extended period [3.24]. The stability of the MOF can be explained based on Pearson's HSAB principle. Sn(II), being a hard Lewis acid, can form a relatively stronger coordination bond with hard Lewis base, *i.e.*, carboxylate, resulting in the formation of a rigid interconnected framework structure [3.25]. Besides, the stability of MOF increases with the increasing inertness of the metal ion [3.26].

Sn(II)-dicarboxylate coordination polymers have been reported to be hydrothermally or solvothermally synthesized under alkaline conditions producing known homoleptic 1D and 2D architectures or 3D frameworks consisting of tin-oxide as secondary building units (SBUs) [3.27,3.28]. Recently, air and moisture stable Sn(II) coordination polymers have been reported with polytopic carboxylate based organic linkers [3.29]. Tin being an environmentally benign material, has been used widely in food packaging. Tin salts possess low toxicity to the human body as it is poorly absorbed and rapidly excreted in the form of faeces [3.30]. From the commercial point of view, Sn(II) salt act as a low-cost precursor for material synthesis [3.31]. To the best of our knowledge, tin-based MOF has not been explored for wastewater applications, and there is a scarcity in studies with coordination polymers of Sn(II). The present chapter focuses on the adsorptive removal of different anionic dyes from aqueous solution using Sn(II)-BDC MOF. The material was synthesized using hydrothermal DMF free synthesis route using Sn(II) as inorganic metal ion and BDC as a source of the organic linker. The aqueous stability of the synthesized material was confirmed. The adsorption efficiency of different anionic dyes, like Congo red (CR), Erichrome black T (EBT), Eosin yellow (EY), and Methyl red (MR) were compared with cationic dyes *viz.* Methylene blue (MB), Crystal violet (CV), Rhodamine B (RhB), and Bismark brown (BB). Batch adsorption experiments were carried out to study the effect of dose, initial dye concentration, contact time, and temperature on the removal efficiency. The experimental data were fitted into three linear forms of kinetic models, and the plausible mechanism for adsorption was proposed. Finally, the multi-cyclic

efficiency and reusability of the synthesized material were also tested. The Sn(II)-BDC MOF proved to be a promising adsorbent with excellent aqueous stability for preferential removal of anionic dyes.

3.2 Results and Discussion

3.2.1. Characterization of Sn(II)-BDC MOF

The FT-IR spectrum of Sn(II)-BDC MOF, as depicted in Fig. 3.1a reveals the characteristic peak at $\sim 580\text{ cm}^{-1}$, which relates to Sn–O stretching vibration [3.32, 3.33]. Further, the peaks at 1539 cm^{-1} , 834 cm^{-1} , 735 cm^{-1} can be attributed to the C=O and C-H stretching vibrations, respectively [3.34,3.35]. The surface area of the Sn(II)-BDC MOF was found to be much less with pores predominantly in the microporous range. The surface area was calculated via the BET method in the relative pressure P/P_0 range of 0.05-0.3, and the BJH method was adopted for the analysis of pore size distribution. The specific surface area, pore-volume, and pore diameter were found to be $17\text{ m}^2\text{g}^{-1}$, $0.07\text{ cm}^3\text{g}^{-1}$, and 1.8 nm , respectively. The N_2 adsorption-desorption isotherm (Fig. 3.1b) indicated a Type-IV isotherm with H1-type hysteresis loop, suggesting a capillary condensation of the gas at high relative pressure in the mesopores of the material [3.36]. The surface area of our synthesized material was comparable with the previously reported Sn-based MOF ($15.29\text{ m}^2\text{ g}^{-1}$) with carboxylate based ligand [3.37]. Both the synthesis was carried using water as a solvent, and according to literature, the choice of solvent affecting the coordination environment in MOF synthesis is still unclear [3.38]. Thermogravimetric analysis (TGA) illustrated a two-step degradation of the Sn(II)-BDC MOF (Fig. 3.1c). The first stage of weight loss was about 5% owing to the release of the absorbed water molecules at a temperature of $250\text{ }^\circ\text{C}$. The second stage weight loss of about 30% was mainly due to the degradation of the MOF structure at a temperature above $400\text{ }^\circ\text{C}$. The material was found to be stable at a temperature as high as $400\text{ }^\circ\text{C}$. FESEM analysis revealed the rhomboidal morphology of the material, and the EDX spectrum confirmed the presence of Tin (Sn), Carbon (C), and Oxygen (O) at weight percentages of 43.8%, 25.6%, and 30.5%, respectively (Fig. 3.1d). In general, the low stability of the MOFs in water limits their application in wastewater treatment. Therefore, it is of significant importance to test the stability of the synthesized material in an aqueous environment. For this purpose, the as-synthesized MOF material was suspended in water and left undisturbed for five days at room temperature [3.39]. FTIR and PXRD analysis indicated that the characteristic peaks of the

Sn(II)-BDC MOF before and after incubation in water did not alter significantly (Fig. 3.1e, f), confirming the integrity of the compound upon prolonged exposure in water and its aqueous stability. The PXRD pattern revealed the crystalline nature of the as-synthesized Sn(II)-BDC MOF with major peaks at $2\theta = 8.9^\circ, 14.7^\circ, 18.2^\circ, 23.4^\circ, 24.4^\circ, 26.1^\circ,$ and 39.2° , respectively (Fig. 3.1f).

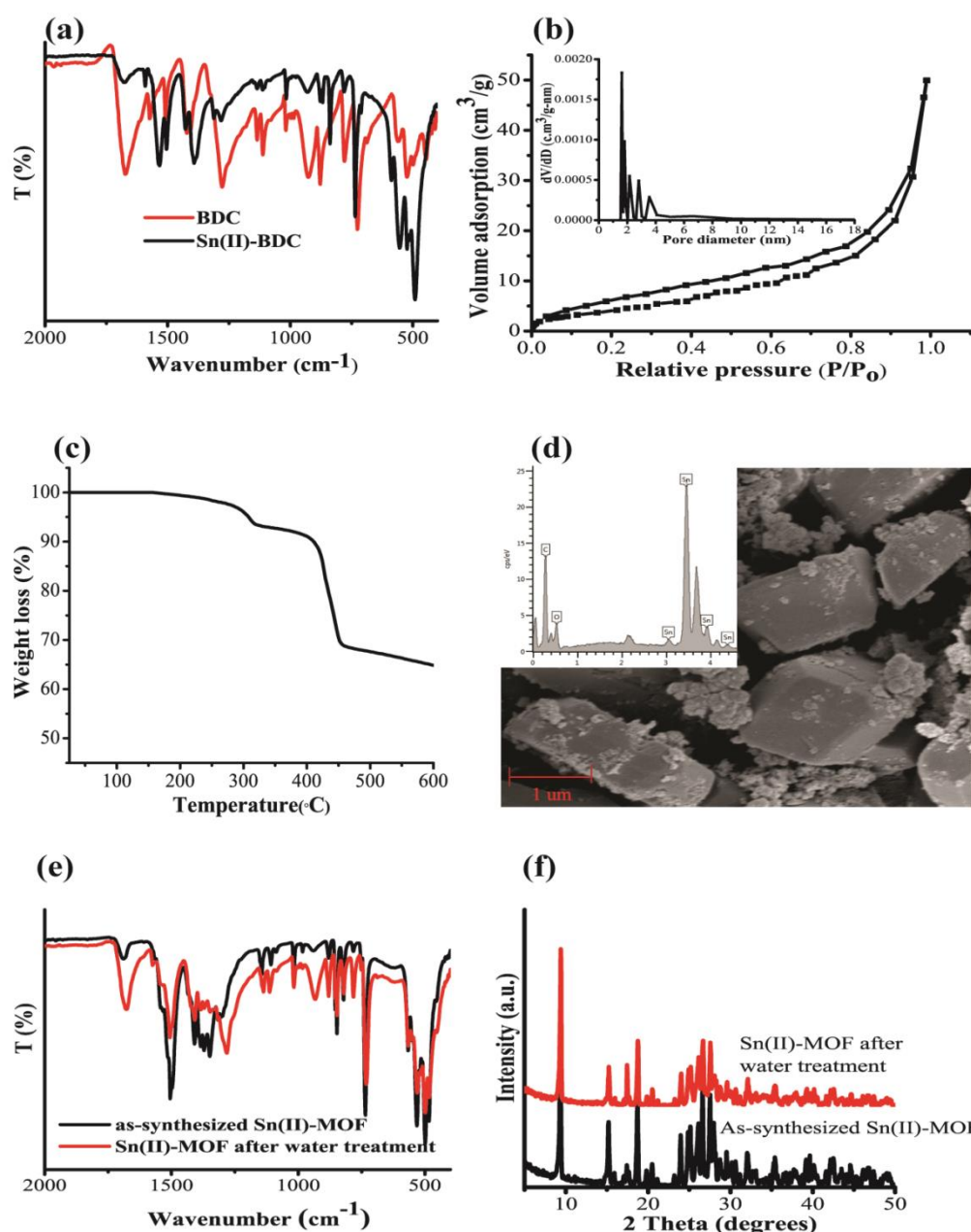


Fig. 3.1 (a) FT-IR, (b) N₂ adsorption-desorption isotherm (INSET: pore-size distribution curve), (c) Thermogravimetric (TGA), (d) FESEM-EDX analysis of Sn(II)-BDC MOF, and (e, f) FT-IR and PXRD plot of the MOF after soaking in water for 48 h.

3.3. Adsorption experiments

3.3.1. Preferential adsorption of different dyes

Comparative adsorption efficiency of different organic dyes (cationic and anionic) with an initial concentration of 100 mg L^{-1} is illustrated in Fig. A3.1. The result demonstrated enhanced and preferable adsorption of anionic dyes. The removal efficiency of the cationic dyes (MB, RhB, BB, and CV) was not significant compared to the anionic dyes, and hence, further elaborated adsorption studies were conducted with the three anionic dyes (CR, EBT, and EY). The preferential adsorption of anionic dyes suggested electrostatic interaction with the negatively charged dye and positively charged Sn(II)-BDC MOF surface, as evident from the positive zeta potential value ($+9.7 \text{ mV}$) at neutral pH (Fig. A3.2).

3.3.2. Effect of adsorbent dose

The influence of Sn(II)-BDC MOF dose on the dye removal efficiency at room temperature was investigated. The adsorbent dose was varied from $1.0 - 5.0 \text{ g L}^{-1}$ at a constant incubation time of 2 h. It was observed that the adsorption capacity, $q_e \text{ (mg g}^{-1}\text{)}$ increased with an increase in the adsorbent dose (Fig. 3.2a), which may be due to the availability of more surface area and active sites at a high dose. The curve finally leveled off beyond 3.0 g L^{-1} dose, which can be attributed to the saturation of the active sites available for adsorption. Further studies were carried out at a minimum dose of 1 g L^{-1} to improve the process economics.

3.3.3. Effect of pH

The pH of a medium influences the surface properties of a material, thereby affecting its physicochemical behavior in an aqueous medium, particularly its adsorption capacity. Hence, dye-adsorption studies were conducted at a pH ranging from 4.0 to 9.0. The adsorption profile was found to be the same for all three anionic dyes and revealed a decrease in adsorption capacity with an increase in pH (Fig. 3.2b). At lower pH, the surface of the Sn(II)-BDC MOF is protonated, thereby providing favorable interaction with the anionic dyes. On the contrary, the negative charges on the MOF surface increase at higher pH due to the deposition of OH⁻ ions on the Sn(II)-BDC surface, thus causing electrostatic repulsion with the negatively charged dye molecules.

3.3.4. Kinetic Study

A series of adsorption experiments were performed at 25 °C for all three anionic dyes to determine the equilibration time. The kinetic study was conducted with an adsorbent dose of 1 g L⁻¹ at an initial dye concentration of 100 mg L⁻¹. It was clear from the adsorption profile that the steady-state reached at 150 min for EBT and 250 min for EY and CR, respectively (Fig. 3.2c). The q_e values for dyes EBT, CR, EY were determined to be 98.45 mg g⁻¹, 97 mg g⁻¹, 99.5 mg g⁻¹ at the steady-state. The high q_e values indicate significant adsorption capacity of the MOF adsorbent for all the dyes.

Pseudo-first and second-order kinetic models (Eqs. 1 and 2) were adopted to evaluate the kinetic mechanism for adsorption of the dyes.

$$\ln(q_e - q_t) = \ln q_e - k_1 t \quad (1)$$

$$\frac{t}{q_t} = \frac{1}{k_2 q_e^2} + \frac{t}{q_e} \quad (2)$$

where q_t and q_e are adsorption capacity at time t and equilibrium respectively, and k_1 and k_2 denote the first-order and second-order kinetic rate constants, respectively. Pseudo-second order kinetic model linearized curve fits were plotted for all the three anionic dyes (Fig. 3.3a,b,c). The correlation coefficients (R^2) and kinetic rate constant (k) values for three linearized form of kinetic models were calculated (Table 3.1). The adsorption of three anionic dyes EBT, CR, and EY on Sn(II)-BDC MOF followed the pseudo-second-order kinetic model as evident from a higher correlation coefficient (R^2) value compared to other kinetic models.

Weber-Morris model was used to determine whether intra-particle diffusion is the rate-limiting factor in dye adsorption. The aforesaid kinetic model is expressed by Eq. 4

$$q_t = (k_i)t^{0.5} + c \quad (3)$$

where k_i is an intra-particle diffusion rate constant, q_t is dye adsorption capacity at time t , and c (mg g⁻¹) is a constant revealing boundary layer thickness. The lower values of the correlation coefficient (R^2) of this model suggest that intra-particle diffusion is not the only rate-limiting step in dye adsorption and that another simultaneous phenomenon like surface sorption is also taking place, which perhaps accounts for the high adsorption efficiency of different dyes. The summary of the kinetic parameters for three anionic dyes CR, EBT, and EY is listed in Table 3.1.

Table 3.1 Kinetic parameters for the adsorption of different anionic dyes

	First-order kinetics		Second-order kinetics		Intra-particle diffusion		
	k_1 (min ⁻¹)	R ²	k_2 (g mg ⁻¹ min ⁻¹)	R ²	k_i (mg g ⁻¹ min ^{-0.5})	c (mg g ⁻¹)	R ²
EBT	0.021	0.927	0.0001	0.975	9.48	14.89	0.994
CR	0.013	0.917	0.0001	0.98	6.156	14.04	0.851
EY	0.011	0.971	0.00008	0.991	5.548	1.35	0.957

3.3.5. Thermodynamic study

Adsorption experiments were performed at different temperatures (298 K, 308 K, and 318 K), keeping initial dye concentration and adsorbent dose constants at 100 mg L⁻¹ and 1 g L⁻¹, respectively, to get an insight into the thermodynamic aspect of the adsorption behavior. It was observed that an increase in temperature led to an increase in adsorption capacity q_e (mg g⁻¹) for all three dyes. The thermodynamic aspect of the system is explained by the Gibbs free energy equation, which correlates the thermodynamic parameters enthalpy change (ΔH°), entropy change (ΔS°), and Gibbs free energy change (ΔG°) by the following equation:

$$\Delta G^\circ = -RT \ln(k_c) \quad (4)$$

where R is the universal gas constant (8.314 J mol⁻¹ K⁻¹), T is the temperature (K), k_c is the equilibrium stability constant calculated at different temperature using the following equation:

$$k_c = Q_e / C_e \quad (5)$$

where Q_e and C_e are the equilibrium concentration in the solid and aqueous phase, respectively. The enthalpy and entropy of adsorption were estimated from the van't Hoff equation indicated below:

$$\ln k_c = \left(\frac{-\Delta H}{R} \right) \left(\frac{1}{T} \right) + \frac{\Delta S}{R} \quad (6)$$

The thermodynamically feasible and spontaneous nature of the adsorption process can be validated from the negative values of ΔG° (Table 2), where more negative values at higher temperatures correlate with an increase in adsorption efficiency [3.46] as shown in Fig. 3.2d. The positive value of enthalpy (ΔH) entails that the process is endothermic, and with an increase in temperature, there is an increase in the equilibrium constant. The rise in temperature from 298K to 318K resulted in better adsorption capacity. A ΔH value ranging

from $83 - 830 \text{ kJ mol}^{-1}$ indicates chemisorption, while a value ranging from $8-25 \text{ kJ mol}^{-1}$ indicates physisorption [3.47-3.49]. In the present study, the ΔH of the anionic dyes EBT, CR, and EY were 128.49, 137, and 715 kJ mol^{-1} , respectively, which suggest that the adsorption of the dyes on Sn(II)-BDC is a chemisorption process. The entropy or randomness of the system was evident from the positive entropy (ΔS) values. Further, the entropy value signified that there is an increase in disorder at the solid-liquid interface [3.50].

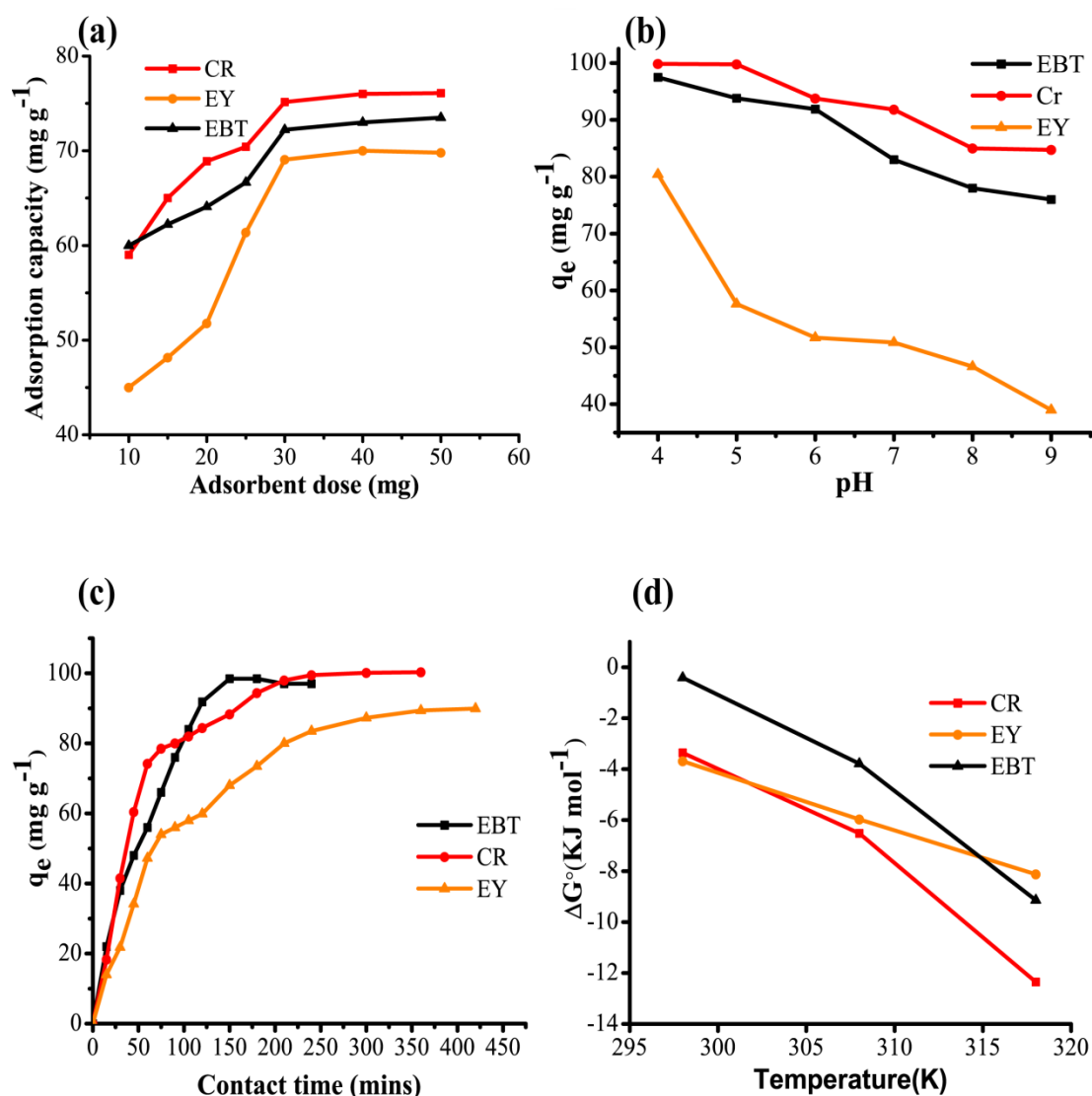


Fig. 3.2 (a) Equilibrium studies of EBT, CR, and EY on Sn(II)-BDC MOF, (b) Influence of pH on adsorption capacity, (c) Effect of dose on the adsorption capacity of EBT, CR, and EY, and (d) Effect of temperature on ΔG° for the adsorption of the dyes.

Table 3.2 Summary of thermodynamic parameters

Dyes	Temperature (K)	ΔG (kJ mol ⁻¹)	ΔH ((kJ mol ⁻¹)	ΔS (J mol ⁻¹ K ⁻¹)
EBT	298	-0.41	128.49	424
	308	-3.782		
	318	-9.138		
CR	298	-3.359	137.50	464.4
	308	-6.519		
	318	-12.349		
EY	298	-3.682	715	2390
	308	-5.971		
	318	-8.127		

3.3.6. Adsorption isotherm

To elucidate the nature of the interaction between the adsorbent-adsorbate and to determine the maximum adsorption capacity of Sn(II)-BDC MOF, adsorption equilibrium isotherm was studied by varying the initial dye concentration (25 – 200 mg L⁻¹), keeping the MOF dose constant at 1 g L⁻¹. The amount of dyes adsorbed at equilibrium was calculated from Eq. 7:

$$q_e = \frac{(C_0 - C_e)V}{W} \quad (7)$$

where q_e is the equilibrium adsorption capacity (mg g⁻¹), C_0 , and C_e are the initial and equilibrium concentrations of the dyes in mg L⁻¹. V in L is the volume of the solution, and W (g) is the mass of the adsorbent. The adsorption isotherm of different anionic dyes (CR, EBT, and EY) were analyzed by Langmuir and Freundlich isotherm models.

The obtained experimental data were fitted in Langmuir (Eq. 8) and Freundlich (Eq. 9) isotherm equations. The Langmuir isotherm model equation is as follows:

$$\frac{C_e}{Q_e} = \frac{C_e}{q_m} + \frac{1}{K_L q_m} \quad (8)$$

where C_e is the equilibrium concentration of the dyes, Q_e is the equilibrium adsorption capacity, q_m is the maximum adsorption capacity, and K_L is the Langmuir constant.

The Freundlich model, which is based on heterogeneous adsorption, is as follows:

$$\ln Q_e = \ln K_f + \frac{1}{n} \ln C_e \quad (9)$$

where K_F is the Freundlich constant, and n is an empirical parameter related to the intensity of adsorption.

The experimental data fitted well with the Langmuir isotherm model (Fig. 3.3d, e, f), as it is evident from the higher correlation coefficient (R^2) value (Table 3.3). Hence the adsorption of the different anionic dyes on the adsorbent surface is considered to be monolayer adsorption with all the adsorption sites being independent of one another [3.40]. The maximum adsorption capacity for CR, EBT, and EY was calculated to be 95.2 mg g^{-1} , 125 mg g^{-1} , and 208.3 mg g^{-1} , respectively (Table 3.3).

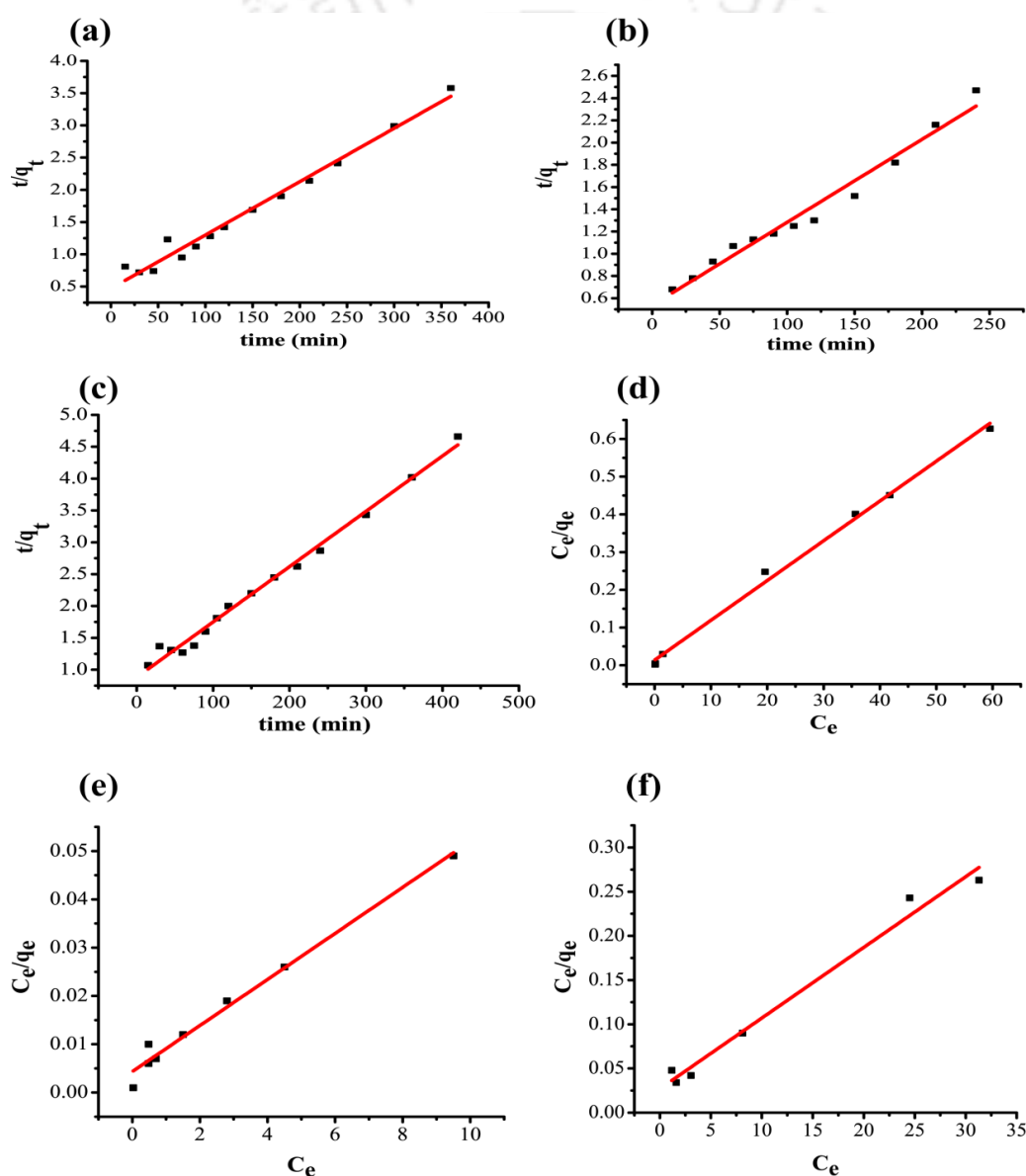


Fig. 3.3 Second-order kinetics plot for the adsorption of (a) EBT, (b) EY, (c) CR onto MOF surface, and Langmuir isotherm fitting for (d) EBT, (e) EY, (f) CR, respectively.

Table 3.3 Summary of Langmuir and Freundlich isotherm parameters

Adsorption isotherm	Isotherm parameters	CR	EY	EBT
Langmuir	$q_{e,exp}$ (mg g^{-1})	96.3	203.1	128
	q_m (mg g^{-1})	95.2	208.3	125
	K_L (L g^{-1})	0.76	1.12	0.29
	R^2	0.996	0.983	0.984
Freundlich	n	0.213	2.58	2.59
	K_f ($(\text{L mg}^{-1})^{1/n} \text{mg g}^{-1}$)	3×10^{-4}	90.83	33.44
	R^2	0.808	0.93	0.815

Partition coefficient (PC) is expressed as a ratio of the adsorbate on the surface of the adsorbent to its liquid phase concentration at equilibrium [3.41]. The true performance of adsorbent material is reflected by the PC because the removal efficiency and adsorption capacity depend on the operating conditions of an adsorption process [3.42]. PC indicates the actual performance of an adsorption system at an equivalent level and overcomes the drawback associated with adsorption capacity. Comparing the performance of a material based on adsorption capacity at high initial loading with that of lower loading can lead to biased evaluation [3.43]. Moreover, PC values help compare the adsorption performance of different materials under varying conditions [3.44]. Table 4 depicts the performance metrics of Sn(II)-BDC MOF in comparison with various other reported adsorbents. The PC values for CR, EBT, and EY were calculated to be 48.5, 65.63, and 62.18 $\text{mg g}^{-1} \mu\text{M}^{-1}$, respectively, at an initial concentration of 100 mg L^{-1} . At higher initial concentration, the surface-active sites get saturated with the dye molecules resulting in a large no of dye molecules remaining in the solution phase at equilibrium. As a consequence, the adsorbent material appears to have a reduced performance (*i.e.*, low partition coefficient) in such conditions. High PC values and maximum adsorption capacity exhibited by Sn(II)-BDC MOF (Table 3.4) make it an excellent material for adsorptive removal of CR, EBT, and EY dyes. Better PC values correlate to the enhancement in adsorption affinity. The presence of larger pores results in high removal efficiency for organic dyes.

The adsorption capacity of different dyes with an initial concentration of 100 mg L^{-1} on Sn(II)-BDC MOF at variable breakthrough (BT) or equilibrium points are indicated in Table 3.5. At 10% BT, the adsorption capacity of CR, EBT, and EY was found to be 21.8 mg g^{-1} , 38 mg g^{-1} , and 41.5 mg g^{-1} , respectively. The lower adsorption capacity of CR at 10% BT compared to

Table 3.4. Performance metrics for Sn(II)-BDC MOF and other related adsorbent materials reported in the literature for adsorptive removal of CR, EBT, and EY dyes.

Adsorbent	Adsorbate	Initial concentration (mg L ⁻¹)	Maximum removal efficiency (%)	pH	q _m (mg g ⁻¹)	Partition Coefficient (mg.g ⁻¹ .μM ⁻¹)	Reference
Co Al-LDH nanocomposite	EBT	100	70	2	530	17.6	[3.56]
CuMgAl LDH		70	80	7	90.50	6.46	[3.57]
NiFe-LDH		100	91.50	2	124.65	14.65	[3.58]
MnO ₂ coated zeolite		100	79	7	12.35	0.58	[3.59]
Sn(II)-BDC MOF		100	98.50	6	98.45	65.63	This work
γ-Al ₂ O ₃ Nanoparticle	EY	100	99.36	4	47.78	79.6	[3.60]
Sn(II)-BDC MOF		100	98.4	4	99.5	62.18	This work
Cd(II)-MOF	CR	50	97.00	-	97	64.6	[3.61]
Zn(II)-Nanoplate MOF		50	53.00	-	47	2.00	[3.62]
MIL-68 (In)		1200	93.90	7	1204	16.72	[3.63]
MIL-100 (Fe) MOF		200	89.68	-	597.85	28.96	[3.64]
[Cd2(oba)2(4-bpdb)2]n.(DMF)x		50	97.30	-	97.30	72.07	[3.65]
[Cd(oba)(4,40-bipy)]n.(DMF)y		50	92.00	-	92.00	23.00	[3.65]
Iron oxide nanoparticle		200	67.00	5	67.10	1.01	[3.66]
Sn(II)-BDC MOF		100	98	6	97	48.50	This work

EBT and EY indicates the slow adsorption of CR, which may be due to its comparatively large molecular size. At 100% BT, the large adsorption capacity obtained for CR (97 mg g⁻¹), EBT (98.45 mg g⁻¹), and EY (99.5 mg g⁻¹) suggested that not only the pores but the surface charge and active sites of Sn(II)-BDC MOF play a significant role in dye adsorption. The -OH groups and -COO⁻ groups present in EY and EBT dyes likely interact with the positively charged Sn(II)-BDC MOF surface via electrostatic interactions leading to higher adsorption capacity. The EY dye being comparatively smaller in size, can quickly diffuse through the micropores present in the adsorbent and get absorbed in the active sites inside the pores, which is evident from its higher adsorption capacity (q_m) compared to the other dyes (Table 3.3). At neutral pH, sulfonate groups of CR dye (Dye-SO₃Na) are dissociated to form anions that electrostatically interact with the positively charged MOF surface resulting in surface sorption. However, the

larger size (about 2 nm) of the CR dye compared to the other anionic dyes may limit its diffusion through the pores of the adsorbent material leading to comparatively lower adsorption capacity. Therefore, the molecular size of the dye molecules controls the adsorption and hence affects the adsorption capacity of the adsorbent material [3.45]. The adsorption capacity of the cationic dyes (MB, CV, RhB, and BB) was not significant compared to the anionic dyes (data not shown).

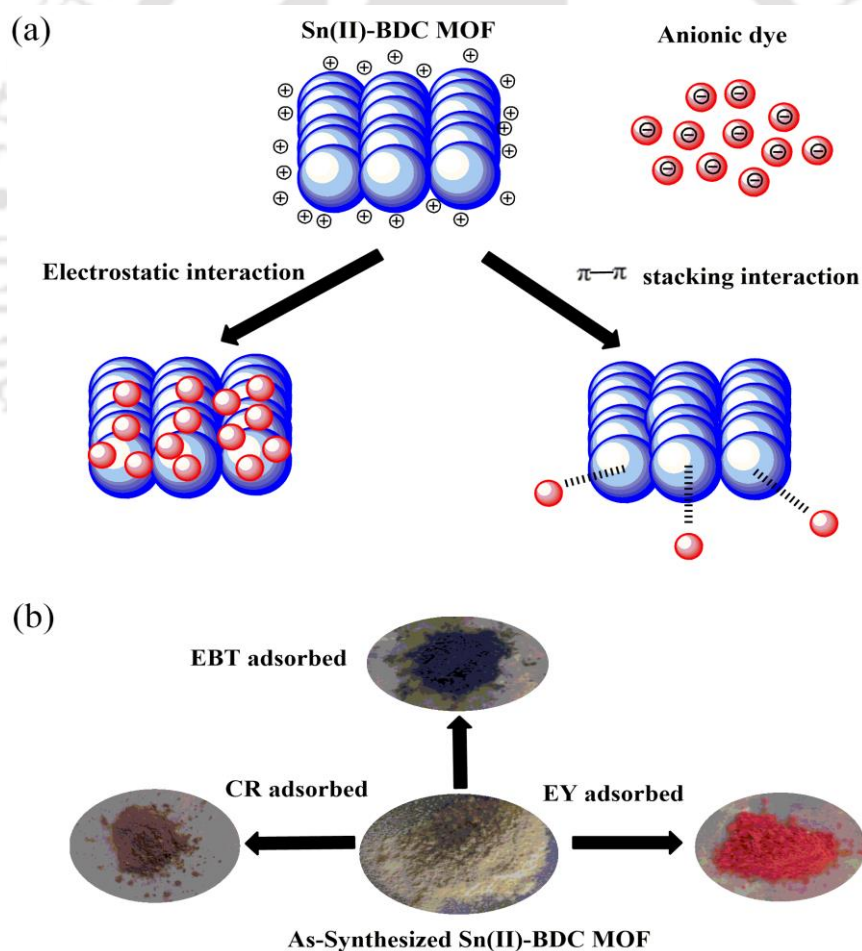
Table 3.5 Adsorption capacity and equilibrium concentration at different breakthrough (BT) points for CR, EBT and EY dyes

Equilibrium (%)	Equilibrium concentration (c), mg L ⁻¹			Adsorption capacity (q _e), mg g ⁻¹		
	CR	EBT	EY	CR	EBT	EY
5	86.00	78.00	81.7	14.00	22.00	18.30
10	78.20	62.00	58.5	21.80	38.00	41.50
25	52.80	44.00	25.8	47.20	56.00	74.20
50	40.10	8.14	15.61	59.90	91.86	84.39
75	26.50	3.00	5.61	73.50	97.00	94.39
100	3.00	1.55	1.50	97.00	98.45	98.50

3.3.7. Plausible mechanism of adsorption

Zeta potential measurement was performed before and after the adsorption to get an insight into the adsorption mechanism. The zeta potential (Fig. A3.2) of the Sn(II)-BDC MOF was determined by direct dispersion of 1 mg of as-synthesized material in 10 ml water. In a neutral solution, the surface of the MOF was found to be positively charged, while the dyes (CR, EBT, and EY) are negatively charged [3.51]. Thus these anionic dyes get readily adsorbed on the surface of Sn(II)-BDC MOF through electrostatic interaction while adsorption of cationic dyes (MB, CV, BB, and RhB) was comparatively much lower owing to electrostatic repulsion. The Lewis base (NH₂) in CR interacts with the Lewis acid Sn sites present in Sn(II)-BDC MOF, thereby promoting favorable adsorption. Also, as reported in earlier works, π - π interaction between the benzene rings of the organic dyes and the MOF material is a significant factor for adsorption [3.52, 3.53]. The proposed mechanism of dye adsorption is illustrated in Scheme 3.1. The low surface area (17 m² g⁻¹) of the adsorbent was not a limiting factor for dye removal

efficiency. Despite having a low surface area ($1.24 \text{ m}^2 \text{ g}^{-1}$) NMIL-100 (Fe) MOF showed high adsorption capacity for both anionic and cationic dyes due to the presence of surface-active sites and functional groups [3.36]. In another report, MIL-53 (Fe) having a low surface area of $23 \text{ m}^2 \text{ g}^{-1}$ displayed high adsorption capacity towards methyl red dye because of its breathing effect [3.54]. The abundant amount of C=O and –OH functional groups present in Sn(II)-BDC MOF adsorbent plays a vital role in dye adsorption (Fig. 3.4a). Further, the PXRD pattern (Fig. 3.4b) of the as-synthesized material revealed intense sharp diffraction peaks at $2\theta = 8.9^\circ$, 14.7° , 18.2° , 26.1° . Post adsorption of EY dye displayed a new peak at $2\theta = 25.8^\circ$, which is a characteristic peak of EY confirming the adsorption of the dye [3.55]. More importantly, the structural integrity of the Sn(II)-BDC MOF is retained after dye adsorption as supported by the presence of the significant peaks (at $2\theta = 8.9^\circ$, 14.7° , 18.2°) of the Sn(II)-BDC MOF.



Scheme 3.1 (a) Proposed mechanism for adsorption of anionic dyes on Sn(II)-BDC MOF (b) Pictorial representation of Sn(II)-BDC MOF before and after dye adsorption.

3.4 Desorption and recyclability

Desorption experiments were carried out to determine the feasibility of regenerating the dye-saturated Sn(II)-BDC MOF for reuse. The desorption study was performed at a pH range of 8–12 using 0.1 M NaOH for the dyes adsorbed at pH \sim 6. It was observed that the desorption efficiency was directly proportional to an increase in solution pH (Fig. 3.4c). At pH > 11, the desorption efficiency was maximum, amounting to \sim 50%, \sim 80%, and \sim 99% for CR, EY, and EBT, respectively. At higher pH, the adsorbent surface is deprotonated, which causes electrostatic repulsion with the anionic dye molecules. The reusability and multicycle efficiency of the material was also tested. The relative adsorption efficiency (average of all three dyes) was calculated to be as high as \sim 86% after the third cycle of reuse (Fig. 3.4d). The optical characteristics of the dye molecules remain unchanged before adsorption and after the desorption process, which in turn confirms the chemical integrity of the dyes during the adsorption process (Fig. A3.3, Fig. A3.4).

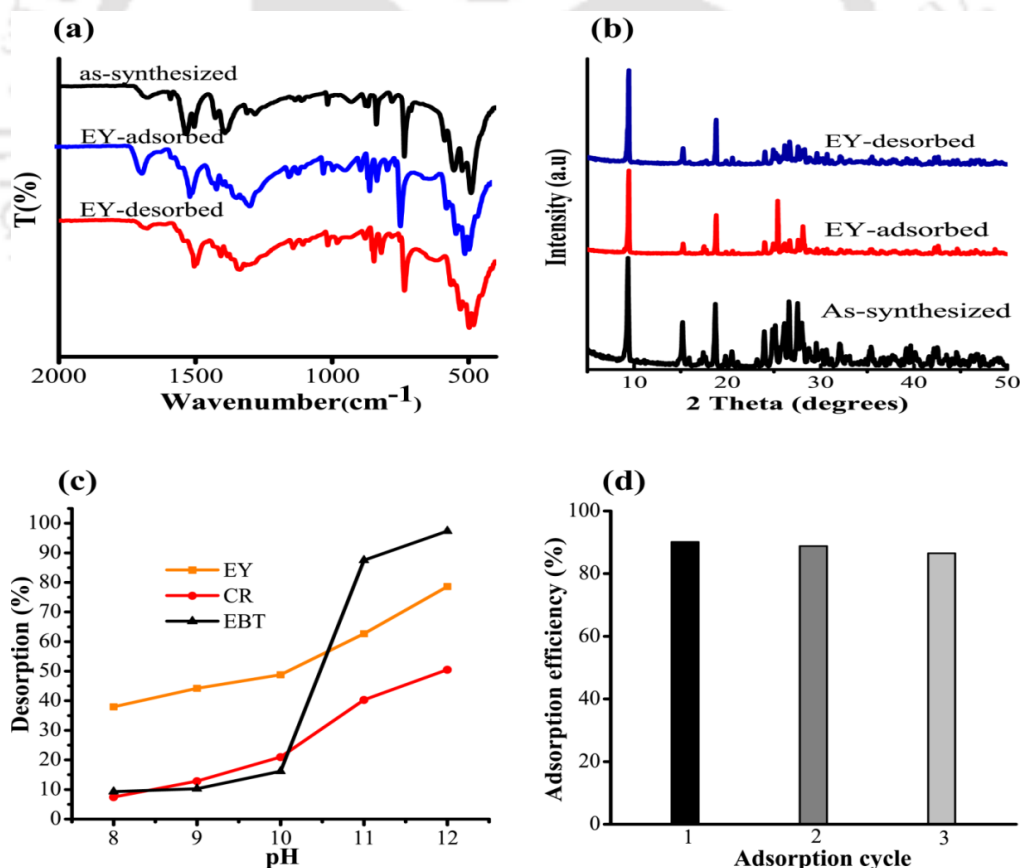


Fig. 3.4 (a) FT-IR spectra, (b) PXRD pattern of Sn(II)-BDC MOF: as-synthesized, after adsorption and after desorption of EY, (c) Desorption efficiency of EY, CR, and EBT at different pH and (d) multicycle adsorption efficiency of Sn(II)-BDC MOF with EY.

3.5 Conclusion

In this study, novel Sn(II)-BDCMOF was successfully synthesized, and its application in the removal of anionic pollutant dye was studied in detail. The results revealed that the adsorption followed the pseudo-second-order kinetic model, and the equilibrium adsorption data fitted well with the Langmuir isotherm model. The proposed mechanism for the adsorption is primarily electrostatic interaction between the positively charged MOF surface and negatively charged anionic dyes. π - π stacking interaction between the aromatic rings of the organic linker present in Sn(II)-BDC MOF and the dye molecules were also one of the critical factors for efficient adsorption. The maximum adsorption capacity (q_m) based on the Langmuir isotherm model for three anionic dyes (CR, EBT, and EY) were found to be 95.2 mg g⁻¹, 125 mg g⁻¹, and 208.3 mg g⁻¹, respectively. Literature reported majority of MOFs are usually unstable in an aqueous medium. However, the reported MOF in this work is sufficiently stable in aqueous solution for a longer time. The adsorbent displayed excellent recyclability with adsorption efficiency ~86% even after the third adsorption-desorption cycle. The cheaper source of precursor material and the simple eco-friendly synthesis of the Sn(II)-BDC MOF without the use of any toxic solvents makes it an attractive option for dye adsorption. Also, the thermal and aqueous stability of the Sn(II)-BDC MOF for an extended period adds to its advantage as a robust adsorbent material. Therefore, the synthesized material can be a promising adsorbent for remediation of organic dye contaminated wastewater.

References

- [3.1] A. Ayar, O. Gezici and M. Küçükosmanoğlu, *J. Hazard.Mater.*, 2007, **146**, 186.
- [3.2] Q. Qin, J. Ma and K. Liu, *J. Hazard.Mater.*, 2009, **162**, 133.
- [3.3] T. Robinson, B. Chandran and P. Nigam, *Water Res.*, 2002, **36**, 2824.
- [3.4] B. Saha, S. Das, J. Saikia and G. Das G. *J. Phys. Chem. C.*, 2011, **115**, 8024.
- [3.5] S.A. Parsons and B. Jefferson, *Introduction to Potable Water Treatment Processes*; Blackwell Publishing: Oxford, United Kingdom, 2006.
- [3.6] H.Y. Shu, C.R. Huang and M.C. Chang, *Chemosphere*, 1994, **29**, 2597.
- [3.7] A. Gurses, C. Dogar, M. Yalcin, M. Acikyildiz, R. Bayrak and S. Karaca, *J. Hazard.Mater.*, 2006, **131**, 217.
- [3.8] U. Pagga and K. Taeger, *Water Res.*, 1994, **28**, 1051.
- [3.9] K. Santhy and P. Selvapathy, *Bioresour.Technol.*, 2006, **97**, 1329.
- [3.10] C. Li, Z. Xiong, J. Zhang and C. Wu, 2015, **60**, 3414.
- [3.11] V.K. Gupta, R. Kumar, A. Nayak, T.A. Saleh and M. Barakat, *Adv. Colloid Interface Sci.*, 2013, **193**, 24.
- [3.12] C. Yang, L. Li, J. Shi, C. Long and A. Li, *J. Hazard. Mater.*, 2015, **284**, 50.
- [3.13] M.T. Yagub, T.K. Sen, S. Afroze and H.M. Ang, *Adv. Colloid Interface Sci.*, 2014, **209**, 172.
- [3.14] T.A. Vu, G.H. Le, C.D. Dao, L.Q. Dang, K.T. Nguyen, P.T. Dang, H.T. Tran, Q.T. Duong, T.V. Nguyen and G.D. Lee, *RSC Adv.*, 2014, **78**, 41185.
- [3.15] M. Anbia, V. Hoseini and S. Sheykhi, *J. Ind. Eng. Chem.*, 2012, **18**, 1149.
- [3.16] K. Sun, L. Li, X. Yu, L. Liu, Q. Meng, F. Wang and R. Zhang, *J. Colloid Interface Sci.*, 2017, **486**, 128.
- [3.17] D. Kukkar, K. Vellingiri, A. Deep and K.H. Kim, *Sens. Actuators, B.*, 2018, **273**, 1346.

- [3.18] J. Liu, J.T. Culp, S. Natesakhawat, B.C. Bockrath, B. Zande, S.G. Sankar, G. Garberoglio and J.K. Johnson, *J. Phys. Chem. C*, 2007, **111**, 9305.
- [3.19] S.H. Huo and X.P. Yan, *J. Mater.Chem.*, 2012, **22**, 7449.
- [3.20] H.F. Garces, H.M. Galindo, L.J. Garces, J. Hunt, A. Morey and S.L. Suib, *Microporous Mesoporous Mater.*, 2010, **127**, 190.
- [3.21] J. Liu, N. Wang, H. Zhang and J. Baeyens, *J. Environ. Manage.*, 2019, **238**, 473.
- [3.22] E. Yilmaz, E. Sert E and F.S. Atalay, *J. Taiwan Inst. Chem. Eng.*, 2016, **65**, 323.
- [3.23] J.Z. Gu, W.G. Lu, L. Jiang, H.C. Zhou and T.B. Lu, *Inorg. Chem.*, 2007, **46**, 5835.
- [3.24] K. Leus, T. Bogaerts, J.D. Decker, H. Depauw, K. Hendrickx, H. Vrielinck, V. Speybroeck and P.V. Voort, *Microporous Mesoporous Mater.*, 2016, **226**, 110.
- [3.25] S. Yuan, J.S. Qin, C.T. Lollar and H.C. Zhou, *ACS Cent.Sci.*, 2018, **4**, 440.
- [3.26] S.H. Jhung, S.H., N.A. Khan and Z. Hasan, *CrystEngComm.*, 2012, **14**, 7099.
- [3.27] X. Wang, L. Liu, T. Makarenko and A.J. Jacobson, *Cryst.Growth Des.*, 2010, **10**, 3752.
- [3.28] A.C. Wibowo, M.D. Smith and H.C. Loye, *Solid State Sci.*, 2011, **13**, 607.
- [3.29] G.M. Lima, R.I. Walton, G.J. Clarkson, R.S. Bitzer and J.D. Ardisson, *Dalton Trans.*, **47**, 8013.
- [3.30] K.A. Winship, *Adverse Drug React. Acute Poisoning Rev.* 7, 1988, 19.
- [3.31] S. Parimala, C. Selin, A. Gnanamani and A.B. Mandal, *Current Res. in Chemistry.*, 2012, **4**, 60.
- [3.32] J. Zhang and L. Gao, *J. Solid State Chem.*, 2004, **177**, 1425.
- [3.33] K.C. Song and Y. Kang, *Mater.Lett.*, 2002, **42**, 283–289.
- [3.34] S. Dadfarnia, A.H. Shabani, S.E. Moradi and S. Emami., *Appl. Surf.Sci.*, 2015, **330**, 85.
- [3.35] A. Banerjee, R. Gokhale, S. Bhatnagar, J. Jog, M. Bharadwaj, B. Lefez, B. Hannover and S. Ogale, *J. Mater. Chem.*, 2012, **37**, 19694.
- [3.36] S. Duan, J. Li, X. Liu, Y. Wang, S. Zeng, D. Shao, T. Hayat, *ACS Sustainable Chem. Eng.*, 2016, **4**, 3368.
- [3.37] Z. Sun, C. Cao and W.Q. Han, *RSC Adv.*, 2015, **5**, 72825.
- [3.38] R. Seetharaj, P.V. Vandana, P. Arya and S. Mathew, 2019, **12**, 295.
- [3.39] A.J. Howarth, A.W. Peters, N.A. Vermeulen, T.C. Wang, J.T. Hupp and O.K. Farha, 2016, **29**, 26.
- [3.40] T. Wang, P. Zhao, N. Lu, H. Chen, C. Zhang and X. Hou, *Chem. Eng. J.*, 2016, **295**, 403.
- [3.41] K. Gupta and O.P. Khatri, *Chem. Eng. J.*, 2019, **19**, 31612.
- [3.42] K. Vikrant and K.H. Kim, *Chem. Eng. J.*, 2019, **358**, 264.
- [3.43] C.J. Na, M.J. Yoo, D.C. Tsang, H.W. Kim and K.H. Kim, 2018, **366**, 452.
- [3.44] J.E. Szulejko, K.H. Kim and J. Parise, *Sep. Purif. Technol.*, 2019, **212**, 980.
- [3.45] J. Liu, N. Wang, H. Zhang and J. Baeyens, *J. Environ. Manage.*, 2019, **238**, 473.
- [3.46] V.K. Gupta, A. Mittal and V. Gajbe, *J. Colloid Interface Sci.*, 2005, **284**, 89.
- [3.47] J. Saikia and G. Das, *J. Environ. Chem. Eng.*, 2014, **2**, 1165.
- [3.48] T. Shen, J. Luo, S. Zhang and X. Luo, *J. Environ. Chem. Eng.*, 2015, **3**, 1372.
- [3.49] T. Wang, P. Zhao, N. Lu, H. Chen, C. Zhang and X. Hou, *Chem. Eng. J.*, 2016, **295**, 403.
- [3.50] S. Duan, J. Li, X. Liu, Y. Wang, S. Zeng, D. Shao and T. Hayat, *Sustainable Chem. Eng.*, 2016, **4**, 3368.
- [3.51] L.n. Jin, X.Y. Qian, J.G. Wang, H. Aslan and M. Dong, *J. Colloid Interface Sci.*, 2015, **453**, 270.
- [3.52] E. Haque, J.W. Jun and S.H. Jhung, *J. Hazard.Mater.*, 2011, **185**, 507.
- [3.53] S.H. Huo and X.P. Yan, *J. Mater.Chem.*, 2012, **22**, 7449.
- [3.54] E. Yilmaz, E. Sert and F.S. Atalay, *J Taiwan Inst Chem E.*, 2016, **65**, 323.
- [3.55] T. Anitha and S. Kumar, *J. Water Process Eng.*, 2016, **13**, 127.
- [3.56] N.D. Mu'azu, N. Jarrah, T.S. Kazeem, M. Zubair and M. Al-Harathi, *Appl Clay Sci.*, 2018, **161**, 161:23.
- [3.57] D. Bharali and R.C. Deka, *Colloids Surf., A.*, 2017, **525**, 525.
- [3.58] M. Zubair, N. Jarrah, M.S. Manzar, M. Al-Harathi, M. Daud, N.D. Mu'azu and S.A. Haladu, *J. Mol. Liq.*, 2017, **230**, 344.
- [3.59] D.M. Aguila and M.V. Ligaray, *Int. J. Environ. Sci. Dev.*, 2015, **6**, 824.
- [3.60] M. S. Thabet and A. M. Ismaiel, *J. Encapsulation Adsorpt. Sci.*, 2016, **6**, 70.
- [3.61] M.Y. Masoomi, M. Bagheri and A. Morsali, *Ultrason.Sonochem.*, 2017, **37**, 244.
- [3.62] N. Abdollahi, M.Y. Masoomi, A. Morsali, P.C. Junk and J. Wang, *Ultrason.Sonochem.*, 2018, **45**, 50.

- [3.63] L.N. Jin, X.Y. Qian, J.G. Wang, H. Aslan and M. Dong, *J. Colloid Interface Sci.*, 2015, **453**, 270.
[3.64] S.E. Moradi, S. Dadfarnia, A.M. Shabani and S. Emami, *Desalin. Water Treat.*, 2015, **56**, 709.
[3.65] M.Y. Masoomi, A. Morsali and P.C. Junk, *CrystEngComm.*, 2015, **17**, 686.
[3.66] B. Saha, S. Das, J. Saikia and G. Das, *J. Phys. Chem. C*, 2011, **115**, 8024.



Annexure 3

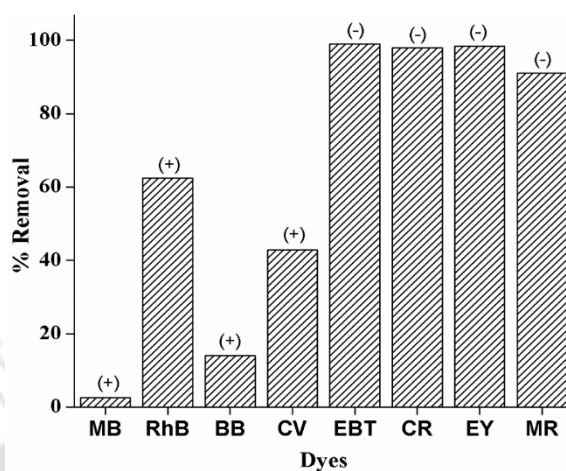


Fig. A3.1 Comparative anionic (-) and cationic (+) dyes removal.

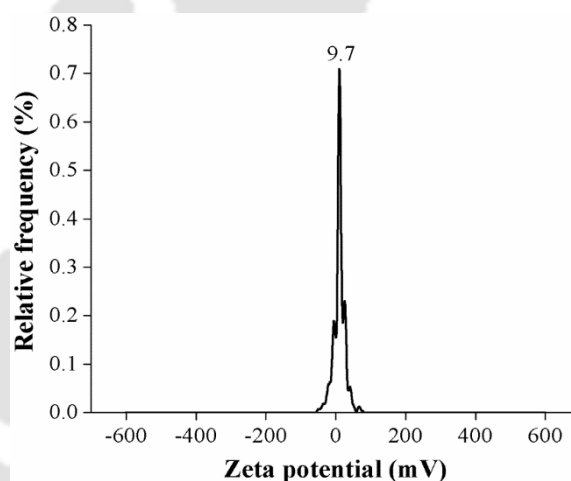


Fig. A3.2 Zeta potential of Sn(II)-BDC MOF at neutral pH by direct dispersion in water.

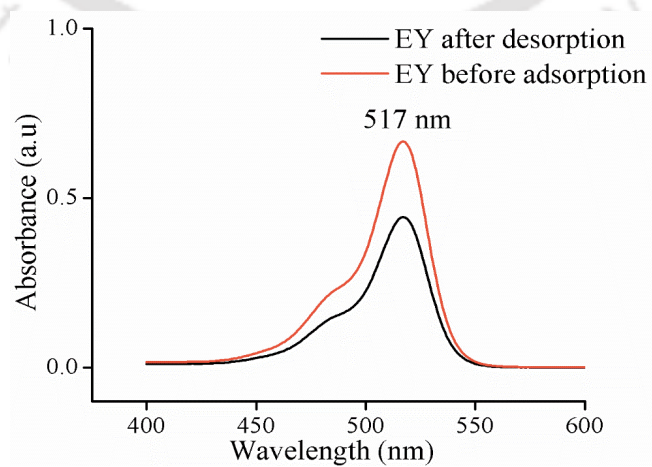


Fig. A3.3 UV-vis spectra for the maximum absorbance of EY dye before adsorption and after desorption.

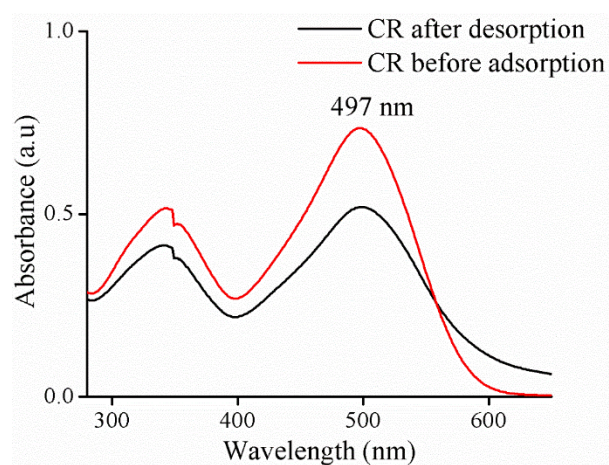
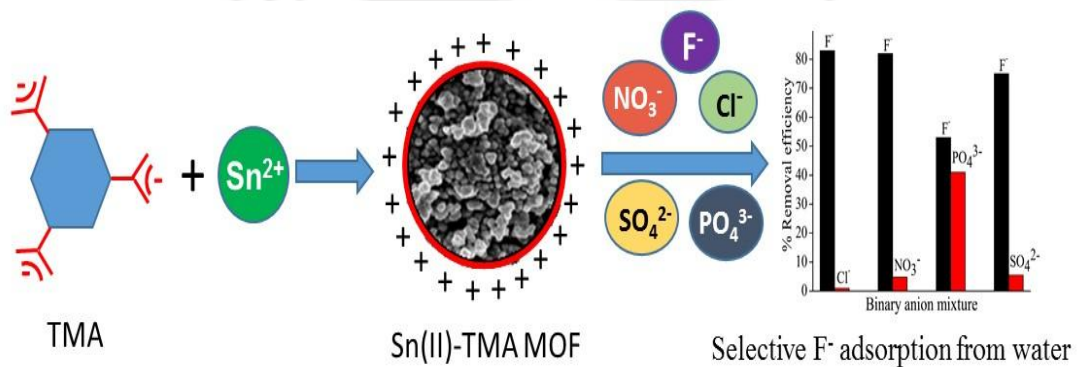


Fig. A3.4 UV-vis spectra for the maximum absorbance of CR dye before adsorption and after desorption



Chapter 4

Facile synthesis of a novel aqua-stable Sn(II)-TMA metal-organic framework (MOF): Promising adsorbent for fluoride over a broad pH range



4.1 Background and Focus of the Chapter

Safe and pure drinking water is a prime concern for human beings. But due to rapid urbanization and increasing industrial activities, the groundwater is becoming polluted with toxic compounds. Fluoride is one such toxic element causing groundwater pollution. Both natural and anthropogenic sources contribute to the high fluoride concentration in the groundwater. Fluoride is one of the essential elements for the human body, which is required in trace amounts of $0.5\text{-}1.0\text{ mg L}^{-1}$ [4.1]. However, excess fluoride consumption above 1.5 mg L^{-1} in potable water can cause dental/skeletal fluorosis as well as neurological disorder [4.2]. Besides, high fluoride concentration in drinking water causes lesions of the liver, thyroid, and endocrine glands. Therefore, the World Health Organization (WHO) has designated fluoride as one of the hazardous contaminants of potable water and limited its consumption to 1.5 mg L^{-1} to protect consumers from fluorosis problems [4.3]. Therefore, defluoridation of drinking water is one of the critical issues which is widely being studied.

Various techniques for fluoride removal were investigated, which include ion exchange [4.4], precipitation/coagulation [4.5], adsorptions [4.6, 4.7], reverse osmosis, and electrocoagulation [4.8, 4.9]. Among them, adsorption has drawn full attention due to its simplicity, relative cost-effectiveness, and higher removal efficiency [4.10]. Over the past years, different adsorbents such as carbon-based adsorbents [4.11, 4.12], aluminium-based adsorbents [4.13, 4.14], biosorbents [4.15, 4.16], metal oxide, and hydroxides [4.17] and other materials [4.18-4.20] have been used for fluoride removal studies. However, these adsorbent materials suffer from various drawbacks such as low adsorption capacity, dependence on a small range of pH, and inference of co-existing anions (bicarbonate, nitrate, sulfate, phosphate, etc.) during fluoride adsorption [4.21, 4.22].

Metal-organic frameworks (MOFs) are highly porous materials (coordination polymers) consisting of inorganic metal ions connected to organic linkers via coordination bonds. In general, porous materials are divided into two categories: organic and inorganic, each of which having its advantages and disadvantages [4.23]. The organic type possesses high surface area but with non-uniform and irregular pores. The inorganic type has high thermal and mechanical stability with regular pore size. However, the surface area is limited compared to organic materials. The limitations of both organic and inorganic types can be overcome by the use of the metal-organic framework, which is a hybrid of inorganic-organic material possessing high surface area, durability, and regular pore

size [4.24, 4.25]. MOFs have shown potential applications in various fields, including catalysis, gas storage/adsorption, separation, drug delivery, chemical sensor, luminescence, adsorption of hazardous environmental pollutants, etc [4.26-4.28]. However, the reduced water stability of MOFs limits their applications in the aqueous environment due to hydrolysis of the metal-linker coordination bond when exposed to water [4.29]. Till date, very few MOFs like MIL-53(Fe, Cr, Al), UiO-66(Zr, Hf), and Zifs-7,-8,-9 are reported to be stable under aqueous environment [4.30].

Sn(II)-dicarboxylate coordination polymers have been reported to be hydrothermally or solvothermally synthesized under alkaline conditions producing known homoleptic 1D and 2D architectures or 3D frameworks consisting of tin-oxide as secondary building units (SBUs) [4.31, 4.32]. Recently, air and moisture stable Sn(II) coordination polymers have been reported with polytopic carboxylate based organic linkers [33]. Tin being an environmentally benign material, has been used widely in food packaging. Tin salts possess low toxicity to the human body as it is poorly absorbed and rapidly excreted in the form of feces. Among the inorganic metal ions for MOF synthesis Sn(II) is the least explored. Sn(II), a hard lewis acid, can form a strong coordination bond with carboxylate, which is a hard lewis base resulting in the formation of a stable and rigid framework. Also, from the economic point of view, Sn(II) salt act as a low-cost precursor for material synthesis. In this chapter, we demonstrated the efficient use of Sn(II)-TMA MOF as a novel adsorbent material for fluoride removal from aqueous solution. To the best of our knowledge, tin-based MOF has not been explored for water treatment applications, and there is a scarcity in studies with coordination polymers of Sn(II). The aqueous and thermal stability of the synthesized material was confirmed. Batch adsorption experiments were carried out to study the effect of dose, initial concentration, contact time, temperature, ionic strength, and co-existing ions on the fluoride removal efficiency. The experimental data were fitted into three linear forms of kinetic models, and the plausible mechanism for adsorption was proposed. Finally, the practical applicability of the synthesized material was explored for fluoride removal from actual water samples.

4.2 Results and discussion

4.2.1. Characterization of Sn(II)-TMA MOF

The FT-IR spectrum of Sn(II)-TMA MOF in Fig. 4.1a shows the characteristics peak at $\sim 590\text{ cm}^{-1}$, which relates to Sn-O stretching vibration. The peaks at 1621 and 1383 cm^{-1} correspond to the C=O functional group and C-C stretching vibration of the benzene

ring [4.34, 4.35]. The broad peak at 3408 cm^{-1} is attributed to the loosely bound water molecules in the pores of the MOF. Peaks ranging from 600 cm^{-1} to 1300 cm^{-1} can be attributed to the out of plane C-H bending vibrations [4.36]. The PXRD pattern in Fig. 4.1b reveals three broad peaks at 2θ corresponding to 26° , 33° , and 52° . In Fig. 4.1c, the TGA plot shows a two-stage weight loss with an increase in temperature from 25°C to 700°C . The $\sim 18\%$ weight loss under stage I from 200°C onwards attributed to the release of the absorbed water molecules from the pores of the material. The stage II weight loss of $\sim 16\%$ between $300\text{--}520^\circ\text{C}$ correlates to the release of the organic ligand (TMA) and partial thermal degradation of the material [4.37-4.39].

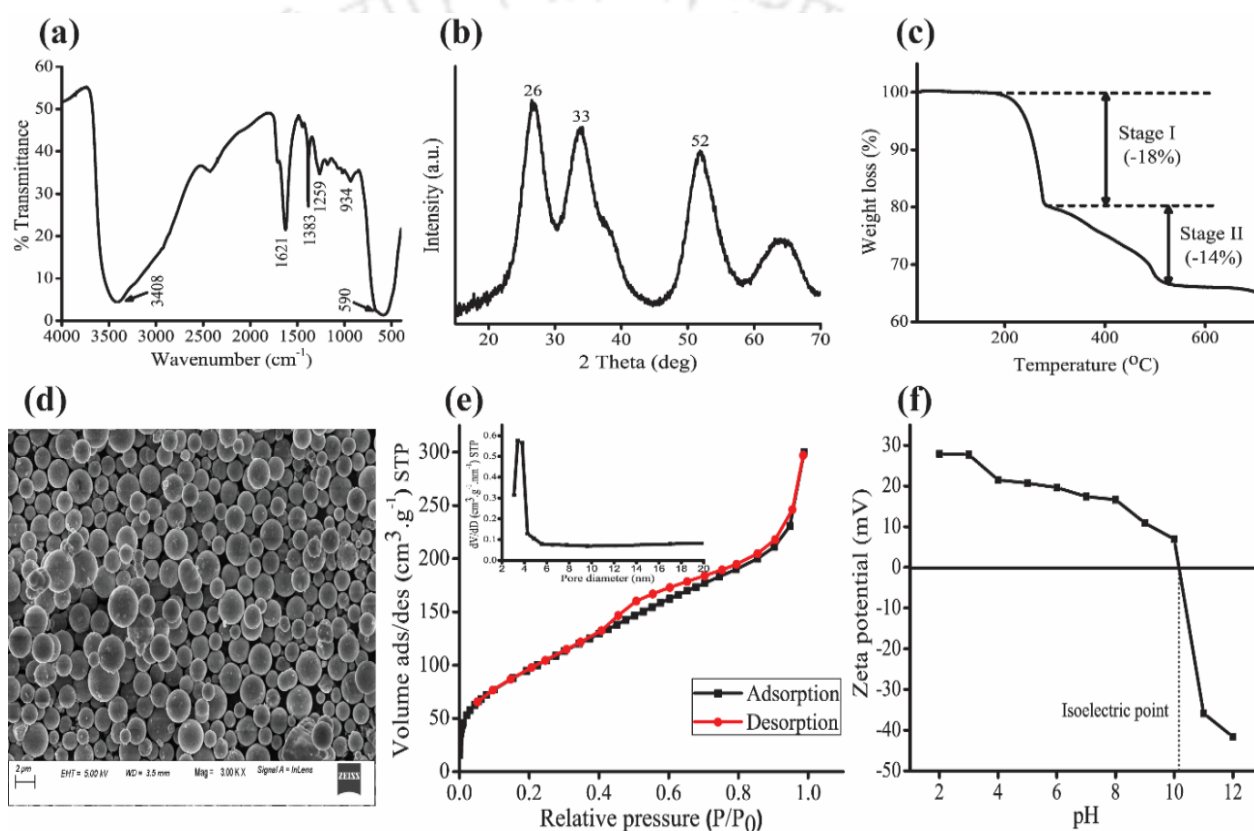


Fig. 4.1 (a) FT-IR, (b) PXRD, (c) Thermogravimetric analysis (TGA), (d) FESEM image, (e) N_2 adsorption-desorption isotherm, and (f) Zeta potential Vs. pH plot of the Sn(II)-TMA MOF.

Hence, the TGA data reveals the thermal stability of the adsorbent at a high temperature of 300°C with a final residual mass of $\sim 65\%$ at 700°C . The surface morphology of the material studied by FESEM in Fig. 4.1d displays evenly distributed spherical particles with a smooth surface. In Fig. 4.1e N_2 adsorption-desorption experimental analysis revealed the specific surface area and pore volume at $360.8\text{ m}^2\text{ g}^{-1}$ and $0.46\text{ cm}^3\text{ g}^{-1}$, respectively. The BET (Brunauer–Emmett–Teller) method was adopted for measurement of the surface area, and the pore size distribution was calculated from the

BJH method. The Sn(II)-TMA MOF was found to be mesoporous with an average pore size of 4 nm. Zeta potential was measured at increasing pH from 2 to 12 in Fig. 4.1f. The point of zero charge (pH_{pzc}) was measured at 10.2 from the zeta potential Vs. pH plot. The Sn(II)-TMA MOF displayed a wide range of pH independence (pH 2-pH 10) and is observed to be positively charged at the given range [4.40].

4.2.2. Aqueous stability

The as-synthesized MOF was found to be stable in aqueous solution with a high yield of 98.1% after 10 days of incubation, which ensures that the material did not undergo hydrolysis in water.

Further, the FT-IR and powder XRD pattern confirmed the integrity of the material in aqueous solution [4.41], Fig. A4.1 and A4.2. It is clear from the FT-IR and XRD pattern that the characteristic peaks are similar to the pristine material. Besides, the FESEM analysis in Fig. A4.3 (A, B) before and after water exposure revealed the morphology of the Sn(II)-TMA MOF remained unchanged, thereby establishing its water stability.

4.2.3. Effect of adsorbent dose

The effect of Sn(II)-TMA dose on the fluoride removal efficiency was determined with an initial fluoride concentration of 10 mg L^{-1} at 298 K for 2 h. Fig. 4.2a depicts the increase in fluoride removal efficiency as the adsorbent dose was increased from 0.5-2.5 g L^{-1} , and the curve leveled off after 2 g L^{-1} may be due to the saturation of adsorption sites with the adsorbate. An optimum dose of 1 g L^{-1} was considered for further adsorption studies to improve the overall process economy.

4.2.4. Effect of pH on fluoride removal

The pH of natural water is sensitive to the changes in weather, environment, and geographic location. Therefore, the effect of solution pH on the fluoride removal efficiency was investigated with an initial fluoride concentration of 10 mg L^{-1} at 298 K. It was noted that fluoride removal efficiency was stable and consistent from pH 2 to pH 12. Importantly, there is a minimal reduction (84 - 80%) in removal efficiency with an increase in pH 3 to pH 10. Therefore, Sn(II)-TMA MOF showed broad pH independence and is thoroughly competent in the removal of fluoride at low pH 3 as well as high pH 10. The pH_{pzc} at 10.2 calculated from the zeta potential as a function of pH plot further confirms at $\text{pH} < 10$ the Sn(II)-TMA is positively charged while at $\text{pH} > 10$, the material is negatively charged. The removal efficiency decreased from 80% at pH 10 to 56% at pH 11 as it is reflected from negative zeta potential

value of -35.9 mV, in Fig. 4.2b. The decrease in removal efficiency can be attributed to the deprotonation of the material surface at $\text{pH} > 10$ hence causing electrostatic repulsion between the surface hydroxyl groups and negatively charged fluoride ions. In addition to electrostatic repulsion, the competition of the high concentration of OH^- ions generated at high pH with fluoride ions for the active adsorption sites on Sn(II)-TMA MOF also contributes to the decrease in fluoride removal efficiency [4.42, 4.43]. Further, the effect of H^+ ions on fluoride removal under acidic conditions ($\text{pH} \sim 3$) was investigated and compared with the control in Fig. A4.4. The Sn(II)-TMA MOF exhibited $\sim 86\%$ fluoride removal efficiency, while negligible fluoride removal was observed in control.

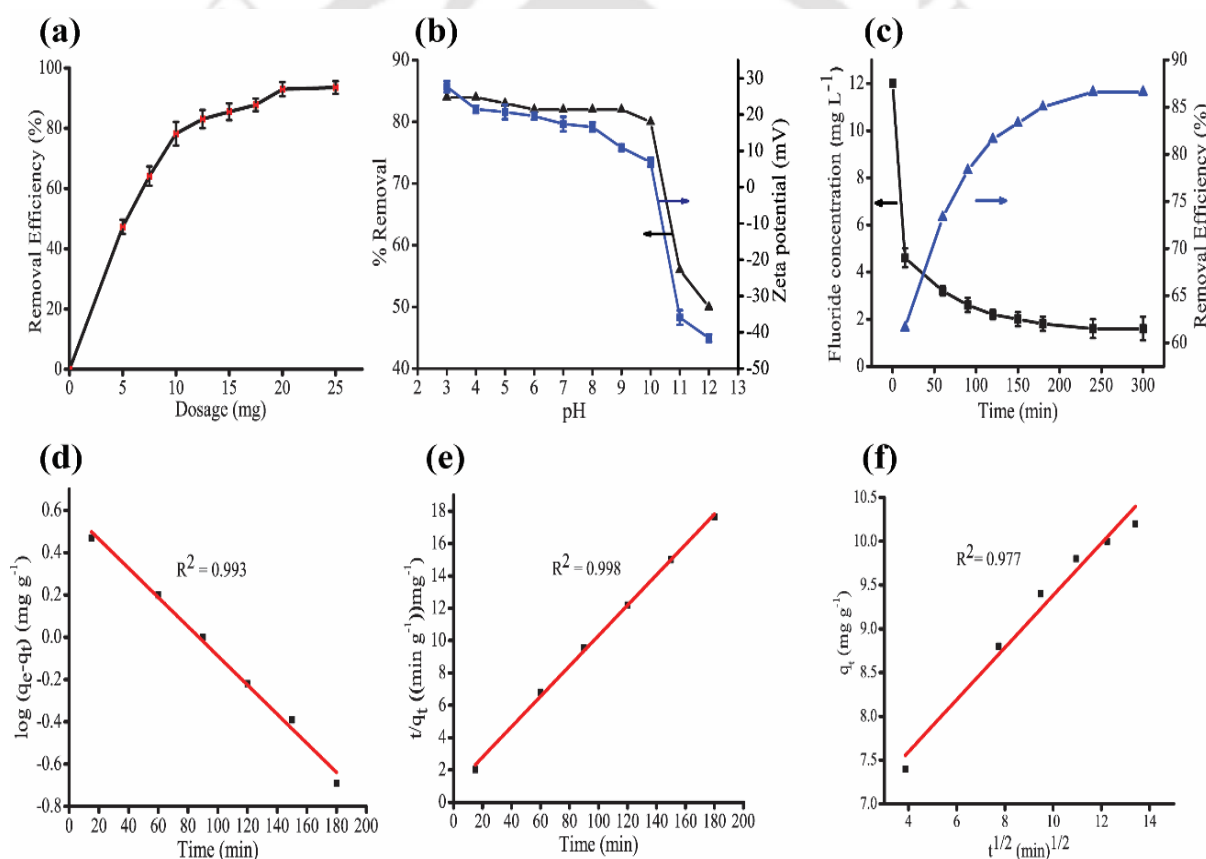


Fig. 4.2 (a) Effect of dose on removal efficiency, (b) Removal efficiency and zeta potential as a function of pH, (c) Adsorption equilibrium as a function of contact time, and (d, e, f) Pseudo-first-order, pseudo-second-order, and intra-particle diffusion model linear fitting.

4.2.5. Effect of contact time

The contact time effect was studied to determine the kinetics of fluoride adsorption and equilibration time for maximum fluoride adsorption. Fig. 4.2c illustrates the initial rapid adsorption of fluoride at an initial concentration of 12 mg L^{-1} . The removal efficiency

reached 62% within 15 min contact time while the equilibration reached slowly at 150 min. The equilibrium fluoride removal capacity of Sn(II)-TMA was obtained at 10 mg g⁻¹, and the equilibrium fluoride concentration was determined to be at 1.6 mg L⁻¹.

To evaluate the rate and kinetics of the adsorption process, three linear forms of kinetic models viz. pseudo-first-order, pseudo-second-order, and Weber and Morris intraparticle diffusion models were adopted, refer to Fig. 4.2 d, e, f. The linear forms of the above models are expressed as Eqs. (1), (2) and (3) respectively [4.44, 4.45]:

$$\log(q_e - q_t) = \log q_e - \frac{k_1}{2.303} t \quad (1)$$

$$\frac{t}{q_t} = \frac{1}{k_2 q_e^2} + \frac{1}{q_e} t \quad (2)$$

$$Qt = kt^{0.5} + C \quad (3)$$

where q_e and q_t are the fluoride adsorption capacity (mg g⁻¹) on Sn(II)-TMA MOF at equilibrium and at time t (min), respectively. k_1 (min⁻¹), k_2 (g min⁻¹ mg⁻¹), k (mg g⁻¹ min^{-0.5}) are the pseudo-first-order, pseudo-second-order, intraparticle diffusion rate constants, respectively, and C is the intercept relating to the boundary layer thickness. The kinetic parameters are outlined in Table A4.1. The experimental data fitted well with both pseudo-first-order and pseudo-second-order kinetic models suggesting that the adsorption of fluoride is a combination of both physisorption and chemisorption. The linear part of the plot does not pass through the origin, as depicted in Fig. 4.2f suggesting that intraparticle diffusion is not the only rate-controlling step for fluoride adsorption and that surface adsorption is also involved. The F⁻ ions may have adsorbed into the pores of Sn(II)-TMA MOF. The radius of fluorine (0.13 nm) is much smaller than the pore size of Sn(II)-TMA MOF, which is in the mesoporous range, suggesting the increasing possibility of F⁻ ions adsorption into the pores of the adsorbent [4.46].

Table 4.1 Kinetic parameters for adsorption of fluoride on Sn(II)-TMA MOF

q_e (exp) (mg g ⁻¹)	Pseudo-first order model			Pseudo-second order model			Intraparticle diffusion model		
	$q_{e,cal}$ (mg g ⁻¹)	k_1 (min ⁻¹)	R^2	$q_{e,cal}$ (mg g ⁻¹)	k_2 (g mg ⁻¹ min ⁻¹)	R^2	C (mg g ⁻¹)	k_{int} (mg g ⁻¹ min ^{-0.5})	R^2
10.2	10.82	0.006	0.99	10.64	0.009	0.998	20.78	3.28	0.977

4.2.6. Adsorption isotherm

To investigate the mechanism of fluoride adsorption and to determine the maximum adsorption capacity, equilibrium isotherm was studied by in the initial concentration range (5–150 mg L⁻¹) while keeping the dose constant at 1 g L⁻¹. To estimate the maximum adsorption capacity at equilibrium and to study the adsorption behavior the experimental data were analyzed by Langmuir and Freundlich isotherm models (Eq. 4, Eq. 5)

The Langmuir isotherm model equation, which is based on monolayer adsorption, is as follows [4.47]

$$\frac{C_e}{Q_e} = \frac{C_e}{q_m} + \frac{1}{K_L q_m} \quad (4)$$

where q_m is the maximum adsorption capacity, and K_L is the Langmuir constant, which indicates the affinity of fluoride towards the adsorbent.

The Freundlich model, which is based on heterogeneous adsorption, is as described as [4.48]

$$\ln Q_e = \ln K_f + \frac{1}{n} \ln C_e \quad (5)$$

where K_f is the Freundlich constant, and n is an empirical parameter related to the intensity of adsorption.

The experimental data had a better fit with the Langmuir isotherm model, as it is evident from the higher correlation coefficient (R^2) value. The adsorption isotherm parameters are summarized in Table 4.2. The Langmuir and Freundlich isotherm model fitting is represented in Fig. 4.3a, b. The Langmuir model assumes monolayer adsorption with homogeneous uniform surface active sites for fluoride adsorption.

The monolayer adsorption suggests chemisorption process [4.49] is involved in fluoride adsorption on Sn(II)-TMA MOF. The maximum fluoride adsorption capacity (q_m) was calculated at 30.86 mg g⁻¹, which is in close agreement with the experimentally obtained value of 30.25 mg g⁻¹. The fluoride Langmuir adsorption capacity (q_e) of different MOF based adsorbents is illustrated in Table A4.2. Further, to explain the favourability of the fluoride adsorption, the dimensionless separation factor R_L of Langmuir isotherm was determined. R_L is defined by Eq (6) as follows [4.50]

$$R_L = \frac{1}{1 + K_L C_0} \quad (6)$$

where C_0 and K_L are the initial fluoride concentration and Langmuir isotherm constant, respectively. R_L indicates the favourability of the adsorption process where $R_L < 1$ suggests favorable adsorption, while $R_L > 1$ suggests unfavorable adsorption [4.51]. The calculated R_L values in the different fluoride initial concentration range (5-150 mg L⁻¹) are depicted in Table A4.1, which signifies favorable fluoride adsorption on Sn(II)-TMA MOF.

Table 4.2 Langmuir and Freundlich adsorption isotherm parameters for fluoride adsorption.

Adsorption isotherm	Isotherm constants	Values (Fluoride)
Langmuir	q_m (mg g ⁻¹)	30.86
	K_L (L g ⁻¹)	0.104
	R^2	0.98
Freundlich	n	0.362
	K_f ((L mg ⁻¹) ^{1/n} mg g ⁻¹)	0.006
	R^2	0.917

4.2.7. Effect of temperature

The study of the thermodynamic behavior of the fluoride adsorption on Sn(II)-TMA MOF was carried out at increasing temperatures (303 K to 323 K) to understand the nature of the adsorption process. The thermodynamic parameters, namely Gibbs free energy change (ΔG°), enthalpy change (ΔH°), and entropy change (ΔS°), were determined and listed in Table 4.3. The Gibbs free energy change (ΔG°) was determined using Eq. (7):

$$\Delta G = -RT \ln K_0 \quad (7)$$

where ΔG° (KJ mol⁻¹) is the Gibbs free energy change, R is the universal gas constant (8.314 J mol⁻¹ K⁻¹), T is the temperature in Kelvin, and $\ln K_0$ is the thermodynamic equilibrium constant (mol⁻¹).

The following Eq. (8) relates the Gibbs free energy change (ΔG°) with the enthalpy (ΔH°), entropy change (ΔS°), and temperature (T) of adsorption study.

$$\Delta G^\circ = \Delta H^\circ - T\Delta S^\circ \quad (8)$$

The values of ΔH° (kJ mol^{-1}) and ΔS° ($\text{kJ mol}^{-1} \text{K}^{-1}$) were calculated from the slope and intercept respectively of the VantHoff plot between $\ln(K_o)$ and $-1/T$. The values were obtained at 10.1 kJ mol^{-1} and $45.89 \text{ kJ mol}^{-1} \text{K}^{-1}$, respectively. The positive ΔH° and ΔS° values confirm the adsorption process is endothermic and that there is a high degree of randomness at the adsorbent-adsorbate interface, respectively. The endothermic nature of the adsorption process further reveals that the increase in temperature favored the fluoride adsorption on the Sn(II)-TMA MOF. A large positive ΔS° or a large negative ΔH° generally implies spontaneous adsorption. In our findings, both ΔH° and ΔS° values are positive. Hence, the driving force for fluoride adsorption on Sn(II)-TMA MOF is governed by the entropy effect (ΔS°) rather than the enthalpy change (ΔH°). In Fig. 4.3c more negative ΔG values of -2.56 , -4.31 , -4.51 , and $-4.76 \text{ kJ mol}^{-1}$ with the increase in temperature from 303 to 323 K indicates that the adsorption process is thermodynamically feasible and spontaneous at the higher temperature.

Table 4.3 Summary of the Thermodynamic parameters

Anion	Temperature (K)	ΔG (kJ mol^{-1})	ΔH (kJ mol^{-1})	ΔS ($\text{J mol}^{-1}\text{K}^{-1}$)
Fluoride	298	-2.56	10.1	45.89
	313	-4.31		
	318	-4.54		
	323	-4.76		

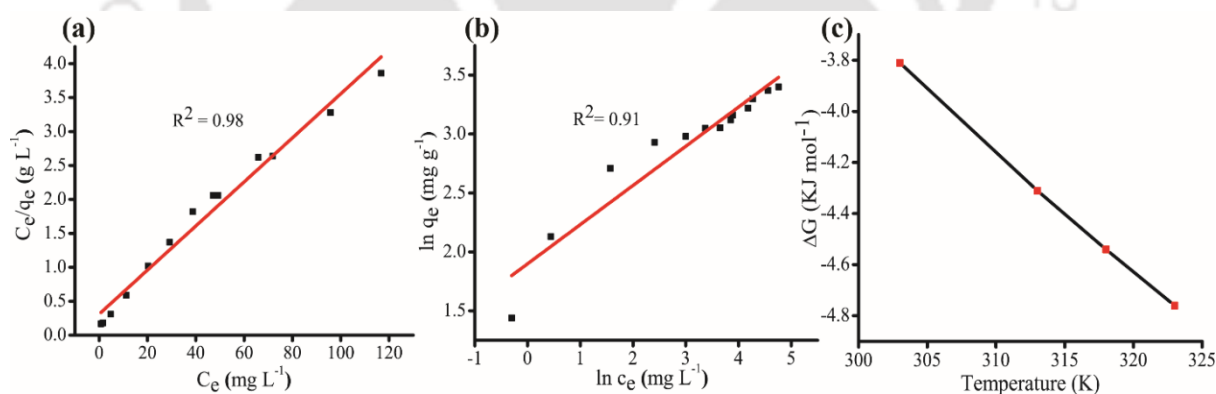


Fig. 4.3. (a, b) Langmuir and Freundlich isotherm model and (c) Gibbs free energy change (ΔG°) at different temperatures.

4.2.8. Effect of co-existing anions

The influence of co-existing anions, including Cl^- , NO_3^- , PO_4^{3-} , and SO_4^{2-} on the fluoride removal efficiency, was tested. A binary mixture of each of the anions (50 mg L^{-1}) with 10 mg L^{-1} fluoride concentration was prepared. It was observed that Cl^- , NO_3^- , and SO_4^{2-} have minimum effect on the fluoride removal efficiency (about 80%) even

though their concentrations (50 mg L^{-1}) are five times higher than that of fluoride (10 mg L^{-1}), refer Fig. 4.4a. However, it was observed that PO_4^{3-} had a limiting effect on fluoride removal efficiency. The high pH value of NaH_2PO_4 solution may cause deprotonation of the Sn(II)-TMA MOF surface where electrostatic repulsion occurs between the negatively charged adsorbent surface and F^- ions in the solution [4.52]. Also, the PO_4^{3-} ions compete with F^- ions for the active adsorption sites, which cause a reduction in fluoride removal efficiency to 55%. Hence the above findings indicate that electrostatic repulsion, high pH value, and competitive adsorption together lead to a decrease in fluoride removal efficiency in the presence of PO_4^{3-} ions. The adsorption experiment with Sn(II)-TMA was also performed in the multi-anion mixture solution (Cl^- , NO_3^- , PO_4^{3-} , and SO_4^{2-}) having five times concentration (50 mg L^{-1}) compared to fluoride (10 mg L^{-1}). In Fig. A4.5 it was observed that the relative fluoride removal efficiency remained unaffected despite the presence of the co-existing anions in much higher concentration. Therefore, the Sn(II)-TMA MOF displayed promising anti-interference activity and selective fluoride adsorption performance in the presence of co-existing anions.

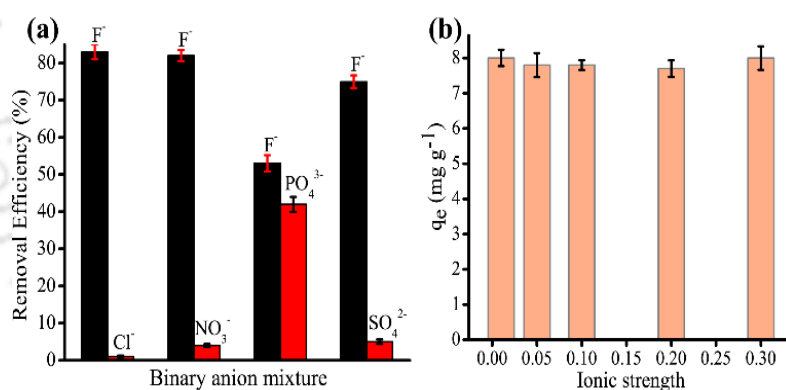


Fig. 4.4 (a) Effect of co-existing anions on fluoride removal efficiency and (b) Effect of ionic strength of solution on fluoride adsorption capacity (q_e).

4.2.9. Effect of ionic strength

The impact of ionic strength of the medium on equilibrium fluoride adsorption capacity was investigated by increasing the ionic strength from 0.01 M to 0.3 M by appropriate dilution of 1M NaCl solution. The initial fluoride concentration was kept at 10 mg L^{-1} . It was observed that an increase in ionic strength had a very minimal effect on the fluoride adsorption capacity, as illustrated in Fig. 4.4b. The result indicates the

suitability of Sn(II)-TMA MOF for practical application in treating fluoride contaminated high ionic strength water samples.

4.2.10. Proposed mechanism for adsorption

To elucidate the mechanism of adsorption, the FT-IR spectrum before and after fluoride adsorption was recorded (Fig. A4.6). It was observed that the -OH stretching vibrations at 3413 cm^{-1} for pristine Sn(II)-TMA material shifted to a higher frequency region (3429 cm^{-1}) after fluoride adsorption, which demonstrates that the surface -OH is the active site that plays an essential role in adsorption [4.53, 4.54]. However, the carboxylate peaks positions at 1625 cm^{-1} and 1384 cm^{-1} of Sn(II)-TMA MOF post adsorption remained unchanged, which shows the stability of the material in fluoride solution. Moreover, in Fig. A4.7, the PXRD pattern before and after defluoridation, confirms the integrity of the Sn(II)-TMA MOF post adsorption in water. It is being reported that the metal sites in MOF can electrostatically interact with the negatively charged fluoride ions because of unsaturated coordination on metal sites where it becomes partially positively charged [4.55, 4.56]. The coordinatively unsaturated Sn(II) centers in Sn(II)-TMA MOF were coordinated by -OH. The adsorption of the fluoride ion occurred at the metal centers in the MOF, resulting in the formation of coordination bond with the metal centers with the simultaneous displacement of -OH. To further investigate the adsorption mechanism, zeta potential and particle size analysis of the material was carried out after adsorption. It was observed that there is a decline in zeta potential value from $+29.5\text{ mV}$ to $+10.8\text{ mV}$ and an increase in particle size from 670 nm to 1611 nm after adsorption of fluoride, refer to Table 4.4. The aggregation and saturation of the adsorption sites with fluoride ions may lead to an increase in particle size and polydispersity index (PDI) while decreasing the zeta potential. The result suggests a clear state of electrostatic interaction, which drives the adsorption of negatively charged fluoride anions on the positively charged Sn(II)-TMA MOF surface.

Table 4.4 Summary of particle size, zeta potential, and polydispersity index (PDI) for pristine Sn(II)-TMA MOF and Sn(II)-TMA MOF post fluoride adsorption.

	Pristine Sn(II)-TMA	Fluoride adsorbed Sn(II)-TMA
Particle size (nm)	670	1611
Zeta Potential (mV)	+29.5	+10.8
PDI (%)	27.8	29.2

4.2.11. Fluoride adsorption from the real water sample

To confirm the feasibility of our material in practical water applications, water samples from the domestic tap, and the lake of Kamrup District, IIT Guwahati, India, were collected. The water samples were filtered and spiked with 10 mg L⁻¹ fluoride concentration each. The adsorption study was conducted at 1 g L⁻¹ Sn(II)-TMA dose with a contact time of 3 h. The fluoride removal efficiency for tap water and the lake water was obtained at 82% and 77% with an equilibrium concentration of 1.8 mg L⁻¹ and 2.3 mg L⁻¹, respectively. The equilibrium fluoride concentration for treated tap water is close to the WHO guideline of 1.5 mg L⁻¹ for drinking water. Increasing the Sn(II)-TMA dose to 1.5 g L⁻¹, however, reduced the fluoride concentration to 1.3 mg L⁻¹, which is within the desirable limit. The relatively low removal efficiency for lake water may be due to the high interference of PO₄³⁻ ions. Sn(II)-TMA MOF showed relatively good performance for fluoride removal from real water samples. After fluoride adsorption, the Sn(II)-TMA MOF material was regenerated using 0.01 M NaOH. It was observed that there is no significant decrease in fluoride removal efficiency even after three adsorption-desorption cycles, which displays the potential reusability of the material.

4.3 Conclusion

In this work, we have reported successful synthesis and application of Sn(II)-TMA MOF in fluoride removal from water. The material showed excellent aqueous stability even after prolonged exposure to water. Sn(II)-TMA MOF exhibited efficient fluoride removal performance over a broad pH range of 3-10 and high ionic strength of the solution. The increase in fluoride removal efficiency with an increase in temperature from 298 K to 323 K suggests the spontaneity and feasibility of fluoride adsorption at high temperatures, as reflected by negative ΔG° values. The material displayed a large adsorption capacity of 30.86 mg g⁻¹, which is comparable with the previously reported MOF based adsorbents. The experimental data followed both pseudo-first-order and pseudo-second-order kinetic models suggesting that fluoride adsorption on Sn(II)-TMA MOF is a combination of physisorption and chemisorption. The results indicate that electrostatic interaction plays a significant role in fluoride adsorption from water. The practical use of Sn(II)-TMA MOF for removal of fluoride from real water samples

reveals its potential as a novel adsorbent for the treatment of fluoride contaminated water.

References

- [4.1] S. Jagtap, M.K. Yenkie, N. Labhsetwar and S. Rayalu, *Chem. Rev.*, 2012, **112**, 2454–2466.
- [4.2] Y. Nie, C. Hu and C. Kong, *J. Hazard.Mater.*, 2012, **233-234**, 194-199.
- [4.3] Guidelines for Drinking-water Quality, Health Criteria and Other Supporting Information, 21st, World Health Organisation, 1996.
- [4.4] C. Castel, M. Schweizer, M.O. Simonnot and M. Sardin, *Chem. Eng. Sci.*, 2000, **55**, 3341-3352.
- [4.5] E.J. Reardon and Y. Wang, *Environ. Sci. Technol.*, 2000, **34**, 3247-3253.
- [4.6] S.G. Wang, Y. Ma, Y.J. Shi and W.X. Gong, *J. Chem. Technol. Biotechnol.*, 2000, **84**, 1043–1050.
- [4.7] Y. Yu, L. Yu and J.P. Chen, *Chem. Eng. J.*, 2015, **262**, 839-846.
- [4.8] P.I. Ndiaye, P. Moulin, L. Dominguez, J.C. Millet and F. Charbit, *Desalination*, 2005, **173**, 25-32.
- [4.9] F. Shen, X. Chen, P. Gao and G. Chen, *Chem. Eng. Sci.*, 2003, **58**, 987-993.
- [4.10] M. Mohapatra, S.Anand, B.K. Mishra, D.E. Giles and P. Singh, *J. Environ. Manage.*, 2009, **91**, 67–77.
- [4.11] E.V. Alvarez, L.H. Velazquez-Jimenez, L.F. Chazaro-Ruiz, P.E. Diaz-Flores and J.R. Rangel-Mendez, *J. Colloid Interface Sci.*, 2015, **455**, 194–202.
- [4.12] M.H. Dehghani, G.A. Haghighat, K. Yetilmezsoy, G. McKay, B. Heibati, I. Tyagi, S. Agarwal and V.K. Gupta, *J. Mol. Liq.*, 2016, **216**, 401-410.
- [4.13] S. Ghorai and K.K. Pant, *Chem. Eng. J.*, 2004, **98**, 165–173.
- [4.14] W.X. Gong, J.H. Qua, R.P. Liua and H.C. Lana, *Chem. Eng. J.*, 2012, **189–190**, 126– 133.
- [4.15] S.P. Kamble, S. Jagtap, N.K. Labhsetwar, D. Thakare, S. Godfrey, S. Devotta and S.S. Rayalu, *Chem. Eng. J.*, 2007, **129**, 173-180.
- [4.16] Y.H. Li, S. Wang, A. Cao, D. Zhao, X. Zhang, C. Xu, Z. Luan, D. Ruan, J. Liang, D. Wu and B. Wei, *Chem. Phys. Lett.*, 2001, **350**, 412-416.
- [4.17] Y.F. Zhou and R.J. Haynes, *Crit. Rev. Environ. Sci. Technol.*, 2010, **40**, 909-977.
- [4.18] L. Lv, J. He, M. Wei and X. Duan, *Ind. Eng. Chem. Res.*, 2006, **45**, 8623–8628.
- [4.19] A.K. Yadav, C.P. Kaushik, A.K. Haritash, A. Kansal and N. Rani, *J. Hazard.Mater.*, 2006, **128**, 289-293.
- [4.20] T. Zhang, Q. Li, H. Xiao, Z. Mei, H. Lu and Y. Zhou, *Appl. Clay Sci.*, 2013, **72**, 117–123.
- [4.21] Y. Ku and H.M. Chiou, *Water Air Soil Pollut.*, 2002, **133**, 349-361.
- [4.22] M. Pontié, C. Diawara, A. Lhassani, H. Dach, M. Rumeau, H. Buisson and J.C. Schrotter, *Advances in Fluorine Science.*, 2006, **2**, 49-80.
- [4.23] M. Massoudinejad, M. Ghaderpoori, A. Shahsavani and M.M. Amini, *J. Mol. Liq.*, 2016, **221**, 279-286.
- [4.24] O.M. Yaghi, M. O'keeffe, N.W. Ockwig, H.K. Chae, M. Eddaoudi and J. Kim, *Nature.*, 2003, **423**, 705.
- [4.25] A.U. Czaja, N. Trukhan and U. Müller, *Chem. Soc. Rev.*, 2009, **38**, 1284-1293.
- [4.26] L. Huanli, Z. Hongying, C. Tongcheng, Q. Lin, W. Yanbin and Z. Guohua, *J. Mol. Catal. A Chem.*, 2015, **400**, 81–89.
- [4.27] L.E. Kreno, K. Leong, O.K. Farha, M. Allendorf, R.P.V. Duyne and J.T. Hupp, *Chem. Rev.*, 2012, **112**, 1105–1125.
- [4.28] J. Rocha, L.D. Carlos, F.A. Paz and D. Ananias, *Chem. Soc. Rev.*, 2011, **40**, 926-940.
- [4.29] J.Z. Gu, W.G. Lu, L. Jiang, H.C. Zhou and T.B. Lu, *Inorg. Chem.*, 2007, **46**, 5835-5837.
- [4.30] K. Leus, T. Bogaerts, J.D. Decker, H. Depauw, K. Hendrickx, H. Vrielinck, V. Speybroeck and P.V. Voort, *Microporous Mesoporous Mater.*, 2016, **226**, 110-116.
- [4.31] X. Wang, L. Liu, T. Makarenko and A.J. Jacobson, *Cryst. Growth Des.*, 2010, **10**, 3752-3756.
- [4.32] A.C. Wibowo, M.D. Smith and H.C. Loye, *Solid State Sci.*, 2011, **13**, 607-615.
- [4.33] G.M. Lima, R.I. Walton, G.J. Clarkson, G.J., R.S. Bitzer and J.D. Ardisson, *Dalton Trans.*, 2018, **47**, 8013-8022.
- [4.34] K.Y. Lin, Y.T. Liu and S.Y. Chen, *J. Colloid Interface Sci.*, 2016, **461**, 79-87.
- [4.35] M.R. Azhar, H.R. Abid, H. Sun, V. Periasamy, M.O. Tade and S. Wang, *J. Colloid Interface Sci.*, 2017, **490**, 685-694.

- [4.36] J. Chen, C. Shu, N. Wang, J. Feng, H. Ma and W. Yan, *J. Colloid Interface Sci.*, 2017, **495**, 44-52.
- [4.37] M. Nehra, N. Dilbaghi, N.K. Singhal, A.A. Hassan, K.H. Kim and S. Kumar, *Environ. Res.*, 2019, **169**, 229-236.
- [4.38] Z. Hu, M. Khurana, Y.H. Seah, M. Zhang, Z. Guo and D. Zhao, *Chem. Eng. Sci.*, 2015, **124**, 61-69.
- [4.39] S.J. Garibay and S.M. Cohen, *Chem. Commun.*, 2010, **46**, 7700-7702.
- [4.40] H. Liu, W. Guo, Z. Liu, X. Li and R. Wang, *RSC Adv.*, 2016, **6**, 105282-105287.
- [4.41] K.Y. Lin, Y.T. Liu and S.Y. Chen, *J. Colloid Interface Sci.*, 2016, **461**, 79-87.
- [4.42] N. Zhang, X. Yang, X. Yu, Y. Jia, J. Wang, L. Kong, Z. Jin, B. Sun, T. Luo and J. Liu, *Chem. Eng. J.*, 2014, **252**, 220-229.
- [4.43] G.C. Velazquez-Peña, M.T. Olgún-Gutiérrez, M.J. Solache-Ríos and C. Fall, *J. Fluorine Chem.*, 2017, **202**, 41-53.
- [4.44] S. Chatterjee and S. De, *Sep. Purif. Technol.*, 2014, **125**, 223-238.
- [4.45] L. Lin, Z. Lei, L. Wang, X. Liu, Y. Zhang, C. Wan, D.J. Lee and J.H. Tay, *Sep. Purif. Technol.*, 2013, **103**, 15-20.
- [4.46] A. Salifu, Fluoride Removal from Groundwater by Adsorption Technology, CRC Press. (2017)
- [4.47] H. Zhang, T. Li, Z. Yang, M. Su, L. Hou, D. Chen and D. Luo, *Sep. Purif. Technol.*, 2017, **188**, 293-302.
- [4.48] T.A. Saleh, A. Sari and M. Tuzen, *Chem. Eng. J.* 2017, **307**, 230-238.
- [4.49] H. Cai, L. Xu, G. Chen, C. Peng, F. Ke, Z. Liu, D. Li, Z. Zhang and X. Wan, *Appl. Surf. Sci.* 2016, **375**, 74-84.
- [4.50] B. Chen, J. Wang, L. Kong, X. Mai, N. Zheng, Q. Zhong, J. Liang and D. Chen, *Colloids Surf. A*, 2017, **520**, 612-621.
- [4.51] S.K. Swain, S. Mishra, P. Sharma, T. Patnaik, V.K. Singh, U. Jha, R.K. Patel and R.K. Dey, *Ind. Eng. Chem. Res.*, 2010, **49**, 9846-9856.
- [4.52] X.H. Zhu, C.X. Yang and X.P. Yan, *Microporous Mesoporous Mater.*, 2018, **259**, 163-170.
- [4.53] P. Kumar, A. Pournara, K.H. Kim, V. Bansal, S. Rapti and M.J. Manos, *Prog. Mater. Sci.*, 2017, **86**, 25-74.
- [4.54] X. Zhao, D. Liu, H. Huang, W. Zhang, Q. Yang and C. Zhong, *Microporous Mesoporous Mater.*, 2014, **185**, 72-78.
- [4.55] T. Asadi, M.R. Ehsani, A.M. Ribeiro, J.M. Loureiro and A.E. Rodrigues, *Chem. Eng. Technol.*, 2013, **36**, 1231-1239.
- [4.56] H. Fei, J. Shin, Y.S. Meng, M. Adelhardt, J. Sutter, K. Meyer and S.M. Cohen, *J. Am. Chem. Soc.*, 2014, **136**, 4965-4973.

Annexure 4

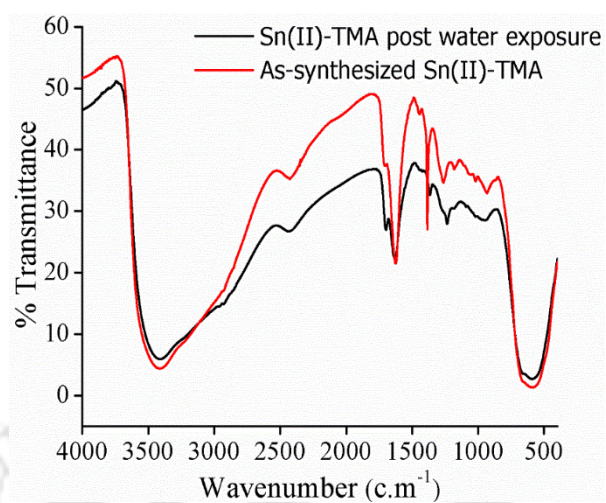


Fig. A4.1 FT-IR spectrum of Sn(II)-TMA MOF before and after water exposure.

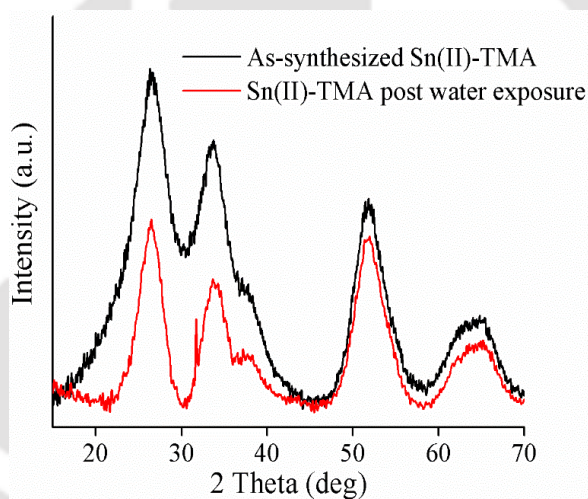


Fig. A4.2 PXRD pattern of Sn(II)-TMA MOF before and after water exposure.

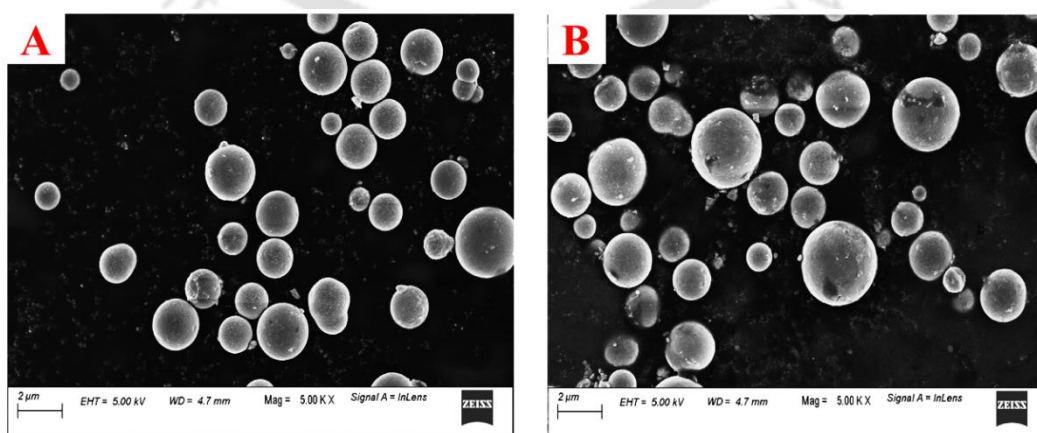


Fig. A4.3 FESEM image of (A) as-synthesized Sn(II)-TMA MOF, and (B) Sn(II)-TMA MOF after water exposure.

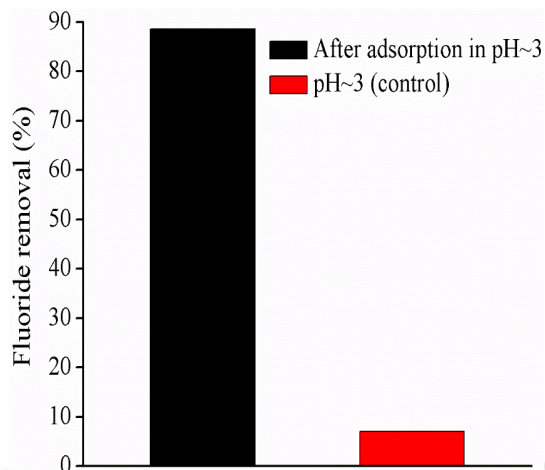


Fig. A4.4 Fluoride removal (%) in pH~3 (control) and after adsorption with Sn(II)-TMA MOF in pH~3 solution.

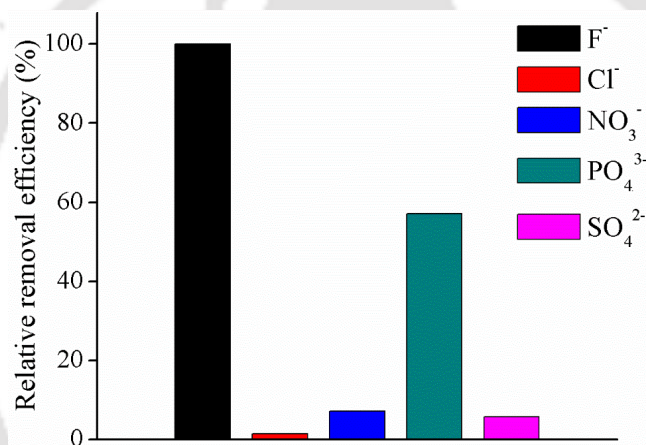


Fig. A4.5 Preferential fluoride removal in presence of five times concentration of co-existing anions (50 mg L⁻¹ each) compared to fluoride concentration (10 mg L⁻¹).

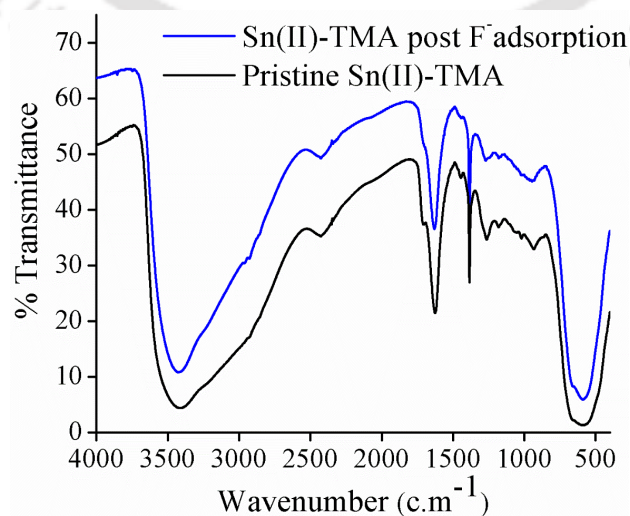


Fig. A4.6 FT-IR spectrum of Sn(II)-TMA MOF pre and post fluoride adsorption.

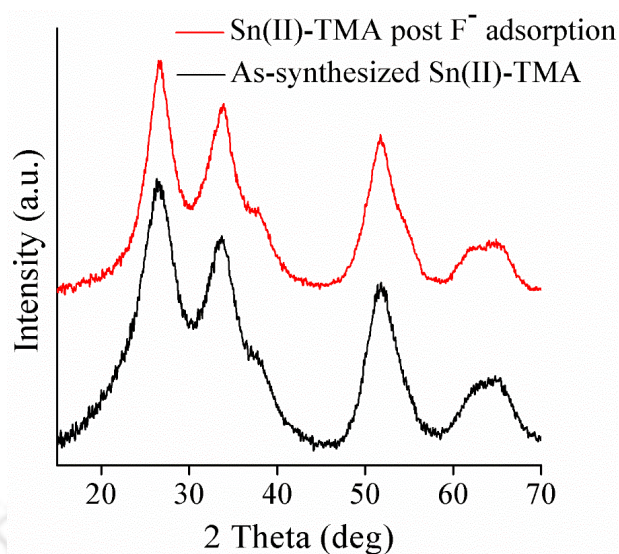


Fig. A4.7 PXRD pattern of Sn(II)-TMA MOF pre and post fluoride adsorption.

Table A4.1 Calculated R_L values based on the Langmuir model at different fluoride initial concentrations (C_0)

C_0 (mg L ⁻¹)	5	10	20	40	60	80	100	150
R_L	0.93	0.49	0.32	0.193	0.13	0.1	0.08	0.06

Table A4.2 Comparative adsorption capacities (Q_e) of different MOF based adsorbents for fluoride removal.

Sl No.	MOF based adsorbent	pH	T (K)	t (min)	Q_e (mg g ⁻¹)	Reference
1	MOF-801 (Zr)	2-10	303	120	40	[A4.1]
2	La MOF (Ce)	3-7	298	120	103.95	[A4.2]
3	AlFu (Al)	7	303	1440	550	[A4.3]
4	UiO-66-NH ₂ (Zr)	3-7	303	30	55.70	[A4.4]
5	UiO-66 (Zr)	7	298	360	41.5	[A4.5]
6	UiO-66 (Zr)	6.8	303	80	41.36	[A4.6]
7	MIL-96 (Al)	3-10	298	240	31.69	[A4.7]
8	Sn(II)-TMA (Sn)	3-10	298	150	30.86	Present work

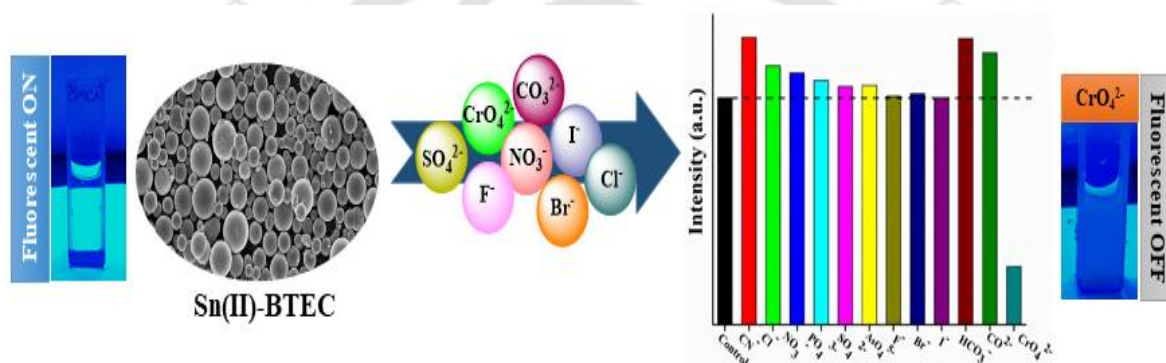
References

- [A4.1] X.H. Zhu, C.X. Yang and X.P. Yan, *Microporous Mesoporous Mater.*, 2018, **259**, 163-170.
- [A4.2] A.Ma, F. Ke, J. Jiang, Q. Yuan, Z. Luo, J. Liu and A. Kumar, *Cryst.Eng.Comm.*, 2017, **19**, 2172-2177.
- [A4.3] S. Karmakar, J. Dechnik, C. Janiak and S. De, *J. Hazard.Mater.*, 2016, **303**, 10-20.
- [A4.4] K.Y. Lin, Y.T. Liu and S.Y. Chen, *J. Colloid Interface Sci.*, 2016, **461**, 79-87.
- [A4.5] M. Massoudinejad, M. Ghaderpoori, A. Shahsavani and M.M. Amini, *J. Mol. Liq.*, 2016, **221**, 279-286.
- [A4.6] X. Zhao, D. Liu, H. Huang, W. Zhang, Q. Yang and C. Zhong, *Microporous Mesoporous Mater.*, 2014, **185**, 72-78.
- [A4.7] N. Zhang, X. Yang, X. Yu, Y. Jia, J. Wang, L. Kong, Z. Jin, B. Sun, T. Luo and J. Liu, *Chem. Eng. J.*, 2014, **252**, 220-229.



Chapter 5

Hydrolytically stable Sn(II)-BTEC hybrid material: A selective fluorogenic probe for selective detection of chromate ions in aqueous medium

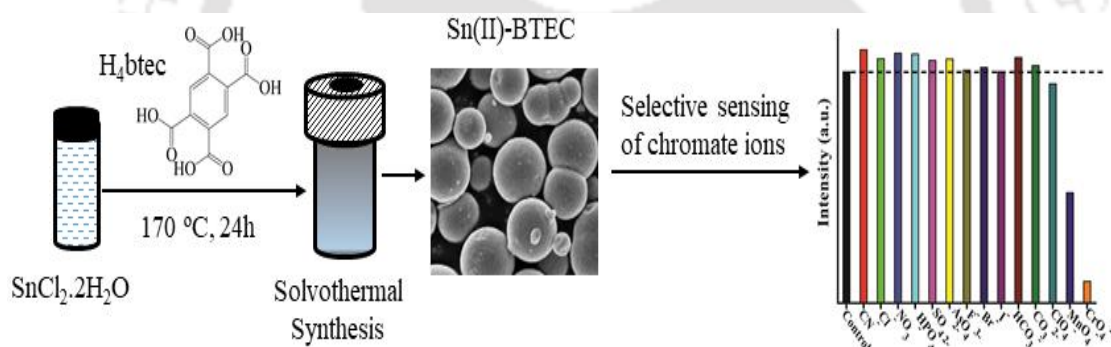


5.1 Background and Focus of the Chapter

The pressing global threat of water pollution has attracted widespread attention towards the sequestration of the toxic contaminants from water sources. Chromate (CrO_4^{2-}), an oxoanion, is one of the simplest non-biodegradable environmental pollutants, has been widely used in various industrial applications such as electroplating, pigment production, metallurgy, leather tanning, etc. [5.1]. The carcinogenic and mutagenic nature of the anion can cause skin allergy, lung cancer, protein disruption, and DNA damage in the human body when consumed in the excess amount [5.2-5.4]. European Protection Agency (EPA) has listed CrO_4^{2-} as one of the priority pollutants [5.5]. Hence detection and sequestration of CrO_4^{2-} anions from aqueous medium have gained widespread attention. So far, different methods such as adsorption [5.6], photocatalytic degradation [5.7, 5.8], resins [5.9], ion exchange [5.10, 5.11], membrane separation [5.12] have been explored for chromate removal from aqueous solution. Among these methods, adsorption is considered the most promising technique because of its simplicity, efficiency, and sensitivity [5.13]. In general, sorbents are classified into two categories: inorganic and organic sorbents. The inorganic sorbents include ACs (activated carbons), zeolites, layered double hydroxides (LDHs), etc. Despite their low cost, these sorbents suffer from drawbacks such as poor selectivity and slow sorption kinetics [5.14]. The organic sorbents like commercially available organic polymer resins are oxidized-decomposed in the presence of dichromate and hence cannot be recycled [5.15]. Besides, the organic sorbents display poor thermal and chemical stability compared to the inorganic sorbents. These limitations actuate the quest for exploiting promising adsorbent material for CrO_4^{2-} -sensing and capture. In the past decade, several chemical sensors have been reported [5.16], but they suffer from various drawbacks such as low sensitivity, bad chemical stability, and poor regeneration ability [5.17]. As a sub-class of porous materials, inorganic-organic hybrid solids represent an interesting class of porous solids, which imparts the rigidity of inorganic solids as well as the functionality of the organic building blocks [5.18]. The presence of porosity, along with multi-functional organic groups, makes them significant contributors in the field of sensing [5.19], catalysis [5.20], gas adsorption/storage [5.21], selective separation/ion exchange [5.22], etc. Sn(II) can be an ideal metal cation for the composite synthesis due to its low toxicity, easy availability, and being a hard Lewis acid can form a stronger coordination bond with the carboxylates imparting stability to the framework [5.23]. In an earlier reported work, air, and moisture stable Sn(II)-based coordination polymers were hydrothermally synthesized using polydentate carboxylic acids under alkaline conditions [5.24]. Recently, Koh et al. reported a gadolinium dicarboxylate based composite material for high potential phosphate adsorption

from the aqueous medium [5.25]. However, fewer attempts are made to synthesize composites based on 1,2,4,5- benzene tetracarboxylic acid (H_4btec) as an organic ligand. H_4btec has been known to be an ideal ligand because of several reasons, particularly the higher symmetry of the ligand may cause the generation of regular structures while the rigidity of the ligand may reduce the possibility of lattice interpenetration in the products [5.26]. Hence, the synthesis of Sn(II)-based composite using H_4btec as an organic ligand can be an attractive option to explore its potential environmental applications.

In this chapter, we report a new, highly stable Sn(II) based porous organic-inorganic composite material. The synthesized material, Sn(II)-BTEC, was applied as a selective luminescent probe for the quantitative and instant detection of CrO_4^{2-} . The material displayed a sensitive quenching phenomenon when exposed to an aqueous solution of chromate. The effect of interfering anions/ cations on the detection of CrO_4^{2-} was examined, and the quenching mechanism also elucidated. Finally, the applicability of Sn(II)-BTEC chemosensor in sensing CrO_4^{2-} from the actual water samples was explored. Overall, a brief outline of our work is represented as Scheme 5.1.



Scheme 5.1 Solvothermal synthesis of Sn(II)-BTEC and its application in selective sensing of chromate (CrO_4^{2-}) ions from aqueous medium.

5.2 Results and discussion

5.2.1. Characterization

The FT-IR spectrum (Fig. 5.1a) of Sn(II)-BTEC reveals a peak at 590 cm^{-1} , which is corroborated to the Sn-O stretching vibration, thereby confirming the metal-linker coordination. The series of peaks at 1015 cm^{-1} and 1126 cm^{-1} are attributed to the C-H in-plane bending vibrations of the aromatic rings present in the H_4btec linker [5.27, 5.28]. The intense sharp peak at 1363 cm^{-1} indicates C=C of the benzene, while the band at 1621 cm^{-1} represents C=O, which confirms the presence of carboxylate [5.29]. The broad peak around 3424 cm^{-1} is ascribed to the O-H stretching vibrations of the adsorbed water molecules [5.30]. Furthermore, the carboxylic peak shifts observed in Fig. A5.1 confirms the successful coordination of the

Sn(II) to the carboxylate ligand. In addition, the Raman spectrum demonstrates an intense peak at 1393 cm^{-1} , which is attributed to the C=C bond of the benzene ring (Fig. A5.2). The band at 1606 cm^{-1} represents the C=O stretching of the carboxylate group [5.31], thereby suggesting the successful coordination of the organic ligand to the Sn(II) metal cation. The series of bands at 875 cm^{-1} and 1015 cm^{-1} signifies the C-H in-plane vibrations of the benzene rings [5.32]. Hence, the Raman spectroscopic analysis confirmed our observation from the FT-IR study regarding the presence of vibrational bands and appropriate functional groups in our synthesized material. The PXRD plot (Fig. 5.1b) displayed three crystalline peaks at $2\theta = 26^\circ$, 33° , and 51° , respectively. N_2 adsorption-desorption experiment (Fig. 5.1c) was performed to analyze the surface area, pore size distribution, and the average pore size of the synthesized material. The surface area from the BET (Brunauer-Emmett-Teller) method was calculated at $213\text{ m}^2\text{ g}^{-1}$ in the relative pressure range of 0.05- 0.3. The pore-size distribution of the material was determined from the BJH (Barrett-Joyner-Halenda) method, and the total pore volume was obtained at 0.35 cc g^{-1} . The N_2 adsorption-desorption curve in Fig. 5.1c typically represents a Type-IV isotherm with a wide distribution of pore sizes. In addition, to confirm the porosity of the material, high-pressure CO_2 adsorption study was performed (Fig. A5.3). It is obvious that the high porosity of the synthesized material contributes to the enhanced diffusion of the CO_2 molecules and its subsequent adsorption [5.33]. The Sn(II)-BTEC displayed good CO_2 sorption potential, which is consistent with the previously reported Sn-based hybrid porous materials (Table A5.1). The detailed study for adsorption isotherm and CO_2 binding affinity are elaborated in the Annexure 5. In Fig. A5.4, the zeta potential of Sn(II)-BTEC, was measured at increasing pH (2-12). The isoelectric point (IEP) at which the net charge on the hydrated surface of the material equals zero was measured at $\text{pH} \sim 10.2$. At $\text{pH} < \text{IEP}$, the surface charge of Sn(II)-BTEC is positively charged. Hence, the material exhibited positive zeta potential value in a broad pH range. The zeta potential of the material at neutral pH was measured at $+26.4\text{ mV}$. The FESEM image (Fig. 5.1 d) displayed a spherical, smooth architecture, which is consistent with the crystalline nature of the material. The particles are well dispersed, showing uniform morphology. The energy-dispersive X-ray spectroscopy (EDX) analysis confirmed the presence of Sn (41%), C (26%), and O (32%) in different weight percentages (Fig. A5.5). It is to be noted here that the EDX peak corresponding to $\text{keV} = 1.5$ represents aluminum (Al), which may be detected due to the sample drop-cast in an aluminum sheet. Besides, the peak detected at $\text{keV} = 2.1$ resembles gold (Au), used in sample coating during EDX analysis. Importantly, none of the elements (Al, Au) are significant concerning the synthesis and

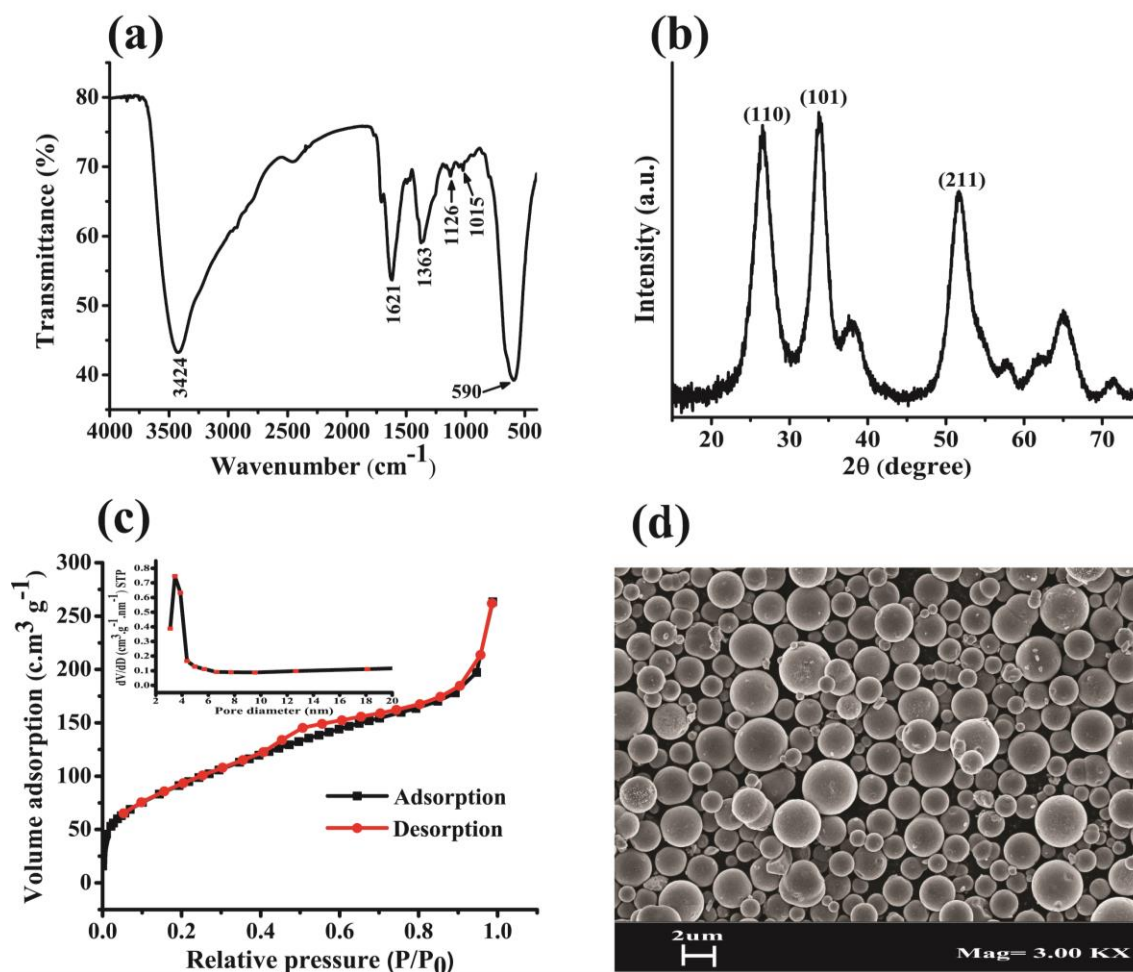


Fig. 5.1 (a) FT-IR spectrum, (b) PXRD pattern, (c) N₂ adsorption-desorption isotherm with pore-size distribution (inset), and (d) FESEM image of Sn(II)-BTEC.

formation of Sn(II)-BTEC. ImageJ histogram analysis revealed the average particle diameter to be 2 μm (Fig. A5.6).

5.2.2. Thermal and aqueous stability analysis

The stability of the composite is one of the limiting factors for their diverse applications. Hence, TGA analysis was carried out to determine the thermal stability of the synthesized Sn(II)-BTEC hybrid material. The TGA plot (Fig. 5.2a) displays a series of weight loss. The first weight loss ($\sim 4\%$) at 100 $^{\circ}\text{C}$ is ascribed to the loss of the absorbed water molecules from the pores of the material. Further, the weight loss ($\sim 7\%$) from 370-570 $^{\circ}\text{C}$ is assigned to the thermal degradation of the H₄btec ligand, which can also be confirmed from the broad exothermic peak of the DSC curve. Therefore, the synthesized Sn(II)-BTEC displayed excellent thermal stability up to 370 $^{\circ}\text{C}$, which can be correlated to the formation of strong metal-ligand coordination bonds. To date, very few organic-inorganic hybrids are reported to be stable in aqueous solution because the metal-ligand bond undergoes hydrolysis in the presence of water molecules, particularly in acidic/basic environment, hence limiting its

application as a chemosensor [5.34, 5.35]. Such a scenario actuates the need of water-stable composite material. The chemical stability of Sn(II)-BTEC was examined by soaking in a series of pH solutions (pH 3, pH 7, and pH 9) for a duration of 48 h. It was observed in (Fig. 5.2b) that the synthesized material retained the similar PXRD patterns when subjected to acidic as well as alkaline pH. The results demonstrate the excellent aqueous stability of Sn(II)-BTEC. The H₄btec ligand with four -COOH groups tend to chelate the Sn(II) cations to form a strong metal-ligand coordination bond. Besides, the high electron density in the benzene rings of the H₄btec ligand leads to an increase in electron density of carboxyl O atoms, which further strengthens the Sn-O bonds resulting in a robust framework [5.36, 5.37].

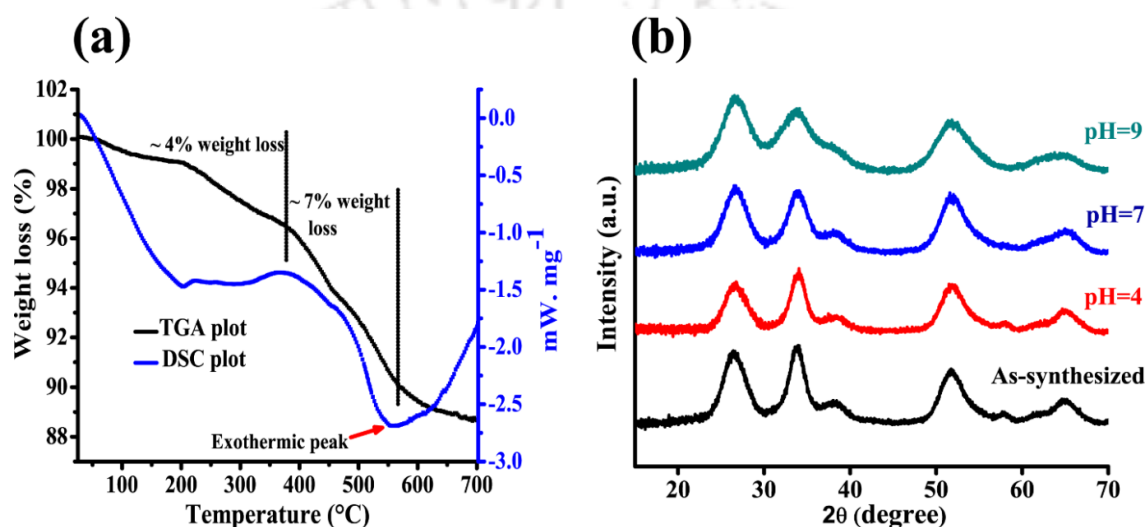


Fig. 5.2 (a) DSC-TGA plot, and (b) Comparative PXRD plot of as-synthesized Sn(II)-BTEC and Sn(II)-BTEC after exposure to varying pH solution.

5.2.3. Luminescence properties

Sn(II)-BTEC dispersed in aqueous medium displayed the maximum absorbance (λ_{max}) at 310 nm during solution state UV-vis measurement (Fig. A5.7). In addition, the $\lambda_{\text{max}} \sim 310$ nm of Sn(II)-BTEC observed during solid-state diffuse reflectance measurement (Fig. A5.7b) further supports the above solution state UV-vis spectroscopic observation. The fluorescence spectra of Sn(II)-BTEC was investigated in an aqueous medium at room temperature, where it exhibited intense emission intensity at 445 nm upon excitation at 310 nm. However, the emission intensity of the free ligand at 445 nm was found to be much weaker under similar conditions (Fig. A5.8). Importantly, approximately 200 fold increase in the emission intensity was observed in comparison to the free ligand. In our case, we observe a linker based emission process that plays a key role in the luminescence of MOFs due to the use of the highly conjugated organic system [5.38]. Interestingly, upon coordination with the metal cations, the organic linkers generally become more rigid, thereby reducing the efficiency of the non-

radiative pathways resulting in an increase in fluorescence lifetime and emission intensity [5.39]. Besides, the emission of Sn(II)-BTEC ($\lambda_{em} = 445$ nm) is observed to be similar to that of the H₄btec linker, which may result due to the ligand centered $\pi-\pi^*$ electronic transitions [5.40] as clearly evident in Fig. A5.7. Such linker based luminescence are previously observed with MOFs based on transition metal cations (Zn^{2+} , Cd^{2+}) because these ions are difficult to oxidize/ reduce due to their core-like d-orbitals [5.41]. Besides, the presence of good surface area and porosity enhanced the fluorescence intensity of the synthesized chemosensor. The influence of pH on the emission intensity of Sn(II)-BTEC was determined by suspending 0.8 mg ml⁻¹ of the material in different pH solutions (pH 4, pH 7, and pH 9) to form a homogeneous dispersion under sonication. The intensity of the emission spectrum at pH 4 displayed a little reduction ~ 20% while the pH 7 and pH 9 exhibited stable emission intensity (Fig. A5.9). Therefore, stable luminescence intensity under acidic (pH 4), as well as alkaline (pH 9) conditions, confirms the excellent stability and applicability of our chemosensor in a wide pH range.

5.2.4. Hexavalent chromate sensing

The studies on selective sensing ability of Sn(II)-BTEC for various anions (I^- , Br^- , CN^- , F^- , Cl^- , NO_3^- , CO_3^{2-} , HCO_3^- , SO_4^{2-} , $H_2PO_4^-$, AsO_4^{3-} , MnO_4^- , ClO_4^- , CrO_4^{2-}) were performed by the gradual addition of 50 mM respective salt solution to the aqueous suspension of Sn(II)-BTEC (Fig. A5.10). The addition of the other anions (except MnO_4^-) did not quench the emission spectrum of Sn(II)-BTEC, even when added in excess. However, the addition of CrO_4^{2-} significantly quenched (>90%) the emission of the chemosensor compared to all other anions (Fig. A5.3a). It is noteworthy to mention that the absorption spectrum of the MnO_4^- ion in the range 300-500 nm partially overlaps the absorption and emission spectrum of the Sn(II)-BTEC resulting in the quenching (~49%) of its emission intensity. Further, the quenching effect of MnO_4^- ions is discussed in detail in the next section of the manuscript. In Fig. A5.3b, the influence of the various anions on the quenching efficiency was examined in binary anion mixture and compared with control (chromate only). It was observed that the addition of CrO_4^{2-} significantly quenched the luminescence intensity of the chemosensor, even in the presence of the interfering anions. Importantly, it was noted that the quenching efficiency of ~85% was achieved in the co-existing solution of CrO_4^{2-} and MnO_4^- in comparison to the quenching efficiency of ~90% in the presence of CrO_4^{2-} alone.

Besides the interfering anions, the actual water sample may comprise different metal cations. Hence, the effect of various metal cations like Ca^{2+} , Pb^{2+} , Cd^{2+} , Mg^{2+} , Ni^{2+} , Cu^{2+} , Co^{2+} , Mn^{2+} , and Zn^{2+} on the quenching efficiency of CrO_4^{2-} was studied. All the metal ions exhibited

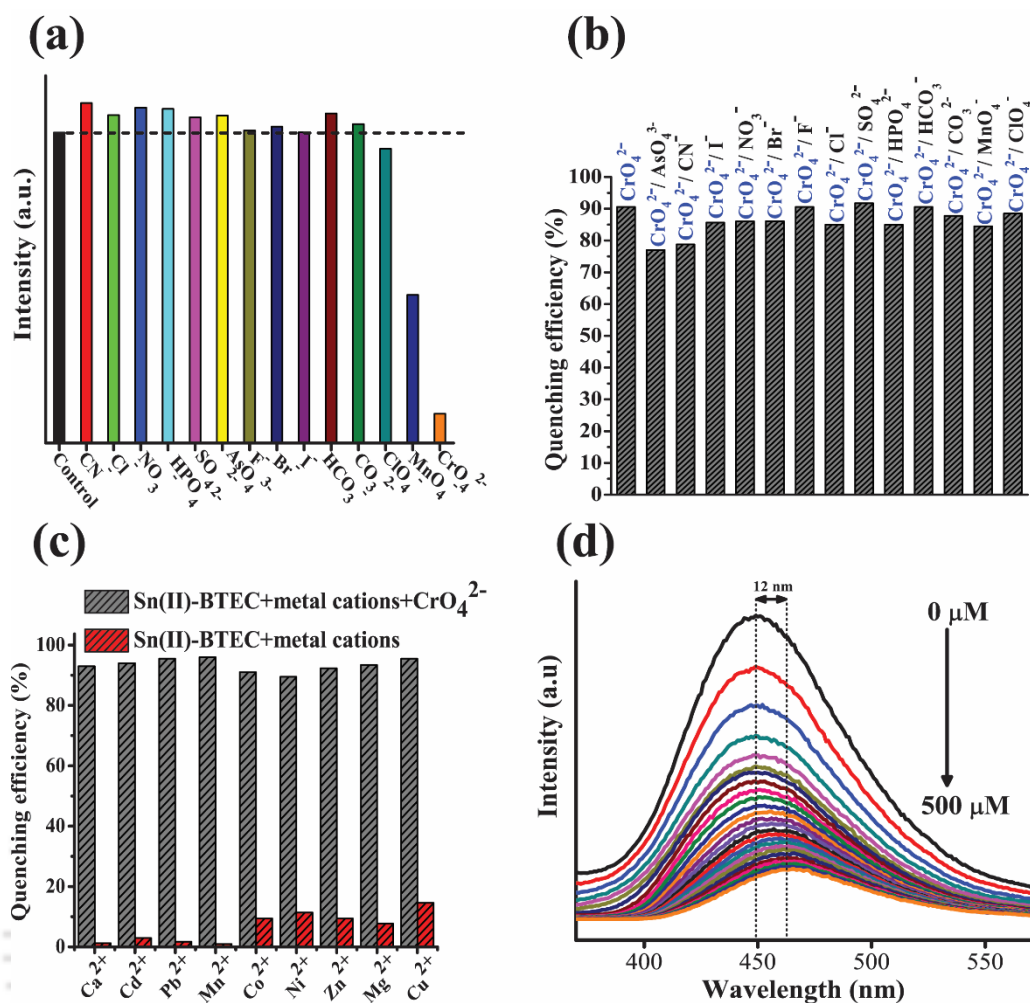


Fig. 5.3 (a) Fluorescence quenching property of different anions upon excitation of Sn(II)-BTEC at 445 nm (b) Quenching of efficiency of Sn(II)-BTEC in the presence of interfering anions, (c) Fluorescence quenching efficiency of different metal cations in the presence and absence of CrO₄²⁻ ions and (d) Fluorescence titration experiment displaying the quenching of luminescence intensity upon incremental addition (0-500 μM) of CrO₄²⁻ anions at an excitation wavelength of 445 nm.

minimal quenching efficiency (<15%), while the addition of CrO₄²⁻ displayed significant quenching (>90%) of the emission spectrum (Fig. A5.3c). Therefore, the findings indicate the remarkable selective quenching effect of Sn(II)-BTEC in the presence of CrO₄²⁻ ions.

To further investigate, the fluorescence response of our chemosensor towards CrO₄²⁻ fluorescence titration experiments (Fig. 5.3d) was carried out with a gradually increasing concentration of CrO₄²⁻ (20-500 μM). The fluorescence titration curve revealed that the emission intensities of Sn(II)-BTEC decreased with a gradual increase in CrO₄²⁻ concentration, where the change in emission intensity is proportional to the concentration of the chromate ions. Also, a redshift of ~ 12 nm towards higher wavelength was observed, which might be due to the excited state energy transfer during interaction with the CrO₄²⁻ ions. The fluorescence quenching mechanism was analyzed by the Stern-Volmer (S-V) equation: $I_0/I =$

$K_{SV} [M] + 1$, (I_0 is the initial fluorescence intensity, I is the intensity after addition of analytes, M (μM) is the concentration of the analytes, and K_{SV} (μM^{-1}) is the Stern-Volmer constant) [5.42]. In Fig. 5.4a, the correlation coefficient (R^2) for the Stern-Volmer plot in the linear lower concentration region was determined to be 0.989 with a K_{SV} value of 8.95×10^3 . The result suggests that the fluorescent quenching followed the Stern-Volmer equation, which indicates a dynamic quenching process [5.43, 5.44]. The high K_{SV} value indicates the relatively high-efficiency quenching of the emission intensity of Sn(II)-BTEC in the presence of CrO_4^{2-} ions. The limit of detection (LOD) for CrO_4^{2-} was calculated using the equation $\text{LOD} = 3\sigma/m$, where σ is the standard deviation of the five blank measurements for Sn(II)-BTEC, and m is the slope of the linear curve (Fig. 5.4b) plotted for the luminescence intensity (I) of Sn(II)-BTEC at the lower concentration region of the chromate ion addition [5.45, 5.46]. The detection limit of the chemosensor for probing CrO_4^{2-} was obtained at $1.92 \mu\text{M}$, which is comparable or better than previously reported organic-inorganic hybrid based probing systems (Table A5.2).

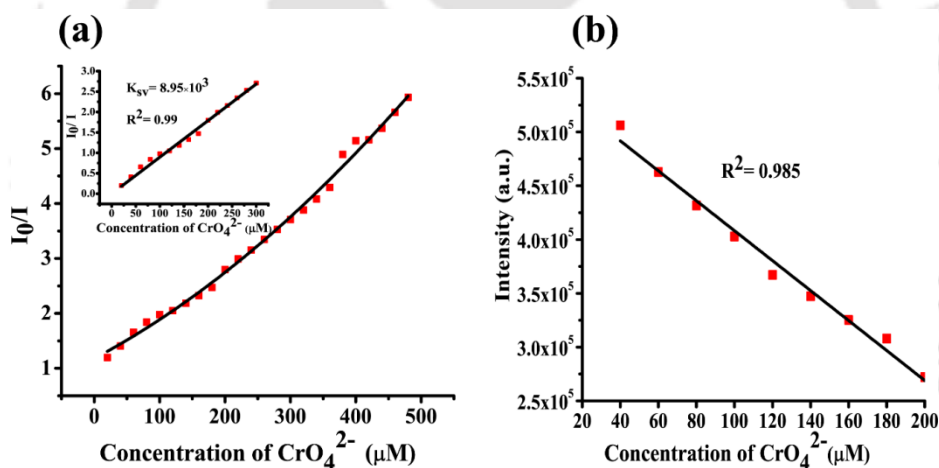


Fig. 5.4 (a) Stern-Volmer plot of I_0/I versus CrO_4^{2-} (inset: plot for determination of K_{SV}) and (b) Limit of detection (LOD) plot at the linear region of luminescence intensity with the incremental addition of CrO_4^{2-} ions.

5.2.5. Mechanism of quenching

The mechanism involved in the luminescent quenching of Sn(II)-BTEC can be attributed to either collapse of the framework or the loss of energy due to collision anions and framework. The PXRD data confirms that the structural integrity of the framework is preserved even after exposure to CrO_4^{2-} ions (Fig. A5.11). Hence, the framework collapse mechanism can be negated. Besides, the luminescence emission intensity of Sn(II)-BTEC followed the S-V equation at lower concentrations indicating that the quenching effect may be ascribed to the collision between anions and the framework (dynamic quenching) [5.45, 5.47]. However, the steady-state measurements involving the linear S-V plot do not alone prove the dynamic

quenching process because sometimes static quenching also results in a linear S-V plot. Therefore to differentiate between static and dynamic quenching processes, a more definitive method, i.e., the time-resolved measurement, was adopted [5.48, 5.49]. We have carried out time-resolved photoluminescence (TRPL) analysis for the Sn(II)-BTEC before and after the CrO_4^{2-} sorption. The photoluminescence (PL) decay pattern is fitted with a bi-exponential function, and the average fluorescence lifetime (τ) is calculated using the following equation [5.50].

$$\tau = \frac{\alpha_1 \tau_1^2 + \alpha_2 \tau_2^2}{\alpha_1 \tau_1 + \alpha_2 \tau_2}$$

The values of the fitting parameter (χ^2), exciton lifetimes (τ_1 , τ_2), and pre-exponential factors (α_1 , α_2) are represented in Table 5.1.

Table 5.1 Calculated parameters from the time-resolved fluorescence study

Sample	χ^2	τ_1 (ns)	τ_2 (ns)	α_1 (%)	α_2 (%)	τ (ns)
Sn(II)-BTEC+ CrO_4^{2-}	1.089	2.747	11.552	6.359	93.641	11.41
Sn(II)-BTEC	1.010	0.992	10.246	14.178	85.822	24.03

Static quenching is assumed to be the result of the formation of non-fluorescent quencher fluorophore complex in the ground state [5.51]. In static quenching, the non-transfer of energy in the excited state results in unaltered average fluorescence lifetime before and after the quenching process. Contrastingly, in dynamic quenching, the average fluorescence lifetime changes due to collision between the quencher molecule and the fluorophore [5.52, 5.53]. Evidently, in our case, the average fluorescence lifetime (τ) decreased from ~24 ns to ~11 ns after the addition of CrO_4^{2-} (Fig. 5.5), which suggests the dynamic nature of the quenching process.

Further to examine the quenching process, UV-vis spectra of the CrO_4^{2-} were recorded and plotted (Fig. A5.12) along with the absorption and emission spectra of Sn(II)-BTEC. The UV-vis absorption spectrum suggests two plausible mechanisms for quenching with chromate ions. Firstly, the broad absorption band of the CrO_4^{2-} ions at 274 nm partially overlaps the absorption band of the Sn(II)-BTEC resulting in competition for the absorption of the excitation wavelength energy between the CrO_4^{2-} ions and the chemosensor [5.54, 5.55]. This will deter the energy transfer to the material architecture, which will result in luminescence quenching. However, the absorption peak of the other anions (except MnO_4^-) was below the absorption band (~310 nm) of Sn(II)-BTEC, reflecting no significant quenching of the

luminescence intensity. Secondly, the emission of the Sn(II)-BTEC suspension at 445 nm partially overlapped the absorption bands of the CrO_4^{2-} (~ 372 nm) and MnO_4^- (~ 525 nm) ions (Fig. A5.12), in contrast, the other anions do not absorb in the 300-450 nm range [5.56]. Such spectral overlap might cause resonance energy transfer from Sn(II)-BTEC to CrO_4^{2-} and MnO_4^- ions and subsequently, quench the emission of Sn(II)-BTEC in the presence of the mentioned anions [5.57, 5.58]. Also, due to the high oxidizing nature of the anions (CrO_4^{2-} and MnO_4^-), electron transfer from the H_4btec ligand present in the Sn(II)-BTEC to the oxidants is quite possible, which deters the $\pi\text{-}\pi^*$ electron transfer [5.59]. It is noteworthy to mention here that though MnO_4^- reduce the emission intensity of Sn(II)-BTEC (quenching efficiency $\sim 49\%$), Sn(II)-BTEC displayed the highest quenching efficiency ($\sim 90\%$) in the presence of CrO_4^{2-} ions. Overall, the excellent quenching effect of Sn(II)-BTEC caused by the CrO_4^{2-} ions can be attributed to the decrease in the energy transfer between $\pi\text{-}\pi^*$ orbitals in H_4btec , where the electron-rich π system of Sn(II)-BTEC acts as a donor for the acceptor CrO_4^{2-} in aqueous solution upon excitation in the UV region. The above discussed mechanistic insight of CrO_4^{2-} sensing agrees well with the earlier literature reports [5.51, 5.60].

Moreover, the high surface area and presence of permanent porosities in the synthesized material provides high interaction sites where enhanced interaction between the host and guest occurs, thereby promoting the delocalization of electrons [5.61]. It is to be noted here that the possibility of fluorescence quenching due to the inner filter effect (IFE) has been precluded because the absorption and the emission spectrum of Sn(II)-BTEC do not overlap each other. More importantly, in the IFE process, the average fluorescence lifetime (τ) of a fluorescent material remains unchanged [5.13]. However, the reduction in average fluorescence lifetime (τ) in our TRPL study and the spectra overlap observed in the UV-vis absorption study clearly suggests electron and energy transfer processes as the predominant mechanism of fluorescence quenching.

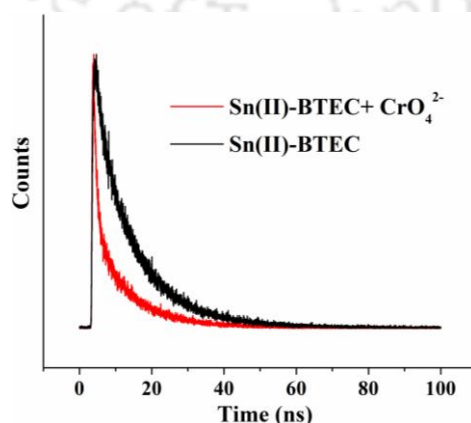


Fig. 5.5 Time-resolved fluorescence lifetime decay profile of Sn(II)-BTEC before and after the addition of CrO_4^{2-} ions.

5.2.6. Real water application

It is essential to investigate the utility of Sn(II)-BTEC chemosensor in environmentally relevant conditions. Therefore, water samples from different sources *viz.* lake water (IIT Guwahati lake, Kamrup district), laboratory tap water, and Brahmaputra river were collected and filtered with 0.22 μm filter paper. The pH of the water samples at 25 $^{\circ}\text{C}$ was measured to be 7.3, 7.5, and 7.5 for the river, lake, and tap water, respectively. To analyze the quenching effect in real water samples, an approximate 0.5 mg ml^{-1} of Sn(II)-BTEC was dispersed in de-ionized (DI) water and sonicated to form a fine homogeneous dispersion. In Fig. 5.6a, the addition of 1 mM CrO_4^{2-} displayed $\sim 90\%$ quenching efficiency, which is comparable with the control (DI water). The results further prove the remarkable anti-interference activity of the chemosensor towards sensing of CrO_4^{2-} ions in actual water samples. Furthermore, the utility of Sn(II)-BTEC as a chemosensor for the detection of a trace amount of CrO_4^{2-} from real water samples was investigated. For this purpose, the water samples *viz.* DI water, tap water, lake water, and river water were spiked with 2 μM of CrO_4^{2-} . Each sample was analyzed, and the CrO_4^{2-} concentration was estimated from the calibration curve. The results indicated good agreement between the spiked and measured CrO_4^{2-} concentration with recovery values in the range of 95.5% - 90.35%. The findings are tabulated in Table 5.2.

Table 5.2 Determination of CrO_4^{2-} ion concentration using Sn(II)-BTEC chemosensor in real samples

Sample	Amount of CrO_4^{2-} spiked (μM)	Amount of CrO_4^{2-} detected (μM)	Recovery (%)
DI water	2	1.910 ± 0.03	95.5
Tap water	2	1.858 ± 0.05	92.9
Lake water	2	1.807 ± 0.04	90.35
River water	2	1.815 ± 0.05	90.75

Also, the Atomic absorption spectroscopy (AAS) analysis was performed on the real water samples to validate our results in practical environmental applications. The water samples (tap, lake, and river water) were spiked with 10 mg L^{-1} hexavalent chromium, Cr(VI), and 0.5 g L^{-1} of Sn(II)-BTEC was added to it at room temperature. The samples were equilibrated in an orbital shaker for 1 h, filtered, and analyzed for equilibrium concentration (C_e) of Cr(VI). In Fig. 5.6b, the C_e values of Cr(VI) for tap water, lake water, and river water were obtained at 30 $\mu\text{g L}^{-1}$ and 80 $\mu\text{g L}^{-1}$ respectively, which is below the U.S-EPA permissible limit of 100 $\mu\text{g L}^{-1}$. The high surface area and presence of large pore volume in Sn(II)-BTEC expose the adsorption sites resulting in high Cr(VI) adsorption efficiency ($\sim 99\%$). The FESEM mapping confirms the presence of Cr(VI) adsorbed on the surface of Sn(II)-BTEC while the EDX analysis

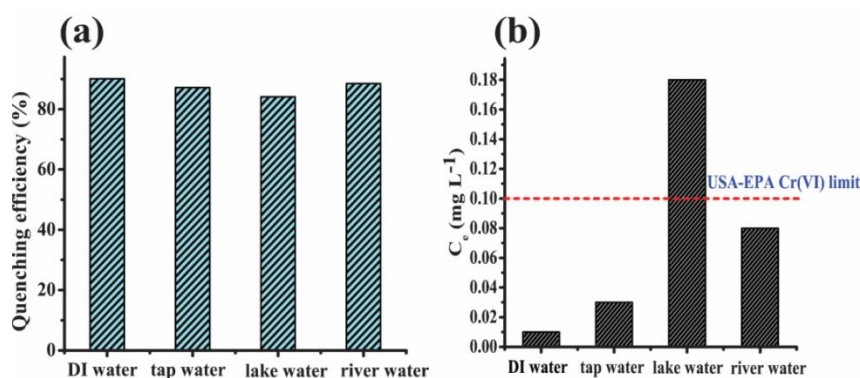


Fig. 5.6 (a) Fluorescence quenching of Sn(II)-BTEC for detection of CrO_4^{2-} ions in de-ionized (DI) water, tap water, lake water, and river water (b) Cr(VI) sorption ability of Sn(II)-BTEC from different water samples highlighting the equilibrium concentration (C_e) after sorption.

displays the elemental composition (Sn: 37.6%, O: 31.6%, C: 29.4%, Cr: 1.4%) of Sn(II)-BTEC in different weight percentages after Cr(VI) adsorption (Fig. A5.13). Besides, the UV-vis study (shown in Fig. A5.14) illustrates the disappearance of λ_{max} at 372 nm corresponding to the CrO_4^{2-} peak, which confirms the sorption of CrO_4^{2-} ions on Sn(II)-BTEC. Therefore, the synthesized Sn(II)-BTEC adsorbent displayed excellent Cr(VI) adsorption performance, which proves its efficacy in practical environmental applications.

5.3. Conclusion

In summary, a novel Sn(II)-BTEC, porous organic-inorganic hybrid composite has been synthesized in a simple eco-friendly solvothermal synthesis route. The material displayed excellent thermo-stability and aqueous stability in a broad pH range. The synthesized chemosensor exhibited selective luminescent sensing of the chromate anions from the aqueous medium with a limit of detection as low as 1.92 μM . The presence of metal cations or anions did not affect the fluorescence property of the material while detecting the chromate ions from the aqueous medium. The selective quenching property can be attributed to the transfer of energy/electrons and the absorption of the excitation light. The study with real environmental samples proved the Sn(II)-BTEC to be a promising fluorescent probe in detecting CrO_4^{2-} . The AAS analysis confirmed the efficient reduction of Cr(VI) within the acceptable limit prescribed by U.S-EPA after adsorption on Sn(II)-BTEC. The observation from the AAS study is in good agreement with the UV-vis absorption data regarding the effective removal of Cr(VI). The results prove that the synthesized Sn(II)-BTEC could be used as a selective fluorogenic probe for efficient chromate detection from environmentally relevant samples.

References

- [5.1] B. Dhal, H.N. Thatoi, N.N. Das and B.D. Pandey, *J. Hazard. Mater.*, 2013, **250-251**, 272–291.
- [5.2] A. Zhitkovich, *Chem. Res. Toxicol.*, 2005, **18**, 3–11.
- [5.3] D. Bagchi, S.J. Stohs, B.W. Downs, B. M. Bagchi and H.G. Preuss, *Toxicology.*, 2002, **180**, 5–22.
- [5.4] R. Vonburg and D. Liu, *J. Appl. Toxicol.*, 1993, **13**, 225–230.
- [5.5] L. Keith and W. Telliard, *Environ. Sci. Technol.*, 1979, **13**, 416–423.
- [5.6] C. Jung, J. Heo, J. Han, N. Her, S.J. Lee, J. Oh, J. Ryu and Y. Yoon, *Sep. Purif. Technol.*, 2013, **106**, 63–71.
- [5.7] R. Liang, F. Jing, L. Shen, N. Qin and L. Wu, *J. Hazard. Mater.*, 2015, **287**, 364–372.
- [5.8] N. Li, Y. Tian, J. Zhao, J. Zhang, J. Zhang, W. Zuo and Y. Ding, *Appl. Catal., B*, 2017, **214**, 126–136.
- [5.9] Z. Lv, C. Liang, J. Cui, Y. Zhang and S. Xu, *RSC Adv.*, 2015, **5**, 18213–18217.
- [5.10] L.L. Li, X.Q. Feng, R.P. Han, S.Q. Zang and G. Yang, *J. Hazard. Mater.*, 2017, **321**, 622–628.
- [5.11] J.A. Korak, R. Huggins and M. Arias-Paic, *Water Res.*, 2017, **118**, 141–151.
- [5.12] M. Owlad, M.K. Aroua, W.A. Daud and S. Baroutian, *Water, Air, Soil Pollut.*, 2009, **200**, 59–77.
- [5.13] Z.J. Lin, H.Q. Zheng, H.Y. Zheng, L.P. Lin, Q. Xin and R. Cao, *Inorg. Chem.*, 2017, **56**, 14178-14188.
- [5.14] X. Yuan, Y. Wang, J. Wang, C. Zhou, Q. Tang and X. Rao, *Chem. Eng. J.* 2013, **221**, 204–213.
- [5.15] K. Xiao, F. Xu, L. Jiang, N. Duan, S. Zheng, *Chem. Eng. J.*, 2016, **283**, 1349–1356.
- [5.16] W. Chen, F. Cao, W. Zheng, Y. Tian, Y. Xianyu, P. Xu, W. Zhang, Z. Wang, K. Deng, and X. Jiang, *Nanoscale*, 2015, **7**, 2042-2049; M.A. Qazi, U. Ocak, M. Ocak, S. Memon and I.B. Solangi, *J. Fluoresc.*, 2013, **23**, 575-590; G. Dong, Y. Zhu, H. Tian, F. Li, S. Xin, Y. Qin, *Res. Chem. Intermed.*, 2015, **41**, 1191-1201; Z. Zhang, C. Sha, A. Liu, Z. Zhang and D. Xu, *J. Fluoresc.*, 2015, **25**, 335-340; A. Zazoua, R. Kherrat, M.H. Samar, A. Errachid, N. Jaffrezic-Renault, F. Bessueille and D. Léonard, *Mater. Sci. Eng., C*, 2008, **28**, 1014-1019.
- [5.17] C.S. Cao, H.C. Hu, H. Xu, W.Z. Qiao and B. Zhao, *Cryst. Eng. Comm*, 2016, **18**, 4445-4451.
- [5.18] A.P. Wight and M.E. Davis, *Chem. Rev.*, 2002, **102**, 3589-3614.
- [5.19] K. Sarkar, K. Dhara, M. Nandi, P. Roy, A. Bhaumik, and P. Banerjee, *Adv. Funct. Mater.*, **2009**, 19, 223-234.
- [5.20] A. Corma, U. Díaz, T. García, G. Sastre and A. Velty, *J. Am. Chem. Soc.*, 2010, **132**, 15011-15021.
- [5.21] G. Ferey, C. Serre, T. Devic, G. Maurin, H. Jobic, P. L. Llewellyn, G. De Weireld, A. Vimont, M. Daturi and J.S. Chang, *Chem. Soc. Rev.*, 2011, **40**, 550–562; M. Paul, N. Pal, M. Ali and A. Bhaumik, *J. Mol. Catal. A: Chem.*, 2010, **330**, 49–55.
- [5.22] T.Y. Ma, H. Li, A.N. Tang, and Z.Y. Yuan, *Small*, 2011, **7**, 1827-1837.
- [5.23] A. Ghosh and G. Das, *New J. Chem.*, 2020, **44**, 1354-1361.
- [5.24] G.M. de Lima, R.I. Walton, G.J. Clarkson, R.S. Bitzer and J.D. Ardisson, *Dalton Trans.*, 2018, **47**, 8013-8022.
- [5.25] K.Y. Koh, C. Wang, and J.P. Chen, *J. Colloid Interface Sci.*, 2019, **543**, 343-351.
- [5.26] M. Halouani, M. Abdelhedi, M. Dammak, N. Audebrand and L. Ktari, *Open J. Inorg. Chem.*, 2013, **3**, 100-108.
- [5.27] A. Uygun, A.G. Yavuz, S. Sen and M. Omastová, *Synth. Met.*, 2009, **159**, 2022-2028.
- [5.28] Q. Lu and Y. Zhou, *J. Power Sources*. 2011, **196**, 4088-4094.
- [5.29] I. Fleming and D.H. Williams, *Spectroscopic methods in organic chemistry*, New York: McGraw-Hill, 1966.
- [5.30] X. Feng, Y.F. Wang, Z.Q. Shi, J.J. Shang and L.Y. Wang, *Inorg. Chem. Commun.*, 2012, **22**, 131-136.
- [5.31] D. Saha, R. Zacharia, L. Lafi, D. Cossement and R. Chahine, *Int. J. Hydrogen Energy*, 2012, **37**, 5100-5107.
- [5.32] N. Marshall, W. James, J. Fulmer, S. Crittenden and G.T. Rowe, 2018, *ChemRxiv*. Preprint.
- [5.33] F. Pantò, S.G. Leonardi, E. Fazio, P. Frontera, A. Bonavita, G. Neri, P. Antonucci, F. Neri and S. Santangelo, *Nanotechnology*, 2018,**29**, 305501.
- [5.34] X. Zhang, Y.Z. Zhang, D.S. Zhang, B. Zhu and J.R. Li, *Dalton Trans.*, 2015, **44**, 15697–15702.
- [5.35] H. Jasuja and K.S. Walton, *Dalton Trans.*, 2013, **42**, 15421–15426.
- [5.36] N.C. Burtch, H. Jasuja and K.S. Walton, *Chem. Rev.*, 2014, **114**, 10575–10612.
- [5.37] C. Wang, X. Liu, N.K. Demir, J.P. Chen and K. Li, *Chem. Soc. Rev.*, 2016, **45**, 5107–5134.
- [5.38] J. Heine and K. Müller-Buschbaum, *Chem. Soc. Rev.*, 2013, **42**, 9232–9242.
- [5.39] M. Pamei and A. Puzari, *Nano-Structures & Nano-Objects*, 2019, **19**, 100364.

- [5.40] Y. Wu, G.P. Yang, Y. Zhao, W.P. Wu, B. Liu and Y.Y. Wang, *Dalt. Trans.*, 2014, **44**, 3271–3277
- [5.41] J.J. Perry Iv, P.L. Feng, S.T. Meek, K. Leong, F.P. Doty and M.D. Allendorf, *J. Mater. Chem.*, 2012, **22**, 10235–10248.
- [5.42] G.X. Wen, Y.P. Wu, W.W. Dong, J. Zhao, D.S. Li and J. Zhang, *Inorg. Chem.*, 2016, **55**, 10114–10117.
- [5.43] H.X. Zhao, L.Q. Liu, Z. De Liu, Y. Wang, X.J. Zhao and C.Z. Huang, *Chem. Commun.*, 2011, **47**, 2604–2606.
- [5.44] S.J. Toal, K.A. Jones, D. Magde and W.C. Trogler, *J. Am. Chem. Soc.*, 2005, **127**, 11661–11665.
- [5.45] R. Lv, J. Wang, Y. Zhang, H. Li, L. Yang, S. Liao, W. Gu and X. Liu, *J. Mater. Chem. A.*, 2016, **4**, 15494–15500.
- [5.46] B. Joarder, A.V. Desai, P. Samanta, S. Mukherjee and S.K. Ghosh, *Chem. Eur. J.*, 2015, **21**, 965–969.
- [5.47] T.Q. Song, J. Dong, H.L. Gao, J.Z. Cui and B. Zhao, *Dalton Trans.*, 2017, **46**, 13862–13868.
- [5.48] P.K. Behara and A.K. Mishra, *J. Photochem. Photobiol. A*, 1993, **71**, 115–118.
- [5.49] J. Sujatha and A.K. Mishra, *J. Photochem. Photobiol. A*, 1997, **104**, 173–178.
- [5.50] M.S. Ansari, A. Banik and M. Qureshi, *Carbon*, 2017, **121**, 90–105.
- [5.51] K.F. Lee, M.H. David and T.C. Werner, *J. Chem. Educ.*, 1992, **69**, 424.
- [5.52] F.A. Michael, E.E. Mary, W.F. Steven, J.N. Cedrin and J.A. Christopher, *J. Chem. Soc., Perkin Trans. 2*, 1995, 385–388.
- [5.53] G. Avudaiappan, K.A. Jacob, L.V. Theresa, A.M. Shebitha, K. Hiba, P.K. Shenoi, V. Unnikrishnan, and K. Sreekumar, *React. Funct. Polym.*, 2019, **137**, 71–78.
- [5.54] A. Helal, M.N. Shaikh, and M.A. Aziz, *J. Photochem. Photobiol. A*, 2020, **389**, 112238.
- [5.55] W. Liu, Y. Wang, Z. Bai, Y. Li, Y. Wang, L. Chen, L. Xu, J. Diwu, Z. Chai, and S. Wang, *ACS Appl. Mater. Interfaces*, 2017, **9**, 16448–16457.
- [5.56] S. Nandi, A. Mondal, H. Reinsch and S. Biswas, *Inorg Chim Acta.*, 2019, **497**, 119078.
- [5.57] S. Li, L. Lu, M. Zhu, C. Yuan, and S. Feng, *Sens. Actuators, B*, 2018, **258**, 970–980.
- [5.58] X. Sun, S. Yao, C. Yu, G. Li, C. Liu, Q. Huo and Y. Liu, *J. Mater. Chem. A*, 2018, **6**, 6363–6369.
- [5.59] S. Rapti, D. Sarma, S.A. Diamantis, E. Skliri, G.S. Armatas, A.C. Tsipis, Y.S. Hassan, M. Alkordi, C.D. Malliakas, M.G. Kanatzidis, and T. Lazarides, *J. Mater. Chem. A*, 2017, **5**, 14707–14719.
- [5.60] S. Rapti, A. Pournara, D. Sarma, I.T. Papadas, G.S. Armatas, A.C. Tsipis, T. Lazarides, M.G. Kanatzidis and M.J. Manos, *Chem. Sci.*, 2016, **7**, 2427–2436.
- [5.61] D. Chen, C. Liu, J. Tang, L. Luo, and G. Yu, *Polym. Chem.*, 2019, **10**, 1168–1181.

Annexure 5

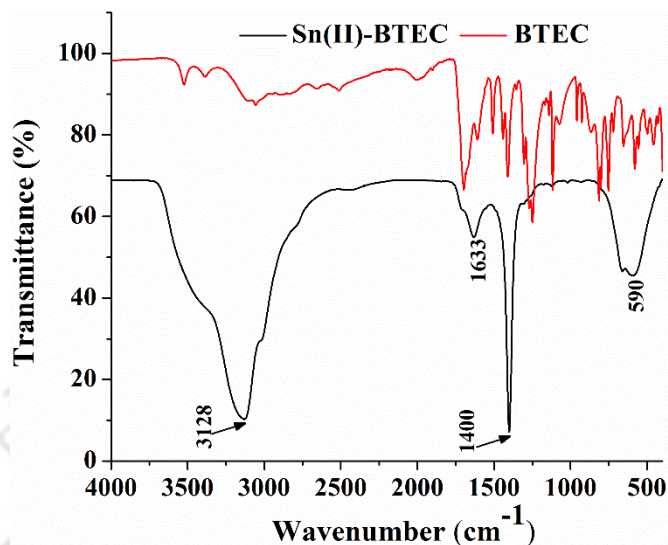


Fig. A5.1 Comparative IR spectrum of the synthesized Sn(II)-BTEC and BTEC

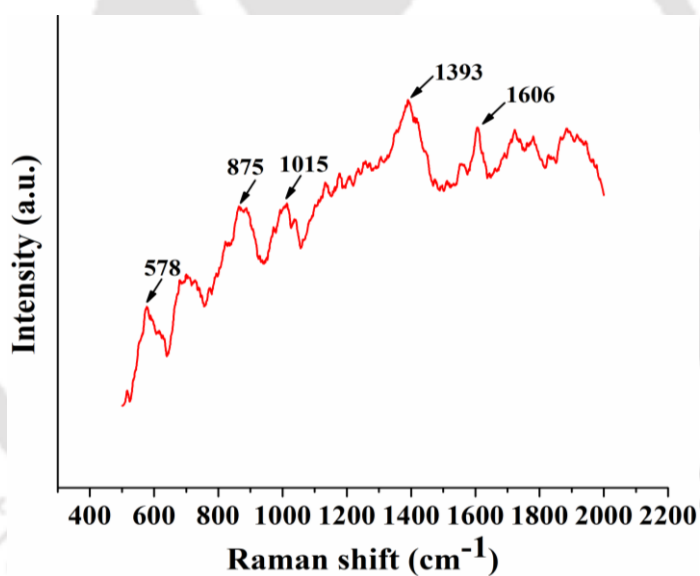


Fig. A5.2 Raman spectra of as-synthesized Sn(II)-BTEC hybrid material.

CO₂ adsorption study

Due to the available porosity and water as well as thermal stability of Sn(II)-BTEC, its CO₂ sorption potential was explored. The CO₂ adsorption experiment was performed at increasing temperatures of 293 K, 318 K, and 343 K, respectively, and a pressure range of 0-10 bar. Fig. A5.3a represents the adsorption isotherm of CO₂ on the adsorbent Sn(II)-BTEC. The adsorption of CO₂ can be well described by the virial isotherm model using second virial coefficients. The virial isotherm model is described as the following equation

$$\ln \frac{P}{N} = \left\{ \left(k_0 + \frac{k_1}{T} \right) + \left(b_0 + \frac{b_1}{T} \right) N + \left(c_0 + \frac{c_1}{T} \right) N^2 \right\}$$

where P is the pressure (bar), N is the amount of CO_2 adsorbed (mmol g^{-1}), T is the temperature (K), and b, c is the virial coefficients.

Further, to investigate the CO_2 binding affinity of Sn(II)-BTEC, the isosteric heat of adsorption ($-\Delta H$) was determined from the virial equations. Fig. A5.3b elucidates the isosteric heat of adsorption at increasing CO_2 loading. It can be observed that the isosteric heat of adsorption gradually increases ($22\text{-}26 \text{ kJ mol}^{-1}$) from low CO_2 loading to high CO_2 loading and then drops slightly, which means that there is a weak interaction between CO_2 molecule and the surface of the adsorbent at high CO_2 loading [A5.4]. In our case, a low $-\Delta H$ value of $\sim 26 \text{ kJ mol}^{-1}$ in the region of ambient pressure is due to the physisorption of CO_2 molecules on Sn(II)-BTEC [A5.3b]. Moreover, a more moderate $-\Delta H$ is advantageous as the amount of energy required during the regeneration process of the adsorbent would be much less. Van der Waal's interaction may act as the driving force for CO_2 adsorption on the adsorbent material. Despite having a comparatively lower surface area, the CO_2 adsorption capacity of our synthesized material is found to be comparable with the reported phosphonate based organic-inorganic hybrids (Table A5.1). Hence, Sn(II)-BTEC demonstrated a promising CO_2 adsorption potential, which is consistent with the previous literature reports based on Sn-based organic-inorganic hybrid adsorbents.

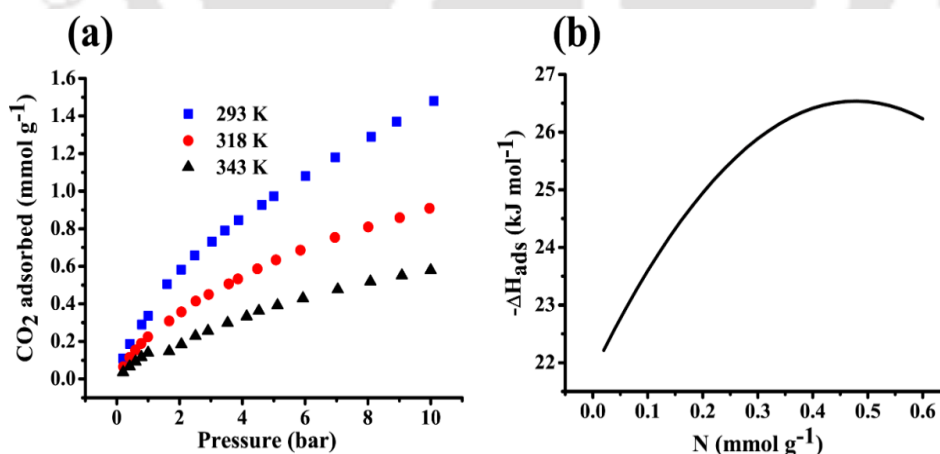


Fig. A5.3 (a) CO_2 adsorption isotherm of Sn(II)-BTEC in a pressure range of 0-10 bar and (b) Isosteric heat of adsorption with an increase in CO_2 loading.

Table A5.1 Comparison of the CO₂ adsorption capacity of different Sn-based organic-inorganic hybrids.

Sn-based hybrids	Surface area (m ² g ⁻¹)	Temperature (K)	Pressure (bar)	CO ₂ adsorbed (mmol g ⁻¹)	References
Sn(IV) phosphonate	723	298	5	0.91	[A5.6]
Sn(IV) triphosphonate	502	273	1.2	2.17	[A5.7]
Sn(II)-BTEC	213	293	5	0.97	This work

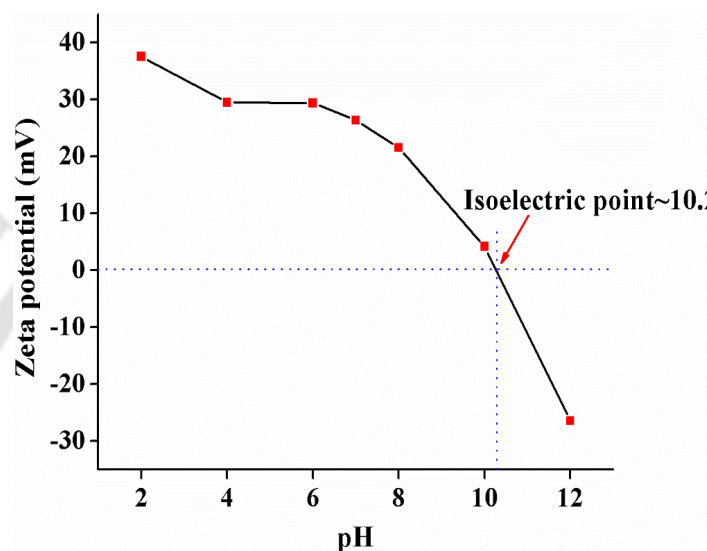


Fig. A5.4 Zeta Potential as a function of pH.

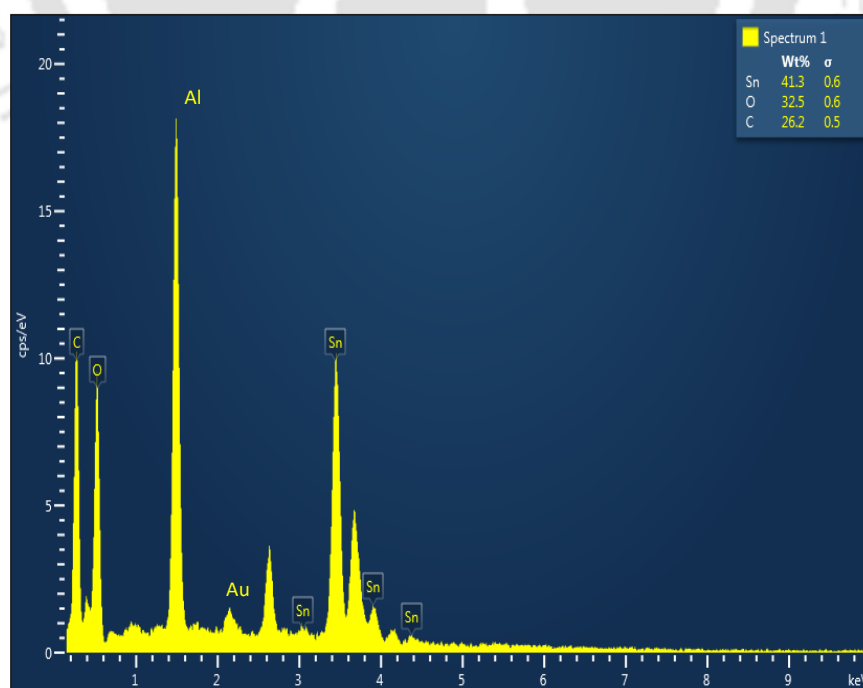


Fig. A5.5 EDX spectroscopy of Sn(II)-BTEC.

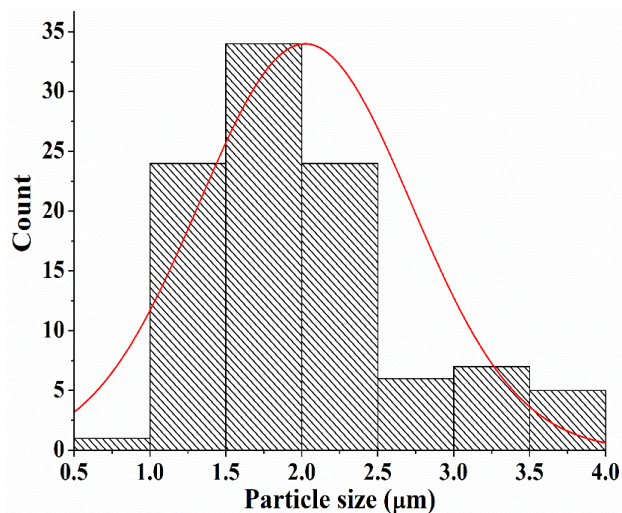


Fig. A5.6 Particle size distribution of Sn(II)-BTEC represented by a histogram.

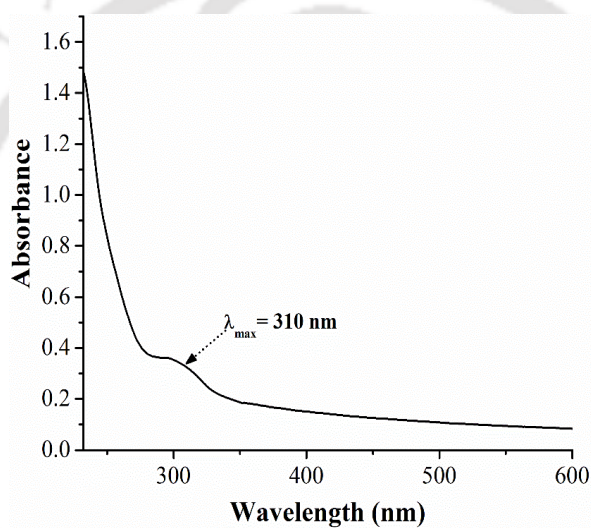


Fig. A5.7 (a) UV-vis spectrum for the maximum absorbance (λ_{\max}) of Sn(II)-BTEC in an aqueous medium.

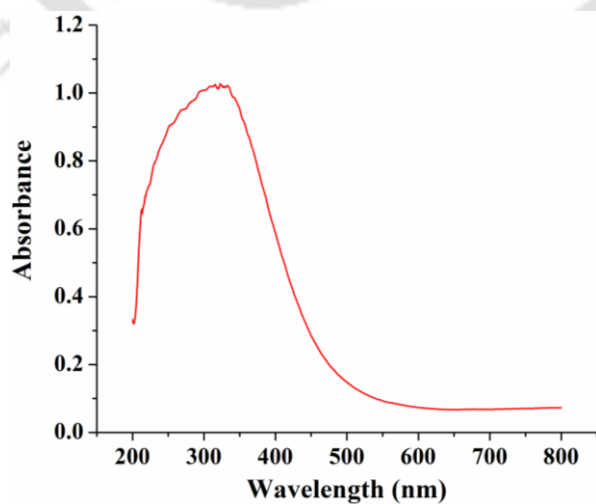


Fig. A5.7 (b) Solid-state diffuse reflectance spectra of Sn(II)-BTEC displaying $\lambda_{\max} \sim 310$ nm.

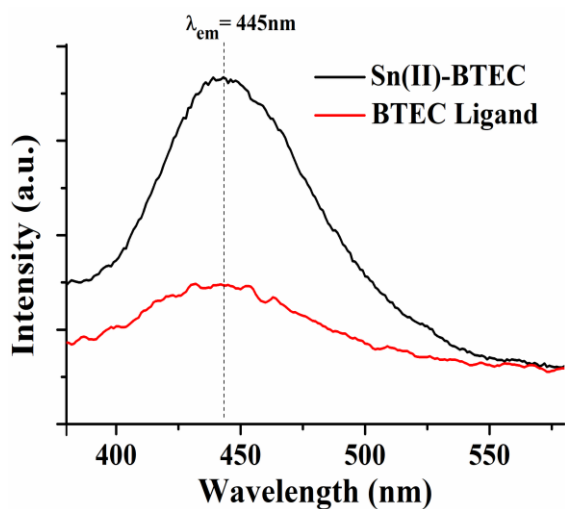


Fig. A5.8 Emission intensity of BTEC ligand versus Sn(II)-BTEC upon excitation at 310 nm.

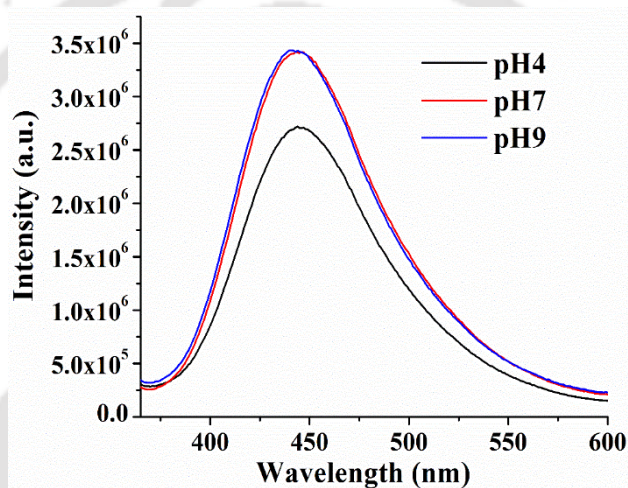


Fig. A5.9 Emission intensity of Sn(II)-BTEC at increasing pH upon excitation at 310 nm.

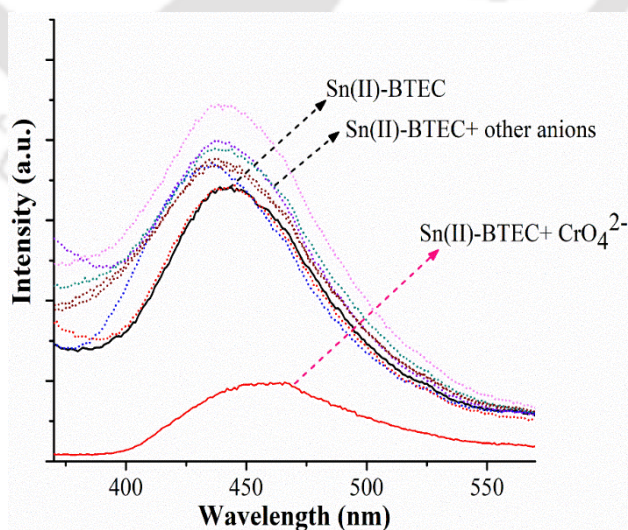


Fig. A5.10 Emission intensity of Sn(II)-BTEC in the presence of other anions and its quenching upon addition of CrO_4^{2-} ions.

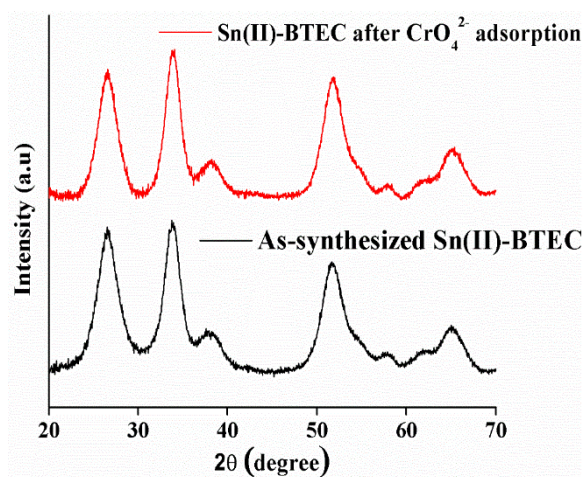


Fig. A5.11 PXRD pattern of Sn(II)-BTEC before and after CrO₄²⁻ adsorption.

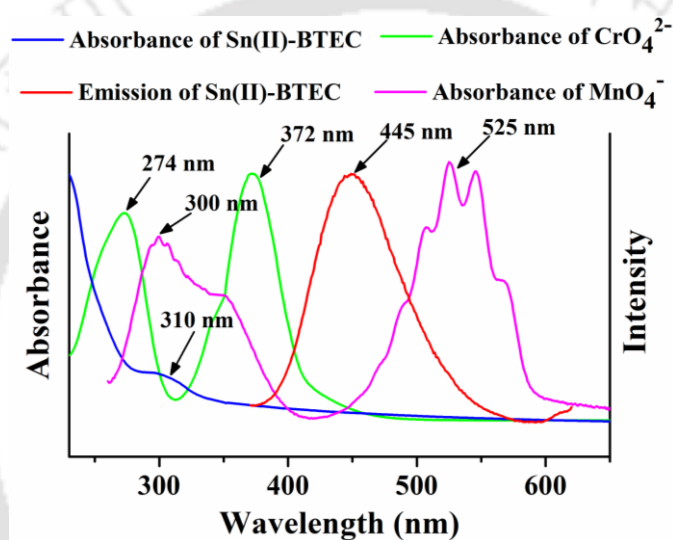


Fig. A5.12 UV-vis absorption spectra of Sn(II)-BTEC, CrO₄²⁻ and MnO₄⁻ ion, and the emission spectra of Sn(II)-BTEC in an aqueous medium.

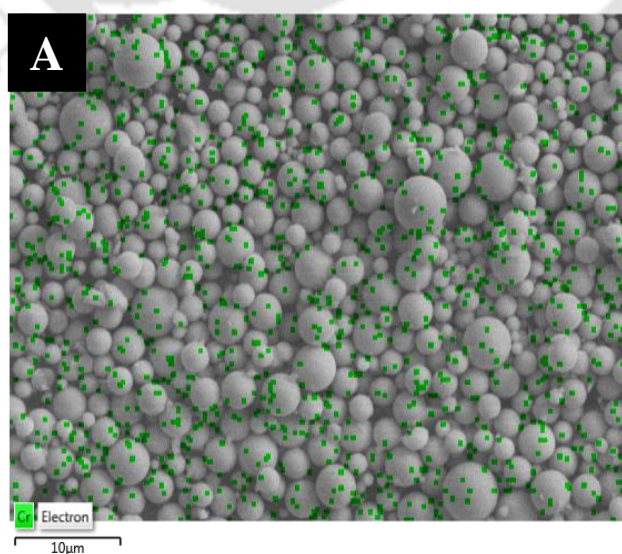


Fig. A5.13 (A) FESEM image mapping for Cr(VI)(green dots) adsorbed on Sn(II)-BTEC

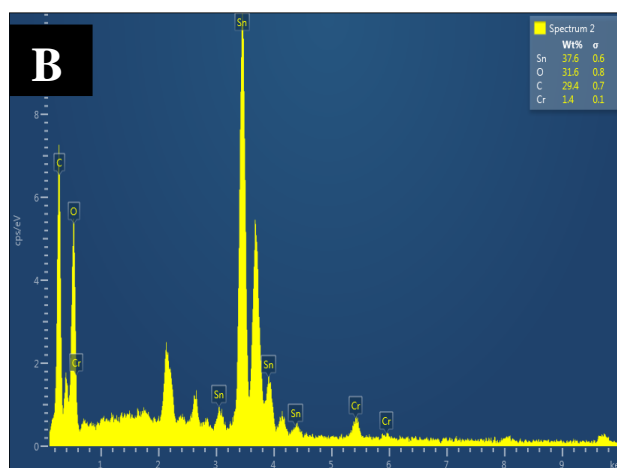


Fig. A5.13 (B) EDX Spectrum of Sn(II)-BTEC after Cr(VI) adsorption.

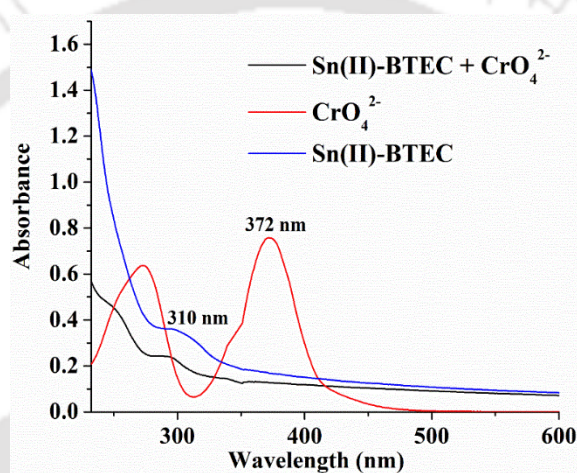


Fig. A5.14 UV-vis spectrum of CrO_4^{2-} before and after adsorption on Sn(II)-BTEC.

Table A5.2 Comparison of various organic-inorganic hybrid based sensors for the sensing of CrO_4^{2-} .

Sensors	K_{sv} (M^{-1})	Detection limit (μM)	Refs
$[\text{Zn}_2(\text{TPOM})(\text{NH}_2\text{-BDC})_2] \cdot 4\text{H}_2\text{O}_n$	4.45×10^3	4.8	[A5.8]
$[\text{Y}(\text{BTC})(\text{H}_2\text{O})_6]_n \cdot 0.1\text{Eu}$	1.18×10^3	0.03	[A5.9]
$[\text{Zn}(\text{btz})]_n$	3.19×10^3	10	[A5.10]
$[\text{Zn}(\text{tz})\text{H}_2\text{O}]_n$	2.35×10^3	20	[A5.10]
$[\text{Zn}(\text{IPA})(3\text{-PN})]_n$	1.00×10^3	18.33	[A5.11]
$[\text{Cd}(\text{IPA})(3\text{-PN})]_n$	1.30×10^3	2.52	[A5.12]
$[\text{Eu}_2(\text{tpbc})_4 \cdot \text{CO}_3 \cdot \text{H}_2\text{O}] \cdot \text{DMF} \cdot \text{solvent}$	4.85×10^3	0.33	[A5.13]
$[\text{Cd}_3(\text{cpota})_2(\text{phen})_3]_n \cdot 5\text{nH}_2\text{O}$	6.9×10^3	0.418	[A5.14]
NU-1000 (Zr)	13.37×10^3	1.8	[A5.15]
Sn(II)-BTEC	8.95×10^3	1.92	This work

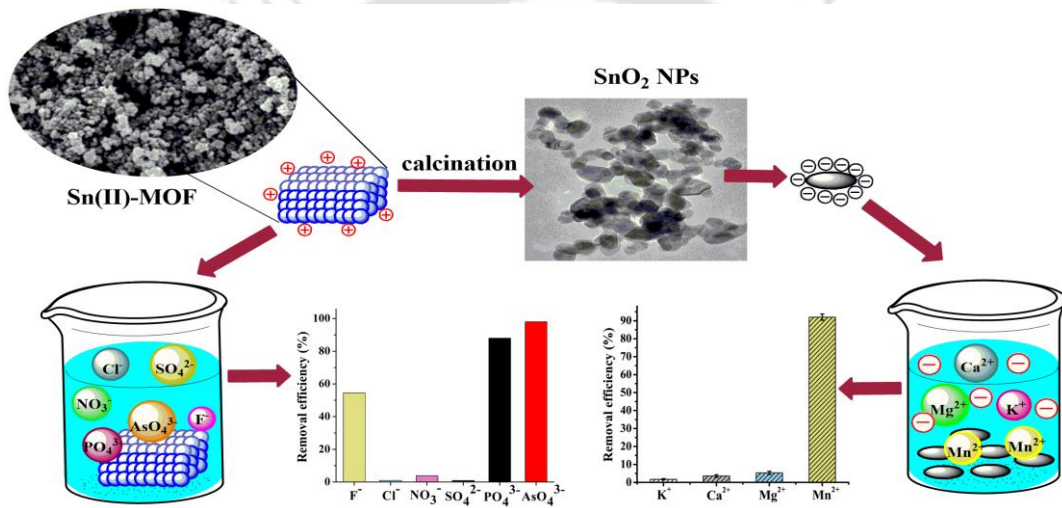
References

- [A5.1] Y. Yang, P. Shukla, S. Wang, V. Rudolph, X.M. Chen and Z. Zhu, *Rsc Adv.*, 2013, **3**, 17065-17072.
- [A5.2] L. Hou, L.N. Jia, W.J. Shi, Y.Y. Wang, B. Liu and Q.Z. Shi, *Dalton Trans.*, 2013, **42**, 3653-3659.
- [A5.3] L. Hou, W.J. Shi, Y.Y. Wang, Y. Guo, C. Jin and Q.Z. Shi, *Chem. Commun.*, 2011, **47**, 5464-5466.
- [A5.4] Z. Zhang, S. Xian, Q. Xia, H. Wang, Z. Li and J. Li, *AIChE J.*, 2013, **59**, 2195-2206.
- [A5.5] R. Kishor and A.K. Ghoshal, *Chem. Eng. J.*, 2015, **262**, 882-890.
- [A5.6] A. Dutta, M. Pramanik, A.K. Patra, M. Nandi, H. Uyama, and A. Bhaumik, *Chem. Commun.*, 2012, **48**, 6738-6740.
- [A5.7] R.K. Mah, M.W. Lui and G.K. Shimizu, *Inorg. Chem.*, 2013, **52**, 7311-7313.
- [A5.8] G.X. Wen, Y.P. Wu, W.W. Dong, J. Zhao, D.S. Li and J. Zhang, *Inorg. Chem.*, 2016, **55**, 10114-10117.
- [A5.9] X. Shen and B. Yan, *RSC Adv.*, 2015, **5**, 6752-6757.
- [A5.10] T.W. Duan, B. Yan and H. Weng, *Micropor. Mesopor. Mat.*, 2015, **217**, 196-202.
- [A5.11] C.S. Cao, H.C. Hu, H. Xu, W.Z. Qiao and B. Zhao, *Cryst. Eng. Comm.*, 2016, **18**, 4445-4451.
- [A5.12] B. Parmar, Y. Rachuri, K.K. Bisht, R. Laiya and E. Suresh, *Inorg. Chem.*, 2017, **56**, 2627-2638.
- [A5.13] J. Liu, G. Ji, J. Xiao and Z. Liu, *Inorg. Chem.*, 2017, **56**, 4197-4205.
- [A5.14] S. Li, L. Lu, M. Zhu, C. Yuan and S. Feng, *Sens. Actuators, B.*, 2018, **258**, 970-980.
- [A5.15] Z.J. Lin, H.Q. Zheng, H.Y. Zheng, L.P. Lin, Q. Xin and R. Cao, *Inorg. Chem.*, 2017, **56**, 14178-14188.



Chapter 6

Environmentally benign synthesis of Sn(II)-MOF using waste PET bottles as an organic precursor and its derivative SnO₂ NPs: Efficient adsorption of cation and anion from aqueous medium



6.1 Background and focus of the chapter

Arsenic (As) is a severely toxic metalloid element which possesses a global threat to our environment [6.1]. Natural geochemical processes and uncontrolled anthropogenic activities such as mining, burning of fossil fuels, use of crop desiccants, etc., have contributed to arsenic pollution of the groundwater [6.1], [6.2]. Prolonged exposure to arsenic-contaminated water may lead to cancers of the skin, kidney, lungs, liver, and bladder [6.3], [6.4]. Considering the risk of human health hazards due to arsenic contamination, the World Health Organization (WHO) has revised the permissible limit for arsenic in drinking water from 50 to 10 $\mu\text{g L}^{-1}$ [6.5], [6.6]. Though arsenic exists in various oxidation states, the inorganic arsenic is usually oxidized to pentavalent arsenate, As(V) in the natural water systems [6.7]. Arsenate is highly mobile in the aqueous environment and easily accumulated in the human body through the food chain. Hence, effective and efficient removal of arsenate from water is a topic of high priority.

On the other hand, phosphate is an essential nutrient for the growth of the organisms present in our ecosystem, often found in the discharge of municipal wastewater and some industrial wastewater [6.8]. However, excessive phosphate concentration in aquatic systems causes accelerated and undesirable marine growth resulting in eutrophication [6.9]. Eutrophication is detrimental to water quality and creates an imbalance in the aquatic ecology [6.10]. In this regard, the Central Pollution Control Board (CPCB), India, has limited the phosphate concentration at 5 mg L^{-1} for discharge into the inland surface water [6.11]. Therefore, a cost-effective treatment method is necessary to reduce phosphate concentration from the point sources before discharging into the water bodies.

Numerous techniques, *viz.* coagulation/flocculation, precipitation, ion-exchange, membrane separation, adsorption, electrochemical methods, bioremediation, have been investigated for the removal of the related oxyanions: arsenate and phosphate [6.4, 6.12–6.15]. Among these methods, adsorption is considered one of the most promising techniques owing to its simplicity, ease of operation, cost-effectiveness, high removal efficiency, and no sludge generation [6.16], [6.17]. Over the years, intensive studies have been carried out in a quest to develop promising adsorbent materials. Nevertheless, the adsorption capacity of conventional adsorbent materials like activated carbon [6.17], activated alumina [6.18], and zeolites [6.19] have been observed to be unsatisfactory, which actuates the need to seek new adsorbents with better adsorption performance. In recent years, the metal-organic frameworks (MOFs) have emerged as a new class of hybrid porous material composed of inorganic metal ions (metal nodes) connected to the organic linkers via a strong coordination bond [6.20]. MOFs have

attracted tremendous interest among research communities because of their tunable pore-size, high surface area, exposed active sites, customizable chemical functionality, and high thermal stability [6.21]. However, the cost of the organic linker is critical to MOF synthesis for large scale practical applications. Terephthalic acid (BDC), which is a key organic linker for MOF synthesis, can be extracted from the waste PET bottles, thereby improving the economy of the MOF synthesis process as well as reducing the environmental menace associated with the current practice of waste PET landfilling [6.22–6.24]. Recently a few research groups have reported the synthesis of MOFs (Cu, Cr, Fe, Zr, Al) utilizing waste PET materials as precursors [6.25–6.28]. Despite the successful synthesis of the value-added MOF materials, their applications in relevant research fields are still very scarce. Interestingly, Sn(II), as a cheap and readily available precursor salt for MOF synthesis, could be an attractive option because of its environmentally benign nature and good moisture stability [6.29, 6.30]. To the best of our knowledge, the utilization of such PET derived MOF materials in anions removal from the aqueous medium is not yet explored.

Manganese (Mn^{2+}), mainly exists in groundwater and surface water, is considered to be highly toxic, non-biodegradable, and probably carcinogenic [6.31]. Various anthropogenic activities and natural processes like the dissolution of minerals from rocks, soil leachate, etc., have significantly contributed to the worldwide contamination of Mn^{2+} in the groundwater [6.32]. Though manganese is an essential constituent in our biological system, its excess amount in the drinking water causes nervous system toxicity associated with Parkinsonism syndrome and endocrine disruption [6.32], [6.33]. Because of such health hazards, the WHO has restricted the permissible manganese limit in drinking water to 0.4 mg L^{-1} [6.5]. However, the Bureau of Indian Standards (BIS 2012) suggests an allowable limit of 0.3 mg L^{-1} for manganese in drinking water [6.34]. Hence, it is vital to reduce the manganese concentration in the drinking water within the acceptable limits. In literature, there are numerous available reports on heavy metal adsorption on adsorbent materials such as activated carbon, zeolites, polymers, etc. However, such sorbent materials suffer from the drawback of lower relative adsorption efficiency [6.35]. In this context, metal oxide-based nanomaterials are a promising alternative for heavy metal adsorption. Such nanomaterials possess specific features favorable for adsorption, like suitable surface sorption sites, specific surface charge, large surface area, and high adsorption capacity, particularly at nanoscale size [6.36]. Although in the past decade, several metal-oxide nanomaterials (ZnO , Fe_2O_3 , TiO_2 , etc.) have been synthesized and explored, the reports on tin oxide (SnO_2) nanoparticles for heavy metal remediation is still very limited. In this context, a MOF template pyrolysis pathway could be explored to produce metal

oxide nanoparticles with controlled morphology alleviating the problems of agglomeration, particularly associated with the conventional precipitation techniques comprising complex aqueous chemistry, which often leads to impurities [6.37]. Additionally, such nanostructured materials possess high surface area, large surface area to volume ratio, and abundant surface functional groups, facilitating enhanced adsorptive properties [6.38].

Herein, we report the solvothermal synthesis of novel water and thermostable Sn(II) MOF, (**1**) based on PET derived BDC. To the best of our knowledge, the synthesis of Sn(II)-MOF utilizing PET derived BDC is not reported earlier. Besides, the synthesis has been carried out under mild conditions and in an eco-friendly facile method avoiding the use of toxic reagents and solvent like dimethylformamide (DMF). After confirming successful synthesis using FT-IR and PXRD, the utility of **1** was examined in the removal of phosphate (PO_4^{3-}) and arsenate (AsO_4^{3-}) from the aqueous medium. Besides, the effect of interfering anions, namely fluoride (F^-), chloride (Cl^-), nitrate (NO_3^-), and sulfate (SO_4^{2-}), was investigated. Importantly, the applicability of **1** in the remediation of arsenate and phosphate from environmentally significant real water samples was explored. Moreover, the present findings elucidate the significance of surface charge reversal where the positively charged Sn(II)-MOF is converted to negatively charged SnO_2 nanoparticles via the MOF template calcination route. A batch adsorption experiment for Mn^{2+} adsorption on the synthesized SnO_2 NPs was performed, and various adsorption parameters were evaluated in detail. All in all, the present works focus on a simple integrated approach in addressing the environmental concern associated with waste PET bottles by its effective recycling and valorization into promising adsorbent material in the form of Sn(II)-MOF.

6.2 Results and Discussion

6.2.1. Characterization of PET derived BDC

The FT-IR analysis (Fig. 6.1a) of the PET derived BDC produced an identical spectrum comparable to the commercial BDC (Himedia), which confirms the successful derivation of BDC from the waste PET bottles. Also, the PXRD pattern (Fig. 6.1b) ensures the peaks of PET derived BDC positioned at $2\theta = 17^\circ$, 25° , and 27° are characteristically identical to the BDC (Himedia) [6.23]. The FESEM analysis (Fig. 6.1c, d) revealed a similar morphology of both PET derived BDC and commercially available BDC (Himedia).

6.2.2. Characterization of Sn(II)-MOF, (**1**)

In Fig. 6.2a, the FT-IR bands at 1558 cm^{-1} (C—O) and 1403 cm^{-1} (C—C) confirms the presence of carboxylate groups in the as-synthesized **1**. The band at 1635 cm^{-1} is attributed to

the C=O bonding, and that of 3450 cm^{-1} is ascribed to the stretching vibration of the hydroxyl group, indicating the presence of bound water molecules [6.9]. The series of peaks at 1287 cm^{-1} and 1100 cm^{-1} , 1017 cm^{-1} represents C—H bending vibration, and the bands at 740 cm^{-1} and 676 cm^{-1} can be assigned to the out-of-plane vibrations of the benzene ring, whereas the characteristic band at 502 cm^{-1} corresponds to the Sn—O stretching vibration [6.39], suggesting the coordination of the oxygen atom with Sn. N_2 adsorption-desorption experiment (Fig. 6.2b) was performed to determine the surface area, average pore size, and total pore volume of the as-synthesized **1**. The BET (Brunauer–Emmett–Teller) surface area was

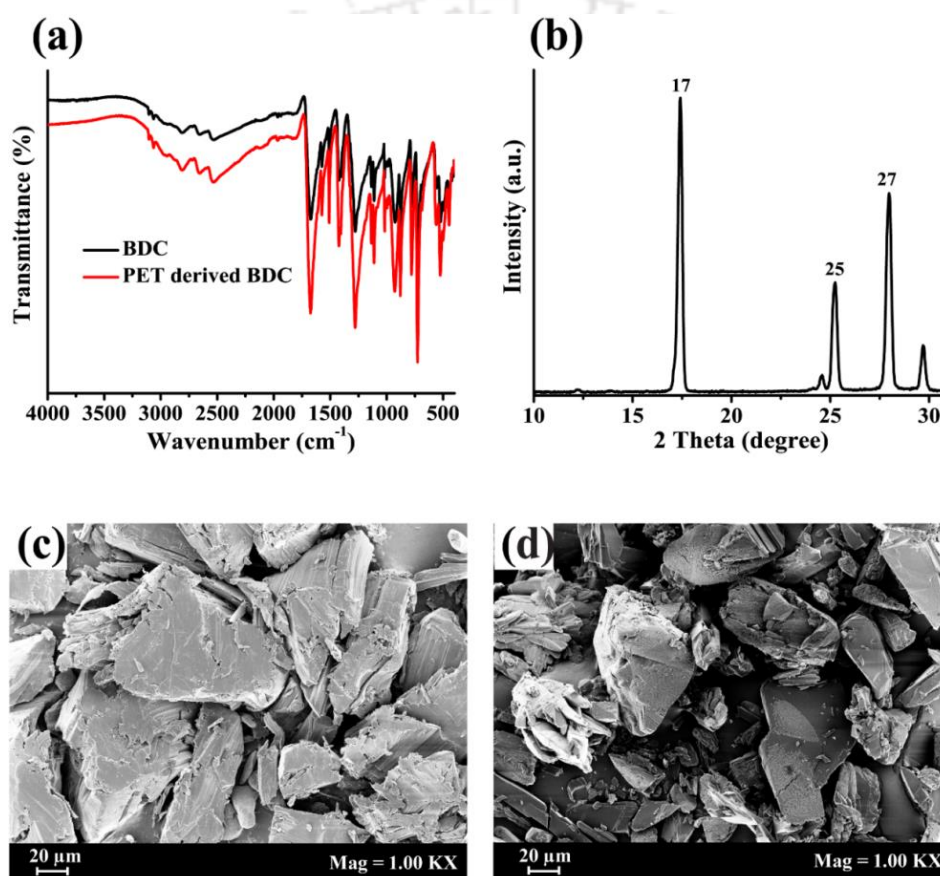


Fig. 6.1 (a) Comparative FT-IR spectrum of PET derived BDC Vs. Commercially available BDC (Himedia, India), (b) PXRD pattern of PET derived BDC, (c) FESEM image of commercially available BDC, and (d) FESEM image of PET derived BDC.

calculated to be $292\text{ m}^2\text{ g}^{-1}$ with a total pore volume of $1.08\text{ cm}^3\text{ g}^{-1}$. The synthesized **1** is observed to be mesoporous, with an average pore size of 4.3 nm. Further, the pore-size distribution curve (inset: Fig. 6.2b) reveals the pores predominantly in the mesoporous region. The TGA analysis determined the thermostability of **1** in a temperature range of 25–800 $^{\circ}\text{C}$ (Fig. 6.2c). An initial weight loss of $\sim 12\%$ was observed due to the evaporation of the adsorbed water molecules at a temperature from 25 $^{\circ}\text{C}$ to 510 $^{\circ}\text{C}$. The final weight loss of $\sim 7\%$ may be attributed to the partial degradation of **1** in the temperature range of 510 $^{\circ}\text{C}$ to 775 $^{\circ}\text{C}$.

Therefore, the TGA curve reveals high thermostability of the material up to 510 °C with a total weight loss of ~19% over the temperature range of 25 °C to 800 °C. Apart from thermostability, the aqueous stability of **1** was examined by soaking in water with an incubation period of 24 h, and thereafter the PXRD data was recorded. In Fig. 6.2d the major peaks of as-synthesized **1** corresponding to $2\theta = 31^\circ$, 45° , and 56° matched closely with the (110), (200), (211) planes of the tetragonal barium titanate. The PXRD peaks were observed to be well preserved and identical even after exposure to water, thereby confirming the structural integrity of **1**. The unchanged PXRD pattern of **1** before and after water exposure proves its water stability for prolonged period. The FESEM image of the synthesized Sn(II)-MOF depicts a spherical morphology along with some agglomeration (Fig. A6.1)

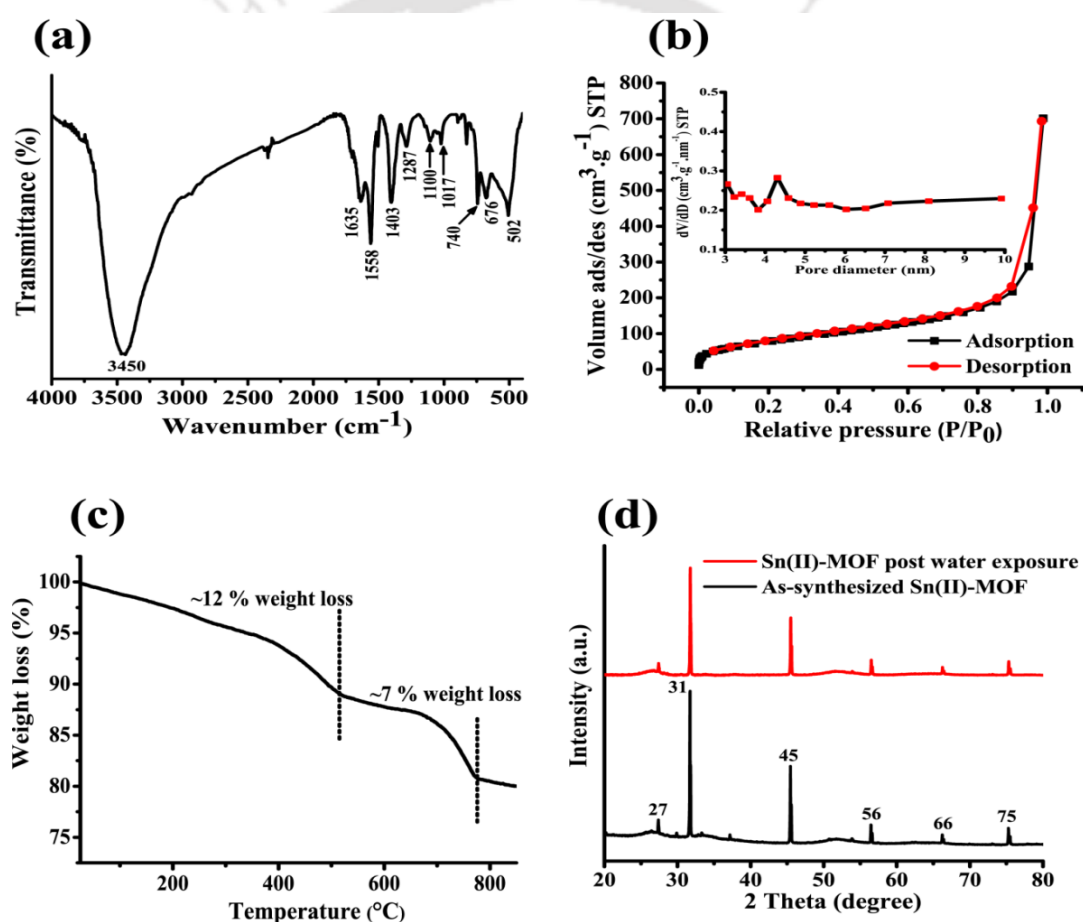


Fig. 6.2 (a) FT-IR spectrum of as-synthesized Sn(II)-MOF, (b) N₂ adsorption-desorption isotherm and pore size distribution curve (inset) of Sn(II)-MOF, (c) Thermogravimetric analysis (TGA) plot of Sn(II)-MOF, and (d) Comparison of PXRD pattern of as-synthesized Sn(II)-MOF pre and post water exposure.

6.2.3. Characterization of SnO₂ NPs

In Fig. 6.3a, the FT-IR analysis reveals the functional groups responsible for the formation of the SnO₂ NPs calcined at 600 °C using Sn(II)-MOF as the template. The broad peak at 3125

cm^{-1} indicates the presence of hydrogen-bonded $-\text{OH}$ group on the surface of SnO_2 NPs [6.40]. The peak at 1638 cm^{-1} is attributed to the $\text{C}=\text{O}$ stretching vibration, while the intense peak at 1400 cm^{-1} corresponds to the $\text{Sn}-\text{OH}$ group [6.41],[6.42]. The adjacent hydroxyl groups in SnO_2 NPs undergo condensation to form the surface bridging oxide, which is confirmed from the presence of $\text{Sn}-\text{O}-\text{Sn}$ stretching vibration mode at 675 cm^{-1} [6.40]. The obtained result suggests the formation of SnO_2 NPs with related functional groups closely matching the earlier literature reports. The PXRD pattern was recorded to elucidate the phase purity and crystalline nature of the synthesized SnO_2 NPs. In Fig. 6.3b, the diffraction peaks observed at the 2θ values correspond to (110), (101), (200), (211), (220), (310), (112), (301) planes respectively [6.43]. The PXRD pattern indicates the tetragonal crystalline structure of the SnO_2 NPs (JCPDS No. 41-1445). Moreover, no characteristic peaks for other impurities were observed from the PXRD pattern confirming the purity of the synthesized SnO_2 NPs. The nitrogen adsorption-desorption experiment depicted in Fig. 6.3c was performed to analyze the surface area and the pore size distribution (inset: Fig. 6.3c). The synthesized SnO_2 NPs displayed Type-IV isotherm with type H3 hysteresis loop, which is indicative of the mesoporous materials. The BET surface area was calculated at $\sim 40 \text{ m}^2 \text{ g}^{-1}$ with a total pore volume and average pore size of $0.2 \text{ cm}^3 \text{ g}^{-1}$ and 3 nm , respectively. The specific surface area of the synthesized SnO_2 NPs is observed to be better than the previously reported literature [6.43], [6.44, 6.45]. The FESEM (Fig. 6.3d) analysis displayed uniform spherical morphology of the synthesized SnO_2 NPs with little agglomeration. To gain insight into the morphology and size distribution of the SnO_2 NPs, FETEM microscopic analysis was performed. The FETEM image of the SnO_2 NPs represented in Fig. 6.4a reveals a tetragonal morphology. In Fig. 6.4b, the histogram particle size analysis shows a size distribution of $18\text{-}30 \text{ nm}$ with an average particle size of $\sim 25 \text{ nm}$. The selected area electron diffraction (SAED) pattern (Fig. 6.4c) displayed concentric diffraction rings, which is characteristic of the crystalline structure of SnO_2 NPs. The lattice spacing determined from the SAED pattern corresponds to the (110), (101), (211) lattice planes, respectively. The lattice planes of the SAED pattern matched closely with the tetragonal crystalline nature of the SnO_2 NPs. The high-resolution TEM (HRTEM) image (Fig. 6.4d) reveals clear lattice fringes where the spacing between adjacent lattice fringes is 0.17 nm corresponding to the (211) lattice plane [6.43]. Therefore, the FETEM analysis is consistent and in excellent agreement with the powder the PXRD data, revealing the crystalline nature of the synthesized SnO_2 NPs.

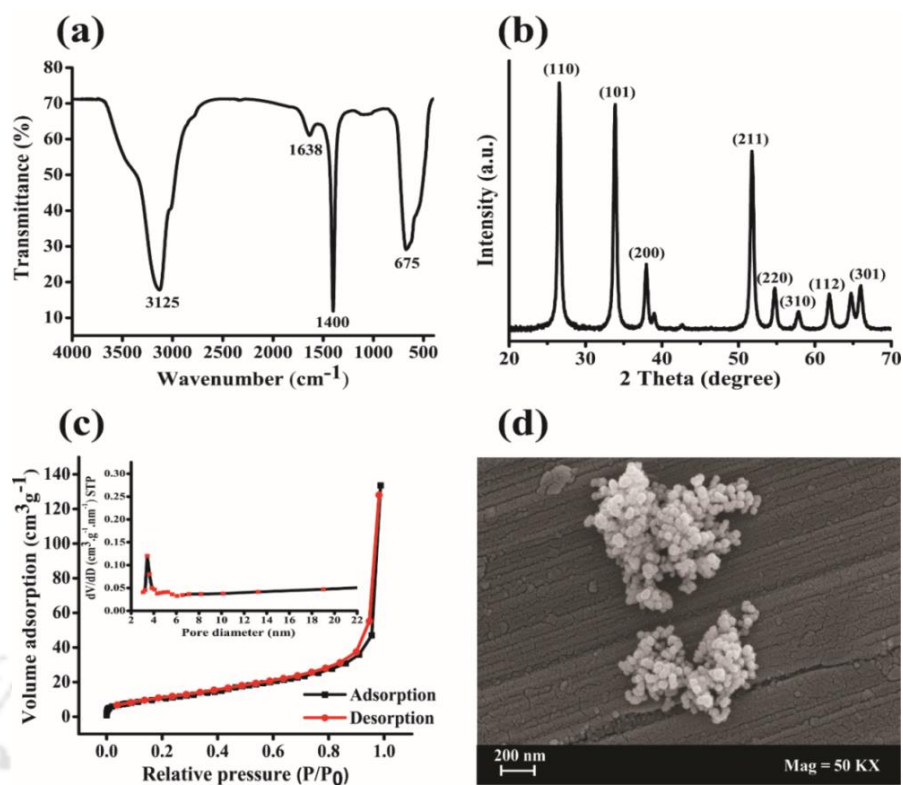


Fig. 6.3 (a) FT-IR spectrum of the SnO₂ NPs, (b) PXRD pattern of the SnO₂ NPs, (c) Nitrogen adsorption-desorption isotherm curve with pore-size distribution plot (inset), and (d) FESEM micrograph of SnO₂ NPs.

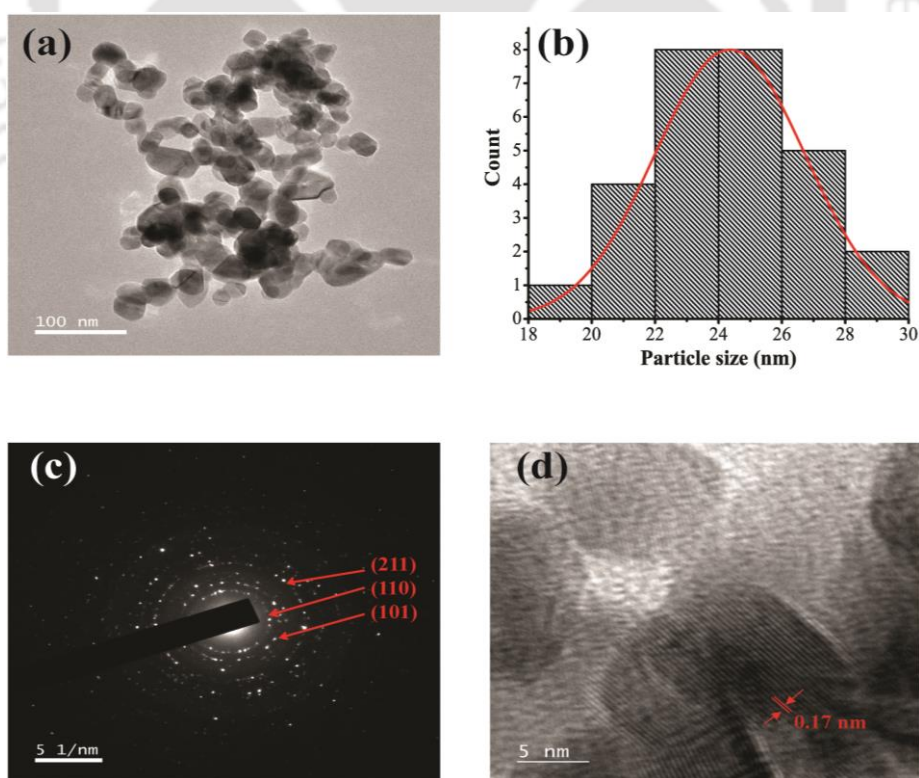


Fig. 6.4 (a) FETEM micrograph of the synthesized SnO₂ NPs, (b) Histogram particle size distribution of the synthesized SnO₂ NPs, and (c-d) SAED pattern and HRTEM image of SnO₂ NPs.

6.3 PART I: Adsorption of Arsenate and Phosphate

6.3.1. Effect of pH

The pH of the solution plays a vital role in water treatment, where it affects the mechanism of adsorption by altering the interaction between the adsorbate and adsorbent, mainly by controlling the surface charge of the adsorbent and ionization of the adsorbate in the aqueous medium [6.46]. The optimum pH for arsenate and phosphate removal was evaluated by determining the removal efficiency at varying pH (2-11). In Fig. 6.5b, it was observed that **1** displayed maximum removal efficiency of arsenate and phosphate in the acidic pH range (2-6) due to protonation of the adsorbent surface, resulting in electrostatic interaction with the negatively charged anions. In contrast, a sharp decline in removal efficiency is observed at alkaline pH (8-11) because of the deprotonation of the adsorbent surface at higher pH [6.47]. DLS (dynamic light scattering) experiment was performed to validate the pH effects on removal efficiency. The zeta potential versus pH plot is represented in Fig. A6.2. The findings of DLS analysis confirmed the point of zero charge (PZC) at 7.8, which is a critical point for the adsorption performance of the adsorbent [6.48]. Further, the study revealed a decline in zeta potential value with an increase in solution pH. At $\text{pH} < \text{PZC}$, the adsorbent surface is positively charged, which is favourable for the adsorption of negatively charged arsenate and phosphate. The findings from the DLS study highly corroborate our conclusions regarding a decline in removal efficiency at alkaline pH (8-11). At higher pH, the abundant hydroxide ions compete with the target anions for the active adsorption sites [6.49], [6.50]. Furthermore, the electrostatic repulsion between the sorbent and the adsorbate at alkaline pH is unfavorable for the adsorption process [6.48].

6.3.2. Effect of contact time

The removal rate is a critical factor for the treatment of arsenate and phosphate contaminated water, where optimization of operating conditions is vital for practical applications. Hence a time-dependent adsorption study was performed to procure the equilibrium data and elucidate the kinetics of the adsorption process. As contact time increases, the removal efficiency increased until it reached equilibrium within 60 min and 180 min for arsenate and phosphate, respectively (Fig. 6.5a). Initially, the arsenate adsorption rate was high, achieving ~ 88% removal efficiency in the first 15 min contact time and finally reaching equilibrium in 60 min (~98% removal efficiency). The high adsorption rate can be attributed to the presence of active adsorption sites on **1**. For phosphate adsorption, ~65% removal was observed in 60 min contact time while the equilibrium reached slowly in 180 min (~88% removal efficiency). The

concentration of arsenate and phosphate at equilibrium was $21 \mu\text{g L}^{-1}$ and 2.42 mg L^{-1} , respectively.

Further, to investigate the arsenate and phosphate adsorption mechanism on **1** the kinetic data were analyzed with pseudo-first-order and pseudo-second-order kinetic models. The pseudo-first-order and pseudo-second-order kinetic models [6.51] are expressed as Eq. (3) and (4), respectively:

$$\log(q_e - q_t) = \log q_e - \frac{k_1}{2.303} t \quad (2)$$

$$\frac{t}{q_t} = \frac{1}{k_2 q_e^2} + \frac{1}{q_e} t \quad (3)$$

where q_t (mg g^{-1}) is the adsorption capacity at time t (min), q_e (mg g^{-1}) is the equilibrium adsorption capacity, and k_1 , k_2 are the adsorption rate constants.

The fitted parameters obtained from the kinetic models are represented in Table 6.1. The pseudo-second-order kinetic model provides a better fitting with the experimental data, as it is evident from the high correlation coefficient ($R^2 = 0.99$) for arsenate and phosphate adsorption (Fig. 6.5c, d). Moreover, the theoretical adsorption capacity ($q_{e,\text{cal}}$) (arsenate = 0.909 mg g^{-1} , phosphate = 19.01 mg g^{-1}) calculated from the pseudo-second-order kinetic model are in good agreement with the experimental value ($q_{e,\text{cal}}$) (arsenate = 0.943 mg g^{-1} , phosphate = 17.16 mg g^{-1}), as illustrated in Table 6.1. The findings proved the suitability of the pseudo-second-order kinetic model in describing the adsorption of the target anions on Sn(II)-MOF. Therefore, the results suggest that chemisorption may be the primary rate-controlling step in arsenate and phosphate adsorption [6.9].

Furthermore, the kinetic data was analyzed with the nonlinear pseudo-second-order kinetic model [6.61].

$$q_t = \frac{k_2 q_e^2 t}{1 + k_2 q_e t} \quad (5)$$

However, the nonlinear form of the pseudo-second-order kinetic model failed to ensure a good fit with the experimental data of arsenate and phosphate adsorption. The nonlinear pseudo-second-order curve fitting and the kinetic parameters are represented in Fig.A6.3 (a,b) and

Table A6.1. The large differences between $q_{e,exp}$ and $q_{e,cal}$ values, along with a poor correlation coefficient (R^2) (Table A6.1), suggests that the experimental kinetic data cannot be explained by the nonlinear form of the pseudo-second-order model.

The application of the pseudo-first-order and pseudo-second-order kinetic models are limited in the identification of the diffusion mechanism associated with the adsorption process. Therefore, kinetic results were analyzed using the intraparticle diffusion model. The adsorption mechanism generally includes three steps, either one or any combination of which is considered to be the rate-controlling mechanism: (1) diffusion of the adsorbate from the bulk solution to the external surface of adsorbent; (2) External or internal adsorption at specific sites on the surface and the binding process (physical or chemical) influences the adsorption energy; (3) pore diffusion process or solid surface diffusion mechanism which involves the diffusion of adsorbate molecules to an adsorption site. Therefore apart from the kinetic rate laws, the intraparticle diffusion model was explored to analyze the kinetic data using the following Weber-Morris equation [6.51]

$$q_t = k_{ip}\sqrt{t} + C \quad (6)$$

where k_{ip} is an intra-particle diffusion rate constant calculated from the slope of the linear plot q_t versus $t^{0.5}$, C ($\text{mg g}^{-1} \text{min}^{-0.5}$) is the intercept related to the boundary layer/ external mass transfer effect. The model assumes that a plot of q_t versus $t^{1/2}$ gives a straight line when the intraparticle diffusion is the only rate-controlling step in the adsorption process. The Weber-Morris plots of arsenate and phosphate adsorption are depicted in Fig. A6.4 (a,b), and the kinetic parameters are enlisted in Table 6.1. It is obvious from the plots that the adsorption process of the anions is controlled by two distinct stages: the first linear portion (phase I) is attributed to the external surface adsorption, and the second linear portion (phase II) is ascribed to the gradual adsorption step [6.52]. The slope of the linear portion indicated the adsorption rate where a slower adsorption process is attributed to the lower slope [6.51]. In phase I, the sharp slope was ascribed to the rapid diffusion of the anions (arsenate/ phosphate) through the bulk solution to the readily available adsorption sites on the external surface of Sn(II)-MOF. In contrast, phase II defines a more gradual adsorption process where slow diffusion of the anions occurs from the surface sites into the inner pores [6.51]. The values of the rate constants (k_{ip1} and k_{ip2}) were calculated from the slope of the linear plots in Fig. A6.4 (a,b) and represented in Table 6.1. The k_{ip} values for arsenate were calculated at $k_{ip1} = 243.94$, $k_{ip2} = 24.26$ and for phosphate $k_{ip1} = 1.41$, $k_{ip2} = 0.75$. It is evident from the k_{ip} values that the k_{ip1} (intraparticle diffusion rate constant for phase I) is higher than k_{ip2} (intraparticle diffusion rate for constant

phase II) for both arsenate and phosphate, indicating that the initial step (phase I) is rapid followed by a slow step (phase II). It was observed that significant differences exist between the numerical values of the constant K_{ip1} , 243.94 (arsenate), and 1.41 (phosphate). However, it is noteworthy to mention here that the initial concentration of phosphate chosen for the kinetic study was 20 times more than arsenate. The selection of initial concentration was based on the literature survey and actual concentrations of arsenate and phosphate in normal water samples. Hence, K_{ip1} values of the arsenate and phosphate are not feasible to compare at different initial concentrations. All in all, a higher K_{ip1} value observed in cases of both arsenate and phosphate adsorption signifies enhanced external diffusion in phase I because of greater concentration gradient of the anions, and the findings are consistent with the earlier report [6.53].

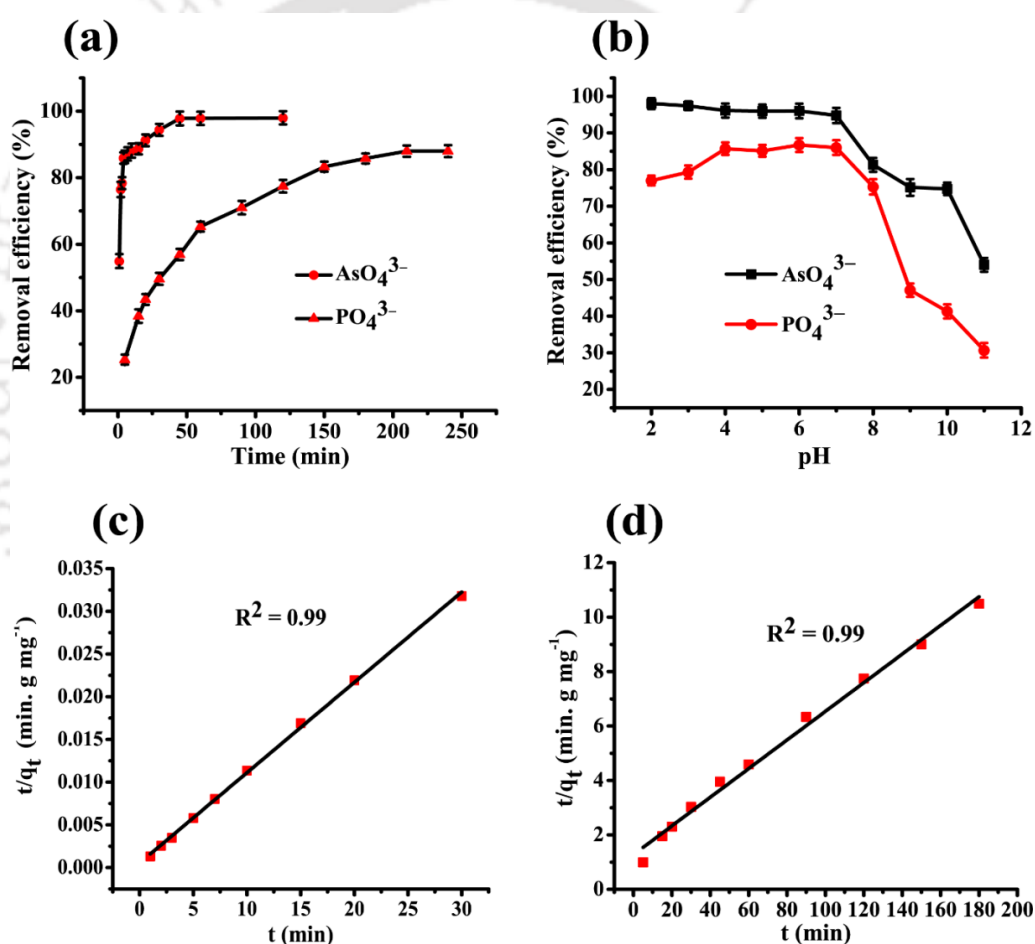


Fig. 6.5 (a) Effect of contact time on arsenate and phosphate removal efficiency of Sn(II)-MOF: volume of solution = 20 mL, dosage of sorbent = 1 g L⁻¹, pH = 7, temperature = 25 °C, initial concentration = 1 mg L⁻¹ (arsenate) and 20 mg L⁻¹ (phosphate), (b) Influence of solution pH on arsenate and phosphate removal efficiency: volume of solution = 10 mL, dosage of sorbent = 1 g L⁻¹, time = 120 min, (c, d) Pseudo-second order linear fitting for arsenate and phosphate adsorption, respectively.

Table 6.1. Pseudo-first-order, pseudo-second-order, Weber-Morris kinetic model linear fitting parameters for arsenate and phosphate adsorption on **1**.

Anions	Experimental value	Pseudo-first order model			Pseudo-second order model			Weber-Morris model			
		$q_{e,cal}$ (mg g ⁻¹)	k_1 (min ⁻¹)	R^2	$q_{e,cal}$ (mg g ⁻¹)	k_2 (g mg ⁻¹ min ⁻¹)	R^2	K_{ip1} (mg g ⁻¹ min ^{-0.5})	R^2	K_{ip2} (mg g ⁻¹ min ^{-0.5})	R^2
Arsenate	0.943	177.86	0.053	0.90	0.909	0.0024	0.99	243.94	0.99	24.26	0.95
Phosphate	17.16	13.80	0.017	0.98	19.01	0.0021	0.99	1.41	0.99	0.75	0.98

6.3.3. Adsorption isotherm

The experimental equilibrium data were analyzed with adsorption isotherm models to determine the adsorption capacity of **1**. The Langmuir and Freundlich isotherm models [6.54] were employed to fit the experimental data (Fig. 6.6a, b). The Langmuir model, which is based on monolayer adsorption, is expressed as Eq. (7).

$$\frac{C_e}{Q_e} = \frac{C_e}{q_m} + \frac{1}{K_L q_m} \quad (7)$$

where C_e is the equilibrium concentration (mg L⁻¹) of the anions, Q_e is the adsorption capacity at equilibrium (mg g⁻¹), q_m is the maximum adsorption capacity (mg g⁻¹), K_L (L mg⁻¹) is the Langmuir constant.

The Freundlich isotherm model based on multi-layers adsorption is expressed as Eq. (8).

$$\ln Q_e = \ln K_f + \frac{1}{n} \ln C_e \quad (8)$$

where K_f is the Freundlich constant (mg g⁻¹), and n denotes the favourability of sorption. The value of n varying between 1-10 suggests a favorable adsorption process.

Furthermore, the nonlinear form of the Langmuir model was adopted to analyze the adsorption data. The nonlinear Langmuir equation [6.55] is represented below.

$$q_e = \frac{q_m K_L C_e}{1 + K_L C_e} \quad (9)$$

The nonlinear Langmuir curve fitting of arsenate and phosphate adsorption on Sn(II)-MOF is shown in Fig. A6.5 (a, b), respectively, and the isotherm parameters are represented in Table A6.2.

The evaluation of error analysis was done using root-mean-square standard error (RMSE) values according to the following equation [6.55]

$$RMSE = \sqrt{\frac{1}{n} \sum_{i=1}^n (q_{e, \text{exp}} - q_{e, \text{cal}})^2} \quad (10)$$

where $q_{e, \text{cal}}$, and $q_{e, \text{exp}}$ (mg g^{-1}) are the calculated and experimental values of uptake, respectively; n is the total number of observations. The smaller values of RMSE suggest a better curve fitting [6.56], [6.55].

The calculated smaller *RMSE* values of the linear Langmuir isotherm model confirm its applicability in describing the adsorption of arsenate and phosphate. The Langmuir and Freundlich isotherm parameters are summarized in Table 6.2. As shown in Fig. 6.6 (a, b) the adsorption of arsenate and phosphate are best described by the Langmuir isotherm model with a high correlation coefficient value ($R^2 \sim 0.99$) and smaller RMSE values. Moreover, the maximum adsorption capacity (q_m) of **1** for the target anions calculated from the Langmuir isotherm model is in close agreement with the experimental value (q_{exp}) of 86 mg g^{-1} and 135 mg g^{-1} for arsenate and phosphate, respectively (Table 6.2). Hence, the result indicates the adsorption of the anions on **1** is in the form of a homogeneous monolayer as predicted by the Langmuir isotherm model [6.54], [6.57].

Apparently, the phosphate sorption was superior to that of arsenate because of the difference in the initial concentration range. Importantly, arsenate and phosphate sorption reached steady-state equilibrium within the concentration range of $0.5 - 100 \text{ mg L}^{-1}$ and $10 - 200 \text{ mg L}^{-1}$, respectively. Hence it is obvious that phosphate ions reached adsorption equilibrium at a higher initial concentration range compared to arsenate ions. This might be due to the higher partial negative charge on the oxygen atoms (-0.952) of phosphate ions as compared to oxygen atoms (-0.892) of arsenate [6.58], which contributes to the higher affinity of the phosphate ions towards the positively charged surface of **1**. Although this difference in partial negative charge is relatively small, it affects the nucleophilicity of these ions. Besides, the phosphate possesses a relatively smaller thermochemical radius (2.38 \AA) as compared to radii of arsenate (2.48 \AA) [6.59], which might facilitate a better diffusion into the pores of **1**, resulting in a higher uptake capacity. Such higher adsorption affinity of phosphate against arsenate was reported earlier by

So et al. [6.60]. Notably, **1** exhibited remarkable Langmuir maximum adsorption capacity (q_m) of arsenate and phosphate, comparable with the earlier literature (Table A6.3). The uptake capacity of the synthesized Sn(II)-MOF was found to be better than most other reported MOF-based adsorbents. Unlike most other reported MOF-based adsorbents, the synthesized Sn(II)-MOF performed better at natural pH without the need for any pH adjustments. Besides, Sn(II) metal ions possess low toxicity [6.61] in contrast to most of the metal ions (Al, Zr) used in the previously reported MOF synthesis.

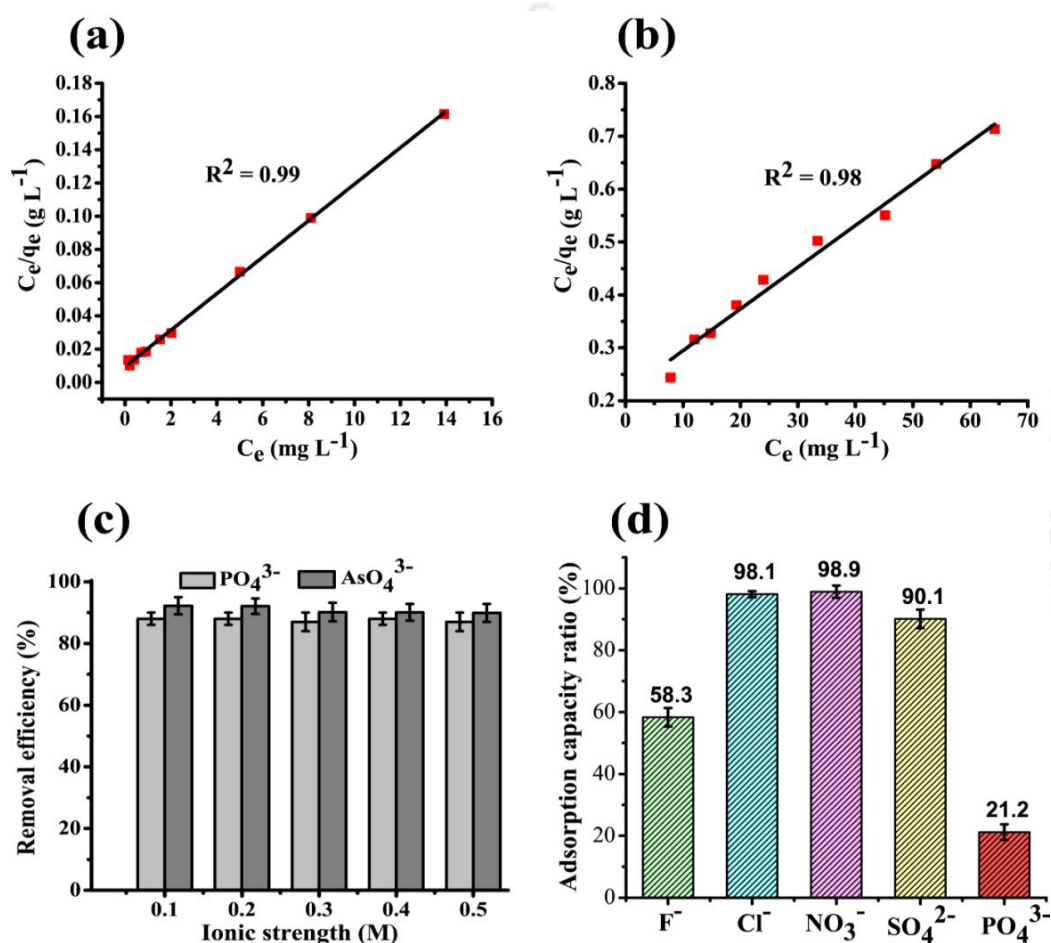


Fig. 6.6 (a,b) Langmuir isotherm model for adsorption of arsenate and phosphate respectively, (c) Effect of ionic strength of solution on arsenate and phosphate removal efficiency: ionic strength range = 0.1 M – 0.5 M, time = 120 min, dosage of sorbent = 1 g L⁻¹, volume = 10 ml, temperature = 25 °C and (d) Effect of interfering anions on the adsorption capacity of Sn(II)-MOF towards arsenate: volume = 10 ml, dosage of sorbent = 1 g L⁻¹, concentration of arsenate = 1 mg L⁻¹, concentration of co-existing anions = 10 mg L⁻¹, time = 120 min, temperature = 25 °C.

Table 6.2. Langmuir and Freundlich isotherm parameters for arsenate and phosphate adsorption on 1.

Adsorption Isotherm	Isotherm parameters	Values			
		Arsenate	RMSE	Phosphate	RMSE
Langmuir	$q_m(\text{mg g}^{-1})$	90.90	0.001	126.58	0.018
	$K_L (\text{L mg}^{-1})$	1.15		0.036	
	R^2	0.99		0.98	
Freundlich	n	2.83	0.250	1.39	0.097
	$K_F (\text{mg g}^{-1})(\text{L mg}^{-1})^{1/n}$	38.86		6.52	
	R^2	0.85		0.95	

6.3.4. Thermodynamic study

The thermodynamic feasibility of the adsorption process was determined by calculating the thermodynamic parameters. The batch adsorption experiment was performed at three different temperatures (293 K, 303 K, and 313 K) at an adsorbent dose of 1 g L^{-1} and an initial analyte concentration of 1 mg L^{-1} (arsenate) and 20 mg L^{-1} (phosphate), respectively. The following equations Eqs. (11) - (13) [6.62] were employed to determine the thermodynamic parameters.

$$\Delta G^\circ = -RT \ln(k_e) \quad (11)$$

$$\ln(K_e) = \frac{\Delta S^\circ}{R} - \frac{\Delta H^\circ}{RT} \quad (12)$$

$$K_e = (1000 \times K_L \times M_{\text{ads}} \times [\text{ads}]_0) / g_e \quad (13)$$

where K_e is the equilibrium constant (dimensionless), 1000 is the correction factor, if the Langmuir constant, K_L , is given in the unit of L mg^{-1} , to convert the unit of Langmuir constant (K_L) from L mg^{-1} to L g^{-1} ; M_{ads} is the molar mass of the adsorbate in g mol^{-1} ; $[\text{ads}]_0$ is the standard concentration of the adsorbate, in mol L^{-1} , which is typically equal to 1 and g_e is the dimensionless activity coefficient of the solution, which for very dilute solutions is also equal to 1; ΔG° is the Gibbs free energy change, ΔH° is the change in enthalpy, ΔS° is the change in entropy, R is the gas constant ($8.314 \text{ J mol}^{-1} \text{ K}^{-1}$). The values of ΔH° and ΔS° were calculated from the slope and intercept of the $\ln(K_e)$ versus $1/T$ plot (VantHoff's plot) using Eq. (12), and the ΔG° values were calculated using Eq. (11).

The thermodynamic analysis of arsenate adsorption on Sn(II)-MOF is represented in Fig. A6.6, and the thermodynamic parameters are tabulated in Table A6.4. The negative ΔG° values

imply the feasibility and spontaneity of the adsorption process at high temperatures. The decrease in ΔG° values (-29.18 to -34.06 kJ mol⁻¹) with the increase in temperature (293 to 313K) suggests the positive effect of higher temperature on the adsorption process [6.62]. Besides, the positive ΔH° (42.25 kJ mol⁻¹) reveals the endothermic nature of the adsorption process, and an increase in temperature favours adsorption [6.51]. The positive value of ΔS° (243.62 J mol⁻¹ K⁻¹) indicated the affinity of Sn(II)-MOF towards arsenate ions and exhibited a high degree of randomness at the solid-liquid interface [6.63]. Besides, the adsorption phenomenon is entropy-driven as reflected from the positive ΔS° value [6.64].

6.3.5. Effect of ionic strength and co-existing anions

In Fig. 6c, the effect of ionic strength (0.1 M-0.5 M) of the medium on the arsenate and phosphate removal efficiency was evaluated. The arsenate and phosphate removal efficiency was observed to be stable at ~91% and ~88%, respectively, in the increasing ionic concentration range of 0.1 M- 0.5 M. It was found that an increase in ionic strength of the medium had a negligible effect on the removal efficiency of the target anions thereby establishing the practical applicability of **1** in treating high ionic strength actual water samples. The presence of co-existing anions is another critical factor that influences the removal capacity of adsorbent material in actual practice. Various co-existing anions like F⁻, Cl⁻, NO₃⁻, PO₄³⁻ and SO₄²⁻ were selected to examine their influence on the adsorption capacity of **1** (Fig. 6.6d). The anions *viz.* F⁻, Cl⁻, NO₃⁻, and SO₄²⁻ displayed no notable influence on the adsorption capacity of **1**. Interestingly, only 21.2% of the maximum adsorption capacity was maintained in the presence of PO₄³⁻, reflecting the significant inhibitory effect of PO₄³⁻ due to its similar nature with AsO₄³⁻ and their competition for the adsorption sites. However, the adverse impact of PO₄³⁻ would be minimal since the mass ratio of PO₄³⁻ to AsO₄³⁻ is much lower in natural water systems [6.1]. The inhibitory effect of the co-existing anions on the AsO₄³⁻ adsorption capacity of **1** followed the order: PO₄³⁻ > F⁻ > SO₄²⁻ > Cl⁻ > NO₃⁻. The observed results are in agreement with the earlier reported literature on arsenate adsorption. To conclude, the co-existing anions, especially PO₄³⁻, exhibit some negative impact on the removal capacity of **1**, whereas the other anions failed to display any remarkable influence on adsorption performance.

6.3.6. Proposed adsorption mechanism

After AsO₄³⁻ and PO₄³⁻ adsorption on **1**, some new FT-IR peaks at 2955 cm⁻¹ and 2930 cm⁻¹ are assigned to the —CH and —CH₂ stretching vibration mode (Fig. A6.7). The appearance of

these peaks confirms the presence of BDC moiety adhered to the surface of **1** after AsO_4^{3-} and PO_4^{3-} adsorption. The interaction of AsO_4^{3-} with **1** in the aqueous medium might release the BDC molecules in a small amount. However, the consistent PXRD pattern after AsO_4^{3-} adsorption confirms the well preserved structural integrity of **1** (Fig. A6.8). In the FT-IR spectrum of as-synthesized **1**, the peak at 740 cm^{-1} signifies the C—H bending vibrations of the benzene. After the adsorption of AsO_4^{3-} and PO_4^{3-} , the peak at 740 cm^{-1} merged to form an intense sharp peak at 670 cm^{-1} attributed to the stretching vibration mode of As-O-Sn and P-O-Sn, indicating that AsO_4^{3-} and PO_4^{3-} are coordinated with **1**. Moreover, the IR spectroscopic study in Fig. A6.2 reveals a red-shift of $\sim 39\text{ nm}$ in conjunction with intensification and broadening of the absorption band at 3412 nm . Such an observation suggests the formation of hydrogen bonds where the surface hydroxyl groups play a significant role in the adsorption of arsenate and phosphate [6.65].

Furthermore, to elucidate the adsorption mechanism DLS (dynamic light scattering) study was performed, and the analyzed parameters are summarised in Table 6.3. The zeta potential of as-synthesized **1** decreased from $+23.6\text{ mV}$ to -0.2 mV and $+0.4\text{ mV}$ after AsO_4^{3-} and PO_4^{3-} adsorption, respectively. A decline in zeta potential can be attributed to the balancing of the positive surface charge on **1** due to electrostatic interaction with the negatively charged anions [6.66], [6.67]. Moreover, the particle size (hydrodynamic diameter) of **1** increased from 670 nm to 2020 nm and 1923 nm after arsenate and phosphate adsorption, respectively. The increment in particle size might be due to the aggregation of the particles to a larger size after adsorption. Hence, the DLS analysis proves that the adsorption of arsenate and phosphate on Sn(II)-MOF is predominantly driven by electrostatic interaction. Also, the FESEM-EDX image captured after adsorption and the elemental analysis data confirms the presence of adsorbed arsenic (As) on Sn(II)-MOF (Fig. A6.9, A6.10).

Table 6.3 DLS summary of pristine Sn(II)-MOF and Sn(II)-MOF after arsenate and phosphate adsorption.

Parameters	Pristine Sn(II)-MOF	Arsenate adsorbed Sn(II)-MOF	Phosphate adsorbed Sn(II)-MOF
Particle size (nm)	670	2020	1923
Zeta potential (mV)	+23.60	+0.40	-0.20

6.3.7. Real water application

The feasibility of **1** as an adsorbent material for treating actual water samples was examined. For this purpose, laboratory tap water, lake water (IIT Guwahati, Kamrup district) were collected, filtered, and spiked with 1 mg L^{-1} of AsO_4^{3-} . The AsO_4^{3-} adsorption was carried out at an adsorbent dose of 1.5 g L^{-1} with an equilibration time of 1 h. After the reaction, the filtered samples were analyzed by AAS, where the equilibrium AsO_4^{3-} concentration (C_e) was measured to be $8.4 \text{ } \mu\text{g L}^{-1}$ (deionized water), $9.3 \text{ } \mu\text{g L}^{-1}$ (tap water), and $17 \text{ } \mu\text{g L}^{-1}$ (lake water) (Fig. 6.7). The equilibrium AsO_4^{3-} concentration in tap water and lake water is comparable with the control deionized (DI) water. It is observed that the adsorbent maintained $\sim 99\%$ removal efficiency while removing AsO_4^{3-} from tap water and deionized water, respectively. Further, the results suggest that co-existing anions in lake water had a negligible effect on the AsO_4^{3-} removal efficiency ($\sim 98\%$). Therefore, **1** displayed excellent arsenate removal performance by reducing the AsO_4^{3-} concentration within the WHO acceptable limit for drinking water.

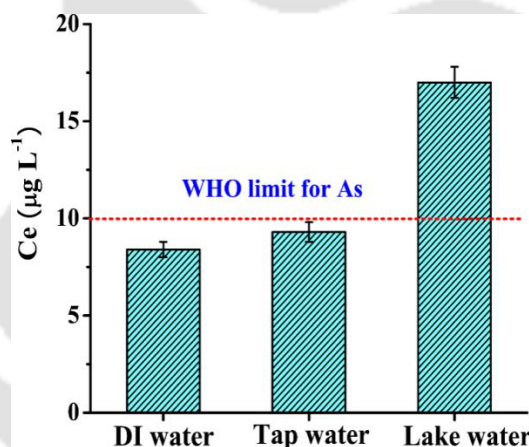


Fig. 6.7 Equilibrium concentration (C_e) of arsenate in DI water, tap water, and lake water after adsorption on Sn(II)-MOF: volume of solution = 20 mL, dosage of sorbent = 1.5 g L^{-1} , initial concentration of arsenate = 1 mg L^{-1} , time = 60 min, temperature = $25 \text{ }^\circ\text{C}$.

6.4 PART-II: Adsorption of Manganese

6.4.1. Influence of pH

The solution pH plays an important role in controlling the adsorption of the metal ions on the adsorbent surface. The adsorption of manganese (Mn^{2+}) was examined in the pH range 2-10 at an optimized SnO_2 NP dose of 0.6 g L^{-1} and an initial Mn^{2+} concentration of 5 mg L^{-1} . Fig. 6.8a depicts a double Y-axis plot representing the removal efficiency and zeta potential as a function of solution pH. The isoelectric point (pH_{PZC}) of the synthesized SnO_2 NPs in the aqueous medium is measured at pH 4. It was observed that the removal efficiency increases

with an increase in solution pH and reaches a plateau level in the pH range 6-10. The adsorbent surface is highly protonated at lower pH (2-3), as reflected from the positive zeta potential values of the zeta potential Vs. pH plot (Fig. 6.8a). Hence, there is an electrostatic repulsion between the protonated surface of SnO₂ NPs and the Mn²⁺ cation resulting in lower removal efficiency (<10%) in pH range 2-3. Also, in such lower pH, the H⁺ ions compete with the Mn²⁺ ions for the active adsorption sites resulting in lower removal efficiency [6.44]. At pH ≥ 4, the adsorbent surface is deprotonated, as suggested by the negative zeta potential values in the pH range 5-10. The negative charges developed on the adsorbent surface in the pH range (5-10) favored electrostatic interaction with the Mn²⁺ cations, resulting in better adsorption performance and higher removal efficiency (~99%). Owing to the high removal efficiency in the pH range 5-7 and to rule out the possibility of precipitation of Mn²⁺ as metal hydroxides at alkaline pH, further adsorption experiments were performed at natural pH.

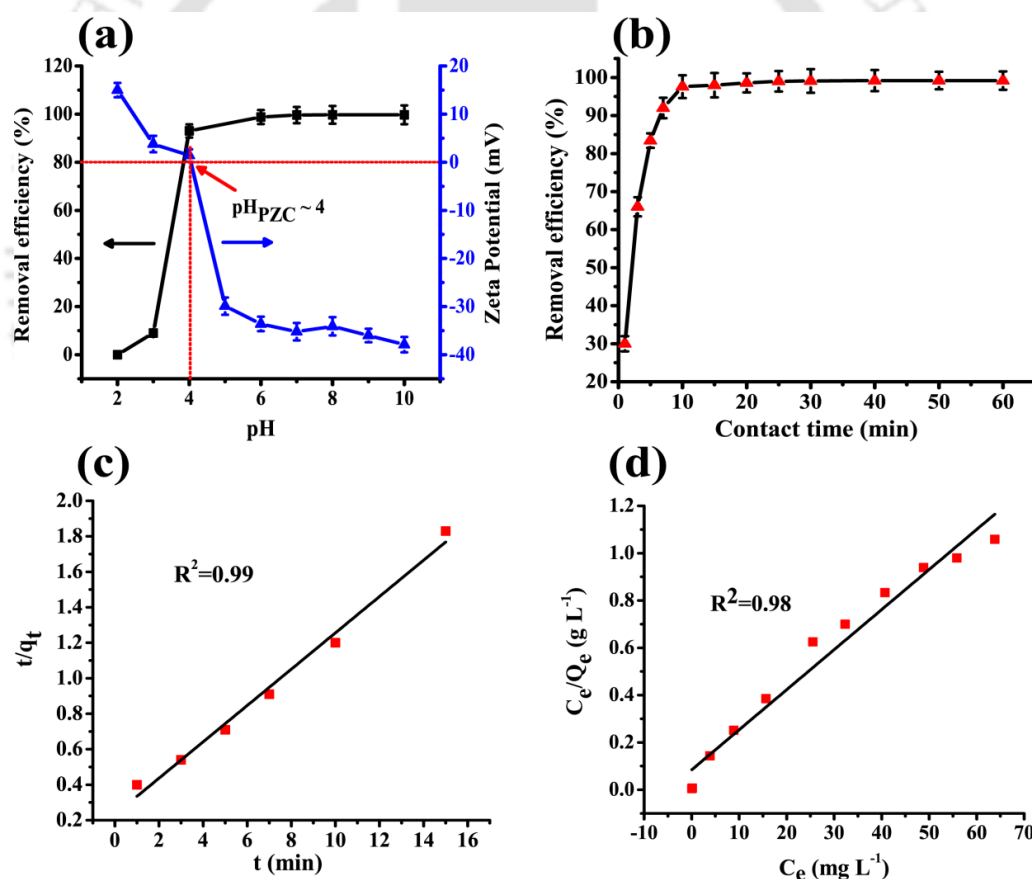


Fig. 6.8 (a) Plot of removal efficiency and zeta potential as a function of solution pH, (b) Effect of contact time on the Mn²⁺ removal efficiency of SnO₂ NPs: initial concentration = 5 mg L⁻¹, volume of solution = 20 mL, dosage of adsorbent = 0.6 g L⁻¹, time = 60 min, temperature = 25 °C, (c) Pseudo-second-order kinetic model linear fitting, and (d) Langmuir isotherm model for Mn²⁺ adsorption on SnO₂ NPs.

6.4.2. Effect of contact time

The effect of contact time on the Mn^{2+} removal efficiency was investigated with an initial Mn^{2+} concentration of 5 mg L^{-1} and an adsorbent dose of 0.6 g L^{-1} at $25 \text{ }^\circ\text{C}$. In Fig. 6.8b, it was observed that the adsorption reached equilibrium very fast at 15 min with $\sim 98\%$ Mn^{2+} removal efficiency, which might be due to the availability of more active adsorption sites in the initial phase of the adsorption process. The final equilibrium concentration of Mn^{2+} was obtained at 0.04 mg L^{-1} at 30 min.

The experimental data were analyzed with pseudo-first-order and pseudo-second-order kinetic models, as illustrated earlier in Eqs. (3) and (4), respectively. In Fig. 6.8c, the pseudo-second-order kinetic model provided good fitting with the experimental data as indicated by the high correlation coefficient value ($R^2 = 0.99$). The calculated adsorption capacity ($q_{e,\text{cal}} = 9.7 \text{ mg g}^{-1}$) from the pseudo-second-order kinetic model is in close agreement with the experimental adsorption capacity ($q_{e,\text{exp}} = 8.16 \text{ mg g}^{-1}$). Therefore, it is possible to conclude that the adsorption of Mn^{2+} ions on SnO_2 NPs followed the pseudo-second-order kinetic model.

In contrast, the apparent lack of linear behavior, as suggested by the poor correlation coefficient value ($R^2 = 0.92$), makes the pseudo-first-order kinetic model unsuitable to describe the kinetic profile of Mn^{2+} adsorption. The evaluated kinetic parameters from the pseudo-first-order and pseudo-second-order kinetic models and their corresponding correlation coefficient values are represented in Table A6.4. Besides, the kinetic data of manganese adsorption was also analyzed with nonlinear pseudo-second-order rate law. However, the nonlinear model was unable to produce a good fit with the experimental kinetic data. The nonlinear pseudo-second-order curve fitting and the kinetic parameters calculated using Eq. (5) are represented in Fig. A6.11 and Table A6.5.

Moreover, the kinetic data analysis using the intraparticle diffusion model (Eq. 6) confirmed that intraparticle diffusion is not the only rate-limiting step controlling the adsorption process, and the external diffusions influence the adsorption process. The multi-linearity observed in Fig. A6.12 indicates the adsorption of Mn^{2+} on SnO_2 is essentially a two-phase process. Phase I involves the rapid diffusion of the manganese ions from the bulk solution to the surface active sites on the SnO_2 NPs. Contrastingly in phase II, slow diffusion of the manganese ions occurs from the surface sites to the inner pores of the SnO_2 NPs adsorbent. Notably, the high value of intraparticle diffusion rate constant in phase I ($K_{\text{ip1}} = 3.18$) (Table A6.4) illustrates the faster diffusion of the Mn^{2+} ions from the bulk phase during the initial stage of the adsorption process. The small value of the intraparticle diffusion rate constant in phase II ($K_{\text{ip2}} = 0.06$) is attributed to the slow diffusion of the arsenate ions until the equilibrium is attained [6.68].

Table 6.4. Pseudo-first-order, pseudo-second-order, and Weber-Morris linear fitting kinetic parameters for Mn²⁺ adsorption on SnO₂ NPs.

Experimental value	Pseudo-first-order model			Pseudo-second-order model			Weber-Morris model			
	q _{e,cal} (mg g ⁻¹)	k ₁ (min ⁻¹)	R ²	q _{e,cal} (mg g ⁻¹)	k ₂ (g mg ⁻¹ min ⁻¹)	R ²	K _{ip1} (mg g ⁻¹ min ^{-0.5})	R ²	K _{ip2} (mg g ⁻¹ min ^{-0.5})	R ²
8.16	6.13	0.30	0.92	9.70	0.04	0.99	3.18	0.96	0.06	0.98

6.4.3. Adsorption isotherm

The experimental data of Mn²⁺ adsorption was analyzed with Langmuir and Freundlich isotherm models to elucidate the nature of adsorption and to determine the maximum adsorption capacity. The experiment was performed in the initial manganese concentration range of 5-100 mg L⁻¹ while keeping the adsorbent dose and contact time constant at 0.6 g L⁻¹ and 60 min, respectively. The Eqs. (4) and (5) were used to compute the Langmuir and Freundlich adsorption isotherm parameters (Table 6.5). The manganese adsorption on SnO₂ NPs is best described by the Langmuir isotherm model (R²= 0.98), suggesting manganese adsorption in the form of a monolayer. The maximum adsorption capacity (q_m= 52.63 mg g⁻¹) of SnO₂ NPs calculated from the Langmuir isotherm model is in close agreement with the experimental adsorption capacity (q_{exp}= 56.96 mg g⁻¹). Besides, the analysis of the adsorption data with the nonlinear Langmuir isotherm model (Eq. 9) failed to ensure a good fit as indicated by the higher RSME values (Fig. S13, Table A6.6) compared to the linear Langmuir model (Table 6.5). The SnO₂ NPs displayed relatively better adsorption performance than most other contemporary adsorbents used in Mn²⁺ removal (Table A6.7). Moreover, the facile synthesis method devoid of any extraneous chemicals and optimum uptake capacity at natural pH establishes the obtained SnO₂ as a potent sorbent for Mn²⁺ removal.

Table 6.5. Langmuir and Freundlich isotherm parameters for Mn²⁺ adsorption on SnO₂ NPs

Adsorption Isotherm	Isotherm parameters	Values	RMSE
Langmuir	q _m (mg g ⁻¹)	52.63	0.15
	K _L (L g ⁻¹)	2.78	
	R ²	0.98	
Freundlich	n	4.2	1.60
	K _f (mg g ⁻¹)	3.75	
	R ²	0.96	

6.4.4. Thermodynamic study

The thermodynamic parameters for Mn^{2+} adsorption on SnO_2 NPs were calculated according to the Eqs. (11-13), previously discussed. The temperature effect on manganese adsorption was evaluated at three different temperatures 298 K, 308 K, and 318 K, respectively. The VantHoff's plot (Fig. A6.14) and the derived thermodynamic parameters are presented in Table A6.8. A positive ΔH° value ($32.55 \text{ kJ mol}^{-1}$) revealed the endothermic nature of the adsorption process [6.44]. Besides, an increase in temperature resulted in an increased K_e of Mn^{2+} ions adsorption (Table A6.8), which reflects the adsorption process was endothermic [6.63]. The positive value of ΔS° ($188.81 \text{ J mol}^{-1} \text{ K}^{-1}$) indicates increasing randomness at the solid-liquid interface with an increase in temperature. The more negative ΔG° values -23.73 , -25.55 , and $-27.51 \text{ kJ mol}^{-1}$ at increasing temperature (298 K – 318 K) demonstrate the spontaneity and thermodynamic feasibility of the manganese adsorption process at higher temperatures [6.63].

6.4.5. Interfering cation effect and real water application

Several common cations like ammonium (NH_4^+), sodium (Na^+), potassium (K^+), calcium (Ca^{2+}), and magnesium (Mg^{2+}) can co-exist in natural water, and they might compete with the target cation Mn^{2+} for the active adsorption sites present in the SnO_2 NPs. Hence an adsorption study was conducted in an aqueous medium comprising a mixture of the common cations (20 mg L^{-1} each) and Mn^{2+} ion (5 mg L^{-1}). The SnO_2 NPs displayed remarkable selectivity in the removal of Mn^{2+} ions among all other cations. The SnO_2 NPs displayed significant Mn^{2+} removal efficiency ($\sim 92\%$), while the removal efficiency of K^+ ($\sim 1.7\%$), Ca^{2+} (3.5%), Mg^{2+} (5%) is found to be negligible (Fig. 6.9a). Also, no removal of NH_4^+ and Na^+ was observed from the cation mixture (data not shown). Hence, SnO_2 NPs demonstrated promising anti-interference activity against some common co-existing cations commonly present in natural water.

The feasibility of the synthesized SnO_2 NPs in treating real water samples contaminated with Mn^{2+} was also explored. Water samples from various water sources *viz.* laboratory tap water, lake water (IIT Guwahati, Kamrup district), and Brahmaputra river water were collected and filtered. A batch adsorption study was performed at room temperature with each of the water samples spiked with 5 mg L^{-1} Mn^{2+} ion, and 0.6 g L^{-1} SnO_2 NPs were added to it. After the reaction, the equilibrium Mn^{2+} concentration (C_e) was analyzed by AAS and measured to be well within the WHO permissible limit for drinking water (Fig. 6.9b). Therefore, the synthesized SnO_2 NPs exhibited excellent Mn^{2+} removal potential while treating environmentally significant water samples.

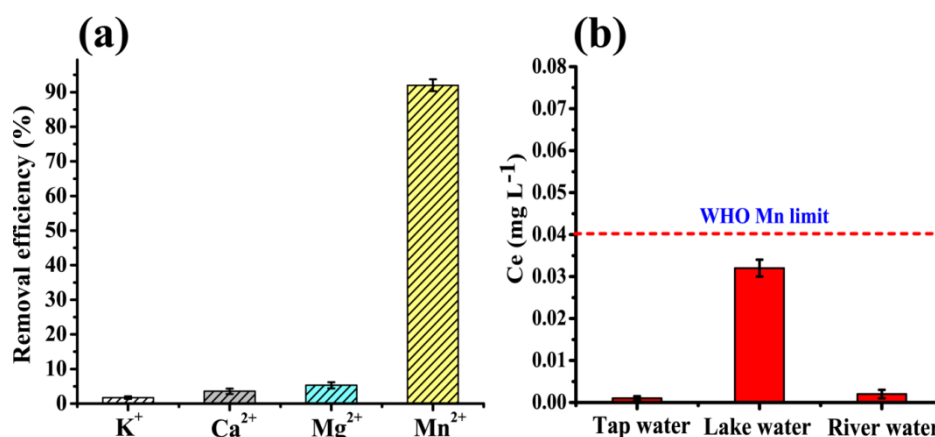


Fig. 6.9 (a) Manganese (Mn^{2+}) removal efficiency of SnO_2 NPs in the presence of other interfering cations: initial Mn^{2+} concentration = 5 mg L^{-1} , concentration of other anions = 20 mg L^{-1} , volume of solution = 10 mL , dosage of adsorbent = 0.6 g L^{-1} , temperature = $25 \text{ }^\circ\text{C}$, time = 30 min and (b) Equilibrium concentration (C_e) of Mn^{2+} in the tap water, lake water and river water aqueous after adsorption on SnO_2 NPs: initial concentration = 5 mg L^{-1} , dosage of sorbent = 0.6 g L^{-1} , volume = 20 mL , time = 30 min , temperature = $25 \text{ }^\circ\text{C}$.

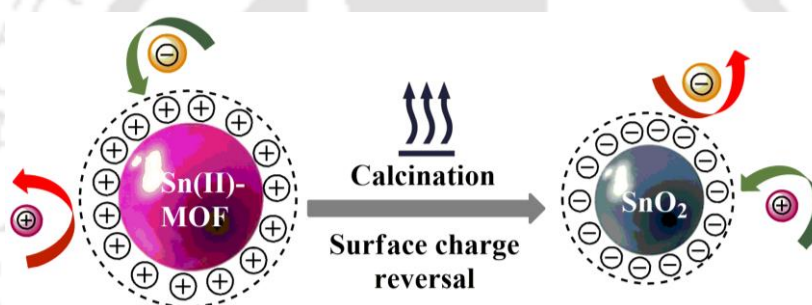
6.4.6. Proposed adsorption mechanism

Electronegativity plays a vital role in controlling the adsorption of metal cations. The more electronegative the metal ions, the stronger is the covalent bond formation with the oxygen atoms located on the surface of the metal oxide nanoparticles [6.44]. According to Pauling's scale of electronegativity, the Mn^{2+} ion is more electronegative compared to the other co-existing cations, namely K^+ , Na^+ , Ca^{2+} , and Mg^{2+} , which results in the higher binding affinity of Mn^{2+} with the SnO_2 NPs. The surface of the SnO_2 NPs in the aqueous medium is attached to the hydroxyl groups, which can change their form according to the solution pH [6.44]. The surface charge of the SnO_2 NPs controls the adsorption/ desorption of the cations, and this occurs due to the ionization of the surface hydroxyl groups depending on the solution pH. In our study, the adsorption was performed at the natural pH (pH~ 6.7) of water, where Mn^{2+} ions are generally present in its divalent ionic form. Therefore, there is a strong electrostatic interaction between the negatively charged surface of the SnO_2 NPs and the Mn^{2+} ion. The DLS analysis (Table 6.6) further validates our observation where zeta potential value of SnO_2 NPs decreased from -36.8 mV to -6.2 mV after Mn^{2+} adsorption due to balancing of surface charge during electrostatic interaction [6.69]. Also, the SnO_2 NPs aggregated into larger size particles after the adsorption of Mn^{2+} ions. Besides, the FESEM-EDX elemental analysis (Fig. A6.15, A6.16) confirms the presence of Mn^{2+} after adsorption on the SnO_2 NPs. The thermal decomposition of the organic building block in Sn(II)-MOF resulted in the reversal of the surface charge. Scheme 6.2 illustrates the role of surface charge reversal wherein the positively and negatively charged surfaces of Sn(II)-MOF and SnO_2 NPs, respectively, electrostatically

interacts with the anions and cations present in an aqueous medium and facilitates their subsequent separation. The presence of abundant oxygen and surface hydroxyl groups contributed to the negative charge of the SnO₂ NPs in the aqueous environment. Therefore, the SnO₂ NPs displayed significant affinity towards the positively charged Mn²⁺ ions, whereas no affinity was observed towards the anions.

Table 6.6. DLS summary of SnO₂ NPs before and after Mn²⁺ adsorption from aqueous medium.

Sample	Zeta potential (mV)	Particle size (nm)
Pristine SnO ₂	-36.80	212
SnO ₂ after Mn ²⁺ adsorption	-6.20	360



Scheme 6.2. Pictorial representation of the role of surface charge reversal in adsorption of anion and cation by Sn(II)-MOF and SnO₂ nanoparticles, respectively.

6.4.7. Regeneration studies

Regeneration is a critical factor that allows the reuse of the sorbent material and improves the overall process economics. The arsenate/ phosphate loaded adsorbent was stirred in 10 mL solution of 0.01 M NaOH for 120 min at a stirring rate of 300 rpm. The obtained adsorbent was washed with distilled water, vacuum dried at 100 °C, and used for further adsorption cycles. In Fig. A6.17, it was observed that Sn(II)-MOF retained 78- 86% and 76- 81% of its original uptake capacity towards arsenate and phosphate, respectively, after the first cycle. Notably, a low loss of uptake capacity after the fourth regeneration cycle demonstrates the potential reusability of the reported Sn(II)-MOF adsorbent. Likewise, the Mn²⁺ loaded SnO₂ NPs were regenerated using 0.01 N HCl as the regeneration medium. The SnO₂ NPs retained 71 - 78% of their natural uptake capacity after the fourth regeneration cycle (Fig. A6.18), demonstrating no significant loss of its adsorption potential. Therefore, the findings confirm the good multi-cyclic reusability of the synthesized sorbents following a simple regeneration process.

6.5 Conclusion

In this work, Sn(II)-MOF was successfully synthesized using waste PET bottles as a source of the organic linker. The material displayed remarkable hydrolytic and thermal stability. The potential of the Sn(II)-MOF as an adsorbent material in the remediation of arsenate and phosphate from an aqueous solution was explored. The synthesized Sn(II)-MOF displayed high arsenate and phosphate removal efficiency of ~98% and ~88%, respectively. The adsorption kinetics followed the pseudo-second-order kinetic model, and the Langmuir isotherm model best describes the adsorption profile of the anions. The maximum adsorption capacity (q_m) of the synthesized Sn(II)-MOF towards arsenate and phosphate are calculated at 90.90 mg g⁻¹ and 126.58 mg g⁻¹, respectively, which agrees well with our experimental adsorption capacity (q_{exp}). Furthermore, the adsorbent exhibited excellent arsenate removal performance from actual water samples reducing the arsenate concentration up to the WHO permissible limit for drinking water. The results revealed electrostatic attraction and hydrogen bonding as the prominent mechanism of adsorption of the target anions. Besides, the excellent adsorption performance of Sn(II)-MOF can be attributed to the large available surface area and high pore volume, which provides numerous active sites for adsorption. Moreover, the interfering anions had minimal effect on the adsorption capacity of Sn(II)-MOF. Besides, an integrated approach was followed where Sn(II)-MOF could be utilized as a precursor for the synthesis of the SnO₂ NPs (~ 25 nm) via the MOF-template calcination route. The present finding also elucidates the role of surface charge reversal in excellent Mn(II) ions removal efficiency from the aqueous medium where electrostatic interaction plays the driving force for adsorption. The highly crystalline SnO₂ NPs displayed excellent colloidal stability, as reflected from the zeta potential value of -36.8 mV. The SnO₂ NPs demonstrated a large manganese adsorption capacity of 52.63 mg g⁻¹ with negligible interference from the co-existing cations. Notably, the SnO₂ NPs proved their potential utility in the remediation of Mn²⁺ ions from the actual water samples. Overall, in this work, we have reported an economically viable approach for recycling waste PET bottles by converting them into value-added adsorbent material, which can be utilized in potential decontamination of water. Further, in the future, this work can be easily scaled up for bulk synthesis of adsorbent material and explored in other environmental allied fields.

References

- [6.1] J. Li, Y. N. Wu, Z. Li, B. Zhang, M. Zhu, X. Hu, Y. Zhang and F. Li, *J. Phys. Chem. C*, 2014, 118, 27382–27387.
- [6.2] D. Chakraborti, M. M. Rahman, B. Das, M. Murrill, S. Dey, S. Chandra Mukherjee, R. K. Dhar, B. K. Biswas, U. K. Chowdhury, S. Roy, S. Sorif, M. Selim, M. Rahman and Q. Quamruzzaman, *Water Res.*, 2010, 44, 5789–5802.
- [6.3] H. J. Sun, B. Rathinasabapathi, B. Wu, J. Luo, L. P. Pu and L. Q. Ma, *Environ. Int.*, 2014, 69, 148–158.
- [6.4] R. Singh, S. Singh, P. Parihar, V. P. Singh and S. M. Prasad, *Ecotoxicol. Environ. Saf.*, 2015, 112, 247–270.
- [6.5] R. W. Herschy, *Encycl. Earth Sci. Ser.*, 2012, 876–883.
- [6.6] WHO, *Geneva World Heal. Organ.*, 1998, 2, 123–152.
- [6.7] C. Wang, X. Liu, J. P. Chen and K. Li, *Sci. Rep.*, 2015, 5, 1–10.
- [6.8] Y. Xu, Y. Dai, J. Zhou, Z. P. Xu, G. Qian and G. Q. M. Lu, *J. Mater. Chem.*, 2010, 20, 4684–4691.
- [6.9] K. Y. Koh, C. Wang and J. P. Chen, *J. Colloid Interface Sci.*, 2019, 543, 343–351.
- [6.10] K. Y. A. Lin, S. Y. Chen and A. P. Jochems, *Mater. Chem. Phys.*, 2015, 160, 168–176.
- [6.11] M. Sawal, *Environ. Rules*, 1986, 2, 545–560.
- [6.12] G. Ungureanu, S. Santos, R. Boaventura and C. Botelho, *J. Environ. Manage.*, 2015, 151, 326–342.
- [6.13] S. Y. Yoon, C. G. Lee, J. A. Park, J. H. Kim, S. B. Kim, S. H. Lee and J. W. Choi, *Chem. Eng. J.*, 2014, 236, 341–347.
- [6.14] W. Zeng, A. Wang, J. Zhang, L. Zhang and Y. Peng, *Chem. Eng. J.*, 2016, 296, 234–242.
- [6.15] Z. Wang, M. Xing, W. Fang and D. Wu, *Appl. Surf. Sci.*, 2016, 366, 67–77.
- [6.16] T. A. Kurniawan, G. Y. S. Chan, W. hung Lo and S. Babel, *Sci. Total Environ.*, 2006, 366, 409–426.
- [6.17] D. Mohan and C. U. Pittman, *J. Hazard. Mater.*, 2007, 142, 1–53.
- [6.18] T. F. Lin and J. K. Wu, *Water Res.*, 2001, 35, 2049–2057.
- [6.19] Y. H. Xu, T. Nakajima and A. Ohki, *J. Hazard. Mater.*, 2002, 92, 275–287.
- [6.20] J. L. C. Rowsell and O. M. Yaghi, 2004, 73, 3–14.
- [6.21] B. J. Abu Tarboush, A. Chouman, A. Jonderian, M. Ahmad, M. Hmadeh and M. Al-Ghoul, *ACS Appl. Nano Mater.*, 2018, 1, 3283–3292.
- [6.22] V. D. Doan, T. L. Do, T. M. T. Ho, V. T. Le and H. T. Nguyen, *Sep. Sci. Technol.*, 2020, 55, 444–455.
- [6.23] J. Ren, X. Dyosiba, N. M. Musyoka, H. W. Langmi, B. C. North, M. Mathe and M. S. Onyango, *Int. J. Hydrogen Energy*, 2016, 41, 18141–18146.
- [6.24] Manju, P. Kumar Roy, A. Ramanan and C. Rajagopal, *Mater. Lett.*, 2013, 106, 390–392.
- [6.25] W. P. R. Deleu, I. Stassen, D. Jonckheere, R. Ameloot and D. E. De Vos, *J. Mater. Chem. A*, 2016, 4, 9519–9525.
- [6.26] K. W. Jung, J. H. Kim and J. W. Choi, *Compos. Part B Eng.*, 2020, 187, 107867.
- [6.27] L. Zhou, S. Wang, Y. Chen and C. Serre, *Microporous Mesoporous Mater.*, 2019, 290, 109674.
- [6.28] X. Dyosiba, J. Ren, N. M. Musyoka, H. W. Langmi, M. Mathe and M. S. Onyango, *Sustain. Mater. Technol.*, 2016, 10, 10–13.
- [6.29] T. Nguyen-Tran, N. M. An, K. D. Nguyen, T. D. Nguyen and T. T. Truong, *J. Sci. Adv. Mater. Devices*, 2018, 3, 471–477.
- [6.30] N. Azizi, S. Dezfili and M. M. Hahsemi, *Sci. World J.*, , DOI:10.1100/2012/908702.
- [6.31] M. H. Qomi, H. Eisazadeh, M. Hosseini and H. A. Namaghi, *Synth. Met.*, 2014, 194, 153–159.
- [6.32] R. Thapa, S. Gupta, H. Kaur and R. Mandal, *Model. Earth Syst. Environ.*, 2018, 4, 161–174.
- [6.33] E. Grygo-Szymanko, A. Tobiasz and S. Walas, *TrAC - Trends Anal. Chem.*, 2016, 80, 112–124.
- [6.34] BIS, *Bur. Indian Stand. Indian Stand. Drink. Water Specif.*, 2012, 2, 11.
- [6.35] J. Yang, B. Hou, J. Wang, B. Tian, J. Bi, N. Wang, X. Li and X. Huang, *Nanomaterials*, , DOI:10.3390/nano9030424.
- [6.36] M. N. Subramaniam, P. S. Goh, W. J. Lau and A. F. Ismail, *Nanomaterials*, , DOI:10.3390/nano9040625.
- [6.37] Y. Song, X. Li, L. Sun and L. Wang, *RSC Adv.*, 2015, 5, 7267–7279.
- [6.38] K. Y. Kumar, H. B. Muralidhara, Y. A. Nayaka, J. Balasubramanyam and H. Hanumanthappa, *Powder Technol.*, 2013, 246, 125–136.
- [6.39] X. Zhou, S. Chen, J. Yang, T. Bai, Y. Ren and H. Tian, *ACS Appl. Mater. Interfaces*, 2017, 9, 14309–14318.
- [6.40] A. Bhattacharjee and M. Ahmaruzzaman, *Mater. Lett.*, 2015, 157, 260–264.
- [6.41] A. Bhattacharjee, M. Ahmaruzzaman, T. B. Devi and J. Nath, *Journal Photochem. Photobiol. A Chem.*, 2016, 325, 116–124.
- [6.42] G. Elango, S. Manoj, S. Santhosh, S. Muthuraja and S. Mohana, *Spectrochim. ACTA PART A Mol. Biomol. Spectrosc.*, 2015, 145, 176–180.
- [6.43] Z. Sun, C. Cao and W. Q. Han, *RSC Adv.*, 2015, 5, 72825–72829.
- [6.44] K. Y. Kumar, T. N. V. Raj, S. Archana, S. B. B. Prasad, S. Olivera and H. B. Muralidhara, *J. Water*

- Process Eng.*, 2016, 13, 44–52.
- [6.45] X. Lu, F. Luo, Q. Xiong, H. Chi, H. Qin and Z. Ji, *Mater. Res. Bull.*, 2018, 99, 45–51.
- [6.46] B. Heibati, M. Ghoochani, A. B. Albadarin, A. Mesdaghinia, A. S. H. Makhlof, M. Asif, A. Maity, I. Tyagi, S. Agarwal and V. K. Gupta, *J. Mol. Liq.*, 2016, 213, 339–344.
- [6.47] S. Chatterjee, N. Guha, S. Krishnan, A. K. Singh, P. Mathur and D. K. Rai, *Sci. Rep.*, 2020, 10, 1–11.
- [6.48] M. Nehra, N. Dilbaghi, N. K. Singhal, A. A. Hassan, K. H. Kim and S. Kumar, *Environ. Res.*, 2019, 169, 229–236.
- [6.49] D. Tang and G. Zhang, *Chem. Eng. J.*, 2016, 283, 721–729.
- [6.50] L. Wang, Y. Xie, J. Yang, X. Zhu, Q. Hu, X. Li and Z. Liu, *RSC Adv.*, 2017, 7, 54291–54305.
- [6.51] N. Zhang, X. Yang, X. Yu, Y. Jia, J. Wang, L. Kong, Z. Jin, B. Sun, T. Luo and J. Liu, *Chem. Eng. J.*, 2014, 252, 220–229.
- [6.52] S. Karaca, A. Gürses, M. Ejder and M. Açıkyıldız, *J. Colloid Interface Sci.*, 2004, 277, 257–263.
- [6.53] S. Hou, Y. N. Wu, L. Feng, W. Chen, Y. Wang, C. Morlay and F. Li, *Dalt. Trans.*, 2018, 47, 2222–2231.
- [6.54] K. Y. A. Lin, Y. T. Liu and S. Y. Chen, *J. Colloid Interface Sci.*, 2016, 461, 79–87.
- [6.55] S. Pal, S. Mukherjee and S. Ghosh, *Environ. Earth Sci.*, 2014, 71, 1593–1603.
- [6.56] N. You, Y. X. Song, H. R. Wang, L. X. Kang, H. T. Fan and H. Yao, *J. Chem. Eng. Data*, 2019, 64, 1378–1384.
- [6.57] H. Cai, L. Xu, G. Chen, C. Peng, F. Ke, Z. Liu, D. Li, Z. Zhang and X. Wan, *Appl. Surf. Sci.*, 2016, 375, 74–84.
- [6.58] M. M. Kish and R. E. Viola, *Inorg. Chem.*, 1999, 38, 818–820.
- [6.59] D. S. Tawfik and R. E. Viola, *Biochemistry*, 2011, 50, 1128–1134.
- [6.60] H. U. Sjø, D. Postma, R. Jakobsen and F. Larsen, *Geochim. Cosmochim. Acta*, 2012, 93, 1–13.
- [6.61] H. Rüdél, *Ecotoxicol. Environ. Saf.*, 2003, 56, 180–189.
- [6.62] Y. X. Song, S. Chen, N. You, H. T. Fan and L. N. Sun, *Chemosphere*, 2020, 255, 126917.
- [6.63] H. T. Fan, W. Sun, B. Jiang, Q. J. Wang, D. W. Li, C. C. Huang, K. J. Wang, Z. G. Zhang and W. X. Li, *Chem. Eng. J.*, 2016, 286, 128–138.
- [6.64] H. T. Fan, Q. Tang, Y. Sun, Z. G. Zhang and W. X. Li, *Chem. Eng. J.*, 2014, 258, 146–156.
- [6.65] J. Li, Y. N. Wu, Z. Li, M. Zhu and F. Li, *Water Sci. Technol.*, 2014, 70, 1391–1397.
- [6.66] G. Zhang, Z. He and W. Xu, *Chem. Eng. J.*, 2012, 183, 315–324.
- [6.67] M. G. Sujana and S. Anand, *Desalination*, 2011, 267, 222–227.
- [6.68] H. Atallah, M. Elcheikh Mahmoud, A. Jelle, A. Lough and M. Hmadeh, *Dalt. Trans.*, 2018, 47, 799–806.
- [6.69] P. Qin, Y. Yang, X. Zhang, J. Niu, H. Yang, S. Tian, J. Zhu and M. Lu, *Nanomaterials*, , DOI:10.3390/nano8010004.

Annexure 6

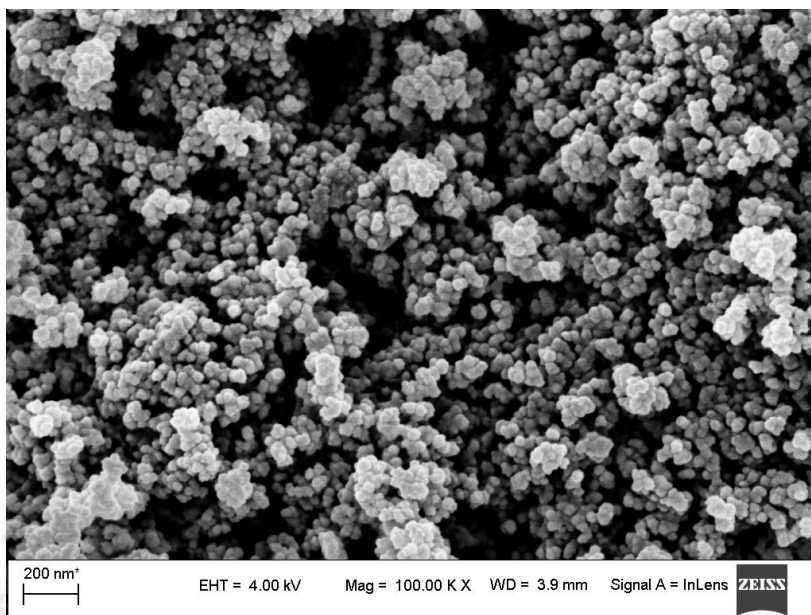


Fig. A6.1. FESEM image of the synthesized Sn(II)-MOF

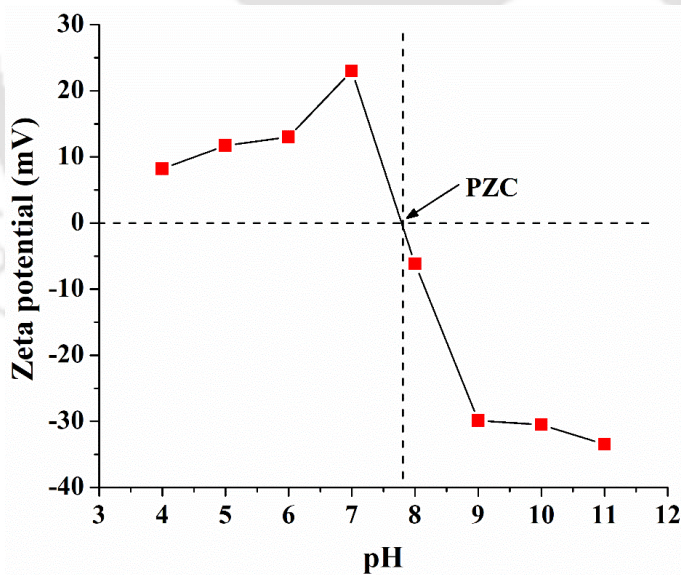


Fig. A6.2. Zeta potential of Sn(II)-MOF as a function of solution pH

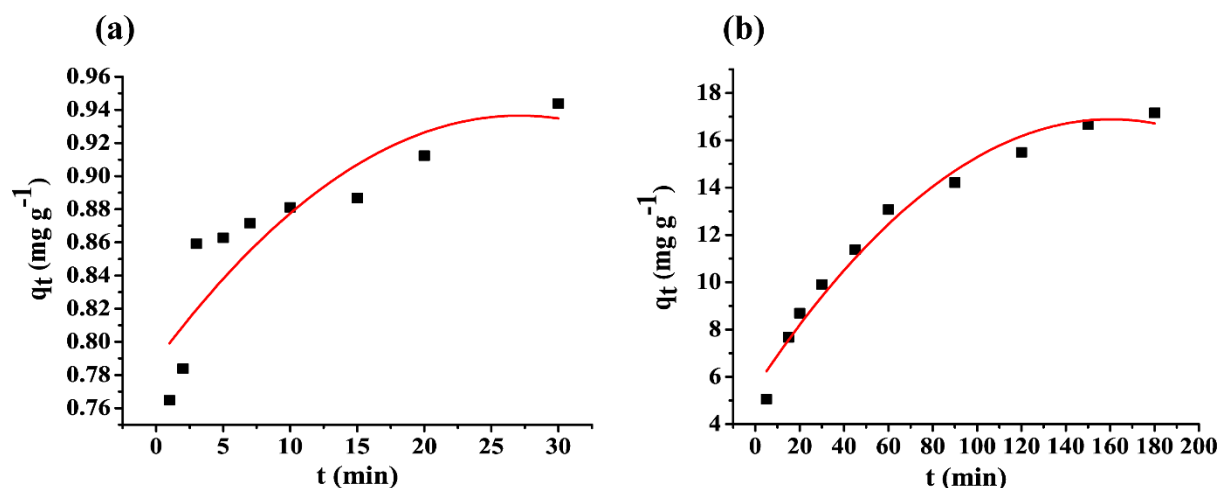


Fig. A6.3. Nonlinear pseudo-second-order curve fitting for (a) arsenate and (b) phosphate adsorption on Sn(II)-MOF.

Table A6.1. Nonlinear pseudo-second-order model fitting parameters for arsenate and phosphate adsorption on Sn(II)-MOF

Anions	Nonlinear pseudo-second order model			
	$q_{e,exp}$ (mg g^{-1})	$q_{e,cal}$ (mg g^{-1})	k_2 ($\text{g mg}^{-1} \text{min}^{-1}$)	R^2
Arsenate	0.943	0.291	4.30	0.74
Phosphate	17.16	4.23	0.005	0.97

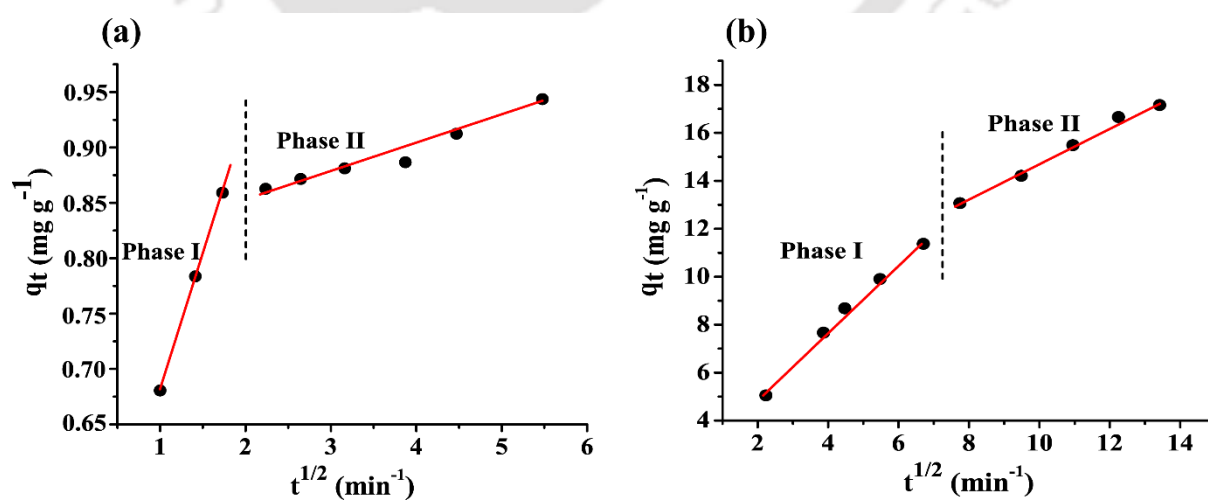


Fig. A6.4. Intra-particle diffusion model for the kinetic data of (a) arsenate and (b) phosphate adsorption onto the Sn(II)-MOF.

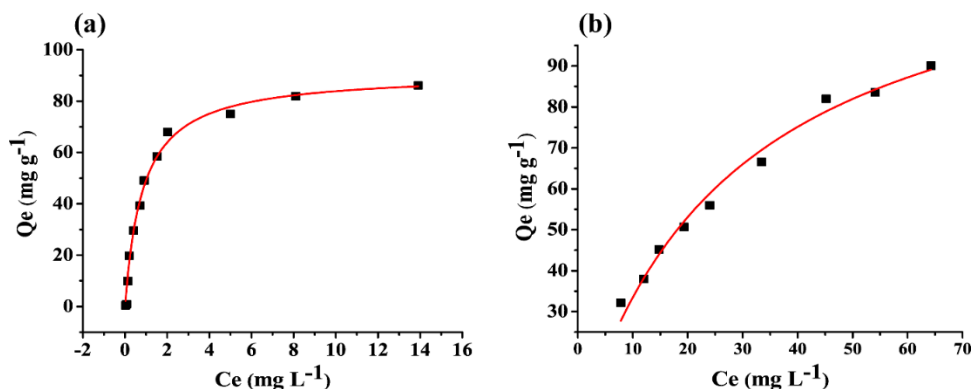


Fig. A6.5. Nonlinear Langmuir isotherm model curve fitting for (a) arsenate and (b) phosphate adsorption on Sn(II)-MOF

Table A6.2. Nonlinear Langmuir isotherm model fitting parameters for arsenate and phosphate adsorption on Sn(II)-MOF

Adsorption Isotherm	Isotherm parameters	Values			
		Arsenate	RMSE	Phosphate	RMSE
Langmuir	q_m (mg g ⁻¹)	90.96	2.11	128.43	2.43
	K_L (L mg ⁻¹)	1.18		0.035	
	R^2	0.98		0.98	

Table A6.3. Comparison of adsorption capacity of different MOF-based adsorbents.

Adsorbent	pH	Anion	Maximum adsorption capacity (mg g ⁻¹)	Ref.
ZIF-8	7	Arsenate	60	[1]
MIL-53(Fe)	5		21.27	[2]
MIL-53(Al)	8		105.6	[3]
UiO-66	7		147.7	[4]
MIL-88B(Fe)	6		156.7	[5]
Fe-BTC	4		12.3	[6]
UiO-66	9.2		68.21	[7]
Sn(II)-MOF	7.0		90.90	This work
La-based MOF	6.3		Phosphate	142.01
UiO-66-NH ₂	–	91.97		[9]
PEI impregnated UiO-66 Fe-based	5.0	224.10		[10]
MIL-101(Fe)	–	107.70		[11]
GdBDC	7.0	166.86		[12]
MIL-100(Fe)	4.0	93.55		[13]
Sn(II)-MOF	7.0	126.58		This work

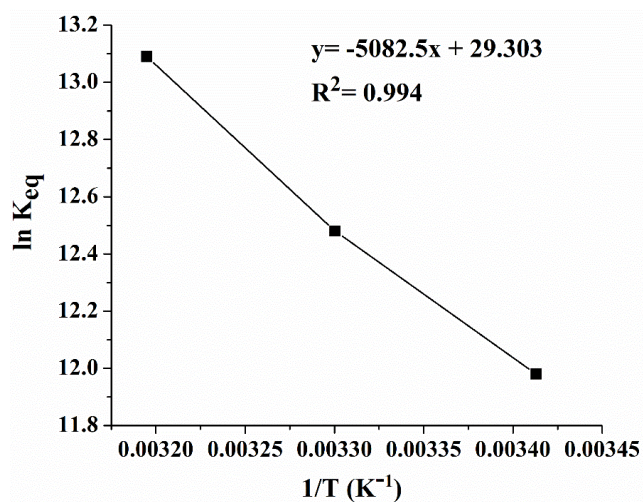


Fig. A6.6. VantHoff's plot for arsenate adsorption on Sn(II)-MOF adsorbent

Table A6.4. Thermodynamic parameters for arsenate adsorption on Sn(II)-MOF adsorbent

Temperature (K)	K _{eq}	ln K _{eq}	ΔH° (kJ mol ⁻¹)	ΔS° (J mol ⁻¹ K ⁻¹)	ΔG° (kJ mol ⁻¹)
293	1,59,756.850	11.98	42.25	243.62	-29.18
303	2,65,057.452	12.48			-31.43
313	4,86,216.500	13.09			-34.06

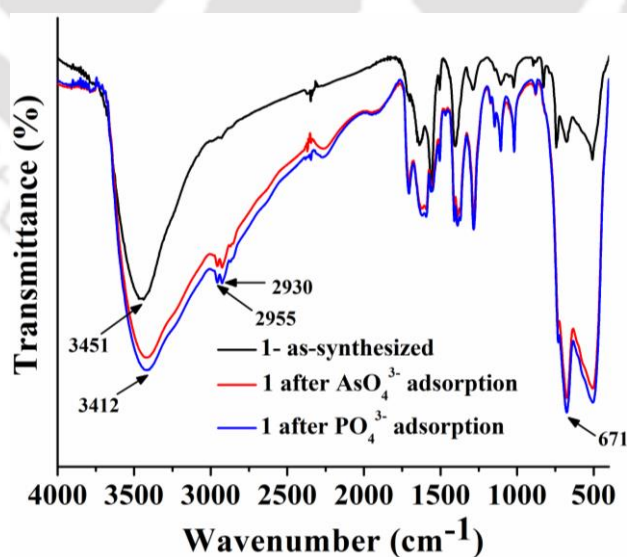


Fig. A6.7. FT-IR spectrum of as-synthesized **1** before and after AsO₄³⁻, and PO₄³⁻ adsorption.

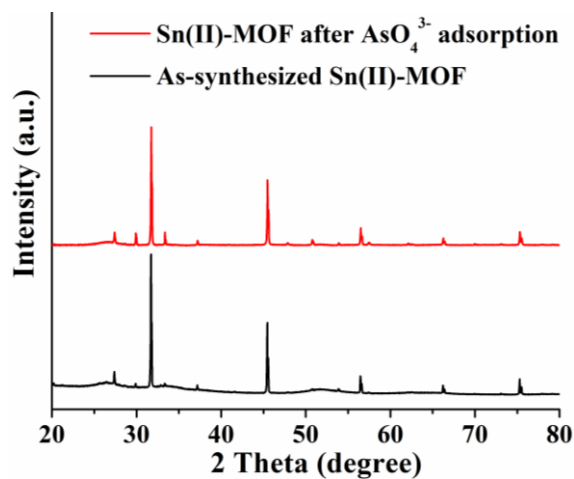


Fig. A6.8. PXRD comparison of as-synthesized Sn(II)-MOF and Sn(II)-MOF after AsO₄³⁻ adsorption from the aqueous medium.

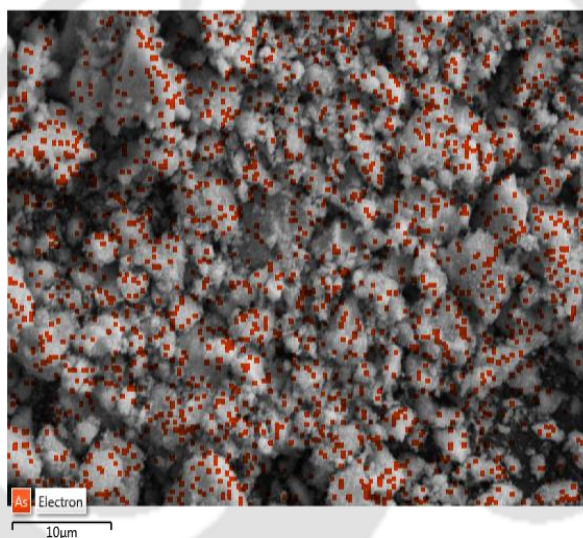


Fig. A6.9. FESEM-EDX mapping of As(V) (red dots) adsorbed on Sn(II)-MOF.

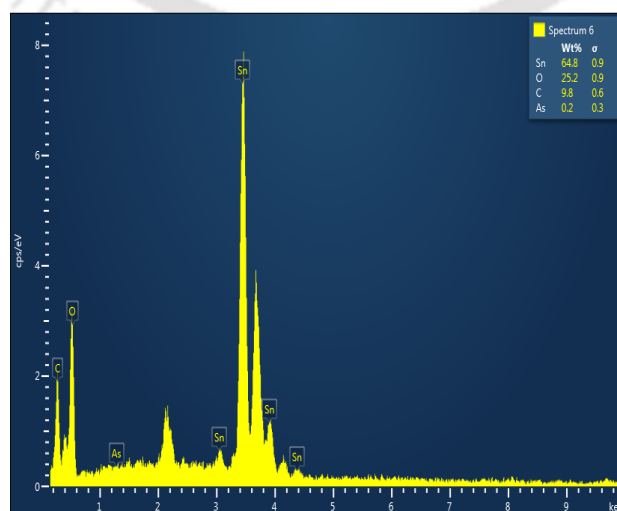


Fig. A6.10. EDX spectrum for elemental analysis after As(V) adsorption on Sn(II)-MOF.

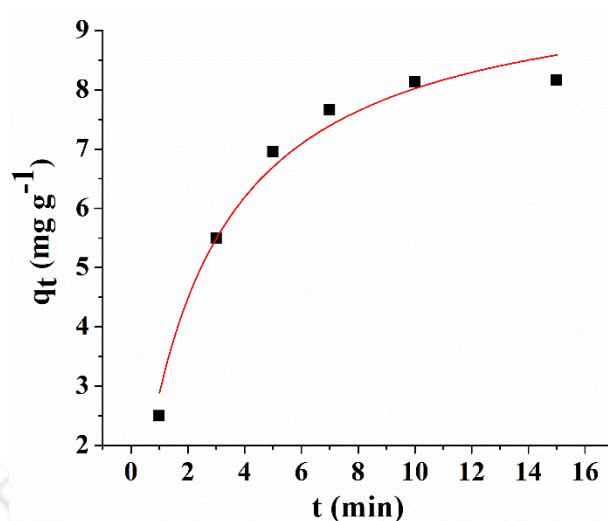


Fig. A6.11. Nonlinear pseudo-second order curve fitting for manganese adsorption on SnO₂ nanoparticles.

Table A6.5. Nonlinear pseudo-second order model fitting parameters for manganese adsorption on SnO₂ nanoparticles

Cation	Nonlinear pseudo-second order model			R ²
	q _{e,exp} (mg g ⁻¹)	q _{e,cal} (mg g ⁻¹)	k ₂ (g mg ⁻¹ min ⁻¹)	
Manganese	8.16	9.99	0.04	0.97

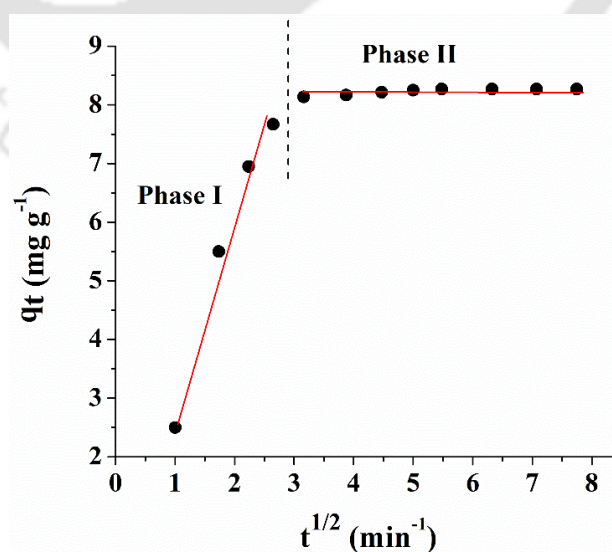


Fig. A6.12. Intraparticle diffusion model for the kinetic data of manganese adsorption onto the SnO₂ nanoparticles.

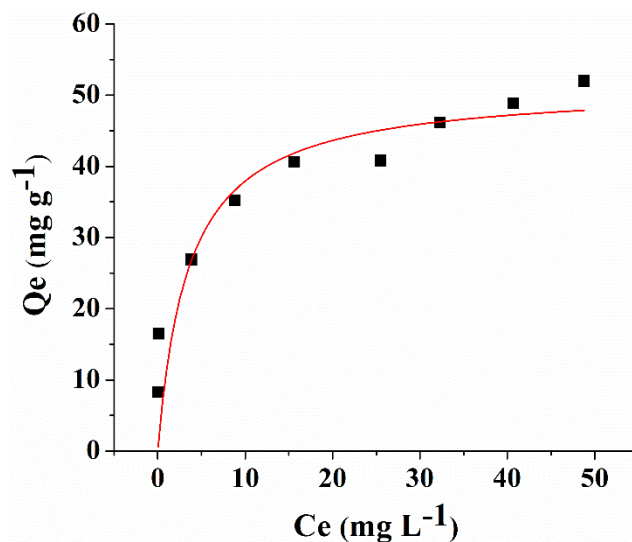


Fig. A6.13. Nonlinear Langmuir isotherm model curve fitting for manganese adsorption on SnO₂ nanoparticles.

Table A6.6. Nonlinear Langmuir isotherm model fitting parameters for manganese adsorption on SnO₂ nanoparticles.

Adsorption Isotherm	Isotherm parameters	Values	RMSE
Langmuir	q_m (mg g ⁻¹)	51.31	5.15
	K_L (L g ⁻¹)	0.28	
	R^2	0.79	

Table A6.7. Comparison of maximum manganese adsorption capacity of different adsorbents

Adsorbent	pH	Maximum adsorption capacity (mg g ⁻¹)	Ref.
Modified zeolite	6	66.10	14
Polyaniline nanocomposite	10	50.25	15
Granular activated carbon	–	2.54	16
Modified alumina	4.4	1.31	17
SnO₂ NP	6.8	52.63	This work

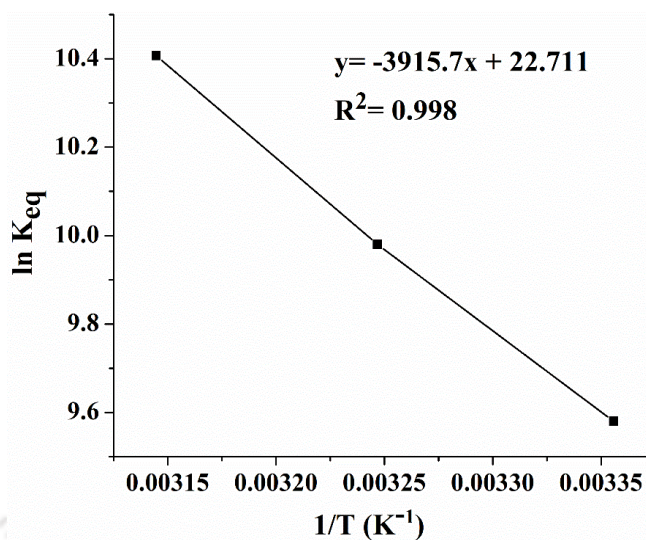


Fig. A6.14. VantHoff's plot for manganese adsorption on Sn(II)-MOF derived SnO₂ nanoparticles.

Table A6.8. Thermodynamic parameters for manganese adsorption on Sn(II)-MOF derived SnO₂ nanoparticles.

Temperature (K)	K _{eq}	ln K _{eq}	ΔH° (kJ mol ⁻¹)	ΔS° (J mol ⁻¹ K ⁻¹)	ΔG° (kJ mol ⁻¹)
298	1,4516.99	9.58	32.55	188.81	-23.73
308	2,1686.84	9.98			-25.55
318	3,3096.38	10.40			-27.51

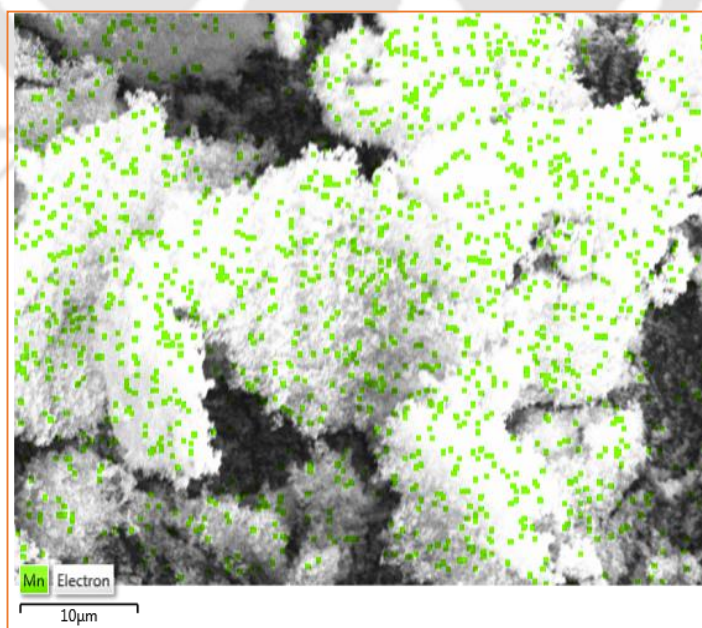


Fig. A6.15. FESEM-EDX mapping of manganese (green dots) adsorbed on SnO₂ NPs.

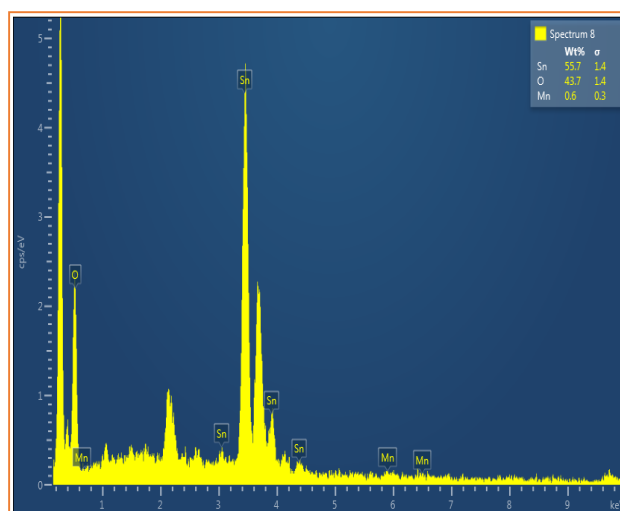


Fig. A6.16. EDX spectrum for elemental analysis after Mn^{2+} adsorption on SnO_2 NPs.

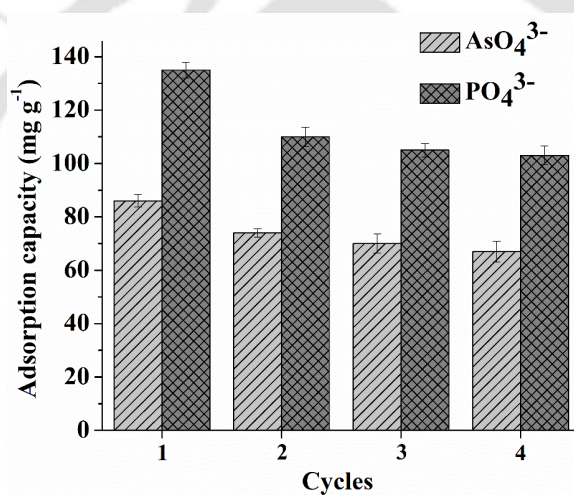


Fig. A6.17. Multi-cycle reusability of the synthesized Sn(II)-MOF in the adsorption of arsenate and phosphate from the aqueous medium

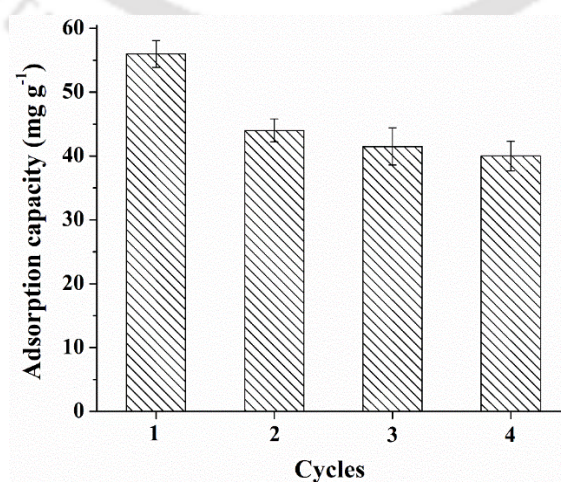


Fig. A6.18. Multi-cycle reusability of the Sn(II)-MOF derived SnO_2 NPs in adsorption of Mn^{2+} from the aqueous medium.

References

- [A6.1] M. Jian, B. Liu, G. Zhang, R. Liu and X. Zhang, *Colloids Surf., A*, 2015, **465**, 67–76.
- [A6.2] T.A. Vu, G.H. Le, C.D. Dao, L.Q. Dang, K.T. Nguyen, Q.K. Nguyen, P.T. Dang, H.T. Tran, Q.T. Duong, T.V. Nguyen and G.D. Lee, *RSC Adv.*, 2015, **5**, 5261-5268.
- [A6.3] J. Li, Y.N. Wu, Z. Li, M. Zhu and F. Li, *Water Sci. Technol.*, 2014, **70**, 1391-1397.
- [A6.4] C. Wang, X. Liu, J.P. Chen and K. Li, *Sci. Rep.*, 2015, **5**, 16613.
- [A6.5] S. Hou, Y.N. Wu, L. Feng, W. Chen, Y. Wang, C. Morlay and F. Li, *Dalton Trans.*, 2018, **47**, 2222-2231.
- [A6.6] B.J. Zhu, X.Y. Yu, Y. Jia, F.M. Peng, B. Sun, M.Y. Zhang, T. Luo, J.H. Liu and X.J. Huang, *J. Phys. Chem. C*, 2012, **116**, 8601–8607.
- [A6.7] X.He, F. Deng, T.Shen, L. Yang, D. Chen, J. Luo, X. Luo, X. Min and F. Wang, *J. Colloid Interface Sci.*, 2019, 539, 223-234.
- [A6.8] H. Liu, W. Guo, Z. Liu, X. Li and R. Wang, *RSC Adv.*, 2016, **6**, 105282–105287.
- [A6.9] K.Y.A. Lin, S.Y. Chen and A.P. Jochems, *Mater. Chem. Phys.*, 2015, **160**, 168–176.
- [A6.10] H. Qiu, L. Yang, F. Liu, Y. Zhao, L. Liu, J. Zhu and M. Song, *Environ. Sci. Pollut. Res.*, 2017, **24**, 23694– 23703.
- [A6.11] Q. Xie, Y. Li, Z.Lv, H. Zhou, X. Yang, J. Chen and H. Guo, *Sci. Rep.*, 2017, **7**, 3316.
- [A6.12] K.Y. Koh, C. Wang and J.P. Chen, *J. Colloid Interface Sci.*, 2019, **543**, 343-351.
- [A6.13] M. Nehra, N. Dilbaghi, N.K. Singhal, A.A. Hassan, K.H. Kim and S. Kumar, *Environ. Res.*, 2019, **169**, 229-236.
- [A6.14] A. Ates and G. Akgül, *Powder Technol.*, 2016, **287**, 285-291.
- [A6.15] M. Hallajiqomi, H. Eisazadeh, *J. Ind. Eng. Chem.*, 2017, **55**, 191-197.
- [A6.16] A. Jusoh, W.H. Cheng, W.M. Low, A. Nora'aini and M.M.M. Noor, *Desalination*, 2005, **182**, 347-353.
- [A6.17] M.U. Khobragade and A. Pal, *J. Environ. Chem. Eng.*, 2014, **2**, 2295-2305.

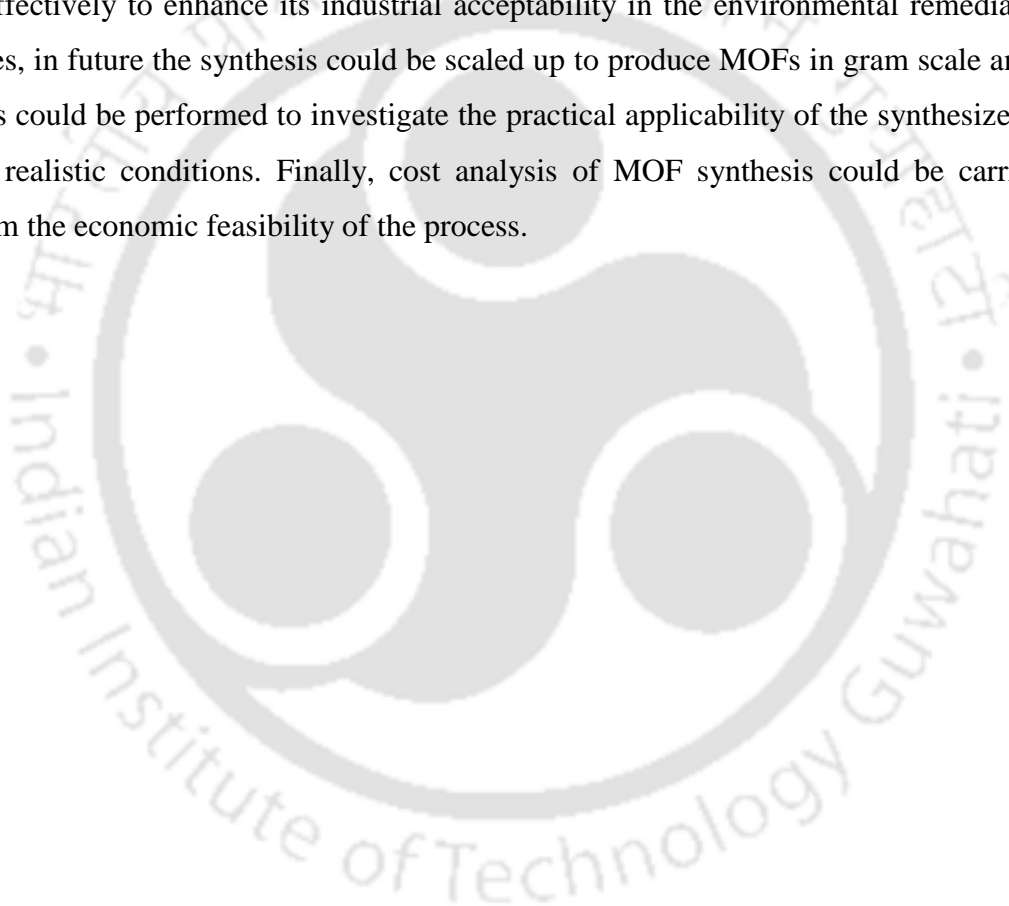
Conclusion and Future Perspective

In summary, the thesis has some substantial and promising results in the domain of sustainable environmental chemistry and engineering where environmentally toxic organic compounds or cations/ anions are captured by a series of hydrothermally/ solvothermally synthesized water-stable Sn-based metal-organic-framework. Notably, the material synthesis was carried out following facile and greener synthetic route under mild conditions, where the use of toxic solvents were avoided. All the synthesized materials exhibited high thermal as well as aqua-stability and were subsequently explored for its water treatment potential. Analytical methods, especially FT-IR, IC, DLS, and AAS, heavily corroborated the efficient sorption of the target analytes on the synthesized adsorbent material. In general, the findings will help understand the relatively underexplored space of Sn(II) as inorganic metal ion for stable composite material synthesis and its potential application in water treatment. Each of the synthesized Sn(II)-MOF unveiled interesting characteristic properties that were exploited in the remediation of toxic environmental pollutants from the aqueous medium.

The rhomboidal shaped benzene-1,4-dicarboxylate based Sn(II)-MOF illustrated excellent anionic dye removal capacity along with multi-cyclic reusability. The findings demonstrated that the low surface area of the adsorbent was not a limiting factor for dye removal from the aqueous medium. The findings clearly suggest that the electrostatic interaction and the presence of the abundant amount of C=O and –OH functional groups played a vital role in preferential adsorption of the anionic dyes. On the other hand, the spherical Sn(II)- benzene-1,3,5-tricarboxylate MOF displayed significant fluoride removal efficiency and remarkable anti-interference activity in the presence of other co-existing anions. Besides, the 1,2,4,5-benzenetetracarboxylate based fluorogenic probe exhibited selective sensing of the CrO_4^{2-} ions from the aqueous medium and displayed good high-pressure CO_2 adsorption potential at atmospheric pressure, which corroborated to its highly porous nature and good internal surface area. Furthermore, the Sn(II)-MOF synthesized using BDC recovered from waste PET bottles demonstrated remarkable removal efficiency towards the environmentally hazardous anions viz. AsO_4^{3-} and PO_4^{3-} .

Moreover, the SnO_2 NPs synthesized following the Sn(II)-MOF calcination route displayed high colloidal stability, as confirmed from the highly negative zeta potential value. The findings also elucidate the role of surface charge reversal in excellent Mn(II) ions removal efficiency from the aqueous medium. Importantly, the present work can prove to be an economically viable method of recycling the waste PET bottle into value-added adsorbent material for the efficient decontamination of water.

In our present work, we have examined the potential of Sn(II) as an inorganic metal cation for MOF synthesis. From the future perspective, Sn(IV) could be an exciting choice for water-stable MOF synthesis because of its high oxidation state and coordination number. The literature reports on Sn(IV)-based MOFs are still very scarce and therefore needs to be explored in detail. The high valency of the Sn(IV) requires excess organic ligand to balance the ionic charges and hence can form a strong coordination bond with the polytopic organic ligand. Besides, a greener synthetic approach is vital for the scalable synthesis of MOFs. In this context, bio-derived solvents like cyrene, which can replace conventional toxic industrial solvents like DMF, could be an attractive choice MOF synthesis. Therefore, the exploration to synthesize biomass-derived solvents is a prerequisite for the development of greener MOFs cost-effectively to enhance its industrial acceptability in the environmental remediation field. Besides, in future the synthesis could be scaled up to produce MOFs in gram scale and column studies could be performed to investigate the practical applicability of the synthesized material under realistic conditions. Finally, cost analysis of MOF synthesis could be carried out to confirm the economic feasibility of the process.



List of Publications

1. **A. Ghosh** and G. Das, Green synthesis of Sn(II)-BDC MOF: Preferential and efficient adsorption of anionic dyes, *Microporous Mesoporous Mater.*, 2020, **297**, 110039. (IF= 4.551).
2. **A. Ghosh** and G. Das, Green synthesis of a novel water-stable Sn(II)-TMA metal– organic framework (MOF): an efficient adsorbent for fluoride in aqueous medium in a wide pH range, *New J. Chem.*, 2020, **44**, 1354-1361. (IF= 3.288).
3. **A. Ghosh**, S. Gumma and G. Das, Hydrolytically stable luminescent Sn(II)-BTEC hybrid material: Selective sensing of chromate ions in aqueous medium, *J. Photochem. Photobiol. A.*, 2020, **403**, 112863. (IF= 3.306).
4. **A. Ghosh** and G. Das, Facile synthesis of Sn(II)-MOF using waste PET bottles as organic precursor and its derivative SnO₂: Role of interfacial charge reversal in adsorption, *J. Environ. Chem. Eng.* 2021, **9**, 105288. (IF= 4.30).
5. **A. Ghosh** and G. Das, Environmentally benign synthesis of fluorescent carbon nanodots using waste PET bottle: Highly selective and sensitive detection of Pb²⁺ ions from the aqueous medium, *New J. Chem.*, doi.org/10.1039/D1NJ00961C (accepted). (IF= 3.288).
6. D. Sachan, **A. Ghosh**, and Gopal Das, Valorization of aquatic weed *Salvinia minima* to value-added material: An eco-friendly biosorbent for preferential removal of dye and heavy metal from aqueous medium, *Int. J. Environ. Sci. Technol* (Ref No. JEST-D-21-00717). (under review). (IF= 3.05).
7. **A. Ghosh** and G. Das. Metal-organic frameworks as superior adsorbents for removal of anionic contaminants from the aqueous environment: A comprehensive review. (manuscript under preparation)
8. **A. Ghosh** and G. Das. Strategies to improve sensitivity and selectivity of MOF-based hybrids. CRC press. (book chapter under preparation).

NAME: Arnab Ghosh

ADDRESS: P-13A Sarsuna Main Road Kolkata-61, India

CONTACT NO: 7086867788

EMAIL ID: arnab.ghosh@iitg.ac.in/ arnabg3@gmail.com



Academic Summary

2015-2021: Ph.D. in Environmental Engineering, Centre for Environment, Indian Institute of Technology, Guwahati, India.

Thesis title: “**Environmentally Benign Synthesis of Sn(II)-based Metal-Organic Framework and its Derivative SnO₂ Nanoparticles for the Decontamination of Water**”.

2011-2013: M.Tech in Environmental Engineering, (CGPA-8.44), National Institute of Technology Karnataka (NITK), Surathkal, India.

2011: Qualified in Graduate Aptitude Test in Engineering (GATE) for Master’s Fellowship.

2006-2010: B.Tech in Biotechnology, (CGPA-8.23), WBUT, West Bengal, India.

2004-2006: Higher Secondary (10+2) in Science, (61.5%) from W.B.C.H.S.E.

2004: Secondary Education, (85%) from I.C.S.E.

Professional Summary

2014-2015: Worked as a Junior Research Fellow (JRF) at National Institute of Technology Durgapur, on the Indo-Brazil project “Synthesis of bioethanol in a membrane integrated hybrid system- A green technology approach”.

2013-2014: Worked as Engineer Trainee at Unitech Water Technologies Pvt. Ltd., Kolkata in the field of water and wastewater treatment process design and techno-commercial offer preparation.

Research Interest

- ❖ Metal-organic frameworks, novel metal oxide nanocomposites, their synthesis and application in environmental cleanup.
- ❖ Sustainable water treatment technologies and remediation of emerging aqueous contaminants like PPCPs, pesticides etc.
- ❖ Eco-friendly synthesis of carbon nanodots using recyclable materials and its application as a chemosensor in sensing toxic ions from aqueous medium.

- ❖ Valorization of industrial or agricultural wastes to biochar/ silica nanoparticles/ zeolites or other novel adsorbents for wastewater treatment.
- ❖ Lignocellulosic bioethanol production following greener approach.

Expertise

- ❖ Proficient in teaching Biotechnology (Biomaterials, r-DNA technology, immunology etc.) and Environmental Engineering (physico-chemical processes for water and wastewater treatment, environmental biotechnology, air, noise and solid waste management etc.) subjects.
- ❖ Planning and execution of research project on the synthesis of conventional and novel porous materials and their tailor-made functionalization for environmental applications.
- ❖ Development of fluorogenic probe for luminescent detection of environmentally relevant anions and cations from aqueous solution.
- ❖ Spectroscopic (UV-vis, Fluorescence, FT-IR) study and analysis.
- ❖ Well trained with equipment viz. Surface Area Analyzer, Ion Chromatography (IC), Atomic Absorption Spectrophotometer (AAS), Dynamic Light Scattering (DLS), Total Organic Carbon (TOC) analyzer and Powder X-Ray Diffraction (PXRD) for sample characterization and analysis.
- ❖ Process optimization and statistical analysis using response surface methodology.
- ❖ Analytical skills and writing of scientific research articles.

Publications

1. **A. Ghosh** and G. Das, Green synthesis of Sn(II)-BDC MOF: Preferential and efficient adsorption of anionic dyes, *Microporous Mesoporous Mater.*, 2020, **297**, 110039. (IF= 4.551).
2. **A. Ghosh** and G. Das, Green synthesis of a novel water-stable Sn(II)-TMA metal– organic framework (MOF): an efficient adsorbent for fluoride in aqueous medium in a wide pH range, *New J. Chem.*, 2020, **44**, 1354-1361. (IF= 3.288).
3. **A. Ghosh**, S. Gumma and G. Das, Hydrolytically stable luminescent Sn(II)-BTEC hybrid material: Selective sensing of chromate ions in aqueous medium, *J. Photochem. Photobiol. A.*, 2020, **403**, 112863. (IF= 3.306).
4. **A. Ghosh** and G. Das, Facile synthesis of Sn(II)-MOF using waste PET bottles as organic precursor and its derivative SnO₂: Role of interfacial charge reversal in adsorption, *J. Environ. Chem. Eng.*, 2021, **9**, 105288 (IF= 4.30).

5. **A. Ghosh** and G. Das, Environmentally benign synthesis of fluorescent carbon nanodots using waste PET bottle: Highly selective and sensitive detection of Pb^{2+} ions from the aqueous medium, *New J. Chem.*, doi.org/10.1039/D1NJ00961C (*accepted*).
6. Deepa Sachan, **A. Ghosh**, and Gopal Das, Valorization of aquatic weed *Salvinia minima* to value-added material: An eco-friendly biosorbent for preferential removal of dye and heavy metal from aqueous medium, *Int. J. Environ. Sci. Technol* (Ref No. JEST-D-21-00717). (*under review*). (*IF= 3.05*).
7. **A. Ghosh** and G. Das. Metal-organic frameworks as superior adsorbents for removal of anionic contaminants from the aqueous environment: A comprehensive review. (*manuscript under preparation*)
8. **A. Ghosh** and G. Das. Strategies to improve sensitivity and selectivity of MOF-based hybrids. *CRC press*. (*book chapter under preparation*).
9. A. Sharma, **A. Ghosh**, R.A. Pandey and S.N. Mudliar, Wet air oxidation pretreatment of mixed lignocellulosic biomass to enhance enzymatic convertibility. *Korean Chem. Eng. Res.*, 2015, **53**, 216-223.

Presentations and Awards

1. Poster presented in '**Recycle 2018**', Indian Institute of Technology, Guwahati.
2. **Awarded** best Oral Presentation in '**2nd International Conference on New Frontiers in Chemical, Energy and Environmental Engineering (INCEEE) 2019**', National Institute of Technology, Warangal.
3. Poster presented in '**Research Conclave 2018**', Indian Institute of Technology, Guwahati.
4. **Awarded** best Oral Presentation in '**Lecture Series-1 2019**', Centre for The Environment, Indian Institute of Technology, Guwahati.
5. Poster presented in '**Modern Trends in Inorganic Chemistry (MTIC-XVIII) 2019**', Indian Institute of Technology, Guwahati.
6. Poster presented in '**International Conference on Advanced Nanomaterials and Nanotechnology (ICANN) 2019**', Indian Institute of Technology, Guwahati.
7. **Awarded** best Poster presentation in '**International Conference on Functional Materials (ICFM) 2020**', Indian Institute of Technology Kharagpur.
8. **Awarded** 3rd prize in Poster presentation in '**Issues and Challenges in Water Treatment and Allied Research for Sustainable Environment (WATER 2020)**', Indian Institute of Technology, Guwahati.

9. Oral presentation in ‘**International Conference on Sustainable Water Resources Management under Changed Climate (ICSWRM) 2020**’, School of Water Resources Engineering, Jadavpur University, Kolkata.

Workshops attended

- One-day Workshop on ‘**Theory and demonstration session on thermal analysis (DSC and TGA) of materials, 2019**’, Department of Chemical Engineering, IIT Guwahati in association with the Indian Institute of Chemical Engineers - Guwahati Regional Centre and the Central Instruments Facility.
- One-day Workshop on ‘**Intellectual Property Rights**’, Research Conclave 2019, IIT Guwahati.

Referees

1. Prof. Gopal Das (Head, Dept. of Chemistry, IIT Guwahati)

Email: gdas@iitg.ac.in

2. Dr. Lal Mohan Kundu (Associate Professor, Dept. of Chemistry, IIT Guwahati)

Email: lmkundu@iitg.ac.in

3. Prof. Sasidhar Gumma (Professor, Dept. of Chemical Engineering, IIT Tirupati)

Email: s.gumma@iittp.ac.in

Declaration:

I hereby declare that all the information furnished in my curriculum vitae are true to the best of my knowledge.

Arnab Ghosh

(Arnab Ghosh)

Place: IIT Guwahati, India